MARTIN MARIETTA ENERGY SYSTEMS LIBRARIES
3 4456 0250870 2

CENTRAL RESEARCH LIBRARY
DOCUMENT COLLECTION

cy. 3

ORNL-4440
UC-25 – Metals, Ceramics, and Materials

FUELS AND MATERIALS DEVELOPMENT PROGRAM

QUARTERLY PROGRESS REPORT

FOR PERIOD ENDING JUNE 30, 1969

LIBRARY
REFERENCE COPY

OAK RIDGE NATIONAL LABORATORY
operated by
UNION CARBIDE CORPORATION
for the
U.S. ATOMIC ENERGY COMMISSION

Printed in the United States of America. Available from Clearinghouse for Federal
Scientific and Technical Information, National Bureau of Standards,
U.S. Department of Commerce, Springfield, Virginia 22151
Price: Printed Copy $3.00; Microfiche $0.65

LEGAL NOTICE

This report was prepared as an account of Government sponsored work. Neither the United States, nor the Commission, nor any person acting on behalf of the Commission:

A. Makes any warranty or representation, expressed or implied, with respect to the accuracy, completeness, or usefulness of the information contained in this report, or that the use of any information, apparatus, method, or process disclosed in this report may not infringe privately owned rights; or

B. Assumes any liabilities with respect to the use of, or for damages resulting from the use of any information, apparatus, method, or process disclosed in this report.

As used in the above, "person acting on behalf of the Commission" includes any employee or contractor of the Commission, or employee of such contractor, to the extent that such employee or contractor of the Commission, or employee of such contractor prepares, disseminates, or provides access to, any information pursuant to his employment or contract with the Commission, or his employment with such contractor.

ORNL-4440

Contract No. W-7405-eng-26

METALS AND CERAMICS DIVISION

FUELS AND MATERIALS DEVELOPMENT PROGRAM QUARTERLY PROGRESS REPORT FOR PERIOD ENDING JUNE 30, 1969

Compiled by

P. Patriarca

Edited by

D. J. Rucker

OCTOBER 1969

OAK RIDGE NATIONAL LABORATORY
Oak Ridge, Tennessee
operated by
UNION CARBIDE CORPORATION
for the
U.S. ATOMIC ENERGY COMMISSION

MARTIN MARIETTA ENERGY SYSTEMS LIBRARIES

3 4456 0250870 2

FOREWORD

This quarterly progress report describes research and development on nuclear fuels and materials performed at the Oak Ridge National Laboratory for the U.S. Atomic Energy Commission. With several exceptions, as noted below in the listing of specific programs, the work is sponsored by the Fuels and Materials Branch of the Division of Reactor Development and Technology. Classified aspects of the Nitride Fuels Development activity and work on fuels and materials for isotopic heat sources are reported separately.

The report is presented in five parts according to AEC Activity titles provided by the Fuels and Materials Branch, RDT.

Program Title	ORNL Division(s)	Person in Charge	Principal Investigator(s)
I. Fuels and Claddings			
Development of Fast-Reactor Oxide Fuels	Metals and Ceramics Chemical Technology Reactor	P. Patriarca	A. L. Lotts J. L. Scott R. E. Brooksbank
Development of High-Performance LMFBR Fuels	Metals and Ceramics Reactor	P. Patriarca	J. L. Scott H. C. McCurdy A. L. Lotts
Fission-Gas Release and Physical Properties of Fuel Materials During Irradiation	Reactor Chemistry	O. Sisman	R. M. Carroll J. G. Morgan
Zirconium Metallurgy	Metals and Ceramics	J. R. Weir, Jr.	P. L. Rittenhouse
II. Coolants			
Alkali-Metal Corrosion Studies	Metals and Ceramics Reactor	W. O. Harms	J. H. DeVan A. P. Litman
III. Radiation Damage to Structural Materials			
Behavior of Refractory Materials Under Irradiation	Reactor Chemistry	G. M. Watson	G. W. Keilholtz

Program Title	ORNL Division(s)	Person in Charge	Principal Investigator(s)
Fast-Neutron Irradiation Effects on Electrical Insulators*	Reactor Chemistry	G. M. Watson	G. W. Keilholtz
Mechanical Properties Research and LMFBR Cladding and Structural Materials Development†	Metals and Ceramics	J. R. Weir, Jr.	H. E. McCoy, Jr.
IV. Techniques of Fabrication and Testing			
Tungsten Metallurgy	Metals and Ceramics	P. Patriarca	H. Inouye W. R. Martin G. M. Slaughter J. O. Stiegler H. E. McCoy, Jr.
Nondestructive Test Development	Metals and Ceramics	W. O. Harms	R. W. McClung
Joining Research on Nuclear Materials†	Metals and Ceramics	G. M. Adamson, Jr.	G. M. Slaughter
Development of LMFBR Tubing Fabrication‡	Metals and Ceramics	G. M. Adamson, Jr.	W. R. Martin
Development of Fuel Element Fabrication	Metals and Ceramics	G. M. Adamson, Jr.	J. V. Cathcart W. R. Martin R. W. McClung

*Sponsored by Reactor Power Systems Branch, Division of Space Nuclear Systems.

†Partially sponsored by Liquid Metals Branch, Division of Reactor Development and Technology.

‡Sponsored by Liquid Metals Branch, Division of Reactor Development and Technology.

Program Title	ORNL Division(s)	Person in Charge	Principal Investigator(s)
V. Engineering Properties of Reactor Materials			
Physical and Mechanical Metallurgy of Refractory Alloys	Metals and Ceramics	P. Patriarca	H. Inouye R. W. McClung D. L. McElroy G. M. Slaughter H. E. McCoy, Jr.
Cladding Materials for Space Isotopic Heat Sources*	Metals and Ceramics	P. Patriarca	R. G. Donnelly H. Inouye

*Sponsored by Isotopes and Materials Branch, Division of Space Nuclear Systems.

CONTENTS

Page

Summary xiii

Part I. Fuels and Claddings

1. Development of Fast-Reactor Oxide Fuels 3
   Preparation of $(U,Pu)O_2$ Fuels 3
   Development of Fabrication Processes 4
      Sphere-Pac 4
      Pelletization of Sol-Gel $(U,Pu)O_2$ 6
      Capsule Fabrication 9
   Characterization of $(U,Pu)O_2$ Fuels 12
      Analytical Chemistry 12
      Thermal Conductivity of Lithium Fluoride 14
      Radial Heat-Flow Apparatus for Measurements at 10 atm and 1400°K 14
      Analytical Characterization 14
      Thermodynamic Calculations: Chemical Effects of Nuclear Burnup on $(U,Pu)O_2$ Fuels 18
      Interaction of Fission Products 21
   Irradiation Testing of $(U,Pu)O_2$ Fuels 22
      Uninstrumented Thermal-Flux Irradiation Tests 23
      ORR Instrumented Tests 27
      Transient Testing of Sol-Gel $(U,Pu)O_2$ 27
      Fast-Flux Irradiation Tests 28
      Irradiation Test Calculations 28
2. Development of High-Performance LMFBR Fuels 29
   Synthesis, Fabrication, and Characterization of Nitride Fuels 30
      Synthesis and Fabrication of Mixed Nitrides 30
      Apparatus for Synthesizing Metal Nitrides 32
      Characterization of Nitride Fuels 32
   Synthesis, Fabrication, and Thermodynamic Properties of Carbonitride Fuels 33
      Manufacture of UC, UN, and U(C,N) from UO_2 33

Compatibility of Mixed-Nitride and Carbonitride Fuels with LMFBR Cladding Alloys 37

Ternary U-V-C System 38

Thermodynamic Investigations of High-Performance Fuel Systems 41

Thermodynamic Stability of UVC_2 42

Measurements of the Physical Properties of (U,Pu)N Alloys 43

Irradiation Testing of Nitride Fuels for LMFBR Applications 43

Thermal-Flux Irradiation Tests 43

Fabrication of ETR Capsules for (U,Pu)N 44

Irradiation Testing of UN in ORR 44

3. Fission-Gas Release and Physical Properties of Fuel Materials During Irradiation 56

The Effect of Stored Energy in UO_2 on Measurements of Thermal Diffusivity During Irradiation 56

Effect of Temperature and Burnup on Release of Fission Gas from $(U_{0.75},Pu_{0.25})O_2$ 56

Release of Fission Gas from UO_2 58

4. Zirconium Metallurgy 59

Texture Effects, Texture Development, and Anisotropy of Properties 59

Texture Development in Zircaloy Tubing 59

Fabrication and Texture Control of Zirconium Tubing 62

Texture Control in Zircaloy Tubing 62

Biaxial Yielding in Zircaloy Tubing 68

Part II. Coolants

5. Alkali-Metal Corrosion Studies 75

Studies of the Corrosion of Vanadium Alloys in Sodium . . . 75

Effects of Oxygen on the Compatibility of Vanadium and Sodium 75

Mass Transfer of Interstitial Impurities Between Vanadium Alloys and Types 304L and 321 Stainless Steel in Sodium 78

Interstitial Contamination of Vanadium and Its Alloys 81

Compatibility of Stainless Steel and Insulation in LMFBR Systems 84

Effect of Insulation on Oxidation of Stainless Steel 84

Corrosion of Refractory Alloys in Lithium, Potassium, and Sodium 89

Effect of Oxygen on Compatibility of Refractory Metals and Alkali Metals 90

Partitioning of Oxygen Between Potassium and Zirconium and Sodium and Zirconium 92

Refractory Alloy – Lithium Thermal Convection Loop Tests 94

T-111 Forced Circulation Liquid Lithium Loop (FCLLL-1) 96

Part III. Radiation Damage to Structural Materials

6. Behavior of Refractory Materials Under Irradiation 111

Irradiation Damage to Nonfissionable Refractory Materials 111

Refractory Metal Carbides 111

Effects of Irradiation on LMFBR Fuels 112

Effects of Helium Gas Produced by Fast Neutrons in Depleted UN 112

Fast-Neutron Effects on Materials for Neutron Absorption in Fast Reactors 113

7. Fast-Neutron Irradiation Effects on Electrical Insulators . . 114

General Survey of Fast-Neutron Effects on Electrical Insulators 114

Silicon Oxynitride 114

Single-Crystal Materials and Other Advanced Materials 115

Irradiation of High-Density Commercial Al_2O_3 Products Considered for Thermionic Insulators 115

8. Mechanical Properties Research and LMFBR Cladding and Structural Materials Development 117

Mechanical Properties of Type 316 and Titanium-Modified Type 316 Stainless Steel 117

Radiation Damage in Incoloy 800 123

Cyclotron Injection of Helium to Simulate Fast-Reactor Irradiation 129

Calculation of Displacement Damage Produced by Light Ions 129
Utilization of EBR-II 132
Examination of EBR-II Safety-Rod Thimble 132
Vanadium Alloy Studies and Effects of Impurities 135
Voids in Vanadium Irradiated in EBR-II 135
Mechanical Properties of Hastelloy N and Related Compositions 137
Aging of Titanium-Modified Hastelloy N 137

Part IV. Techniques of Fabrication and Testing

9. Tungsten Metallurgy 145
Primary and Secondary Working of Tungsten Alloys 145
Mechanical Properties of Extruded Tungsten Tubing . . . 145
Chemical Vapor Deposition of Tungsten Alloys 148
Chemical Vapor Deposition of Tungsten for Tests of Mechanical Properties 148
Chemical Vapor Deposition of Tungsten-Rhenium Alloys 148
Chemical Vapor Deposition of Vanadium 152
Long-Time Creep-Rupture Properties of Tungsten Alloys . . . 152
10. Nondestructive Test Development 155
Electromagnetic Inspection Methods (Eddy Currents) 155
Ultrasonic Inspection Methods 157
Optical Visualization of Ultrasound 157
Frequency Analysis 158
Penetrating Radiation and Holographic Inspection Methods . . 159
Radiation Scattering 159
11. Joining Research on Nuclear Materials 160
The Effect of Minor Variations in Chemical Composition on Weldability 160
Effect of Minor Elements on the Hot Ductility of Inconel 600 161
Effect of Certain Minor Elements on the Ductility of Incoloy 800 at Intermediate Temperatures 166
Development of Welding Procedures for Commercial and Modified Alloys 167

Joining Development in Support of Fast Flux Test Facility 167

The Effect of Defects on the Mechanical Properties of Weldments 175

12. Development of LMFBR Tubing Fabrication 176

Fabrication Studies on Type 316 Stainless Steel 176

Drawing of Type 316 Stainless Steel Tubing 176

Fabrication Studies on Titanium-Modified Type 304 Stainless Steel 181

Evaluation of Drawn and Planetary-Swaged Tubes of Titanium-Modified Type 304L Stainless Steel 181

Biaxial Stress-Rupture Properties of Titanium-Modified Type 304L Stainless Steel Tubing 190

13. Development of Fuel Element Fabrication 192

Fabrication Studies of Dispersion Fuel Plates 192

Crushing of UAl_x Fuel 192

Fabrication of Composite Plates Containing ZrO_2 195

Metallographic Examination of Miniature Composite Plates Bombarded with Protons for Study of Blistering 196

Roll Bonding 197

Susceptibility to Blistering of Fuel Plates Containing Shaped Fuel Cores 198

HFIR Fuel Plates with Increased Fuel Loading 200

Welding and Assembly 203

Joining Fuel Plates to Side Plates 203

Irradiation Testing of Dispersion Fuel Plates 205

Status of Current and Planned Tests in the ETR 205

Characterization of Mini-Type Test Plates Containing U_3O_8 206

Characterization of Mini-Type Test Plates That Contain B_4C 208

Postirradiation Examination of HFIR Fuel Elements . . . 209

Determination of Homogeneity in Fuel Plates 213

Radiographic Densitometry 213

X-Ray Attenuation 213

Radiation Scattering 215

Part V. Engineering Properties of Reactor Materials

14. Physical and Mechanical Metallurgy of Refractory Alloys . . . 219
Basic Physical Metallurgy Studies 219
Solubility, Diffusivity, and Permeability of Interstitials in Refractory Metals 219
Development of Age-Hardening Refractory Alloys 220
Thermodynamics of Spinodally Decomposed Alloys 224
Long-Time, High-Temperature Mechanical Properties of Commercial Refractory Alloys 227
Tantalum Alloys 227
Welding and Brazing 233
Component Fabrication 233
Mechanical Properties of Brazed Joints 234
Physical Properties of Refractory Materials 235
High-Temperature Electrical Resistivity 235
Development of an Electrical Heating Method for Determining Thermal Conductivity 236
15. Cladding Materials for Space Isotopic Heat Sources 237
Studies of Commercial Superalloys 237
Mechanical Properties of Haynes Alloy No. 25 237
Aging Behavior of Superalloys 239
Development of Improved Alloys 241
Creep Studies 241
Evaporation Studies 241

SUMMARY

PART I. FUELS AND CLADDINGS

1. Development of Fast-Reactor Oxide Fuels

We fabricated pellets 85 and 91% of theoretical density for two capsules for transient tests of sol-gel fuel in the Transient Reactor Test Facility (TREAT). All fuel pins for the two TREAT capsules were loaded, welded, and inspected. All welding and brazing development for the assembly of the TREAT capsules was completed, and each subassembly of the capsule was prepared.

Because we have been having considerable difficulty in measuring the release of gas from mixed-oxide fuel at 1750°C, we substantially altered existing equipment to reduce the background from the system. Our preliminary data on the release of gas from microspheres at 1600°C include 0.05 cm^3/g for the coarse microspheres and 0.27 cm^3/g for the fines. We continued studies on plastic deformation of UO_2 in an attempt to determine the effect of atmosphere and temperature on the deformation of UO_2 derived by the sol-gel and ammonium diuranate (ADU) processes. We also continued our work to determine the relationship between lattice parameter composition and O activity of $(U,Pu)O_2$ and to determine the effect of thermal gradients on composition. In addition, thermodynamic calculations were made to determine the distribution of fission products that results from burnup of $(U,Pu)O_2$ fuels. This was done by determining the distribution of bound O atoms after various periods of time at full power.

The irradiation of two instrumented capsules that contain Sphere-Pac $(U,Pu)O_2$ continued normally in the Engineering Test Reactor (ETR). One of these, operating at a linear heat rate of about 16.5 kw/ft achieved a burnup level of about 7.5% fissions per initial metal atom (FIMA). We began examination by neutron radiography and gamma scanning of one ETR capsule, which contained three Sphere-Pac $(^{238}U_{0.85},Pu_{0.15})O_2$ fuel rods and one UO_2 fuel rod and was operated at a linear heat rate of 18 kw/ft to a target burnup level of 5% FIMA. No fuel rod showed evident failure. The neutron radiographs indicated increased diameters on both ends of

the fuel columns for all four rods. Since this indicates flux peaking near the low-density thoria insulators, we are beginning a mathematical analysis of this effect. The second instrumented capsule containing Sphere-Pac $(U,Pu)O_2$ fuel was continued in operation in the Oak Ridge Research Reactor (ORR). The temperature at the center of the fuel has been used to control the operation of the capsule, and to date this central temperature has been raised in steps from 100 to 1350°C. There has yet been no indication of restructuring of the fuel. The hazards analysis for the series I experiments in the transient test program was sent to Argonne National Laboratory for review, and the testing of the first two capsules is now scheduled for August. The five encapsulated fuel rods being irradiated in the Experimental Breeder Reactor-II (EBR-II) subassembly X050 have achieved about 50% of the planned exposure of 7500 Mwd. The planning of a series II unencapsulated test is essentially complete.

In our continuing development of methods of calculation for irradiation tests, we have adapted the PRØFIL code to the situation in which fuel is removed from the reactor after restructuring has occurred and placed in a different reactor position with a different flux environment.

2. Development of High-Performance LMFBR Fuels

The facility for x-ray analysis of (U,Pu)N pellets and powders became operational. Both diffractometer and Debye-Scherrer techniques are included.

Additional information was obtained on the reaction path when UC_2 is converted to U(C,N). The U(C,N) was found to remain near the composition in equilibrium with UC_2 and C for the greater part of the conversion.

Vanadium was found to react with UC to form V_2C and U and with UO_2 to form a new phase, UVC_2. This phase is not stable in the presence of C, but can react to form UC_2 and VC. The UC-VC-V_2C three-phase region may be a good buffering system for use of carbide fuels with stainless steels or Mo alloys.

Both single and polycrystalline UN were irradiated unrestrained to burnups above 2 at. % heavy metal with a peak temperature above 2000°C. Markedly greater swelling was noted for polycrystalline pellets. In pins

with cladding restraint, polycrystalline UN, originally 94% of theoretical density, was found to swell into a central void at a temperature of about 1200°C.

3. Fission-Gas Release and Physical Properties of Fuel Materials During Irradiation

Irradiation of spheroids of $(U_{0.75},Pu_{0.25})O_2$ fuel was terminated after 4.5% heavy metal burnup. The temperature at which breakaway gas release occurred was a linear function of burnup until 3.5% burnup. Thereafter, because of a high rate of gas leakage from the specimen, the temperature at which breakaway gas release occurred did not depend primarily on further burnup.

Release of fission gas, thermal diffusivity, and stored energy are being measured on a hollow cylinder of UO_2.

4. Zirconium Metallurgy

Our studies of texture development in Zircaloy tubing have shown that the texture produced during each fabrication step depends on the ratio of wall reduction to diameter reduction in that step and on the texture that existed before the fabrication. All procedures for forming tubing result in essentially identical textures when they are carried out with similar reductions in area, wall thickness, and diameter. When reduction in wall thickness exceeds the reduction in diameter during a fabrication step, the Zr "sheet texture" is formed; if the reverse is true, the basal poles align parallel to the circumference of the tubing. The concepts of texture development that we have demonstrated have been used to explain texture gradients observed in Zircaloy tubing.

We have developed a practical method of controlling the texture in Zircaloy tubing by considering the interrelationships among variables of tubing fabrication and applying our concepts of texture development. Plots of fabrication variables help us predict the textures that will be formed during any given series of fabrication steps and allow us to design fabrication sequences to produce any of the possible textures desired in the final product.

Simple relationships between the uniaxial yield strength, the intensity of the basal poles of the texture, and the equivalence of certain stress states allow us to construct biaxial yield surfaces for Zircaloy tubing of any texture. These surfaces suggest that differences in biaxial yield stresses between different lots of tubing could exceed 50%. This has been verified experimentally.

PART II. COOLANTS

5. Alkali-Metal Corrosion Studies

Effects of O in Na on its compatibility with V were evaluated in capsule tests at 600°C. In type 304 stainless steel containers, essentially all of the O initially in the Na (up to 4000 ppm) was gettered by the V. The ratio of O in V to O in Na at equilibrium was greater than 10^4. In Mo containers, the percentage of O gettered from Na by V decreased with increasing O concentration in the Na. This apparently resulted from mass transfer of Mo or Fe and Ni from the capsules to the V.

A thermal convection loop test with a ratio of 0.24 between the surface areas of V and stainless steel has operated 1700 hr. Vanadium specimens from dissimilar-alloy static capsule tests of type 304L stainless steel and V showed weight gains and darkened surfaces after 500 hr at 800°C.

To evaluate the effect of interstitial contamination of V and its alloys on mechanical properties, an apparatus has been designed to obtain creep data under controlled environments. In the range 10^{-5} to 10^{-7} torr, we found no pick-up of C or N by V, but O increased at 6×10^{-6} torr and higher. Contamination can be prevented at 1.6×10^{-5} torr by wrapping the specimens with Ta foil. In a study of the oxidation of V from 410 to 890°C, the maximum rate occurred at 550°C at both 2×10^{-7} and 2×10^{-6} torr O_2 pressure.

We have completed all but the very long-term studies of the compatibility of thermal insulation with stainless steels in dry and moist air. We have concluded from metallographic and kinetic data that there is

little effect of contact with insulation on the scaling of either type 304L or 316 stainless steel up to 760°C. We are now assembling the equipment to be used in the second phase of the program in which the effect of an Na leak on compatibility will be evaluated.

The amount of O in Li does not measurably affect the amount of Nb or Ta that will dissolve in it; however, the amount of Nb or Ta that dissolves in K or Na is highly dependent on the O initially in the liquid metal. On the other hand, when Nb or Ta contains O, attack by Li is much more severe and occurs at lower O concentrations than with either Na or K.

To determine the influence of stainless steel components on the partitioning of O between Zr and Na, we conducted static capsule tests at 815°C. In all the tests, the Zr specimens exhibited a surface deposit that increased with increasing O in Na, and chemical results indicated that Fe, Mn, C, O, N, and H had transferred from the stainless steel to the Zr. This caused a decrease in the percentage of O recovered by the Zr as the O concentration of the Na increased.

When compared with those from either hotter or cooler regions, T-222 bend specimens from the intermediate temperature zone (1220 to 1280°C) of a T-222 thermal convection loop that circulated Li for 3000 hr at 1350°C were relatively brittle. Although the N content of these samples had increased slightly during the Li exposure, no significant concentration gradients were found in the specimens. Metallographic examination showed the bend fractures to be intergranular, and we concluded that thermal treatment of the specimens was responsible for the observed loss in ductility.

We have completed the final assembly of a T-111 forced circulation loop (FCLLL-1) designed to circulate Li at 1370°C. The loop was installed in the vacuum test chamber, and the resistance-heated section was cycled between ambient temperature and 1370°C to check for leaks. After we filled the primary circuit with Li, we heated it to 1370°C in increments of 315°C. Some instrumental and operational difficulties were encountered and are currently being corrected.

PART III. RADIATION DAMAGE TO STRUCTURAL MATERIALS

6. Behavior of Refractory Materials Under Irradiation

Irradiation of the carbides of Ti, Zr, Ta, Nb, and W at 150°C and postirradiation annealing experiments completed our carbide series of experiments.

The fabrication of an instrumented assembly for irradiation of depleted nitride fuels in the Engineering Test Reactor (ETR) at 1000°C is now nearly complete. This experiment is designed to evaluate the effects of He gas generated internally through the $^{14}N(n,\alpha)^{11}B$ fast-neutron reaction.

Assemblies are being designed for irradiation of fast-neutron absorbers in the Experimental Breeder Reactor-II (EBR-II). Specimens of B_4C, TaC, and Ta metal will be irradiated at 400 and 750°C.

7. Fast-Neutron Irradiation Effects on Electrical Insulators

Specimens of silicon oxynitride (Si_2ON_2), a new high-temperature electrical insulator, were irradiated at about 150°C to estimated neutron fluences ranging from 0.6 to 3.6×10^{21} neutrons/cm^2 (> 1 Mev). All specimens survived intact, and there was little or no release of N_2 during irradiation.

Other advanced materials such as single-crystal Al_2O_3 (sapphire), high-purity single-crystal MgO, and zirconia-doped transparent polycrystalline Y_2O_3 are being fabricated for low-temperature (about 150°C) irradiations.

The irradiation phase of our exhaustive program on commercial alumina products is nearing completion. The high-temperature (400 to 1230°C) irradiation of a long-term Engineering Test Reactor (ETR) assembly is now complete, and the results can be compared with those previously obtained for an identical short-term assembly. The irradiation of the same alumina products at about 800°C in the Experimental Breeder Reactor-II (EBR-II) core position was started.

8. Mechanical Properties Research and LMFBR Cladding and Structural Materials Development

Tests on type 316 stainless steel after 20% cold work showed that cold working increased the rupture life and decreased the minimum creep rate but hastened the onset of third-stage creep. By contrast, cold working modified type 316 stainless steel increased the duration of second-stage creep. Measurements of the variation with strain rate of the flow stress of modified type 316 stainless steel suggest that carbides precipitate during testing at 500°C.

Incoloy 800 samples were irradiated at 450, 550, 650, and 750°C. Creep tests at 650°C showed generally that with increasing irradiation temperature the rupture life and the strain to fracture decreased and the minimum creep rate increased.

Calculations show that particle accelerators can produce higher rates of atom displacement in metals than reactors can. We will take advantage of this by designing experiments to supplement neutron irradiation. We measured the densities of specimens of type 304 stainless steel from an Experimental Breeder Reactor-II (EBR-II) safety-rod thimble. The greatest decrease in density, 3.35%, was observed in a sample from 2 in. above the midplane of the reactor that had been irradiated to 6.5×10^{22} neutrons/cm^2 (> 0.1 Mev) at an estimated temperature of 410°C.

We found voids in samples of V removed from the EBR-II, whereas V–20% Ti irradiated under the same conditions did not contain voids.

We noted moderate changes in the properties of samples of Hastelloy N modified with Ti that were aged at 650 and 760°C and tested in tension at 650°C. Analysis of the carbides extracted from several samples showed that Ti substitutes for Cr in the carbides as the Ti level increases.

PART IV. TECHNIQUES OF FABRICATION AND TESTING

9. Tungsten Metallurgy

We investigated the use of tensile tests of ring specimens for determining the properties of extruded W tubing as an aid in optimizing the extrusion conditions. Preliminary tests on specimens cut from tube shells that were duplex extruded between 1750 and 1250°C showed that the ductility at 300°C is greater for the material extruded at the lower temperature.

In our chemical vapor deposition program we have produced five deposits of W sheet with low F content. Each deposit provided 55 in.^{2} of 0.060-in.-thick sheet for tests of mechanical properties. In efforts to produce W–5% Re sheet of similar quality, we investigated higher deposition pressures, higher gas flow, periodic reversal of gas flow, and periodic interruption of gas flow. A combination of the latter two techniques appeared most promising. Fully dense deposits of V have been produced by H_2 reduction of both VCl_4 and VF_5 at 1200°C.

Additional long-time creep-rupture data for arc-melted W–5% Re were obtained at 1400, 1650, and 2200°C. The Larson-Miller constant calculated from these results was used to obtain an estimate of the creep-rupture curves at 1800 and 2000°C.

10. Nondestructive Test Development

We are developing new techniques and equipment for nondestructively testing materials and components.

Our analytical work on electromagnetic phenomena has been directed in part to the design of improved coils for measuring conductivity more accurately. We are measuring coil impedance as affected by the presence of defects in a tank of Hg to verify the mathematical theories previously derived.

Sample welds containing flaws are being fabricated for study with the ultrasonic schlieren system. Studies using frequency analysis included observing frequency spectra as a function of the size of the aperture of the collimator. We prepared specimens for frequency analysis of reflections as a function of reflector size and orientation.

Preliminary studies have begun on the use of Compton scattering for measuring the thickness of claddings and coatings.

11. Joining Research on Nuclear Materials

Studies of hot ductility showed that S decreased the hot ductility of alloys rich in Ni and drastically impaired their ability to recover after a thermal exposure to a peak temperature of 1345°C. Manganese did not improve their hot ductility and, indeed, seemed to have a somewhat detrimental effect. Phosphorus was not detrimental.

Scanning and transmission electron microscopy have substantiated that Ti seems to negate the deleterious effect of S in alloys with intermediate Ni content through the formation of compounds. X-ray analysis of extracted precipitates have identified them as titanium disulfide and titanium nitride. Moreover, the beneficial effect of Ti on the ductility minima at 760 to 870°C stems from its ability to enhance recrystallization.

A metallographic study is under way in our stainless steel program in support of the Fast Flux Test Facility. We have seen that both the distribution and amount of ferrite vary greatly as a function of the welding process. Moreover, we observed significant differences within a given weld and within a given cross section.

Nondestructive examination of the weldments in which we deliberately produced discontinuities was completed. Good correlation was shown between through-transmission ultrasonic techniques and radiography. For the specimens under study, radiography proved more sensitive to three-dimensional flaws.

12. Development of LMFBR Tubing Fabrication

We are varying the schedules for mandrel drawing and annealing of type 316 stainless steel to determine the extent to which differences in the technique of fabrication affect the structures and properties of the final product. Interpass annealing temperatures were varied from 925 to 1050°C at a reduction of area per pass of about 20 and 40% for the first and second schedules, respectively. All tubing was tested nondestructively,

and 70% of the tubing appears to meet the Fast Flux Test Facility specification limits for flaws and eccentricity.

We have fabricated tubing of type 304L stainless steel alloy modified with 0.2% Ti by both drawing and planetary swaging for the final reductions. Textures that are characteristic of either drawing or planetary swaging develop after very small reductions, maximum intensities are reached very early in the reduction schedule, and the intensity peaks sharpen with increasing amounts of cold work.

Biaxial stress-rupture properties of Ti-modified type 304L stainless steel indicate that ultrasonically detectable defects reduce rupture life and ductility, particularly for cold-worked tubes in which internal bore defects are difficult to find using nondestructive testing techniques.

13. Development of Fuel Element Fabrication

We continue to demonstrate that roll crushing UAl_x powders increases the yield of a usable product. However, the very high recoveries of about 90% that were previously reported are achieved only when crushed and remelted material is used; a single cycling of the material, with five remelts, yielded a recovery of only 75 to 80%. Variation in the concentration of U between 65 and 71 wt % had no effect on yield.

The volume of voids in pressed and hot-rolled Al powder compacts, similar to the High Flux Isotope Reactor (HFIR) insert, was increased by the addition of 10 to 50 wt % ZrO_2 powder. The increase was less than found with fuel additions.

Extensive examinations by optical and transmission electron microscopy of type 6061 Al samples after cyclotron injection with 0.33 ppm H followed by various anneals revealed no evidence of blisters or bubbles.

Profuse blistering was encountered in plates in which both ends of the wrought Al cores were rounded in an attempt to reduce dogboning. Up to 9% void volume was obtained with plates fabricated for the HFIR outer annulus with 50 wt % loading of burned oxide fuel. No unusual difficulties were encountered in fabricating these plates, but present inspection practices have been shown to be inadequate.

We extended our study of the effect of variations in welding conditions on weld penetration and geometry to include the focusing of the electron beam. Changes in focus position, above and below the work surface, affected the geometry of the weld.

The prototype element for electron-beam welding was assembled and is en route to ORNL. Concurrently, the alterations necessary for housing this element in the electron-beam welding chamber are being made.

The exposure of Ni-plated miniature fuel specimens in the Engineering Test Reactor (ETR) was stopped by a failure from outside causes. During the shutdown, the plates were exposed to very high temperatures; the effects are yet unknown. The experiment to determine the effect of fines on the performance of plates with either burned or high-fired oxide was returned to the loop when the reactor was again placed in operation. Plates for tests of high burnup of a heavily loaded core were prepared and are awaiting insertion. As with the full-size plates, the highest void contents were obtained with the burned oxide fuel. No fabrication effects could be determined that were dependent upon fuel particle size, even with 100% −325 mesh powders.

Examination of a second spent HFIR fuel element was completed except for postirradiation blister-annealing tests. In general, the element was found to be in excellent condition, with no indications of potential failure or significant dimensional changes. The oxide film on the surfaces of the fuel plates in this element was significantly thinner than that found on plates from the previous element, apparently because a thin oxide film was intentionally produced on the surfaces of the plates in the earlier HFIR fuel element before they were placed into operation.

Our studies on the measurement of fuel inhomogeneity by radiographic densitometry were completed, and a report is being prepared. We are continuing to see a rather large discrepancy between the analyses of U content by analytical chemistry and by x-ray attenuation scanning and/or the charged fuel loading.

Preliminary work was begun on the use of Compton backscattered radiation for measuring the thickness of cladding on Al fuel plates.

PART V. ENGINEERING PROPERTIES OF REACTOR MATERIALS

14. Physical and Mechanical Metallurgy of Refractory Alloys

The solubility and diffusivity of N in W were determined to 1800°C. The transformation kinetics and the room-temperature mechanical properties of a Nb–54% Hf alloy aged between 600 and 1400°C were determined. The aging response is due to the precipitation of a fine dispersion of Hf-rich platelets. Spinodal curves, the wavelength of the modulated structure, and a time-temperature-transformation curve for a hypothetical alloy that transforms via spinodal decomposition and exhibits clustering were calculated from the free energy of mixing of binary alloys. The results show that better agreement would be obtained between theory and experiments at the equi-atomic concentration at about 0.5 of the critical temperature.

The creep-rupture properties of T-111 stressed to 35,000 psi at 1205°C decrease with increasing temperature of the anneal before testing. At high stresses, T-111 annealed at 1650°C is weaker than T-111 annealed at 1200°C but it is stronger at low stresses. Graphite and Mo components were successfully fabricated into Cs evaporators by brazing with 47.5% Ti–47.5% Zr–5% Nb. The evaporators successfully operated above 1000°C for 200 hr. A compression test was developed for testing brazed joints in graphite. The electrical resistivity of Ta was measured to 2600°K, and an equation giving its temperature dependence to ±0.029 μΩ-cm is given. Development work continued on an electrical heating method for determining thermal conductivity.

15. Cladding Materials for Space Isotopic Heat Sources

Creep-rupture data for five heats of Haynes alloy No. 25, including welded specimens, have been correlated from 650 to 1050°C by means of the Manson-Haferd parameter. Aging studies on this alloy have revealed a strength maximum and ductility minimum at 700°C which does not appear to be associated with the precipitation of Laves phase Co_2W. Charpy V-notch impact specimens of Haynes alloy No. 25, Hastelloy N, and Haynes

developmental alloy No. 188 are being aged at 650, 700, 800, 850, and 900°C for times to 5000 hr and will subsequently be tested at room temperature and 760°C.

Preliminary creep data on developmental alloys indicate superiority of ordered alloys over both disordered developmental alloys and Haynes alloy No. 25. Long-range order was also shown to decrease evaporation between 950 and 1050°C. Initial evaporation of Ni, Co, and Fe from binary Pt alloys results in Pt enrichment at the surface that, in turn, decreases further evaporation.

PART I

FUELS AND CLADDINGS

1. DEVELOPMENT OF FAST-REACTOR OXIDE FUELS

P. Patriarca A. L. Lotts

The objective of this program is to obtain an economically optimized $(U,Pu)O_2$ fuel cycle for a liquid-metal fast breeder reactor (LMFBR) by extending the performance capability and advancing the fabrication technology of oxide fuels. These fuels have the most advanced technology and greatest potential for reliable operation in first-generation LMFBR's. They have been tested in fast-flux environments but as yet have not been exposed under actual prototypic conditions. Currently, the burnup and heat rate are limited to about 50,000 Mwd/metric ton and 16 kw/ft, respectively, based on irradiation experiments with fuels that are not necessarily optimized for thermal, chemical, and mechanical performance.

The capability of oxide fuels can possibly be improved by adjusting structures or void distribution in the fuels. We emphasize the irradiation of fuels derived from the sol-gel process with thoroughly characterized structures and void distributions different from those of the oxide fuels irradiated heretofore. These include fuels fabricated by Sphere-Pac, vibratory compaction, extrusion, and pelletization. We compare the performance of these with the performance of reference fuels such as pellets derived from mechanically blended powders and coprecipitated material. The development of computer programs to assist in the analysis of test results and the development of a mathematical model to predict the performance of a fuel rod are integrated with the test program.

Preparation of $(U,Pu)O_2$ Fuels

W. T. McDuffee

We prepared a stable PuO_2 sol containing 560 g Pu to be blended with UO_2 sol for studies of development and fabrication of pelletized fuels. We also prepared three batches of UO_2 sol each containing 300 g U enriched to 9% ^{235}U. From these, we recovered a stable sol free of solids containing about 600 g U to be blended with PuO_2 sols for use in developing fabrication techniques.

We developed suitable conditions for calcining powdered shards of UO_2-PuO_2 blends that would provide pellets of satisfactory green strength. We then calcined 950 g of 20% PuO_2–80% UO_2 powder. Of this, we sent a portion containing 500 g heavy metal to Atomics International and reserved the remainder to be used in developing techniques for fabricating pellets.

Development of Fabrication Processes

J. D. Sease

Fast reactors that operate at high specific powers will require fuel pins of small diameter with fuel ranging from 80 to 90% of theoretical density and a high fissile loading. Our work is to develop procedures for Sphere-Pac and pelletization and for fabricating irradiation capsules.

Sphere-Pac (W. L. Moore)

We continued evaluation of the engineering-scale variables of the Sphere-Pac process. We assessed methods of determining the distribution of particle sizes for both the coarse and fine fractions and completed the initial evaluation of the effect of the tube diameter and the height of the coarse bed on the loading time for the fine fraction.

We believe that the distribution of particle sizes, particularly of the fine fraction, will greatly influence the loading characteristics. As a first step in studying this variable, we assessed various means of determining the distribution of particle sizes. For the coarse fraction, we investigated the use of micromesh screens and a microscopic technique. Both methods appeared adequate. For the fine fraction, the Coulter counter and a microscopic technique were investigated with ThO_2 microspheres < 37 μm in diameter. The difference between the results from duplicate samples, as determined by these two methods, is minimal (Fig. 1.1).

In initial loading experiments, we investigated the effect of the tube diameter and the height of the coarse bed on the time required to infiltrate the fine fraction. In this study, the ThO_2 microspheres for the coarse fraction were 530 to 590 μm in diameter, and those for the fine fraction were < 37 μm in diameter. The distribution of particle

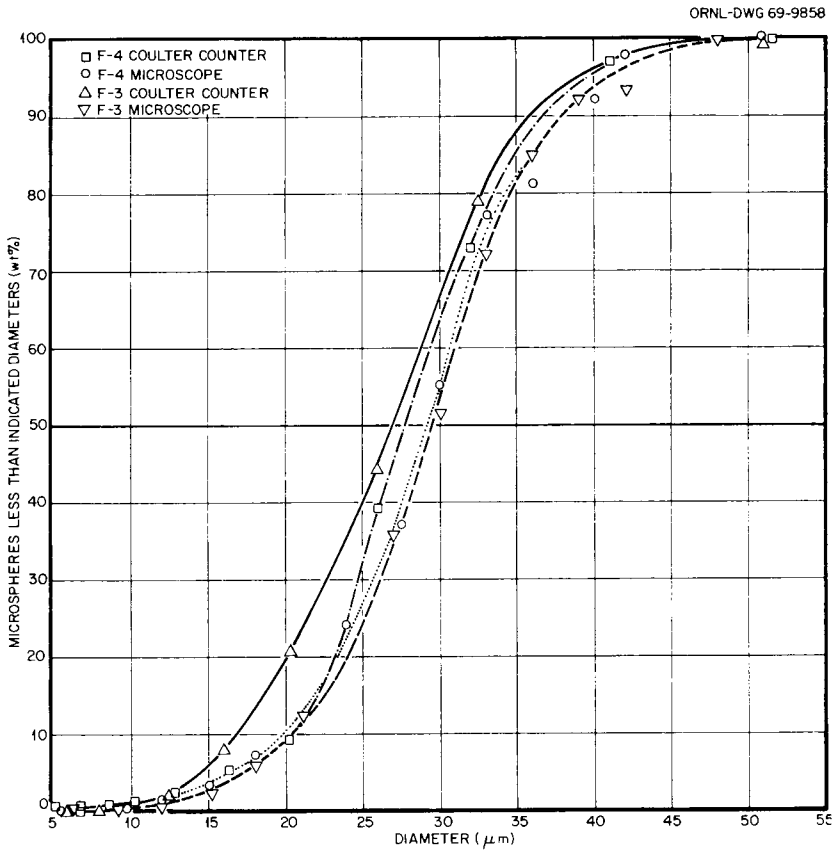

Fig. 1.1. Distribution of Particle Sizes in ThO_2 Microspheres < 37 μm in Diameter.

sizes of the fine fraction is shown in Fig. 1.2. Fuel bed diameters of 0.186, 0.245, 0.305, 0.370, and 0.870 in. were investigated at bed heights of 8, 16, and 24 in. The volumes of all the tubes for these experiments were determined by liquid titration. In loading the coarse beds, we ran a number of preliminary experiments to ensure that the loading rate of the coarse fraction was sufficiently low to minimize dislocation in the coarse packing.

The volume packing of these coarse beds ranged from 59.5 to 63.5%, following a trend of increasing density with increasing bed diameter. The time for loading the coarse microspheres ranged from 1/2 to 1 min for the smallest to largest bed. In the initial infiltration of the fine microspheres into the coarse beds, we found it difficult to obtain reproducible packing and loading times when all of the fines were added at one time. Therefore, we loaded the fine particles in increments of 2 to 4 g, increasing from the smallest to the largest bed, respectively.

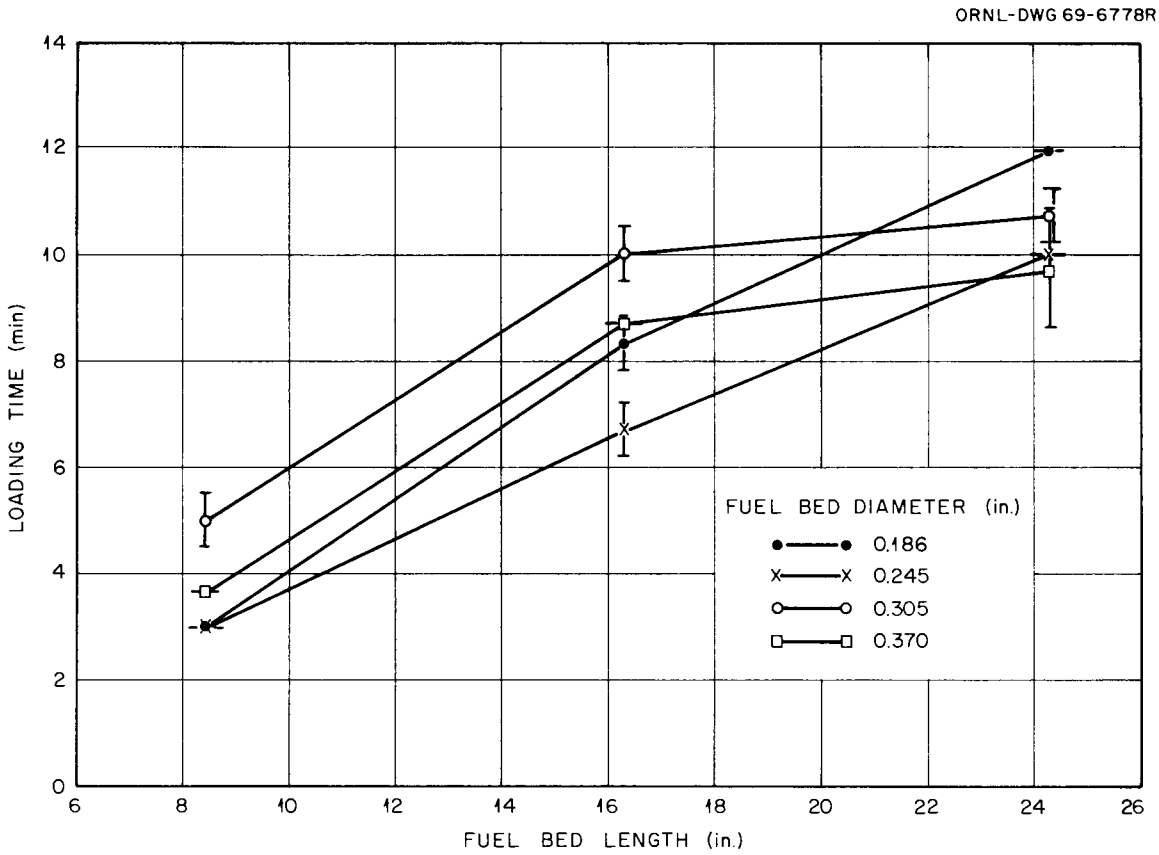

Fig. 1.2. Effect of Tube Diameter and Height of Coarse Bed on Time Required for Loading Fine Fraction of ThO_2 Microspheres.

The total (coarse and fine) volume packing ranged from 81.5 to 85.2%. The effects of the tube diameter and the height of the coarse bed on the time required to load the fine fraction are shown in Fig. 1.2. The time required for loading is nearly directly proportional to the height of the bed for the beds with smaller diameters, while that for the beds with larger diameters appears to be independent of the height of the bed. This effect is probably due to differences in packing at the tube walls. Further investigations are planned to explain these results.

Pelletization of Sol-Gel $(U,Pu)O_2$ (R. A. Bradley)

We continued to fabricate $(U,Pu)O_2$ pellets for the Transient Reactor Test Facility (TREAT) irradiation capsules. These capsules require pellets with densities of 84 and 91% of theoretical and O:metal ratios of 1.980 ± 0.005.

We prepared a 1000-g batch of $(U,Pu)O_2$ by blending UO_2 and PuO_2 sols and drying to a gel at about 100°C in a tray purged with Ar. After grinding the gel to −325 mesh in a fluid energy mill, we calcined the powder to 520°C to remove most of the remaining volatiles, reduce the surface area, and adjust the ratio of O:metal. The calcination conditions were selected to yield powder that could be used to produce pellets of the desired density. A portion of the powder was calcined in Ar–4% H_2 to preserve the agglomerated nature of the material, which is beneficial in making low-density (84% of theoretical) pellets. The remainder of the powder was oxidized by heating in air and then reduced in Ar–4% H_2. This oxidation-reduction treatment breaks up the agglomerates, producing a powder that will yield high-density (90 to 91% of theoretical) pellets. In each case, the final step in the calcination involved stabilizing the ratio of O:metal at about 2.2 by soaking in CO_2 at 520°C for 1 hr. The calcining conditions, surface area, and ratio of O:metal for three batches of calcined powder are summarized in Table 1.1.

Table 1.1. Calcining Conditions and Characterization of $(U,Pu)O_2$ Powder for High- and Low-Density Pellets

Desired Pellet Density	Calcining Conditions	O:Metal Ratio	Surface Area (m^2/g)
Low	Heated at 250°C/hr to 520°C in Ar–4% H_2 and held 4 hr. Held at 520°C in CO_2 for 1 hr. Cooled in CO_2.	2.37	18.2
High	Heated in air at 300°C/hr to 520°C. Changed to Ar–4% H_2 for 4 hr. Changed to CO_2 for 1 hr at 520°C. Cooled in CO_2.	2.23	7.27
High	Heated in air at 300°C/hr to 520°C. Changed to Ar–4% H_2 for 4 hr. Changed to CO_2 for 1 hr at 520°C. Cooled in CO_2.	2.11	7.76

Both types of calcined powder were formed into pellets by uniaxially pressing without a binder at 25,000 to 50,000 psi. As pressed, the pellets had good green strength, sharp edges, and smooth surfaces. We sintered them by heating at 300°C/hr to 1450°C and holding at that temperature for 10 hr. Pellets made from the powder calcined in Ar–4% H_2 had green densities that varied linearly with forming pressure from 41 to 46% of theoretical and sintered densities from 80 to 88% of theoretical. The green densities of pellets pressed from the powder that was first oxidized and then reduced also varied directly as the forming pressure; they were, however, slightly higher than those from the other powder, ranging from 46 to 50% of theoretical. The sintered density, 90.5 ± 1%, was independent of forming pressure. The relationship between forming pressure and green and sintered density for both types of powder is shown in Fig. 1.3.

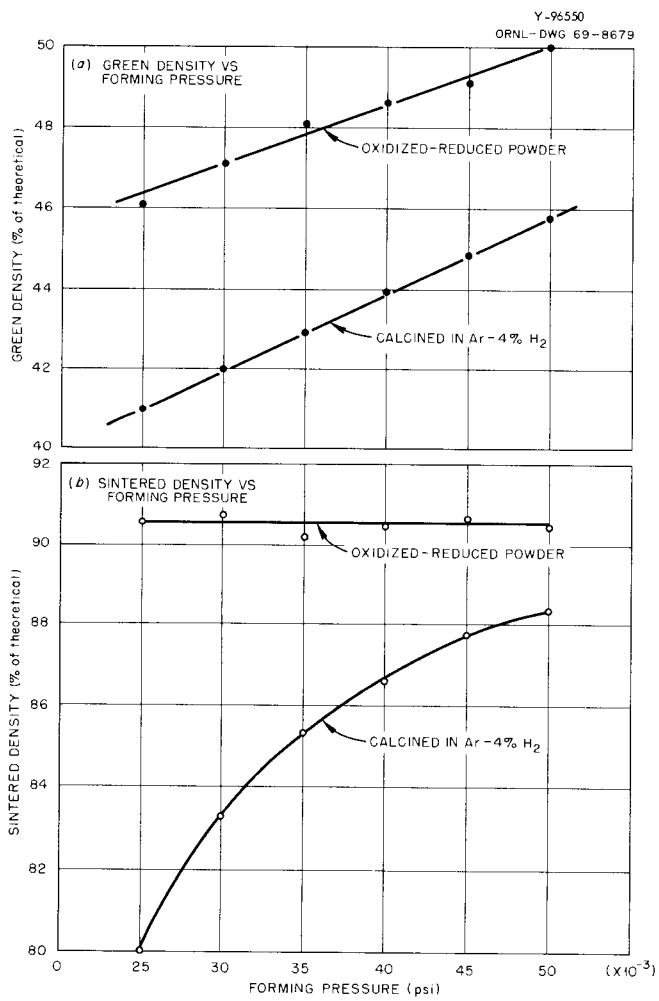

Fig. 1.3. Relationship Between Forming Pressure and Green and Sintered Densities for Calcined Powder.

Seven batches of 40 pellets each were pressed and sintered to produce pellets for the TREAT irradiation capsules. The ratio of O:metal for the pellets in each batch was determined by the thermogravimetric technique. When necessary, the pellets were heat treated at 1450°C in Ar–4% H_2 with Ta foil as a getter to reduce the ratio of O:metal to 1.980 ± 0.010. The O:metal ratios of these seven batches are shown in Table 1.2.

Table 1.2. Ratio of Oxygen to Metal in Pellets for TREAT Irradiation Experiment

Sinter Run Number	Ratio of O:metal After Sintering	Heat Treatment	Ratio of O:metal After Heat Treatment
78	1.995	Good pellets from runs 78 and 79 grouped together for treatment at 1300°C with Ta getter	1.991
79	1.990		
80	1.992	1200°C with Ta getter	1.990
81	1.987	No heat treatment	
82	1.984	1450°C with Ta getter	1.982
83	1.983	No heat treatment	
84	1.982	No heat treatment	

After grinding the pellets to 0.217 in. in diameter on a centerless grinder, we loaded them into the fuel pins for the TREAT irradiation capsules. The fuel pins for the first two TREAT capsules have now been loaded, welded, and inspected.

Capsule Fabrication (R. B. Pratt, M. K. Preston, R. A. Bradley, W. L. Moore)

Our fabrication efforts were concentrated on the construction of two instrumented TREAT capsules (TREAT I and II).

TREAT Capsules. — Over the next several years we plan to fabricate a number of TREAT capsules.[1] The first two capsules, TREAT I and II,

[1]R. B. Pratt, M. K. Preston, R. A. Bradley, and W. L. Moore, Fuels and Materials Development Program Quart. Progr. Rept. March 31, 1969, ORNL-4420, pp. 7–13.

which are scheduled for irradiation testing this summer, are about 75% complete. Activities this quarter have centered about fuel preparation and the fabrication of various subassemblies.

Each fuel rod in TREAT I and II will contain three fueled sections: TREAT I will contain two pellet pins with smear densities of 81 and 88% of theoretical and a Sphere-Pac pin with a smear density of 81%; TREAT II will contain two Sphere-Pac pins and one pellet pin, all three with smear densities of 81%. The pellets[2] and fuel pins have been fabricated. The major problem in Sphere-Pac loading was the uncertainty about the gas content of the fuel.[3] This problem caused us to unload completed pins and outgas the fuel. The loading data for the Sphere-Pac pins are shown in Table 1.3.

Table 1.3. Fuel Loading of TREAT Capsules

Pin Number	$(U,Pu)O_2$ Fuel Weight (g)	Fuel Height	Smear Density (% Theoretical)
TR-IA	49.959	8.03	88.9
TR-IB	45.266	8.00	80.9
TR-IC	44.496	7.98	79.7
TR-IIA	45.885	8.01	82.0
TR-IIB	45.293	8.00	80.9
TR-IIC	45.453	8.10	80.2

A dummy containing all of the components except the fuel was assembled. The various subassemblies for TREAT I and II are also completed. During this quarter, the welding and brazing development was completed, and the remaining hardware problem was resolved. The hardest

[2]R. A. Bradley, "Pelletization of Sol-Gel $(U,Pu)O_2$," pp. 6–9 this report.

[3]W. H. Pechin, "Analytical Chemistry," p. 12 this report.

subassembly to fabricate was the pressure vessel, or nosepiece, which contained the feedthroughs for the thermocouples and heaters. The various components of this subassembly are shown in Fig. 1.4. By a slight redesign and careful cleaning and handling of the components, we were able to make the piece leaktight to 250 psig. Also, some problems in obtaining a pressure seal with the metal O-ring between the nosepiece and the main pressure vessel were resolved by polishing all sealing surfaces to mirror finishes.

Three dummy capsules were filled with Na without great difficulties, but evaluation of the Na bond by eddy-current techniques is complicated by interference from thermocouple leads close to the cladding walls.

The shipping container for the skim rods for the Materials Testing Reactor (MTR) has been modified to accommodate two TREAT capsules for

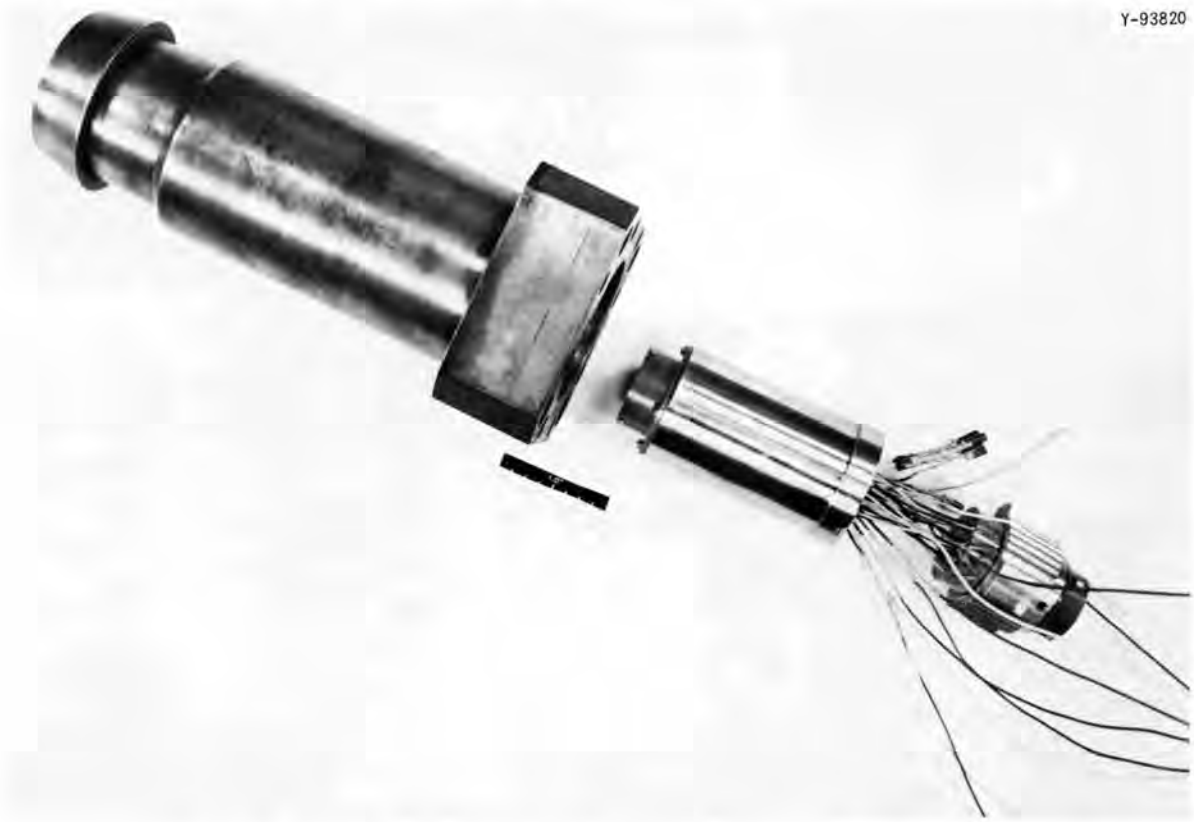

Fig. 1.4. Nosepiece for TREAT Pressure Vessel.

shipment to the reactor site. We expect to receive soon the Department of Transportation's approval for the shipment of alkali metals and fissile materials in containers now approved only for fissile material. We have requested General Electric Company to lend us their T-2 shipping cask in September so that we can return the irradiated capsules to ORNL.

Characterization of $(U,Pu)O_2$ Fuels

J. M. Leitnaker C. S. Morgan
D. L. McElroy W. H. Pechin

The development of sol-gel fuel fabrication requires characterization of both the chemical composition and physical properties of the material to control the process and to meaningfully interpret the irradiation behavior. Thermodynamic studies will contribute to the process development for the fuel and will aid in predicting fuel performance for both irradiation testing and model studies.

Analytical Chemistry (W. H. Pechin)

We have had considerable difficulty in measuring gas release from $(U,Pu)O_2$ at 1750°C. The problems have included a high background, poor reproducibility between samples from the same batch of material, and inconsistency with measurements made at 1200°C.

For these reasons the large, quartz, sample chamber and W crucible were replaced with a small Al_2O_3 tube. As shown in Fig. 1.5, the heat is now supplied from an exterior C susceptor heated by induction. The new equipment includes a device for adding samples after the system is brought to temperature and after the background is measured. The apparatus includes two sample arms that allow four samples to be measured during each heating cycle. The pressure in the system is recorded at intervals for about 20 min. The evolved gas is pumped out of the evolution section and sampled for mass spectrographic analysis.

Trials on this system have shown a background of 0.001 to 0.005 cm^3 compared to 0.20 to 0.30 cm^3 with the old equipment. Preliminary data on microspheres include 0.05 cm^3/g for coarse and 0.27 cm^3/g for fines at 1600°C.

ORNL-DWG 69-8680

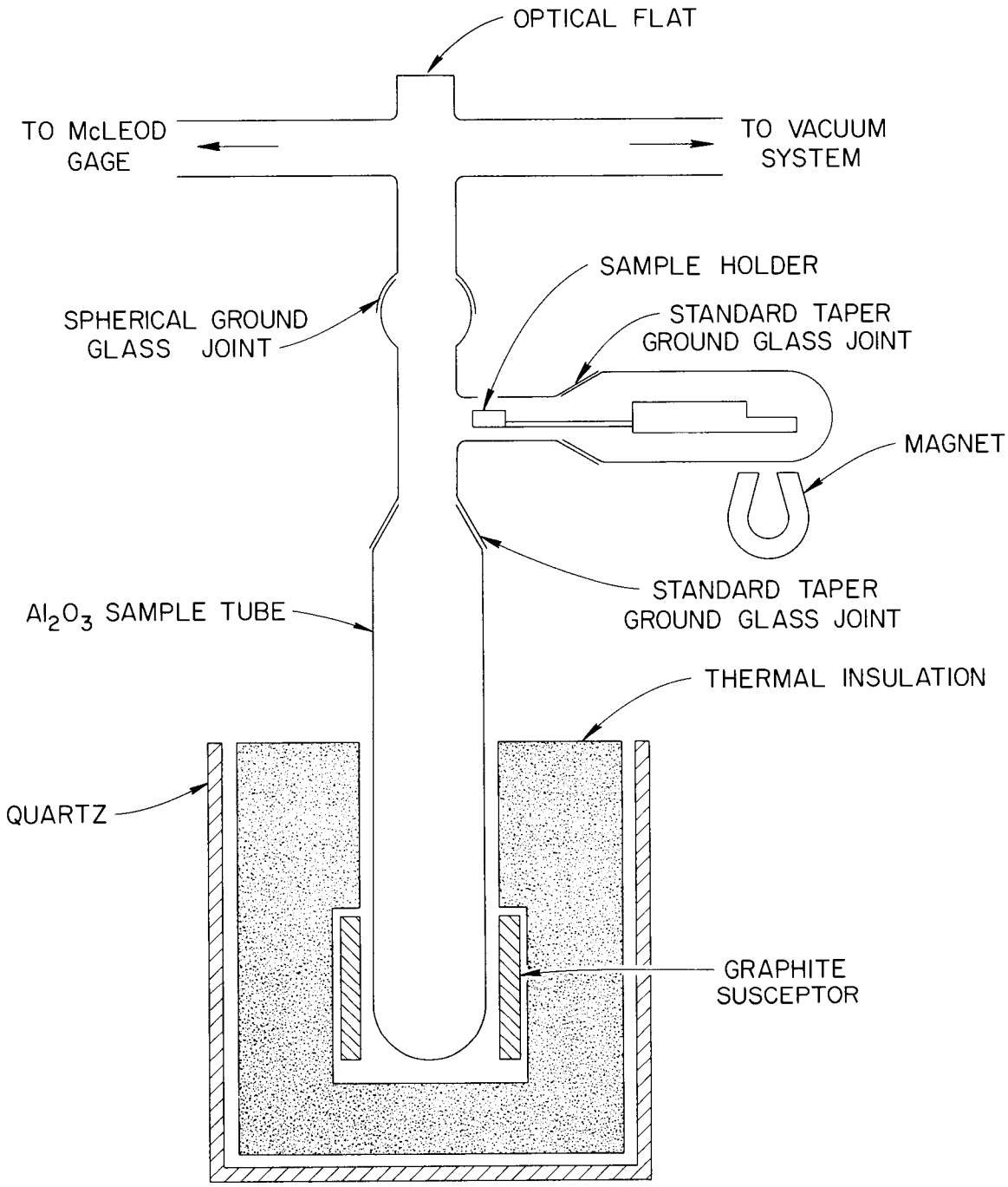

Fig. 1.5. New Apparatus with Small Al_2O_3 Tube for Sample Chamber for Measuring Gas Release From $(U,Pu)O_2$ Fuel.

Thermal Conductivity of Lithium Fluoride (P. H. Spindler, D. L. McElroy)

We measured the thermal conductivity of 100% dense polycrystalline LiF to 1100°K in our radial heat-flow apparatus. These results confirmed the strong thermal-radiation component previously described[4] for single-crystal LiF near the melting point, but have a smaller scatter band. These two sets of results for heat transport are being analyzed in terms of a lattice component and a thermal-radiation component. We determine thermal-radiation component by means of the so-called Rosseland approximation[5] for a coefficient of mean absorption that is dependent on wavelength.

Radial Heat-Flow Apparatus for Measurements at 10 atm and 1400°K (P. H. Spindler, D. L. McElroy)

We are constructing an apparatus that will allow measurements of thermal conductivity to 1400°K at 10 atm in a glove box. Machining of components is 75% complete.

Analytical Characterization (J. M. Leitnaker, K. E. Spear)

The purposes of the experiments reported in this section are (1) to establish standard samples for determination of O content; (2) to establish a reliable method of x-ray determination of the O:metal ratios in both UO_2 and $(U,Pu)O_2$ samples; and (3) to investigate the effect of quenching rate on the ratio of O:metal in both UO_2 and $(U,Pu)O_2$. These tasks are designed to lay the groundwork for eventual determination of the O:metal ratio of mixed oxide fuels in a temperature gradient.

We continued to measure the lattice parameter of samples of UO_2 quenched after heat treatment in an atmosphere of CO and CO_2. We also measured density, C content, and, in most cases, total U content. From these, we could calculate a final O:metal ratio.

---

[4]D. L. McElroy, Fuels and Materials Development Program Quart. Progr. Rept. March 31, 1969, ORNL-4420, pp. 15–19.

[5]S. Rosseland, Astrophisik Auf Atom-Theoretischer Grundlage, Springer, Berlin, Germany, 1931.

A number of conclusions can be drawn from the results reported in Table 1.4. First, C is removed rather readily from UO_2 down to less than 100 ppm C at 1200°C for specimens this size. The ultimate solubility of C in UO_2 in an atmosphere of CO and CO_2 mixed to a ratio of 9 is less than about 50 ppm C at 1000°C and less than about 20 ppm C at 1200°C. These data are significant in that they indicate the pressure of CO that might be experienced in a fuel pin. For oxide fuel samples in which the C present exceeds the solubility by 10 ppm, the pressure of CO and CO_2 is computed to be 1 atm at room temperature for fuel 85% of theoretical density.

Some samples heated at the same temperature for the same time have different densities. (The rate of change in O content upon quenching may be related to density.) Compare, for example, samples 93 and 122 or samples 104, 108, and 115 in Table 1.4. Two factors are operating. The first is the die lubricant. Stearic acid was used to lubricate the die for sample 104 but not for sample 108. The result is a decrease in density of about 4% of the theoretical value for the sample from the unlubricated die. A second effect can be seen by comparing samples 108 and 115. The difference here is the rate of flow for the CO and CO_2 atmosphere; sample 108 had one-third the flow rate of sample 115. The greater density of sample 108 is almost certainly due to the higher O pressure during sintering, which arose because the excess O over an O:metal ratio of 2.0 was not removed rapidly. Samples 117 and 122 are anomalous. Clearly, for a sintering study, the O pressure at every stage should be carefully examined.

One of the principal conclusions that may be drawn from Table 1.4 is based upon the lattice parameter and U content of the UO_2 samples equilibrated at 1200°C in a 9:1 mixture of CO and CO_2. The U content is 88.17 ± 0.02 wt % (or an O:metal ratio of 1.996), and the lattice parameter is 5.47085 ± 17 A, where the quoted uncertainties are the spread and one standard deviation, respectively. There is clearly a bias in these data toward an O:metal ratio of less than 2.000. This difference is apparently real and agrees with our previous work.

Table 1.4. Results for 1/4-in.-diam UO_2 Pellets[a] Heated and Quenched in a 9:1 Mixture of CO and CO_2

Sample[b]	Temperature (°C)	Time (hr)	Lattice Parameter, A[c] Center	Lattice Parameter, A[c] Surface	Carbon[d] (wt %)	Uranium[e] (wt %)	Density[f] (% of Theoretical)
90	1200	1	5.47051 ± 16	5.46931 ± 27	0.008, 0.017, 0.029	88.053	
92	1200	6	5.47157 ± 19[g]	5.47094 ± 21	0.003, 0.002	88.15	94.6
93	1200	16	5.47094 ± 18	5.47081 ± 28	< 0.002	88.17	93.8
96	1000	1	5.46891 ± 25	5.46974 ± 26	0.048	87.77	56.5
97	1000	6	5.47061 ± 20	5.47001 ± 20	0.030	87.92	68.4
104	1000	16	5.47070 ± 29	5.47070 ± 34	0.012, 0.013	88.03	72.5
105	1000	1.3	5.46972 ± 27	5.46916 ± 19	0.019		53.3
106	1000	6	5.47040 ± 19	5.47004 ± 20	0.022, 0.022		61.5
108	1000	16	5.47083 ± 26	5.47079 ± 26	0.005, 0.010, 0.040		64.1
114	1000	1	5.46898 ± 24	5.47030 ± 23	0.0044, 0.0053	87.92	51.1
112	1000	6	5.47001 ± 21	5.46950 ± 21	0.025, 0.027	87.97	54.0
115	1000	16	5.46978 ± 18	5.47000 ± 14	0.0058	87.96	56.6
116	1200	1	5.47029 ± 28	5.47024 ± 25	0.0078	88.12	67.9
117	1200	6	5.47112 ± 20	5.47093 ± 21	0.003, 0.015	88.19	84.3
122	1200	16	5.47066 ± 24	5.47058 ± 21	< 0.002	88.17	75.8

[a]Starting material was $UO_{\sim 2.15}$ with a lattice parameter of 5.46849 ± 23 A.

[b]Samples 90 through 104 and 114 through 122 were pressed with stearic acid used as a die lubricant. For samples 90 through 108, CO-to-CO_2 flow rate was 100 cm^3/min. Samples 90 through 108 initially had about 900 ppm C. Other samples initially had about 180 ppm C.

[c]The calculations for lattice parameter are described in J. M. Leitnaker, "The Ideality of the UC-UN Solid Solution," pp. 317–330 in Thermodynamics of Nuclear Materials, 1967, International Atomic Energy Agency, Vienna, 1968. Uncertainties quoted are standard deviations and refer to the last numbers to the right of the decimal point.

[d]Determined by analytical chemistry.

[e]Determined by combustion in O_2 for 1 hr at 850°C; average of duplicate samples.

[f]Determined by immersion in water.

[g]Not used in averaging.

A number of experimental difficulties have not been resolved and should be given attention if additional accuracy is desired.

First, we observe a small amount of C deposit at the inlet of the gas tube. The list below shows that the equilibrium constant, K, for the reaction

$$2\ CO(g) \rightarrow CO_2(g) + (\text{graphite})\ , \qquad (1.1)$$

is very negative:

Temperature (°K)	log K
500	−13.357
1000	−9.803
1500	−9.385
2000	−9.119

Therefore, CO should not deposit C under the condition of the experiment. A check of the purity of the gas indicated that the mixture was very nearly the requested mixture. The mixing procedure, we learned, involved the use of a lubricated connector; we suspect that hydrocarbon was picked up there. In any case, the amount of C is small, and we doubt that the results are significantly influenced. Nevertheless, we should like to be sure.

Second, the temperature of the x-ray samples is only imperfectly known. A 2 to 3°C variation is likely and more is possible. Thus, we are not sure that the variations we see in lattice parameters are real. A substantial fraction of the surface measurements yield lower lattice parameters (corresponding to higher ratios of O:metal) than those obtained from the center. We are not sure that this represents a real variation, although the consistency of the results at 1200°C makes us suspect the variation is attributable to the sample rather than a variation in the x-ray procedure.

Thermodynamic Calculations: Chemical Effects of Nuclear Burnup on $(U,Pu)O_2$ Fuels (K. E. Spear, J. M. Leitnaker, N. Engel[6])

The ability to predict and understand the equilibrium interactions of a reactor fuel requires, among other things, a knowledge of the effects of nuclear burnup on the fuel. Our calculations of these effects on $(U,Pu)O_2$ fuels are reported here; similar calculations on (U,Pu)N and (U,Pu)C were reported previously.[7]

The fissioning of Pu in $(U,Pu)O_2$ fuels not only forms fission products, but also releases the O atoms that were bound to the Pu. The final state of such a released atom depends on its relative affinity for the fission products that are formed and for the remaining fuel. We have used available thermodynamic and phase data to calculate the equilibrium chemical state of the oxide fuel in a fast-reactor environment.

We have listed in Table 1.5 the relative concentrations of atoms in $(U_{0.8},Pu_{0.2})O_2$ and the distribution of bound O atoms after zero time, 6 months, and 2 years at full power of 185 Mw/metric ton. We assumed that the ^{239}U is equal to 0.9 times the ^{239}Pu that is fissioned.

In calculating the distribution of bound O, we did not consider ternary oxides such as Ba_2ZrO_4 and $SrMoO_3$, but such oxides probably will not affect the final ratio of O:U+Pu since most of them are just additions of the binary oxides we considered. For example, Ba_2ZrO_4 can be thought of as $2BaO \cdot ZrO_2$.

We assumed that the rare-earth atoms form dioxides in solution with the mixed-oxide fuel in our calculations listed in Table 1.5. Studies by Haug, Weigel and Oertel[8] give some evidence for this type of behavior, but further experimentation is needed. The importance of whether the rare earths form dioxides or sesquioxides in the fuel is exemplified by the results listed in Table 1.6.

---

[6]Consultant from Georgia Institute of Technology.

[7]K. E. Spear and J. M. Leitnaker, Fuels and Materials Development Program Quart. Progr. Rept. Dec. 31, 1968, ORNL-4390, pp. 45–48.

[8]H. Haug, F. Weigel and W. Oertel, J. Nucl. Mater. 17, 73–78 (1965).

Table 1.5. Effects of Burnup on a $(U,Pu)O_{2\pm x}$ Fast-Reactor Fuel as a Function of Time at Full Power (185 Mw/metric ton)[a]

Elements	Number of Atoms			Oxides	Number of Bound O Atoms		
	0 Time	6 Months	2 Years		0 Time	6 Months	2 Years
Major Elements							
^{238}U[a]	8,000	7,670	6,680				
^{239}Pu[a]	2,000	1,963	1,853	$(U,Pu)O_{2\pm x}$[b]	20,000	19,284	17,164
^{16}O	20,000	20,000	20,000				
Major Fission Products[c]							
Kr		9	37				
Rb		5	19	Rb_2O		3	10
Sr		16	57	SrO		16	57
Y		6	25	Y_2O_3		9	37
Zr		74	275	ZrO_2		148	550
Nb		4	6	Nb_2O_5		10	15
Mo		77	342	MoO_2		154	684
Tc		21	81	TcO_2			
Ru		86	311	RuO_2			
Rh		14	73	Rh_2O_3			
Pd		38	177	PdO			
Ag		10	38	Ag_2O			
Cd		3	15	CdO			
Te		12	45	TeO_2			
I		10	37	(CsI)[d]			
Xe		82	330				
Cs		72	288	Cs_2O[d]		31	125
Ba		25	100	BaO		25	100
La		21	83	La_2O_3		32	124
Ce		52	172	CeO_2[e]		104	334
Pr		17	77	PrO_2[e]		34	154
Nd		51	225	NdO_2[e]		102	450
Pm		7	22	PmO_2[e]		14	44
Sm		11	53	SmO_2[e]		22	106
Eu		3	10	EuO_2[e]		6	20
Gd		3	13	GdO_2[e]		6	26

[a] We assumed the Pu formed from U is equal to 0.9 times the Pu fissioned.

[b] The ratios of O:U+Pu are given in Table 1.6.

[c] Concentrations of fission products were calculated with the use of a computer program from Hanford converted by E. D. Arnold of the Chemical Technology Division at ORNL.

[d] All of the I is in the form of CsI, and the rest of the Cs is in the form of the oxide Cs_2O.

[e] The rare earths are assumed to be dioxides in solution with the mixed-oxide fuel, but they may be present as sesquioxides. See Table 1.6 for the effects of the state of the rare earths in the final ratio of O:U+Pu.

Table 1.6. Relationship Between the Initial Ratio of O:U+Pu and the Effects of Burnup on the Final Ratio of O:U+Pu and the Fraction of Molybdenum Oxidized[a]

Initial Ratio O:U+Pu	Ratio O:U+Pu After Burnup		Fraction of Mo Oxidized	
	6 Months	2 Years	6 Months	2 Years
	Rare Earths Present as Dioxide[b]			
2.000	2.002	2.011	1.00	1.00
1.990	2.000	2.000	0.47	1.00
1.980	1.997	2.000	0.00	0.85
1.960	1.976	2.000	0.00	0.56
1.940	1.956	2.000	0.00	0.27
	Rare Earths Present as Sesquioxide[b]			
2.000	2.009	2.044	1.00	1.00
1.990	2.000	2.032	0.92	1.00
1.980	2.000	2.020	0.27	1.00
1.960	1.983	2.000	0.00	0.96
1.940	1.963	2.000	0.00	0.67

[a]See Table 1.5 for details of burnup calculations.

[b]The rare earths Ce through Gd may be present as dioxides in solution with the mixed oxide fuel or as sesquioxides.

Table 1.6 gives the ratio of O:U+Pu and the fraction of Mo oxidized after 6 months and 2 years burnup as a function of the initial ratio of O:U+Pu. The top half of the table lists the results calculated by assuming that the rare earths form dioxides, and the bottom half lists the results calculated by assuming that they form sesquioxides.

Our calculations show that if a ratio of O:U+Pu of 2.000 is used for the fresh fuel, all of the Mo fission-product atoms will be oxidized to MoO_2 from the beginning of burnup, and the ratio of O:U+Pu will increase with burnup. If a hypostoichiometric fuel were used, the Mo fission product would remain as metal until the burnup caused the ratio of

O:U+Pu to increase to 2.000. At this point, the O released from burnup would oxidize the Mo to MoO_2, with the ratio of O:U+Pu remaining at 2.000 until all of the Mo were oxidized. After the Mo was all oxidized, the ratio of O:U+Pu in the fuel would begin to increase as burnup progressed. Therefore, by balancing the initial ratio of O:U+Pu and the maximum burnup, it would be possible to ensure that the fuel would never become hyperstoichiometric. Rand and Markin[9] have performed similar calculations and reached the same conclusions.

We previously calculated[7] that the activities of N and C in (U,Pu)N and (U,Pu)C fuels also increase with nuclear burnup. This effect of burnup on the activities of nonmetals in ceramic fast-reactor fuels can result in compatibility problems not encountered with the fuel at zero burnup. Our calculations emphasize the importance of considering burnup effects in analyses of containment for ceramic fuels in any type of reactor.

Interaction of Fission Products (J. M. Leitnaker, K. E. Spear)

Reactions Between Stainless Steel and $(U,Pu)O_2$. — In-reactor transport of type 304 stainless steel components into $(U,Pu)O_2$ fuel has been observed by Argonne National Laboratory.[10] The mechanism suggested was transport of the metals by I in a manner similar to the Van Arkel de Boer process. Since six times as much Cs as I is formed in the course of reactor processes, one might reasonably expect the I to be tied up by Cs as CsI.

From literature data, one can calculate that the reaction

$$2Cs\ I(s) + Fe(s) \rightarrow FeI_2(g) + 2Cs(s) \qquad (1.2)$$

should not proceed to any appreciable extent. In fact, the equilibrium pressure of $FeI_2(g)$ would be about 10^{-32} atm at 900°K. It is inconceivable that any significant transport of Fe would take place under these conditions.

---

[9]M. H. Rand and T. L. Markin, "Some Thermodynamic Aspects of $(U,Pu)O_2$ Solid Solutions and Their Use as Nuclear Fuels," pp. 637–650 in Thermodynamics of Nuclear Materials, 1967, International Atomic Energy Agency, Vienna, 1968.

[10]C. E. Johnson, Argonne National Laboratory, July 22, 1969, private communication.

However, the following reaction seems possible:

$$2CsI(s) + Fe(s) + UO_2(s) + O_2(g) \rightarrow Ca_2UO_4(s) + FeI_2(g). \qquad (1.3)$$

From literature data, at 900°K, $\Delta G°/T$ is calculated to be −40.23 and log K is +8.791. With a (Pu,U) valence of 4.1, the resulting equilibrium O pressure would be 4×10^{-15} atm. Under these conditions the pressure of FeI_2 would be about 3×10^{-6} atm. This should be enough to transport a significant quantity of Fe over the life of a fuel element.

To evaluate the possibility of such a reaction we have designed and constructed a system in which the O potential can be varied over a wide range and in which we can test the accuracy of our calculations. Mixtures of CO and CO_2 are flowed through a stainless steel container in which there is CsI and UO_2. The gas then flows into a chilled condenser to collect any Fe that may have been transported. Early tests have plugged the exit tube, probably because the exit was too cold. A slight modification should eliminate the problem.

Reactions Between Sodium and $(U,Pu)O_2$. — In order to investigate reactions of Na coolant with fuel material in failed pins as well as lay groundwork for a reaction between Cs_2O and $(U,Pu)O_2$ in unfailed pins, we are preparing a number of Na_2-UO_2-O materials. The general procedure is to react UO_2 and Na_2CO_3 in a mixture of CO and CO_2 or in some other pressure of O up to as high as 1 atm. Several uranates have been prepared thus far in exploratory experiments. We are now developing analytical techniques for identifying the constituents of the compounds. Various metallographic polishing techniques are being investigated to lay groundwork for techniques that may be used for polishing in the hot cells.

Irradiation Testing of $(U,Pu)O_2$ Fuels

C. M. Cox

The performance characteristics of mixed $(U,Pu)O_2$ fuels are being evaluated in a variety of irradiation tests for potential application in an LMFBR. We are concentrating on comparative test pellets and

microspheres of sol-gel fuel fabricated by the Sphere-Pac[11] technique. The program includes thermal-flux experiments, which permit use of instrumented capsules and high-burnup levels in relatively short times, and fast-flux experiments, in which the distribution of fission rate and radiation effects on the cladding are more typical of anticipated LMFBR operating conditions. Mathematical models of fuel behavior are being developed in conjunction with the experimental program.

Uninstrumented Thermal-Flux Irradiation Tests (A. R. Olsen, R. B. Fitts, D. R. Cuneo)

The uninstrumented capsules were designed[12] for irradiations in the X-Basket facilities of the Engineering Test Reactor (ETR). Each capsule contains four test rods with 3-in.-long fuel columns. Simultaneous irradiation permits comparisons of various fuel forms. The status of the first ten capsules in this group is given in Table 1.7. As discussed,[13] the last four capsules, 43-116 through 43-119, are being irradiated to provide fuel with fission products that have short half-lives for processing studies. Therefore, no detailed postirradiation examination of these rods is planned. Capsule 43-116 is to be shipped to ORNL the first week in July.

Experiment 43-113 was removed from the reactor during shutdown at the end of the ETR Cycle 103. This experiment will be neutron radiographed before it is again inserted into the ETR in a position with 15% higher unperturbed flux. This step in flux is required to maintain the linear heat rate at 14 kw/ft. The calculated burnup is now 7.5% fissions per initial metal atom (FIMA), and the target burnup is 10% FIMA.

---

[11]R. B. Fitts, A. R. Olsen, and J. Komatsu, Am. Ceram. Soc. Bull. 47(9), 844 (1968).

[12]A. R. Olsen and R. B. Fitts, Metals and Ceramics Div. Ann. Progr. Rept. June 30, 1967, ORNL-4170, pp. 125–127.

[13]A. R. Olsen, C. M. Cox, and R. B. Fitts, Fuels and Materials Development Program Quart. Progr. Rept. March 31, 1969, ORNL-4420, pp. 25–28.

Table 1.7. Uninstrumented Irradiation Screening Tests of Sol-Gel-Derived Urania-Base Bulk Oxide Fuels

Experiment	Fuel		Number of Rods	Peak Burnup (% FIMA[a])	Peak Linear Heat Rate (w/cm)	Current Status (May 1969)
	Form	Composition				
43-99	Sphere-Pac	$(^{235}U_{0.8},Pu_{0.2})O_2$	2	1.5	1640[b]	Report in preparation
43-100	Sphere-Pac	$(^{235}U_{0.8},Pu_{0.2})O_2$	2	1.4	1470[b]	Report in preparation
43-103	Sphere-Pac Pellet	UO_2 (20% ^{235}U) UO_2 (20% ^{235}U)	3 1	5	690	Being examined
43-112	Sphere-Pac	$(^{238}U_{0.85},Pu_{0.15})O_2$ UO_2 (20% ^{235}U)	3 1	0.7	500	Report in preparation
43-113	Sphere-Pac	$(^{238}U_{0.85},Pu_{0.15})O_2$ UO_2 (20% ^{235}U)	3 1	10[c]	500[c]	In-reactor (≅ 7% FIMA[a] burnup)
43-115	Sphere-Pac	$(^{238}U_{0.85},Pu_{0.15})O_2$ UO_2 (20% ^{235}U)	3 1	5[c]	600[c]	Being examined
43-116	Sphere-Pac	$(^{238}U_{0.85},Pu_{0.15})O_2$	4	1.5[d]	600	In reactor
43-117	Sphere-Pac	$(^{238}U_{0.8},Pu_{0.2})O_2$	4	1.5[d]	600[c]	In preparation
43-118	Sphere-Pac	$(^{238}U_{0.8},Pu_{0.2})O_2$	4	1.5[d]	600[c]	In preparation
43-119	Sphere-Pac	$(^{238}U_{0.8},Pu_{0.2})O_2$	4	1.5[d]	600	In preparation

[a]Fissions per initial metal atom.

[b]Rods failed in the reactor from overpowering.

[c]These are target design values.

[d]This is an approximate level. This test will be irradiated for two ETR cycles to produce fuel for reprocessing studies.

We resumed the metallographic examination of experiment 43-103 and began the postirradiation examination of experiment 43-115. Both of these experiments operated at relatively high linear heat rates and achieved a peak burnup level of approximately 5% FIMA. The results of preliminary postirradiation examination for experiment 43-103 were reported previously.[14] This experiment contained only UO_2 (20% ^{235}U) fuel. Three rods, in positions 1, 3, and 4, contained Sphere-Pac fuel with a low (74% of theoretical) smear density, and one rod in position 2 contained pellets with an 87.5% smear density. The gamma scan[14] indicated that some fuel had penetrated the upper ThO_2 insulator for both rods 2 and 3, which operated at peak linear heat rates of 21 and 22 kw/ft, respectively. Metallographic examination of these regions on the two rods is incomplete. However, transverse sections near the center of the fuel column of these rods (Figs. 1.6 and 1.7) show that the basic irradiation performance of pellet and Sphere-Pac fuels is similar. The examination of this experiment should be completed next quarter.

The postirradiation examination of experiment 43-115 is in the early stages. Both the neutron radiographs and the gamma scans indicate that the upper ThO_2 insulators on rods 1, 2, and 3 were penetrated. As with experiment 43-103, no fuel rods failed. The neutron radiographs show increased diameters for the central void on both ends of the fuel column for all four rods. This indicates flux peaking near the low-density ThO_2 insulators. As indicated last quarter,[13] we are beginning a mathematical analysis of this effect. In addition, we plan to increase the length and density of the ThO_2 insulators. We will continue to use ThO_2 to prevent the possibility of ^{238}U from UO_2 insulators affecting our isotopic burnup analysis. Although the postirradiation dimensional measurements are incomplete, there is no evidence of significant diametral changes for the fuel rods. Sampling of the fission gas is scheduled for early in July.

---

[14]A. R. Olsen, R. B. Fitts, and J. Komatsu, Fuels and Materials Development Program Quart. Progr. Rept. Sept. 30, 1968, ORNL-4350, pp. 22–25.

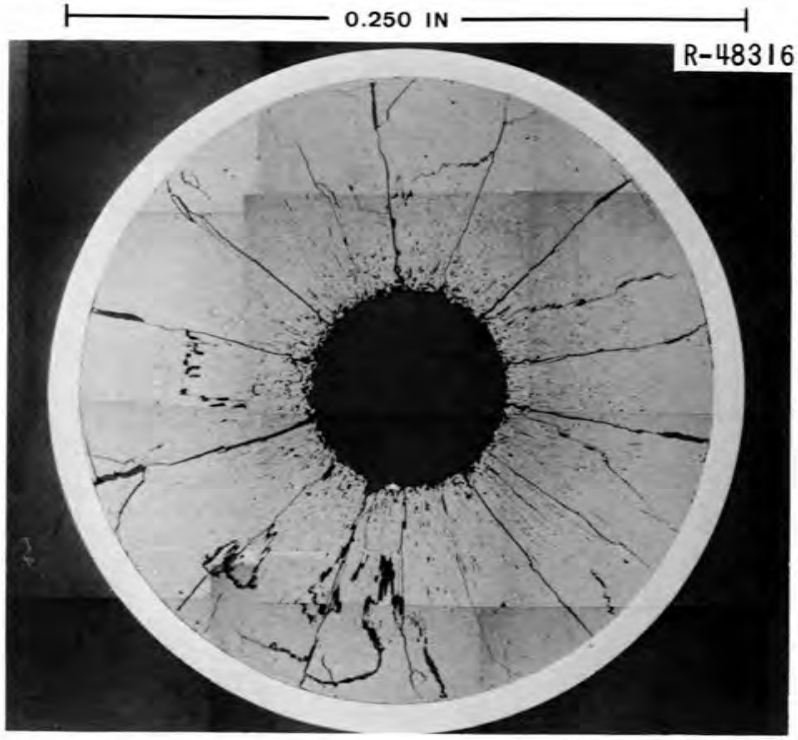

Fig. 1.6. Pellet of UO_2 (20% ^{235}U) Fuel from Rod 43-103-2 Operated at About 22 kw/ft Linear Heat Rate to 50,000 Mwd/metric ton of Uranium Burnup. Initial smear density, 9.58 g/cm^3.

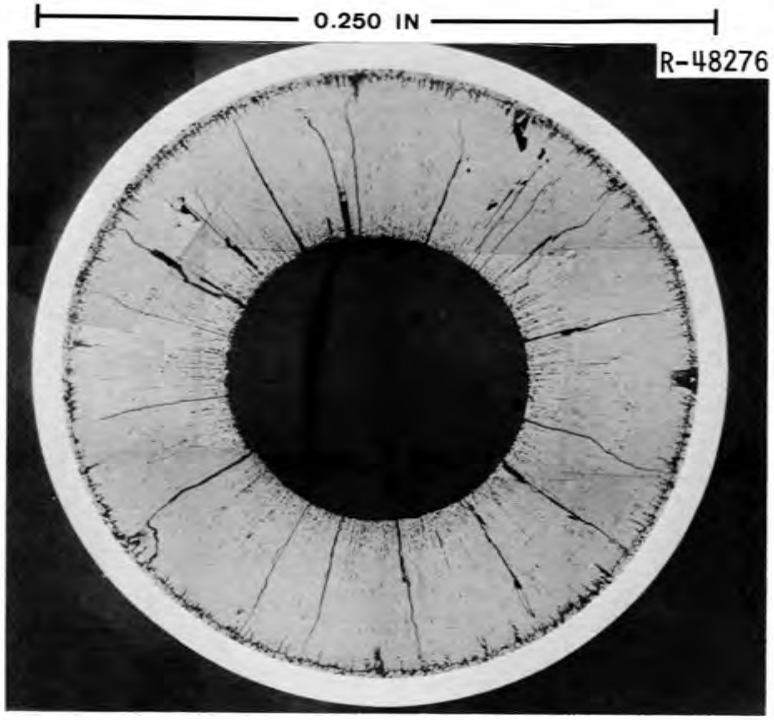

Fig. 1.7. Sphere-Pac UO_2 (20% ^{235}U) Fuel from Rod 43-103-3 Operated at About 20 kw/ft Linear Heat Rate to 50,000 Mwd/metric ton of Uranium Burnup. Initial smear density, 8.03 g/cm^3.

ORR Instrumented Tests (R. B. Fitts, V. A. DeCarlo, K. R. Thoms)

The instrumented irradiations in the Oak Ridge Research Reactor (ORR) are designed to monitor the thermal performance of test fuel rods.[15] The temperatures of the cladding and the fuel center and the rates of heat generation in the fuel rods are continuously measured and recorded. These data are being used to evaluate the thermal characteristics of various fuels in the reactor and the effects of irradiation conditions upon the temperatures and rates of structural change within the operating fuels.

The second capsule in this series, SG-2, is presently in the reactor. The fuel rods were loaded to 81% smear density with Sphere-Pac $(U_{0.8},Pu_{0.2})O_2$ from the batch of fuel to be used for the first series of TREAT tests.[15,16] This test is intended to yield data on the temperature at which rapid restructuring of the fuel begins and to examine the thermal conductivity of Sphere-Pac fuels in the reactor up to this temperature. The central temperature of the fuel is used to control capsule operation, and the temperature drop across the fuel and cladding is monitored to indicate the effective thermal conductivity of the fuel. To date, the central temperature of the fuel has been raised[17] from 100 to 1350°C in small steps. There has been no indication of fuel restructuring at these temperatures.

Transient Testing of Sol-Gel $(U,Pu)O_2$ (C. M. Cox, R. E. Adams)

The hazards analysis for the series I experiments has been sent to the Idaho Division of Argonne National Laboratory for review. If no changes are requested, the first two experiments comparing the transient performance of unirradiated sol-gel-derived Sphere-Pac and pelletized

---

[15]C. M. Cox and R. E. Adams, Fuels and Materials Development Program Quart. Progr. Rept. March 31, 1969, ORNL-4420, pp 30–31.

[16]W. L. Moore, Fuels and Materials Development Program Quart. Progr. Rept. March 31, 1969, ORNL-4420, p. 4.

[17]R. B. Fitts, V. A. DeCarlo, and K. R. Thoms, Fuels and Materials Development Program Quart. Progr. Rept. March 31, 1969, ORNL-4420, pp. 28–29.

$(U_{0.8},Pu_{0.2})O_2$ will be conducted in August. The fuel loadings and expected transient conditions were detailed previously.[15]

Fast-Flux Irradiation Tests (A. R. Olsen)

The series I encapsulated tests[18] are continuing their irradiation in subassembly X050. The exposure as of June 30, 1969, was 3510 Mwd of Experimental Breeder Reactor II (EBR II) operation. The scheduled exposure is 7500 Mwd. Thus, they have achieved 47% of the planned exposure or a calculated peak burnup of about 1.9% FIMA for the rod with the highest heat rate, S-1-C.

The planning of the series II unencapsulated tests is essentially complete. The proposal to obtain approval in principle for these tests, to be included in a 37-pin subassembly, is being drafted.

Irradiation Test Calculations (C. M. Cox, F. J. Homan)

We slightly modified the CALLSPT program[19] so that it can conveniently be used with ANISN energy- and space-averaged neutron cross sections. The modified version is called DEPLETE. We are now using it to calculate isotopic buildup and depletion for irradiation experiments with arbitrary reactor-cycle histories.

The PRØFIL code was adapted to the situation in which fuel is removed from the reactor after restructuring has occurred and placed in a different reactor position with a different flux environment. If the heat rating in the new position is higher than in the old position, additional restructuring will occur. If the new heat rating is lower, the cooler portion of the columnar region will break up somewhat and resemble the equiaxed region. Using the modified code (renamed RERUN), it is possible to predict structure as a function of radial position and calculate the new temperature profile.

---

[18]A. R. Olsen, C. M. Cox, and J. D. Jenkins, Fuels and Materials Development Program Quart. Progr. Rept. March 31, 1969, ORNL-4420, p. 33.

[19]J. E. Bigelow, Oak Ridge National Laboratory, April 1969, personal communication.

2. DEVELOPMENT OF HIGH-PERFORMANCE LMFBR FUELS

P. Patriarca J. L. Scott

The goals of this program are to investigate the properties and behavior of those U- and Pu-based ceramic fuels that we term conductors — such as the mononitrides, carbonitrides, and monocarbides — and to compare their potential as liquid-metal fast breeder reactor (LMFBR) fuel with that of $(U,Pu)O_2$, which by comparison is an insulator. Since the thermal conductivity of the ceramic conductors is about ten times that of $(U,Pu)O_2$, it is theoretically possible to operate a conductor at ten times the power density with the same temperature at the center of the fuel. In practice, heat-transfer limitations, thermal stresses in the cladding, and high rates of swelling at high temperatures limit the power density that can be achieved with thermal conducting fuels to about two or three times that of $(U,Pu)O_2$ — still a challenging improvement. Additionally, the margins for transient overpower in the ceramic conductors are much higher than those for $(U,Pu)O_2$.

We seek to provide the information necessary for evaluating the true potential of nitrides, carbonitrides, and carbides in comparison to each other and to mixed oxides. We need to define the structures, composition, and quality control required to achieve 150,000 Mwd/metric ton at peak linear heat ratings of 30 to 50 kw/ft. We must also demonstrate the possibility of a low-cost fuel cycle for manufacturing fuel with the needed properties. And since austenitic stainless steel is a poor conductor of heat, we seek to establish the physical and thermodynamic criteria for the new cladding material that will probably be required to exploit the conducting fuels.

Our work is now oriented toward fabricating and characterizing (U,Pu)N with controlled low or high porosity distributed in different ways. The requisite void volume in a fuel pin may be provided in several ways if dense fuel is used, such as by a large Na-filled gap between fuel and cladding or by dished or annular pellets. It may also be provided by the internal porosity of low-density fuel pellets. We use both hot pressing and cold pressing and sintering. In our characterization work,

emphasis is being placed on reliable chemical analyses of U, Pu, C, O, and N. We have glove boxes with less than 20 ppm O and 10 ppm moisture that allow us close control of O content, and we have facilities in operation for x-ray, metallographic, thermogravimetric (TGA), and differential thermal (DTA) analyses. We are also assessing the effects of temperature gradient and burnup on the activities of N, C, and O. Finally, we are developing the information needed to design the decisive experiments that will demonstrate the best type of pin for meeting LMFBR requirements.

Synthesis, Fabrication, and Characterization of Nitride Fuels

Synthesis and Fabrication of Mixed Nitrides (E. S. Bomar)

The purpose of this portion of our LMFBR program is to develop methods for preparing feed powders of high purity and to fabricate pellets of variable but controlled density.

We have continued to synthesize both UN and PuN by the hydride-nitride method and now have a reserve of 500 g of UN and 100 g of PuN for fabrication work. As a check on the benefit of repetitive hydriding and dehydriding cycles in obtaining a product of fine particle size, we measured the Brunauer-Emmett-Teller (BET) surface area of uranium hydride after four successive hydriding cycles and after nitriding. The results are tabulated below:

Product	BET Area (m^2/g)
Hydride	
1st	0.22
2nd	1.12
3rd	0.75
4th	0.94
UN	0.33

These limited results place in doubt the benefit of a large number of hydriding cycles for obtaining a fine particle size.

We made the first experimental runs with the grinder to get an indication of the rate at which this equipment grinds UN and an indication of how much impurity is picked up in three separate steel mills.

Figure 2.1 shows that the rate of grinding is not strongly dependent on the size of the charge up to 20 g. The anomalously high level of Fe pickup for the 10-g charge probably reflects a variation in the hardness of the steel mill rather than an effect of charge size.

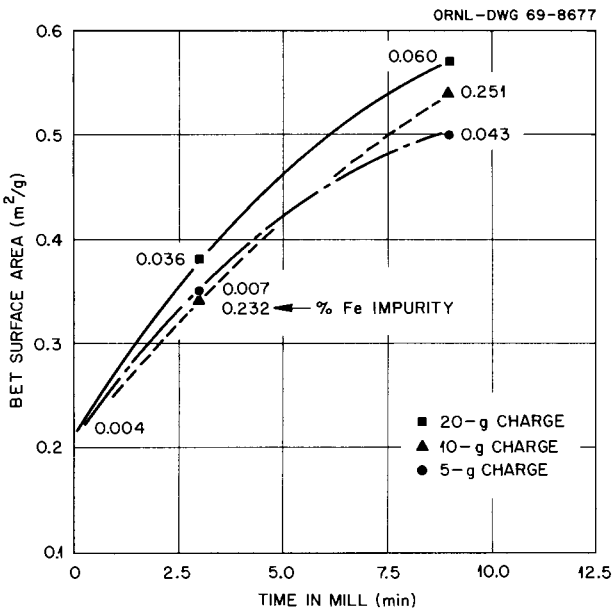

Fig. 2.1. Dependence of Surface Area and Iron Impurity Increase of UN on Milling Time and Charge Size.

We extended our hot-pressing experiments[1] on UN to include mechanical mixtures of UN with 20% PuN. We varied the temperature from 1450 to 1520°C and the pressure from 2000 to 6000 psi. We could not accurately measure density by weighing and micrometer measurements because of fractures at the edges. We are arranging for pycnometric measurements of volume for irregular shapes and are changing our method for removing the pellets to eliminate the breakage problem.

We received and partially installed the glove box for containing the resistance furnace with a W element. All three glasses for this box were broken in shipment; this caused a six-week delay while the replacement glass, which has just arrived, was obtained. Until sintering

[1]E. S. Bomar and Ji Young Chang, Fuels and Materials Development Program Quart. Progr. Rept. Dec. 31, 1968, ORNL-4390, pp. 38–40.

experiments with Pu compounds begin, we will continue to use the furnace for work with UN and ThN.

Apparatus for Synthesizing Metal Nitrides (K. E. Spear, T. G. Godfrey, V. J. Tennery)

An apparatus for synthesizing high-purity metal nitrides in research quantities of 5 to 50 g was described previously.[2] We have since then thoroughly checked it for leaks and slightly modified it. The most significant improvement is the addition to the system of an analyzer for O_2. This analyzer samples the gases (N_2, Ar, H_2) at the entrance to the reaction chamber and monitors the O_2 content continuously. Nitride powder made with this apparatus has contained as little as 200 ppm O.

Characterization of Nitride Fuels (V. J. Tennery, T. G. Godfrey)

X-Ray Diffraction Equipment for Interim Plutonium Facility. — The x-ray diffraction equipment in the Interim Plutonium Facility is now operational. It consists of a GE XRD-5 horizontal goniometer in the left box of a suite of three alpha glove boxes that comprise the x-ray facility. A camera table with a vertical tube and three camera tracks is located in the laboratory area immediately behind the suite of boxes.

Techniques and Procedures for Diffractometry. — We are developing techniques and procedures to ensure cleanliness and control of contamination for x-ray diffractometry in the Interim Plutonium Facility. We are using NaCl and UN as stand-in materials while we are developing the techniques for preparing Pu samples.

Since we want to keep the diffractometer as clean as possible for ease of maintenance, we plan to handle Pu directly only in the preparation box; all comminution, screening, and loading of Pu materials will be restricted to this one box. The adjoining box will be used for inspecting diffractometer specimens and for cutting, sealing, and monitoring the Debye-Scherrer capillaries. The diffractometer specimens, in the form of a parlodian casting in an Al picture frame contained in a thin,

---

[2]K. E. Spear, V. J. Tennery, and J. M. Leitnaker, Fuels and Materials Development Program Quart. Progr. Rept. March 31, 1969, ORNL-4420, p. 45.

heat-sealed plastic envelope, will be passed into the diffractometer box only if they are shown to be clean by an alpha counter in the center box. The Debye-Scherrer capillaries will be handled with micromanipulators and special hardware that can be discarded after one use. The capillary specimens are protected and contained by a gelatin capsule cemented to the brass holder and are passed out of the box after they are checked with the alpha counter.

The techniques we have developed allow us to pass items from box to box by a system of double-folded bags, sleeves, stoppers, and bottles in such a way that no surfaces that have been exposed to Pu in the preparation box are presented to the clean box next to it. All hardware items for preparing diffractometer or Debye-Scherrer specimens will be inserted into the clean box as a package to ensure their cleanliness.

Synthesis, Fabrication, and Thermodynamic Properties of Carbonitride Fuels

Manufacture of UC, UN, and U(C,N) from UO_2 (T. B. Lindemer, J. M. Leitnaker)

The kinetics of the conversion of sol-gel UO_2 to uranium carbides, nitrides, and carbonitrides is being studied to determine the mechanisms that control the rate of the conversion processes. This information, which is fundamental to the design of reactor fuel cycles, is a prelude to the conversion of mixed $(U,Pu)O_2$ to the carbonitride.

Kinetics of the UC_2-N_2 Reaction. — We are continuing to analyze the experimental results obtained on the UC_2-N_2 reaction.[3] Previous reports[4–7] contain the theoretical models used for the analysis of reactions in

---

[3]As used here, UC_2 represents the nominal dicarbide; the ratio C:U is always less than two.

[4]T. B. Lindemer, Fuels and Materials Development Program Quart. Progr. Rept. June 30, 1968, ORNL-4330, pp. 32–39.

[5]T. B. Lindemer and J. M. Leitnaker, Fuels and Materials Development Program Quart. Progr. Rept. Sept. 30, 1968, ORNL-4350, pp. 39–47.

[6]T. B. Lindemer and J. M. Leitnaker, Fuels and Materials Development Program Quart. Progr. Rept. Dec. 31, 1968, ORNL-4390, pp. 42–44.

[7]T. B. Lindemer and J. M. Leitnaker, Fuels and Materials Development Program Quart. Progr. Rept. March 31, 1969, ORNL-4420, pp. 47–55.

spheres, our experimental results, and portions of the analysis of the results. Further analysis is presented here.

The composition of the U(C,N) was studied during the course of the reaction between UC_2 and N_2. At a given percentage of conversion of the UC_2, the composition of the U(C,N) was approximately constant from 1500 to 1700°C. Therefore, data from different measurements on samples at different temperatures could be used in one set of calculations. The lattice parameter of the U(C,N) reacted in a run at 1700°C was determined from Debye-Scherrer x-ray films. For nonequilibrium reaction of N_2 with UC and UC_2 at these temperatures, the N:(C+N) ratio in the U(C,N) can be obtained[8] by linear interpolation between the lattice parameter of UC, 4.9602 A, and UN, 4.8892 A. The experimental data and the N:(C+N) ratio are given in Table 2.1, along with the percentage of conversion of the UC_2 core determined from the measurements of the diameter of the unreacted

[8] J. M. Leitnaker, R. A. Potter, K. E. Spear, and W. R. Laing, "The Lattice Parameter of U(C,N) as a Function of Composition," accepted for publication in High Temperature Science.

Table 2.1. Lattice Parameter and Nonequilibrium N:(C+N) Ratio of U(C,N)[a]

Time (min)	Converted UC_2 (%)	Lattice Parameter (A)	Standard Deviation of Lattice Parameter (A)	N:(C+N)
180	19.5	4.93990	0.00147	0.286
363	37.6	4.93914	0.00099	0.297
542	52.5	4.93836	0.00049	0.303
720	72.4	4.94007	0.00067	0.285
900	86.0	4.93334	0.00114	0.379
1080	87.7	4.92787	0.00038	0.452
1245	95.6	4.92814	0.00028	0.449
1440	98.0	4.92583	0.00054	0.485

[a] Run A5164-12.

UC_2 core, r, and the original diameter of the microsphere, r_o. Figure 2.2 shows the N:(C+N) ratio plotted against the percentage of conversion along with the ratios for U(C,N) in equilibrium with either C and UC_2 or C and N_2 at 1700°C and a N_2 pressure of 380 torr. The U(C,N) can be seen to remain near the composition in equilibrium with UC_2 and C for the greater part of the UC_2 conversion.

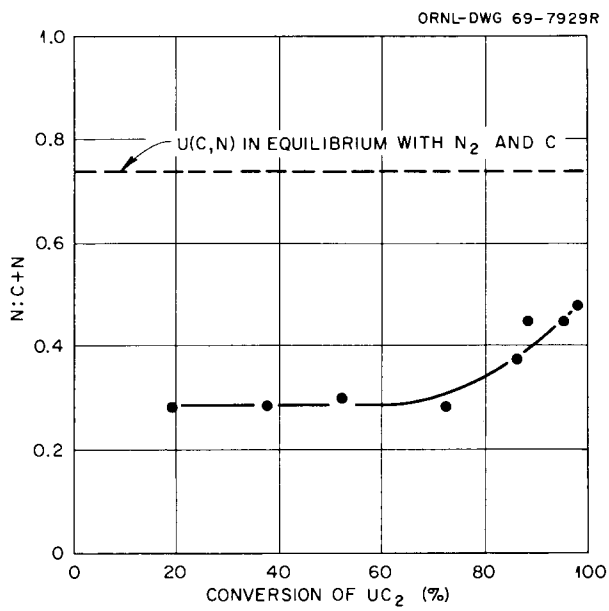

Fig. 2.2. The N:(C+N) Ratio for U(C,N) Produced by the UC_2-N_2 Reaction at 1700°C as a Function of Percentage of UC_2 Converted.

The approximate density of the precipitated C was determined from the x-ray data presented above and the measurements given in Table 2.2 for a specimen (A5163-84) reacted at 1600°C. From these data we calculated the ratio of the apparent volume of C to the original volume of the UC_2 shown in Fig. 2.3. The volume of C on the surface appears to go through a maximum, but this is a false effect because the soft C from the surface of the spheres was abraded in the fluidized bed. The theoretical volume ratio was calculated from the N:(C+N) ratios obtained from the hand-fitted curve in Fig. 2.1 and the reaction

$$UC_{1.86} + y/2\ N_2 \rightarrow U(C_{1-y}N_y) + (0.86 + y)\ C\ .$$

Table 2.2. Average Values of Quantities Measured on Specimens[a] Reacted at 1600°C and 380 torr of Nitrogen

UC_2 Reaction		Volume Fraction Free C		Diameter of Original Microsphere (cm)	Thickness of Outer Layer of C (cm)	Thickness of U(C,N)-Free C Layer (cm)
Extent (%)	Time (min)	U(C,N) Phase	UC_2 Phase			
				$\times 10^{-4}$	$\times 10^{-4}$	$\times 10^{-4}$
0	0		0.010[b]			
28.1	485	0.0745	0.051	236.9	10.93	24.71
45.4	966	0.159	0.125	238.6	13.83	43.55
64.1	1440	0.194	0.163	231.0	14.56	66.83
74.6	1920	0.229	0.201	228.9	19.86	83.93
83.8	2400	0.244	0.221	230.3	22.01	104.78
92.0	2880	0.275	0.213	238.2	18.10	135.4
96.1	3313	0.284	0.212	238.4	14.13	157.8

[a]Run A5163-84.

[b]Based on chemical analysis.

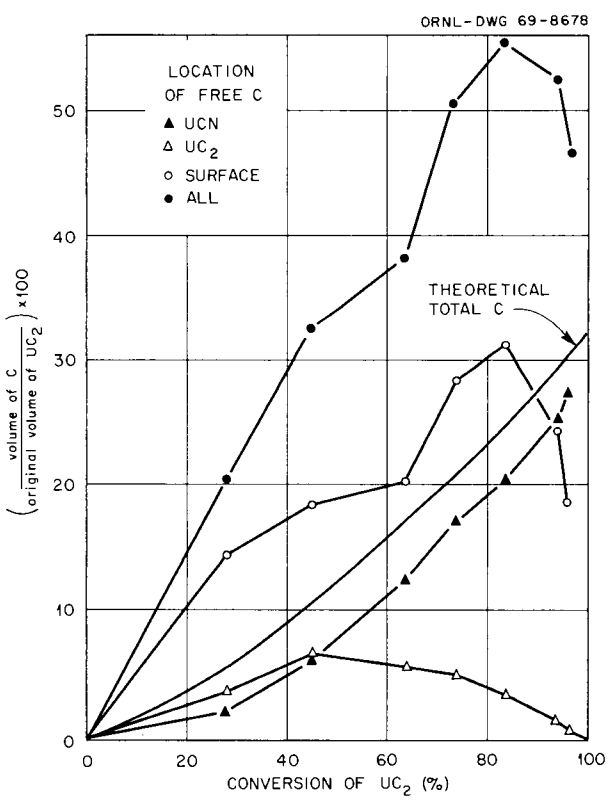

Fig. 2.3. The Observed and Theoretical Occurrence of Free Carbon Produced by the UC_2-N_2 Reaction as a Function of Percentage of UC_2 Converted.

This theoretical ratio, which is plotted in Fig. 2.2, is significantly lower than the observed ratio. The difference between the experimental and theoretical results is apparently caused by a considerable void content in the C, which appears to be only 30 to 50% of theoretical density.

These results and those described in previous issues of this quarterly report have delineated several processes and factors that affect the rates of the chemical conversion reactions. Many of the reactions appear to be controlled by diffusion through the U compounds. The reaction time may therefore be reduced, under certain controlled conditions, by reducing the particle size of the U material, as is found ideally in the mixed UO_2-C sol-gel materials. The possibilities for specific applications of these results are being studied.

Compatibility of Mixed-Nitride and Carbonitride Fuels with LMFBR Cladding Alloys

K. E. Spear

One approach to compatibility in high-performance fuel systems is to characterize the interactions that can occur between the fuel and cladding material, since an understanding of these reactions may point to methods for tailoring the fuel so that the reactions cannot occur and, perhaps, to methods for hindering the reaction kinetics.

We have been studying the chemical and thermodynamic properties of the interactions between V alloys and carbide fuels in the U-V-C system. This study, when combined with the results of investigations of the U-V-N system that are in progress, will show what experiments are needed to obtain a basic understanding of the more complicated quaternary U-V-C-N system. A few selected experiments involving Pu will be needed to determine how this added element affects the basic properties of these systems.

Adding VC to carbonitride fuels may tailor the fuel to force thermodynamic compatibility with stainless steel or Mo alloys when free C is produced as a result of fuel burnup. Such a tailoring of carbide fuels is discussed below. Additions of V(C,N) solutions to carbonitride fuels may also be advantageous.

Ternary U-V-C System (K. E. Spear, T. B. Lindemer, J. M. Leitnaker)

The possible use of V alloys with nitride and carbonitride reactor fuels has generated interest in the U-V-N and U-V-C ternary systems. Results of studies on the U-V-C system are given in this report. Recently, Gorle *et al.*[9] showed a partial phase diagram of this system that contained UVC_2 but did not mention the ternary compound in the text. Their experimental results indicated that V is not thermodynamically compatible with UC but reacts to form V_2C and U. Huet *et al.*[10] have also reported the detection of a new phase, UVC_2, that is similar to $UCrC_2$. We confirmed the existence of UVC_2 and determined its crystal structure to be of the orthorhombic, $UMoC_2$ type.[11]

In the present studies, we have examined the entire U-V-C ternary phase diagram. Three binary U-C, nine binary V-C, and eighteen ternary U-V-C samples were prepared by arc melting mixtures of the elements. These samples were examined by x-ray and/or metallographic techniques after the melting and the various annealing experiments. The samples were annealed for times ranging from a few hours to seven days at 1200°C and higher. Either Ar or vacuum of 10^{-6} to 10^{-7} torr was used for annealing atmospheres.

Metallic impurities in three ternary samples were determined by spectrographic analysis; the results are given in Table 2.3. The high Fe content in sample 13(b) may have resulted from crushing the sample in a hardened steel mortar. The high W content in all three of the analyzed samples is probably due to arc melting the samples with a W electrode. [Also, a W container was used in annealing sample 52(c)].

---

[9]F. Gorle, W. Timmermans, F. Casteels, J. Vangeel, and M. Brabers, "Preparation Processes and Stabilization of Uranium Monocarbide," pp. 481–496 in Thermodynamics of Nuclear Materials, 1967, International Atomic Energy Agency, Vienna, 1968.

[10]J. J. Huet, F. Casteels, A. Cools, P. Diels, J. Dresselaers, R. Lecocq, J. Pelsmaekers, Ph. Van Asbroeck, and J. Vangeel, "Interaction Between Uranium Carbide and Austenitic and Ferritic Stainless Steels," paper presented at the International Symposium on Ceramic Nuclear Fuels, May 5–7, 1969, Washington, D.C. To be published in the proceedings.

[11]K. E. Spear and J. M. Leitnaker, Fuels and Materials Development Program Quart. Progr. Rept. March 31, 1969, ORNL-4420, pp. 58–65.

Table 2.3. Impurities in Three Ternary Uranium-Vanadium-Carbon Samples as Determined by Spectrographic Analysis

Sample Number	Annealing Conditions[a]	Impurity[b] (ppm by Weight)			
		Al	Fe	Si	W
52	A	200	60	200	1000
13	B	25	1000	20	1000
52	C	70	60	20	2000

[a]Annealing conditions: A = quenched from the melt,
B = seven days at 1200°C in Ar atmosphere in Al_2O_3 container,
C = 8 hr at 1500°C and 10^{-7} torr vacuum in W container.

[b]Elements detected in quantities of ≤ 50 ppm by weight in all three samples: B, Bi, Ca, Ce, Co, Cr, Cu, K, Mg, Mn, Mo, Na, P, Pb, S, Th, Ti, Y, Zn, and Zr.

The W is probably in solution with the uranium carbide phase. Analysis showed that sample 13(b) contained 320 ppm O by weight.

The results of x-ray analyses of the ternary U-V-C samples are given in Table 2.4 in order of increasing C content in the samples. These results are shown by the ternary phase diagrams in Fig. 2.4 along with a schematic representation of the sample compositions.

Metallographic results showed that the three-phase region of UC-V_2C-U does exist. The ternary compound UVC_2 was never observed in samples quenched from the melt, and since UVC_2 is formed on annealing at 1600°C, this indicates that UVC_2 undergoes a solid-state decomposition at some temperature between 1600°C and temperatures at which the liquid state forms in samples of this composition. Our results also show that UVC_2 is not stable in the presence of C but can react to form UC_2 and VC.

What are the practical implications of these studies? First, we have confirmed that V is not thermodynamically compatible with UC (or the higher carbides). Second, the three-phase region UC-VC-V_2C may serve as a buffering system for carbide fuels clad with stainless steel or Mo alloys. The addition of enough C to move into the UC-UVC_2-VC three-phase region increases the C activity to a value slightly lower

Table 2.4. X-Ray Analysis of Ternary Uranium-Vanadium-Carbon Samples

Sample Number	Synthetic Composition (mole %)			Annealing[a,b] Conditions	X-Ray Results[c]					
	U	V	C		V_2C	VC	UVC_2	UC	U_2C_3	UC_2
40	30	30	40	A	w			s		
				B	w			s		
				C	w			s		
41	10	50	40	A	m	m		s		
				B	m			s		
				C	m			s		
14	20	36	44	A		vw		s		
				B		w		s		
				C		w		s		
				D		w		s		
46	40	15	45	A	vw			s		
				B	vw			s		
				C				s		
18	30	25	45	A[d]		w		s		
				B			s	w		
				C			s	s		
				D			s	s		
47	10	45	45	A		s		s		
				B		s		s		
				C		s		s		
51	35	15	50	A		vw		s		
				B				s		
				C			m	s		
52	20	30	50	A		m		s		
				B		s	m			m
				C			s			
53	10	40	50	A		s		s		
				B		s		s		
				C		s	s	s		
13	24	25	51	A		w		s		
				B			s			
				C			s			
				D			s	vw		
17	36	11	53	A[d]				s		w
				B			m	s	m	
				D			m	s	m	
56	20	25	55	A		m		s		s
				B		m	w	s		s
				C		w	s			s
57	10	35	55	A		s				s
				B		s	w	s		w
				C		s	s			s
12	28	14	58	A[d]		w		w		s
				B			w	w		s
				D			w	w		s
11	16	24	60	A[d]		m				s
				B		m				s
				D		m				s

[a]Annealing conditions: A = quenched from the melt; B = two days (samples 11–18) or seven days (samples 40–57) at 1200°C in Ar atmosphere in Al_2O_3 container; C = 8 hr at 1500°C and 10^{-7} torr vacuum in W container; D = 4 hr at 1600°C and 10^{-6} torr vacuum in graphite container.

[b]Except as indicated, the starting material was a portion of the arc-melted sample.

[c]Debye-Scherrer x-ray powder photographs made with CuK_α radiation were examined for these results. Relative intensities for each phase are reported as very weak, vw; weak, w; medium, m; and strong, s.

[d]The starting material for annealing under these conditions was residue from annealing under D conditions.

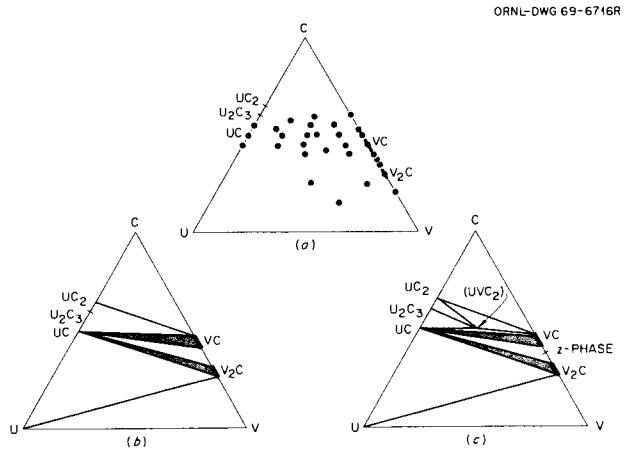

Fig. 2.4. Ternary U-V-C Phase Data and Results. (a) Positions of samples in ternary phase field, (b) results for samples quenched from the melt, and (c) results for samples annealed at 1500 to 1600°C.

than that for the UC-U_2C_3 system. However, this activity is probably great enough to cause the carburization of stainless steels or Mo.

In conclusion, the use of vanadium alloys with carbide fuels will require that the kinetics of the reaction between V and UC in the reactor be slow. The UC-VC-V_2C three-phase region may be a very good buffering system for use of carbide fuels with stainless steels or Mo alloys, particularly since V is a small atom and thus dilutes the density of heavy-metal atoms relatively little and since it has such a low neutron cross section.

Thermodynamic Investigations of High-Performance Fuel Systems

K. E. Spear

The goal of our thermodynamics program for high-performance fuels, the carbides, nitrides, and carbonitrides, is to be able to predict the limiting equilibrium behavior of fuel and cladding in fast-reactor environments. Our experiments, though limited to measurements out of reactor, are of value for defining and understanding the factors that affect fuel performance.

Thermodynamic Stability of UVC_2 (K. E. Spear, T. B. Lindemer, J. M. Leitnaker)

The existence of the ternary compound UVC_2 has been confirmed in phase studies of the ternary U-V-C system.[12] Thermodynamic properties for the formation of UVC_2 may be calculated from these data for the U-V-C phase. These data show that at 1500 to 1600°C, the following reactions proceed from left to right and thus have negative free energies:

$$UVC_2 + 0.81\ C \rightarrow UC_{1.93} + VC_{0.88}\ ,$$

$$0.76\ UC + 0.12\ U_2C_3 + VC_{0.88} \rightarrow UVC_2\ .$$

These facts plus data for the free energy of formation, ΔG_f°, for the binary phases can, therefore, be used to set limits for the ΔG_f° of UVC_2. We have performed the calculations for 1800°K and the following values for ΔG_f°: UC = −25.4; U_2C_3 = −51.8; $UC_{1.93}$ = −26.4; and $VC_{0.88}$ = −21.7 kcal/mole. [The value for U_2C_3 is given in an equation by Storms.[13] The other three values were calculated from data for the free-energy function (fef_T°) and heat of formation ($\Delta H_{f,298}^\circ$). The fef_T° data for U, UC, $UC_{1.93}$ (including randomization entropy of 0.5 eu), and $VC_{0.88}$ were taken from Storms,[13] and those for V and C were taken from Hultgren et al.[14] The values used for $\Delta H_{f,298}^\circ$ were UC = −23.2 (ref. 15); $UC_{1.93}$ = −20.5 (refs. 15,16); and $VC_{0.88}$ = −24.5 (ref. 13) kcal/mole.] The results are that $\Delta G_{f,1800}^\circ$

---

[12] K. E. Spear, T. B. Lindemer, and J. M. Leitnaker, "Ternary U-V-C System," pp. 38–41, this report.

[13] E. K. Storms, The Refractory Carbides, Academic Press, New York, 1967.

[14] R. Hultgren, R. L. Orr, and K. K. Kelley, Supplement to Selected Values of Thermodynamic Properties of Metals and Alloys, Inorganic Materials Research Division, Lawrence Radiation Laboratory, University of California, Livermore, California. Carbon data compiled May 1965; vanadium data compiled May 1966.

[15] E. K. Storms and E. J. Huber, Jr., J. Nucl. Mater. 23, 19–24 (1967).

[16] J. M. Leitnaker and T. G. Godfrey, J. Nucl. Mater. 21, 175–89 (1967).

for UVC_2 must be between −47.3 and −48.1 kcal/mole. We recommend a value of −47.7 ± 1.0 kcal/mole (we estimated the uncertainty from the uncertainties in the auxiliary data we used).

Measurements of the Physical Properties of (U,Pu)N Alloys

S. C. Weaver D. L. McElroy

Because it is important to know temperature distributions to predict irradiation behavior, we are beginning a study of the thermal conductivity of (U,Pu)N alloys. Fuel swelling, release of fission gas, distribution of fission products, redistribution of Pu, and other effects of irradiation very strongly depend on the temperature distribution and, therefore, the thermal conductivity of the fuel. We plan to study the effects of fuel density, including the effects of pore size and shape; the effects of impurities such as C and O; and the effects of varying compositions of U and Pu.

We are now designing and fabricating the equipment. The glove boxes and component parts for the comparative heat-flow apparatus have been designed, and the parts have been ordered. Design is continuing on the component parts for the absolute thermal-conductivity apparatus and on the electrical-resistivity apparatus.

Irradiation Testing of Nitride Fuels for LMFBR Applications

The objective of this program is to establish the irradiation performance of the U,Pu nitrides and carbonitrides. The nitrides and carbonitrides have a thermal conductivity about ten times higher, a theoretical density 30% higher, and a metal content in the compound 7% higher than the oxides. These properties make the nitrides and carbonitrides strong contenders as advanced fuel for an LMFBR.

Thermal-Flux Irradiation Tests (T. N. Washburn)

The initial series of uninstrumented irradiation tests will be conducted in the Engineering Test Reactor (ETR). These tests are of the

"screening" type to evaluate the performance of carbonitrides relative to carbides or nitrides synthesized from metal. Linear heat ratings will be 25 and 35 kw/ft to burnups of 30,000 and 60,000 Mwd/metric ton. Neutron radiography will be used to monitor fuel swelling, and scheduled burnups may be shortened or extended in accordance with the results of this nondestructive test.

The fuel pins will have a 0.010-in. radial gap between the fuel pellet and the inner surface of the cladding. The gap will be filled with Na–19% K to enhance heat transfer. The irradiation program is awaiting final results of an investigation into techniques for loading the NaK to ensure proper bonding. Pellets of UN were made for these loading tests with the assumption that wetting characteristics would be similar to those of (U,Pu)N. Fuel pins for irradiation testing will be fabricated when these loading tests are completed.

Fabrication of ETR Capsules for (U,Pu)N (M. K. Preston, R. B. Pratt, R. A. Bradley, W. L. Moore)

A series of screening irradiation tests of (U,Pu)N fuels are planned for the ETR. The ETR capsules, with double containment, will be basically the same as the other ETR capsules we have made except that the fuel pellets will be bonded to the cladding with Na–19% K instead of He. Prototype equipment for developing the process of loading the NaK was designed and fabricated. Dummy pellets of stainless steel and depleted UN were ground to 0.200 in. in diameter and are ready for use. Containers for transferring the NaK were completed, and the Na–19% K was ordered.

Irradiation Testing of UN in ORR (S. C. Weaver)

A new series of irradiation tests in the Oak Ridge Research Reactor (ORR) was begun to provide basic information on the irradiation behavior of UN. Two UN capsules were irradiation tested. The first capsule, ORR-UN1, was irradiated for 8250 hr until the bottom fuel pin failed. The capsule was then removed for postirradiation examination. The second capsule operated only 220 hr before a loss of NaK caused the temperature in the top pin to rise above 2000°C. The capsule was

reloaded with NaK, but this, too, was soon lost. The capsule was then removed for postirradiation examination. The status of our observations and our preliminary evaluations are presented below.

Capsule Design. — Both capsules were of a well-instrumented design with some new features. A schematic diagram of ORR-UN2 is shown in Fig. 2.5. Each capsule contained three fuel pins, all clad in W-Re derived from arc-cast material: W–26% Re was used in ORR-UN1, and W–25% Re was used in ORR-UN2. The fuel pins were thermally bonded to the primary containment with Na–44% K; T-111, Ta–8% W–2% Hf, was used in ORR-UN1 and Nb–1% Zr in ORR-UN2 for the primary NaK containment. The NaK annulus also contained the cladding thermocouples, which were located at the center line of the top and bottom fuel pins and in the middle of the two fueled regions in the central fuel pin. A 450-psi pressure maintained over the NaK prevented it from boiling. The fuel pins were centered with W spacers between the fuel pins and at the top and bottom of the capsule train to prevent thermal convection by restricting the movement of the NaK. A 0.030-in. He gas gap separated the NaK container from the type 304 stainless steel containment. A 0.001-in. He gas gap separated the stainless steel and Zircaloy-2.

In each capsule, the fuel in the top pin was annular, and that in the bottom pin was solid pellets. The pellets were fabricated by cold pressing and sintering to about 94% of theoretical density. No second-phase oxide was present in any of the fuel. The middle test pin in capsule ORR-UN1 contained 95% dense pellets and single crystals, both immersed in Li, for measuring the unrestrained fuel swelling. In ORR-UN2, the middle pin contained 85 and 95% dense pellets immersed in Li.

Operating History. — Summaries of the operating histories of these two capsules are shown in Table 2.5. Capsule ORR-UN1 operated satisfactorily except for failure of the cladding thermocouples in the first few hours of operation. Because we had a Zircaloy-2 calorimeter on the outer sleeve, we were able to correlate the rate of heat generation with the temperatures indicated by the cladding and central thermocouples during the first few hours of operation. Consequently, we were able to

ORNL-DWG 67-983R2

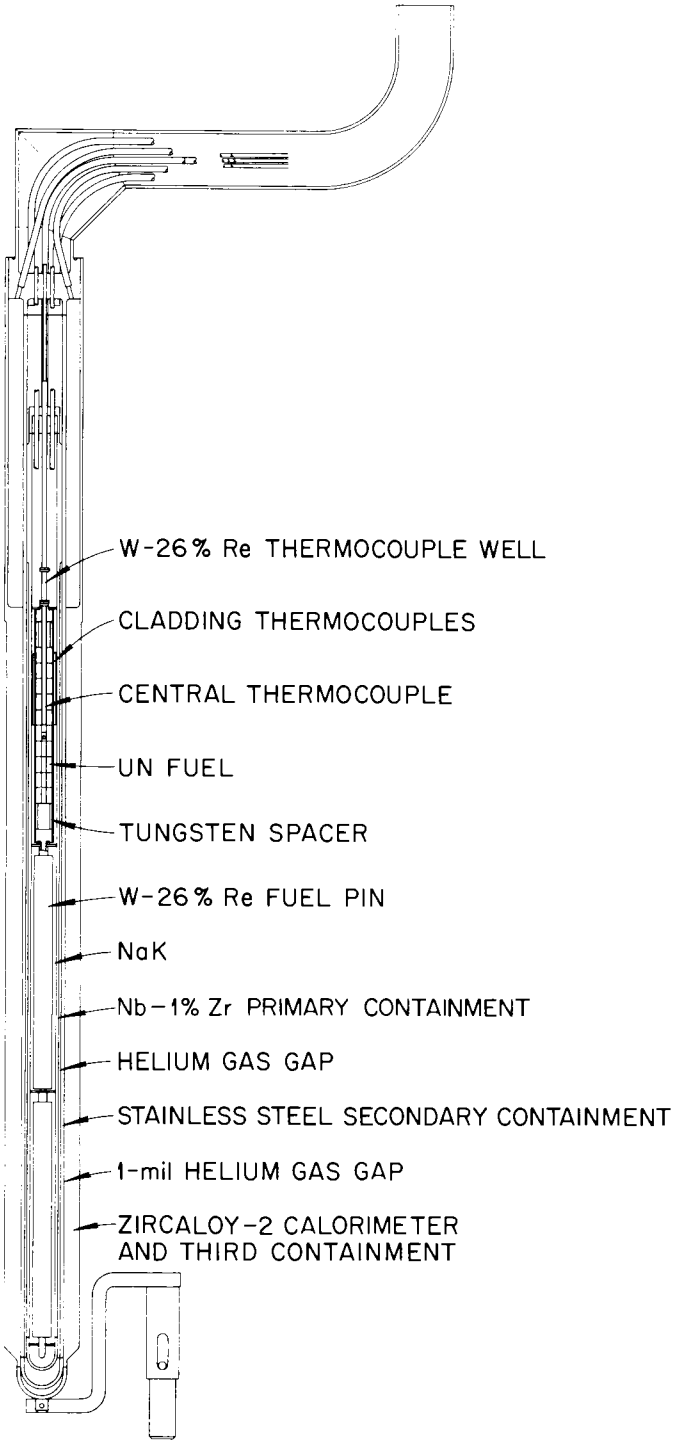

Fig. 2.5. Capsule for Irradiation of UN in the ORR.

Table 2.5. Summary of Operating Conditions in Capsules ORR-UN1 and ORR-UN2

Capsule	Test Pin	Average Temperature, °C		Power Density (kw/cm^3)
		Cladding	Fuel Center	
ORR-UN1	Top	1040	1200	0.61
	Middle	1100	1250	0.72
	Bottom	1200	1400	0.56
ORR-UN2	Top	~ 2000	~ 2100	0.55
	Middle	1175	~ 1325	0.79
	Bottom	1350	1550	0.62

calculate the operating cladding temperatures with reasonable accuracy throughout the life of the capsule.

The capsule continued to operate satisfactorily until the bottom fuel pin failed and released fission gases to the NaK. When these gases were detected during a routine check at the midcycle shutdown, the capsule was removed from the reactor.

Capsule ORR-UN2 failed after only 220 hr of operation. The failure was initiated by NaK entering a crack in a thermocouple sheath. The NaK level rose up the thermocouple due to the 450-psi overpressure and finally leaked out of a loose Conax fitting and dropped onto the stainless steel bulkhead. The NaK continued to be pumped out through the thermocouple until the NaK level dropped to the point where the top pin was uncovered. The central thermocouple in the top element rose to 2040°C before it went off scale. It operated this way for about 48 hr before the capsule was removed from the reactor. In spite of the severe operating conditions, no pins failed.

Postirradiation Examination. — Postirradiation examination of these two capsules yielded a number of significant results that are summarized in Table 2.6.

Fuel pellets in the top fuel pin of ORR-UN1 were intact and in good condition after irradiation testing (Fig. 2.6). The data for fuel swelling were strong evidence that a very strong cladding can make the fuel swell into a central void. In the top half of the pin, a central thermocouple well extended down through the annular hole and prevented

Table 2.6. Summary of Irradiation Test Results

Capsule	Test Pin	Burnup (at. % U)	Fission Gas Released (%)	Fuel Volume Increase (%)	Changes in Pin Diameter (%)
ORR-UN1	Top	1.78	0.14	5.45[e]	< 0.08
	Middle	2.26[a] 2.45[b]	c	f	0.38
	Bottom	1.83	d	5.4	0.46
ORR-UN2	Top	0.05	63.5	0.53[e]	−0.98
	Middle	0.05	8.3	2.04 1.23[g] −1.71	< 0.08
	Bottom	0.05	< 0.01	h	< 0.08

[a]Pressed-and-sintered pellets.

[b]Bi- and tri-crystal pellets.

[c]Fuel pin failed – no gas sample.

[d]Gas sample lost during sampling.

[e]Fuel in upper half of pin surrounded central thermocouple well; this prevented fuel from swelling into central void.

[f]Volume changes so large they could not be measured accurately.

[g]High-density fuel increased in volume while low-density fuel sintered together.

[h]Data not taken.

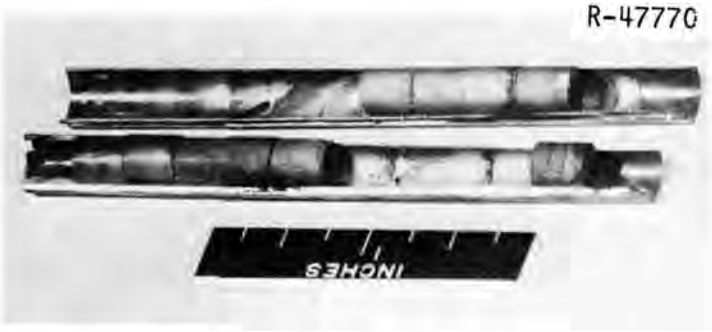

ORNL. NO. 1

Fig. 2.6. Fuel Pellets from the Top Pin in Capsule ORR-UN1 after Testing.

the fuel from swelling inward. In the bottom half of the pin, however, the fuel was free to swell into this central void and apparently did so, as indicated by the larger increases in volume. The fuel released very little of the fission gases, and dimensional changes were within experimental error (0.08%) of being unchanged.

In the middle test pin of ORR-UN1 the increases in the volume of the fuel were large for both the cold-pressed-and-sintered fuel and for the bi- and tri-crystals. Microstructures of the fuel are shown in Figs. 2.7–2.10. The fuel has very large voids, and it appears that the fuel has vaporized from the surface and condensed onto the W-Re cladding. Macroscopic examination also suggested that the fuel had condensed onto the cladding. All indications are that bubbles formed in the Li thermal bond and caused the fuel to become very hot. The middle test pin from ORR-UN2 also showed evidence of this, but not to the same extent, probably because of its significantly shorter irradiation time. In the center of the fuel, the arc-cast material was still nearly fully dense, but the sintered fuel was very porous throughout. In spite of the large fuel swelling, which must have released nearly 100% of the fission gases from the pressed-and-sintered pellets, the pin did not fail, and the increase in pin diameter was small (0.38%). Unfortunately, the sample of fission gas from this pin was lost during the puncturing operation.

The bottom test pin of ORR-UN1 failed (Fig. 2.11) after a cladding strain of only 0.46%. Metallographic examination of the cladding showed that the bottom pin failed because of a loss in ductility due to the formation of sigma phase at the grain boundaries (Fig. 2.12). The cracks were all intergranular, and in many regions a great amount of sigma phase was formed. Sigma phase was probably formed because (a) W–26% Re is near the edge of the boundary between the alpha solid solution and the sigma phase in the W-Re phase diagram, and (b) transmutations of W to Re and Re to Os during thermal irradiations shifted the composition of the alloy into the sigma-phase region. A calculation of the transmutation that occurred is summarized in Table 2.7.

It is significant to note that the maximum change in the diameter of the bottom pin was small, 0.17 in. or 0.46%; the average change in diameter was only 0.25%. It would appear, therefore, that increases in

Fig. 2.7. Typical Appearance of Pressed-and-Sintered Fuel from Middle Pin of ORR-UN1 Near Center of Fuel After Test. As polished. 100×.

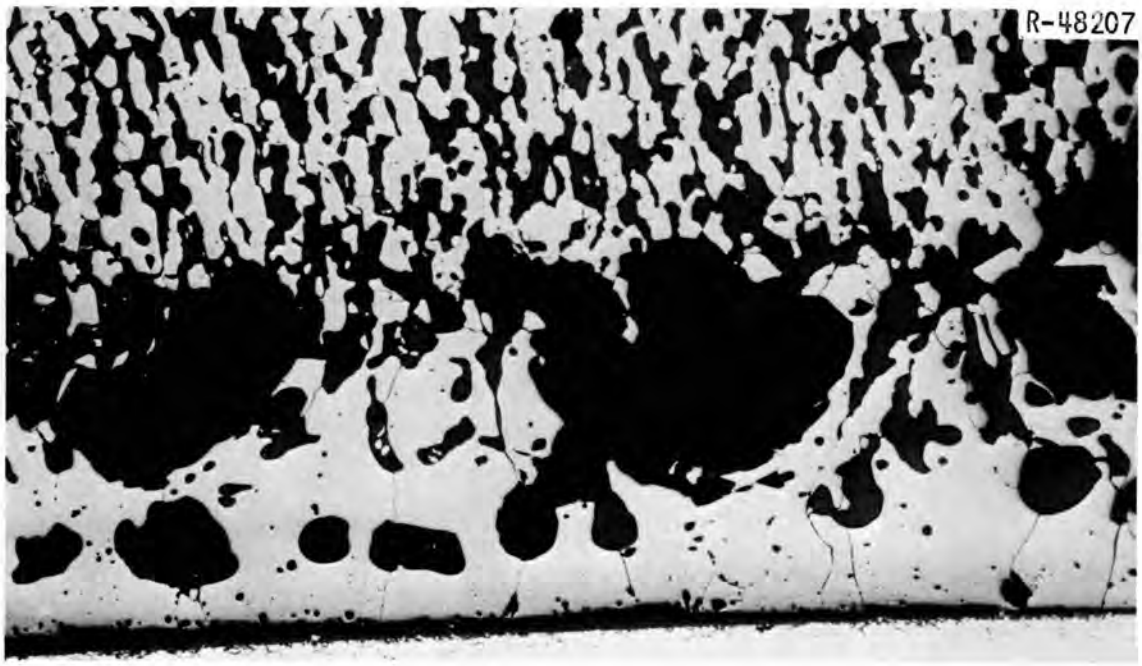

Fig. 2.8. Sintered UN Fuel from Middle Pin of ORR-UN1 Showing W-Re Cladding in the Bottom of the Picture with UN that has Condensed on the Cladding During the Test. As polished. 500×.

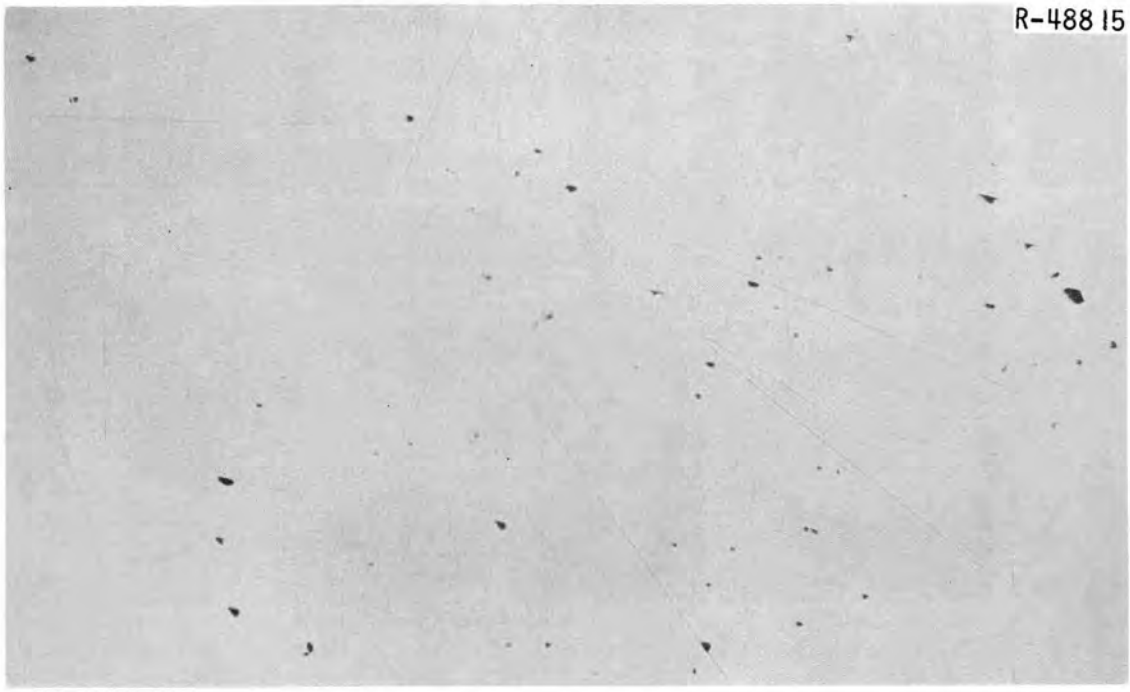

Fig. 2.9. Typical Appearance of Single-Crystal Pellet from Middle Pin of ORR-UN1 Near Center of the Fuel After Irradiation Test. 100×.

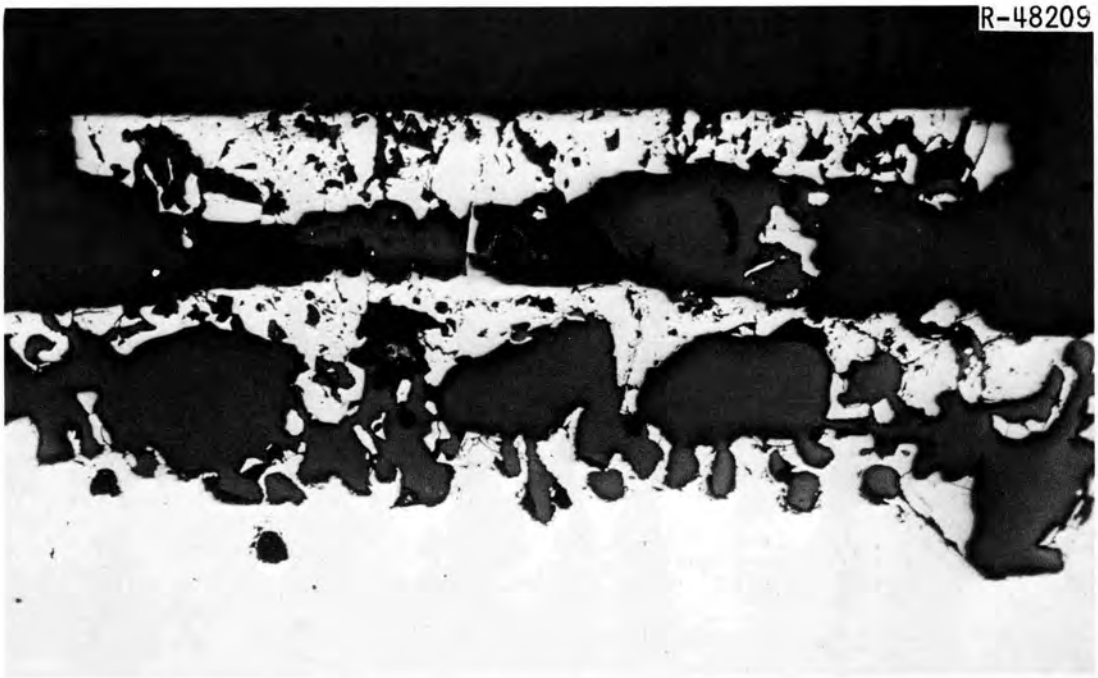

Fig. 2.10. Single-Crystal Pellet from Middle Pin of ORR-UN1 Near W-Re Cladding (at Top of Photo). UN appears to have vaporized from the pellet surface and condensed on the cladding. 100×.

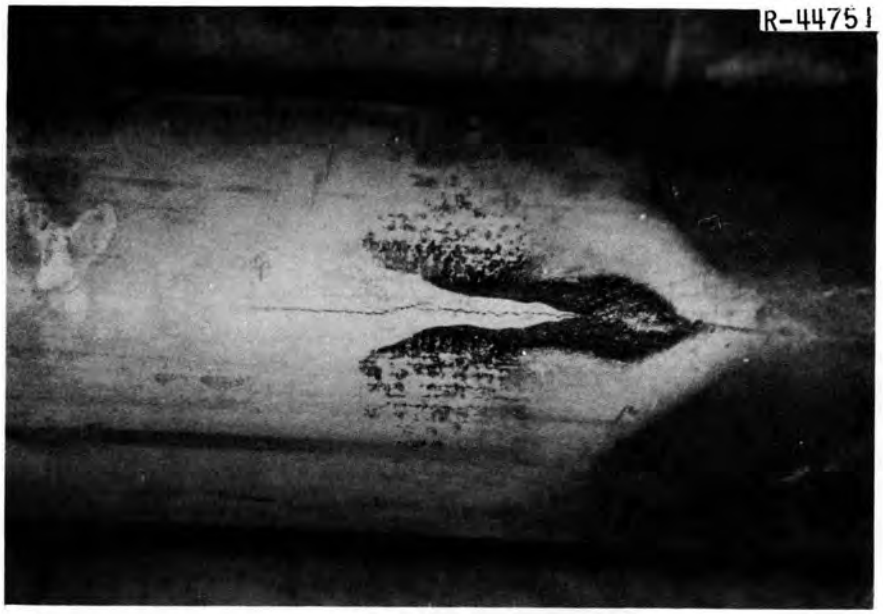

Fig. 2.11. Cracks in Bottom Test Pin of Capsule ORR-UN1. Bottom of pin is to the right.

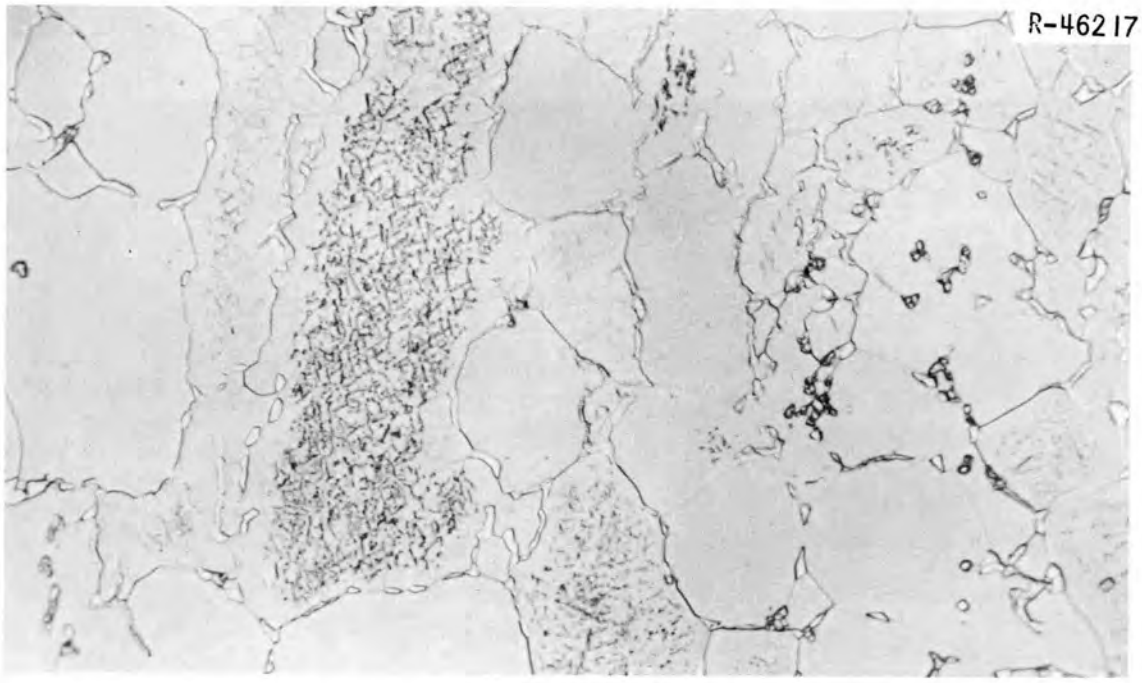

Fig. 2.12. Photomicrograph of W–26% Re Cladding from the Bottom Pin Showing Intergranular Sigma Phase. 500×.

Table 2.7. Calculated Changes in Composition Caused by Transmutations in the Cladding of the Lower Fuel Pin in Capsule ORR-UN1

Element	Composition, wt %	
	Before Irradiation	After Irradiation
W	74.0	73.5
Re	26.0	25.4
Os	0.0	1.0

cladding diameter might be reduced by the use of stronger cladding. The behavior of the top pin certainly seems to indicate that a very strong cladding can be used for force the fuel to swell inward.

The top test pin of ORR-UN2 operated above 2000°C for two days. Because the cladding was very hot and therefore relatively soft, the 450-psi NaK pressure forced the fuel pin to decrease in diameter by 0.98%. This shrinkage forced the cladding down onto the fuel. Although the fuel released 63.5% of its gases, swelling was relatively small because of the low burnup and probably because of the high external pressure on the cladding. The fuel pellets were removed intact except for three pellets that were tightly bonded to the central thermocouple well (Fig. 2.13). None of the pellets appeared to have been detrimentally affected by the severe irradiation condition.

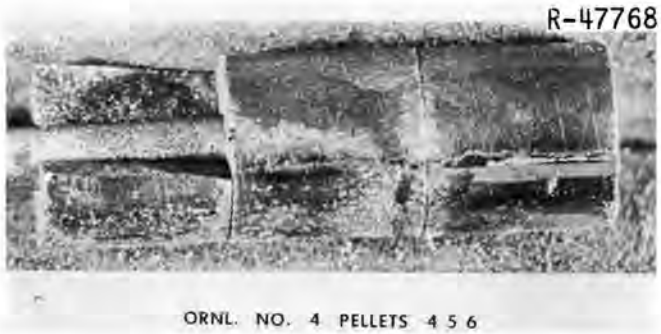

Fig. 2.13. Uranium Nitride Fuel Pellets from Top Pin of Capsule ORR-UN2 after Irradiation Testing. The fuel operated at temperatures above 2000°C.

Again, a difference in fuel swelling was observed in the top of the pin where the central thermocouple prevented the fuel from swelling inward. In the bottom half of the fuel, the fuel apparently did swell into the central void. Metallographic examination of the fuel showed lenticular voids lined up at grain boundaries parallel to the interior surface of the annular pellets (Fig. 2.14). Sweeping of these voids into the central hole might explain the high gas release. It must be noted, however, that there were no columnar grains, which typically characterize motion of lenticular voids.

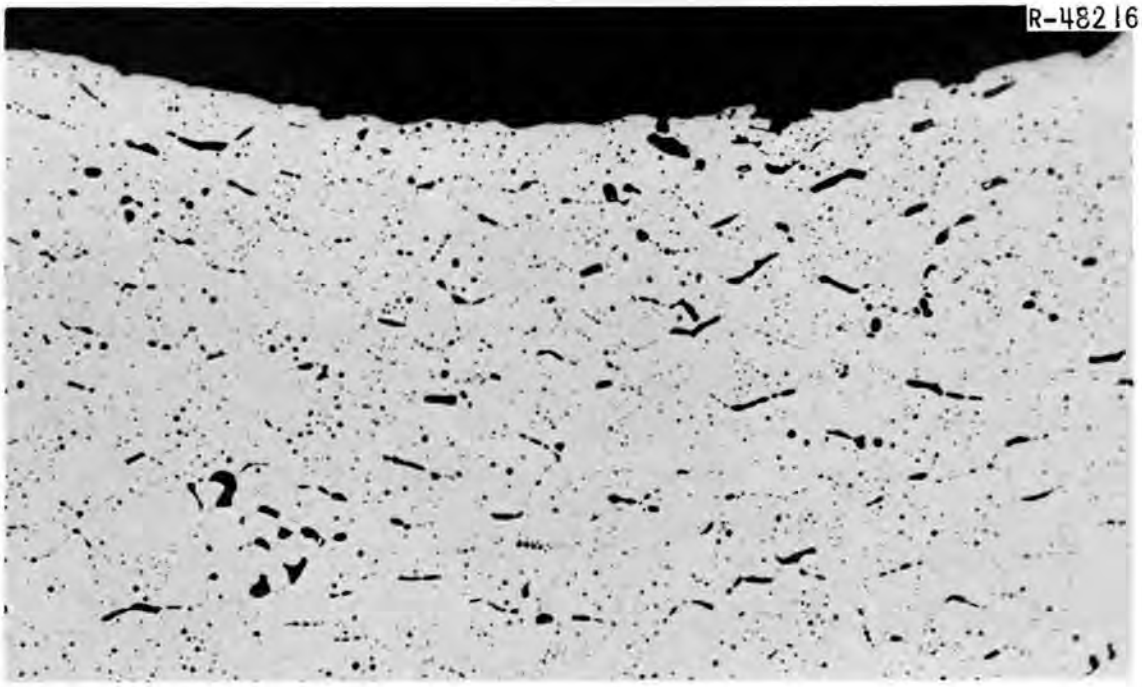

Fig. 2.14. Photomicrograph of the Inside Surface of an Annular Pellet from the Top Pin of Capsule ORR-UN2. The fuel operated above 2000°C. 200×.

The surfaces of the low-density pellets in the middle pin of capsule ORR-UN2 were severely pitted (Fig. 2.15), but not nearly as severely as those in ORR-UN1. This pitting indicates the presence of hot spots probably caused by voids in the Li. It is interesting to note that since this pitting occurred only in the low-density fuel, perhaps the voids formed from some of the larger pores.

Fig. 2.15. Pellets 6 and 7 from the Middle Pin of ORR-UN2. The high-density (95% theoretical density) pellet is on the left; the low-density pellet is on the right.

The bottom test pin from ORR-UN2 swelled little and released less than 0.01% of the fission gas.

3. FISSION-GAS RELEASE AND PHYSICAL PROPERTIES OF FUEL MATERIALS DURING IRRADIATION

O. Sisman

The purpose of this work is to measure the variables that control the release of fission gas from highly characterized nuclear fuels and to evaluate these variables in terms of a generalized model for predicting release from operating fuel materials. Thermal diffusivity is measured in-reactor in analogous experiments.

The Effect of Stored Energy in UO_2 on Measurements of Thermal Diffusivity During Irradiation

R. M. Carroll R. B. Perez

A hollow cylinder of large-grained UO_2 (ref. 1), for use in measurements of thermal diffusivity and stored energy,[2] was installed in a capsule that has low thermal inertia and is being irradiated. We have accumulated a large mass of data that is now being processed by computer and are preparing a report of the mathematical analysis of our method of studying thermal diffusivity during irradiation.

Effect of Temperature and Burnup on Release of Fission Gas From $(U_{0.75},Pu_{0.25})O_2$

R. M. Carroll

The fuel specimen, consisting of 21 spheroids 0.0903 cm in diameter, was cut from pellets of mixed oxide.[1] The spheroids were arranged in a holder made of W that surrounded a central thermocouple as shown in Fig. 3.1.

---

[1]Specimen furnished by Battelle Northwest Laboratory.

[2]R. M. Carroll and R. B. Perez, Fuels and Materials Development Program Quart. Progr. Rept. Dec. 31, 1968, ORNL-4390, pp. 58–64.

ORNL-DWG 68-2205R2

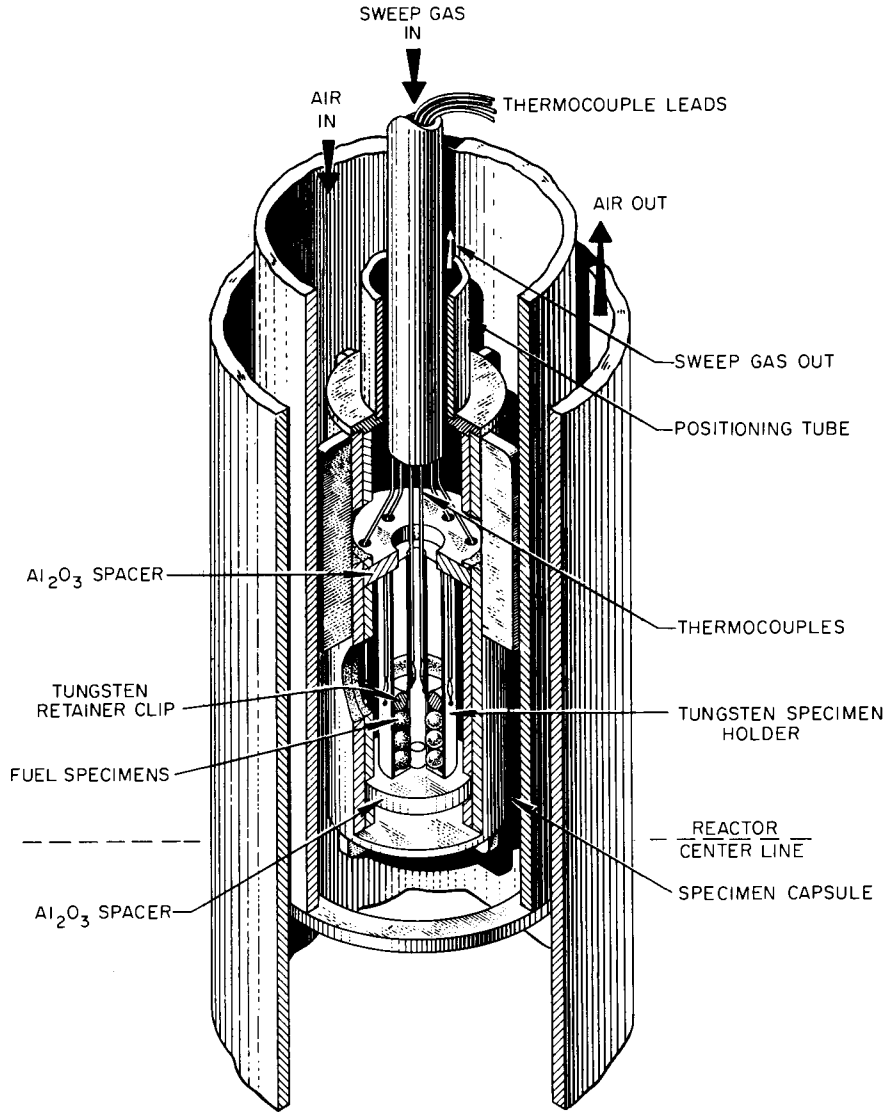

Fig. 3.1. Capsule Containing $(U_{0.75},Pu_{0.25})O_2$ Spheroids.

The initial results of the irradiation and a comparison to the results from earlier pellet specimens were reported.[3] After about 1% burnup, the rate at which fission gas was released began to increase exponentially, even though the irradiation conditions were constant. We interpreted this as the start of breakaway gas release (the point at which the internal gas pressure exceeds the strength of the fuel matrix), since lowering the temperature of the specimen halted the

[3]R. M. Carroll, Fuels and Materials Development Program Quart. Progr. Rept. March 31, 1969, ORNL-4420, pp. 72–74.

increasing gas release. As burnup progressed, breakaway gas release occurred at even lower temperatures, and at about 3.5% burnup the gas pressure at 800°C exceeded the strength of the matrix. We believed that the increasing gas pressure as burnup progressed, rather than a change in the strength of the matrix, was responsible. This was substantiated by the fact that some gas continued to leak from the specimen while the reactor was shut down for ten days. This leakage reduced the pressure within the specimen so that when the reactor again went to power it required temperatures 30°C higher than those just before the reactor was shut down to cause the start of breakaway gas release.

As irradiation progressed beyond 3.5% burnup, the steady-state rate of release of fission gas increased, probably because the constant operation at near breakaway gas release had opened some interconnected porosity in the specimen. At 4.5% burnup, about 15% of the generated ^{133}Xe was escaping from the specimen at 900°C as compared to the 0.3% ^{133}Xe that had been escaping at the start of irradiation. The greater rate of escape reduced the pressure within the specimen so that toward the end of irradiation (4.5% burnup) breakaway gas release did not occur until the temperature of the specimen had reached 930°C.

Postirradiation examination of the microstructures of both the pellet and spheroid specimens is scheduled but has not been completed.

Release of Fission Gas From UO_2

R. M. Carroll R. B. Perez

The release of fission gas from a hollow-cylinder specimen is being measured during the times that thermal diffusivity data are not being taken. Because the work on thermal diffusivity has priority, we have not irradiated the specimen at temperatures over 1100°C for fear of damaging the specimen. Preliminary examinations of the data for gas release show that the specimen is uncracked, has excellent characteristics of gas retention and exhibits the irradiation-induced trapping of fission gas expected of high-density UO_2. The data for gas release from this specimen will be used in a trial computer evaluation of the model for defect trapping after the data for thermal diffusivity have been evaluated.

4. ZIRCONIUM METALLURGY

J. R. Weir, Jr. P. L. Rittenhouse

The object of this program is to optimize the properties of Zr alloy tubing used in nuclear reactors by study of fabrication procedures and their interaction with crystallographic deformation modes. Rather than following the usual practice of designing fuel element cladding on the basis of minimum strength values, we are attempting to control the crystallographic texture in the tubing to permit the strongest direction in the tubing to be matched against the highest service stress. This technique can also be used to control the orientation of potentially embrittling hydride platelets that form from absorption of H_2 that is released by corrosion. Success in this program can reduce the cost of producing nuclear power by making possible longer core life, higher operating temperatures, and the use of tubing with thinner walls.

Texture Effects, Texture Development, and Anisotropy of Properties

Texture Development in Zircaloy Tubing (E. J. Tenckhoff)

We continued our studies of texture development and texture gradients in Zircaloy tubing. We reported[1,2] that the preferred position of basal poles in Zircaloy tubing approaches the radial direction when the tubing is fabricated with a ratio of reduction in wall thickness to reduction in diameter (R_W:R_D) larger than one and approaches the tangential direction when this ratio is smaller than one. This result was derived from schedules of tubing processed with extreme ratios of R_W:R_D. Texture development and texture gradients through the wall of the tubing

---

[1]E. Tenckhoff and P. L. Rittenhouse, Metals and Ceramics Div. Ann. Progr. Rept. June 30, 1968, ORNL-4370, p. 159.

[2]E. Tenckhoff and P. L. Rittenhouse, "Texture Gradients in Thin Walled Zircaloy Tubing," paper presented at the American Society for Testing and Materials Symposium on "Applications Related Phenomena in Zirconium and Hafnium and Their Alloys," Philadelphia, Pa., Nov. 5–7, 1968. To be published in the proceedings.

were explained by consideration of the stresses acting and the strains produced during the particular fabrication process.[2]

These results have now been confirmed by examination of Zircaloy tubing processed with ratios of $R_W:R_D$ that are common in commercial tubing fabrication. More specifically, tubing was produced by tube rocking in one to three passes, drawing in two to eight passes, and planetary ball swaging in two to four passes. All of these started from tube shells of the same size and were processed with many variations in the reduction schedule to tubing of the same final size. Textures were determined after each fabrication step in three layers of the tube wall. Although the ratios of $R_W:R_D$ were less extreme than those used in producing the tubing examined earlier, their effect on texture formation was easily recognized. This confirmed the original conclusion. The dependence of texture development on the ratio of $R_W:R_D$ can be traced step by step through successive fabrication passes regardless of the method of fabrication.

Our studies of texture development and texture gradients across the wall of Zircaloy tubing led to the following generalizations.

1. In tubing fabricated to the same final size from extrusion billets of identical size, different processing conditions — a preponderance of reduction in wall thickness or diameter — cause markedly different final textures. The relationships among tubing reductions, deformation stresses and strains, and texture development in a thin layer of the tubing wall are shown schematically in Fig. 4.1. A random distribution of basal poles is assumed at the start of the deformation. A preponderance of reduction in wall thickness ($R_W:R_D > 1$) promotes a texture with basal poles approaching the radial direction, the center of the (0002) pole figure. If $R_W:R_D = 1$, a random distribution of basal poles is developed in the radial-tangential plane (a "fiber" texture). A preponderance of reduction in diameter ($R_W:R_D < 1$) leads to a spread of basal poles toward the tangential direction.

2. The extent of movement of the basal poles and their intensity distribution depend not only on the ratio $R_W:R_D$ but also on the total reduction in area (R_A) produced in the fabrication step. In the common

ORNL-DWG 69-5592

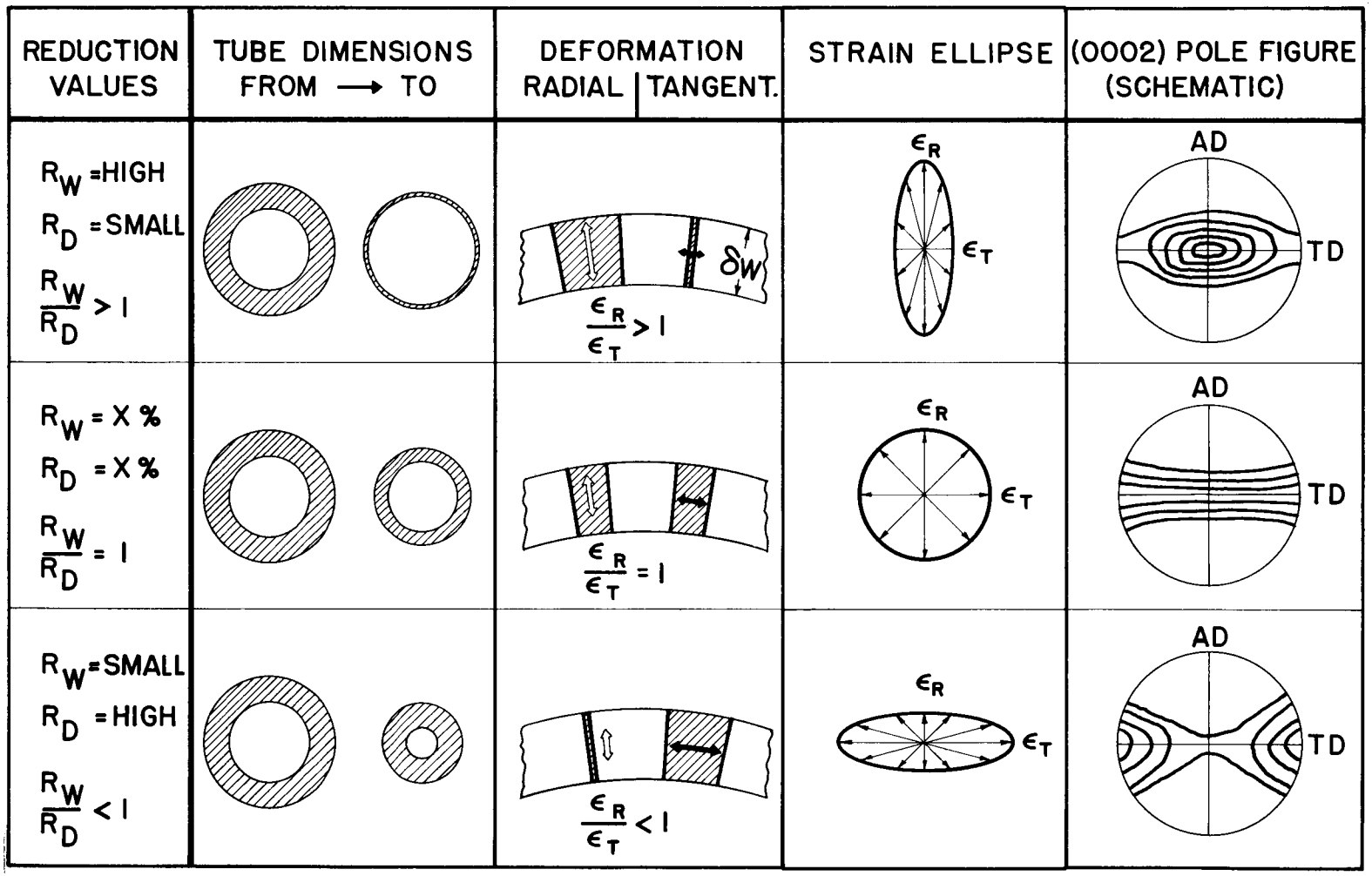

Fig. 4.1. Schematic Demonstration of Texture Development Concepts. The variation of tubing dimensions, deforming stress, its associated strain ellipse, and the resulting texture are illustrated as a function of the ratio of reduction in wall thickness (R_W) to reduction in diameter (R_D).

practice of tube reduction, the effects of reduction in wall thickness and diameter are competitive, and the textures developed are usually intermediate between the extremes. The existence of intensity maxima in positions between the radial and tangential directions can be explained by consideration of the texture of the material before the fabrication step involved.

3. The primary components of the compressive deforming stresses for reductions in wall thickness and diameter are radial, σ_{RD}, and tangential, σ_{TD}, respectively. Therefore, we can assume that changes in the dimensions of the tubing are proportional to the ratio $\sigma_{RD}:\sigma_{TD}$. These stresses produce the plastic strain that finally determines the texture development.

4. These findings were applied to relate the texture gradients observed across the wall of Zircaloy tubing to the stress gradients present during fabrication. Energy is consumed in deforming each successive layer of the tubing wall so that the ratio $R_W:R_D$ can change from layer to layer through the wall. The texture gradient that develops depends on the ratio of stresses in the radial and tangential directions and the corresponding strains that result in each layer of the wall. Figure 4.2 shows three combinations of stress gradients that explain the different texture gradients found in Zircaloy tubing.

5. Finally, essentially identical textures are developed by any of the different fabrication methods – rocking, drawing, planetary ball swaging, and extrusion – when these methods are used to produce the same amount of reduction in area, wall thickness, and diameter.

The results developed in these studies can be used to explain all deformation textures so far observed in Zircaloy tubing and to demonstrate that the texture of Zircaloy tubing can be controlled.

Fabrication and Texture Control of Zirconium Tubing

Texture Control in Zircaloy Tubing (D. O. Hobson)

We found the mechanical properties of Zircaloy tubing to be quite variable, especially under complex stresses simulating those encountered

ORNL-DWG. 69-5591

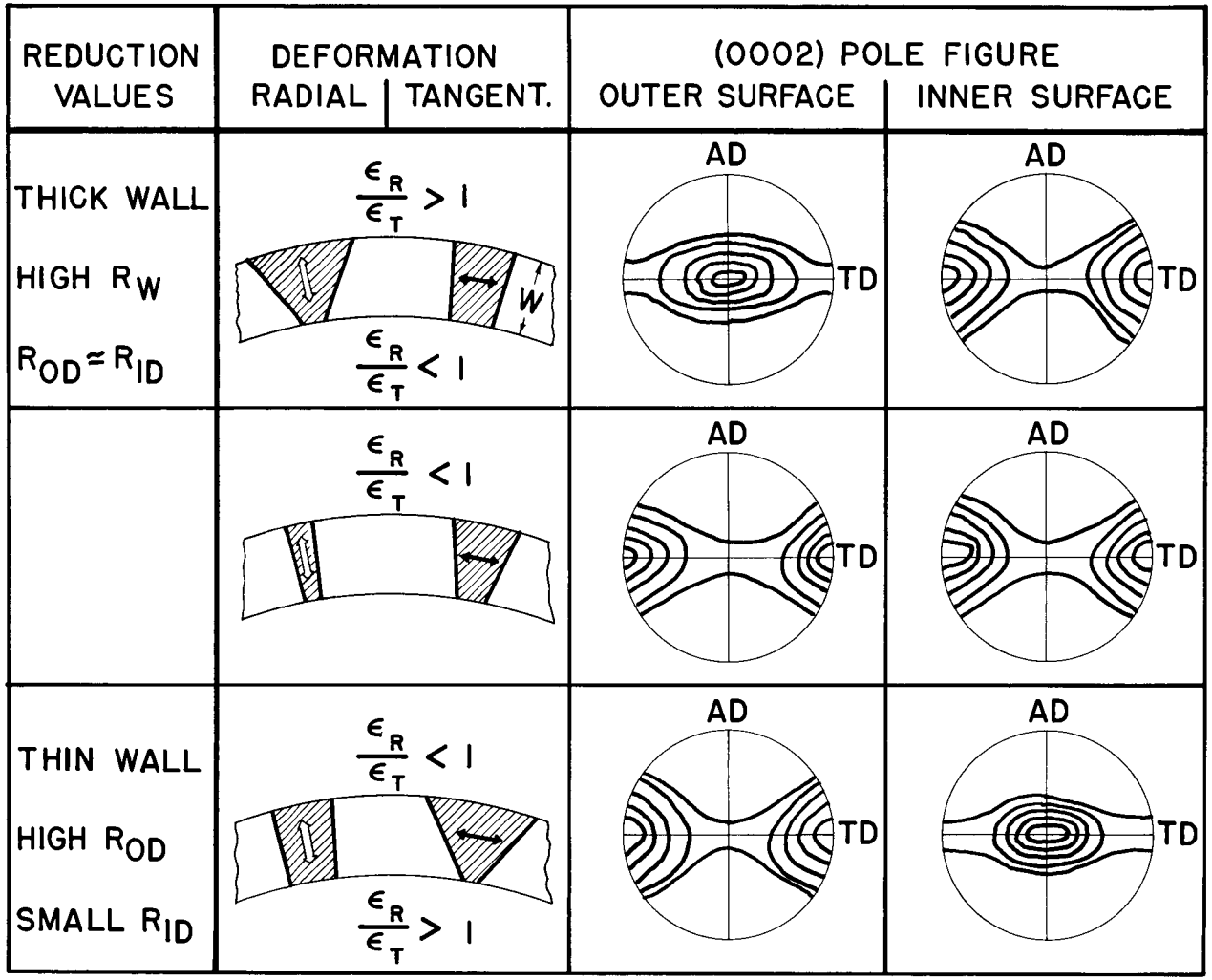

Fig. 4.2. Stress Gradient Combinations and Their Effect on Texture. The effect of the ratio of reduction in wall thickness (R_W) to reduction in inside (R_{ID}) and outside (R_{OD}) diameter on combinations of stress gradients and the resulting texture is shown by three extreme examples. On the pole figures, AD = axial direction, TD = tangential direction.

in reactor service.[3] We traced this variability to the texture formed during manufacture.

We can now control the fabrication textures in Zircaloy tubing; that is, we can design fabrication sequences to achieve any texture within the range of textures possible in Zircaloy. We developed this capability by experimentally determining the texture in tubing fabricated by known schedules[4] and by considering the interrelationships among fabrication variables.

There are seven significant fabrication variables: reduction in area, R_A; reduction in outside diameter, R_{OD}; reduction in inside diameter, R_{ID}; reduction in wall thickness, R_W; primary Q ratio, R_W:R_{ID} (based on starting dimensions); secondary Q ratio, r_w:r_{od} (based on instantaneous dimensions); and D ratio, ID:OD. Any fabrication step causes changes in many or all of these variables.

We found that Zircaloy tubing fabricated with heavier R_W than R_D has a "sheet rolling" texture; that is, the basal poles are near the radial direction of the tubing with a slight spread toward the transverse direction. Equal amounts of R_W and R_D produce a "fiber" texture; that is, the basal poles are distributed randomly perpendicular to the axial direction. Tube sinking – R_D greater than R_W – caused the basal poles to rotate toward the tangential direction in the tubing.

We have developed a graphic method for interrelating the variables in a rigorous and easily understood way. Figure 4.3 (an updating and correction of a figure published in the preceding report of this series) is an example of such a relationship. This plot is the projection of a three-dimensional surface onto the Q_1 (primary Q ratio) versus R_A plane of a three-axis graph, with the third axis containing the values for the D ratio. The complete relationships among the variables are rather more complex than shown here, but such complexity is not needed in practical applications. The curves extending from the

---

[3]P. L. Rittenhouse, "Biaxial Yielding in Zircaloy Tubing," pp. 68–71, this report.

[4]E. J. Tenckhoff, "Texture Development in Zircaloy Tubing," pp. 59–62, this report.

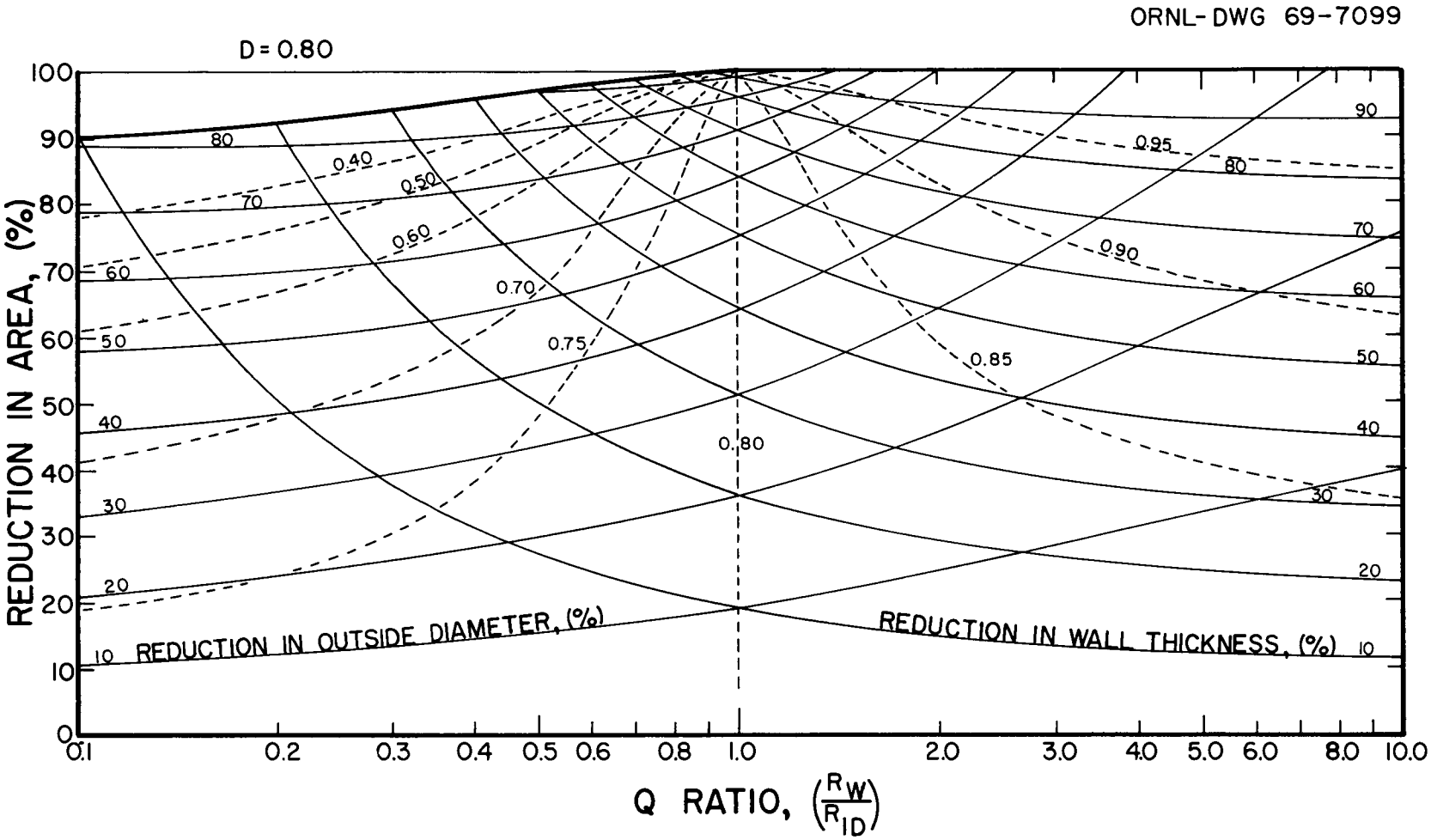

Fig. 4.3. Plot of Fabrication Variables. All of the significant fabrication variables can be graphically interrelated on this plot.

lower left to the upper right of the graph are lines of constant R_{OD}; the curves extending from lower right to upper left are lines of constant R_W. The dashed curves that terminate where $Q_1 = 1.0$ and $R_A = 100\%$ have a more complex meaning: each curve represents a secondary Q ratio of 1.0, and each is also a line of constant D ratio. Physically, this means that a fabrication sequence represented by any one of the dashed lines will produce equal amounts of R_W and R_D and that the ratio of wall thickness to diameter will remain constant.

Given a value of D for the initial tube or tube shell and any two of the other six variables, one can plot a point on the graph from which the rest of the variables may be read. Thus, any fabrication operation that results in a change in tubing dimensions can be plotted as a series of points representing incremental reductions. The increment need not be the entire reduction the tubing undergoes during a reduction step, but may be taken at any point or set of points within the die. For instance, a 70% R_A rocking pass would result in a single point on the plot at the 70% R_A level. The plot would not show, however, how the tubing deformed as it passed through the die. The tapered section formed as the tubing passes through the die can be divided into an arbitrary number of increments. The dimensions of these sections can be measured, the variables calculated, and the fabrication path plotted on the graph. Conversely, a fabrication path can be drawn using the texture criteria discussed above and the die and mandrel reductions read directly from the graph.

Texture in Zircaloy is controlled by using the graphic method to determine the fabrication path that provides the correct balance of ironing and sinking operations to produce basal poles in the desired position. A series of fabrication steps that follows any one of the infinite number of dashed lines (Fig. 4.3) is a neutral operation (i.e., neither ironing nor sinking) and will produce a fiber texture. If the fabrication path lies to the right of the neutral line, the operation is an ironing one, and a sheet rolling texture will be formed. If the path lies to the left of the neutral line, the operation is a sinking one, and a texture with basal poles tangential will be formed. Two sets of such paths are shown in Fig. 4.4. A starting tube with the

ORNL-DWG 69-7100

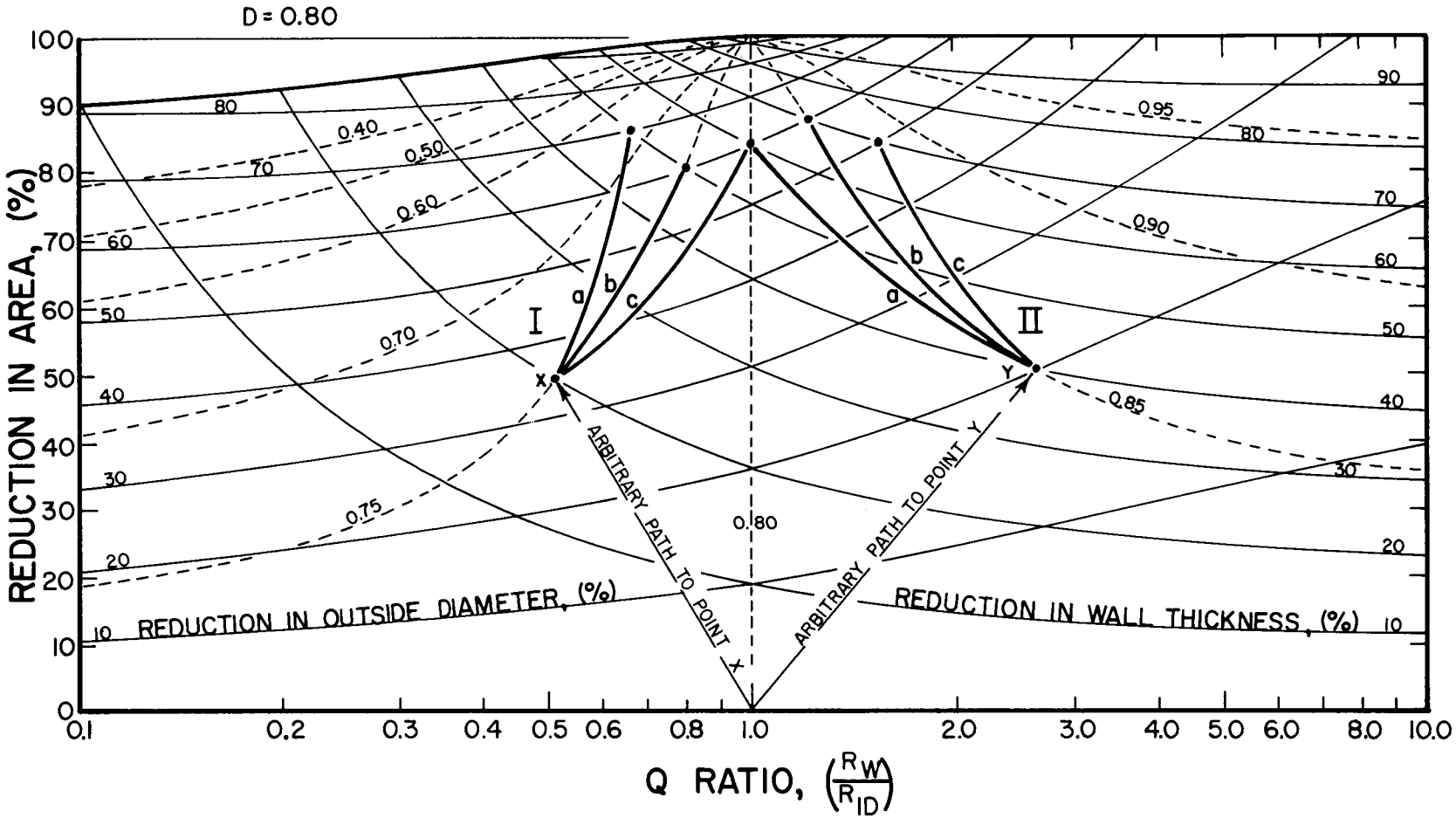

Fig. 4.4. Comparison of Fabrication Paths. The plot of fabrication variables is used to illustrate fabrication paths leading to particular textures.

D ratio = 0.80 is assumed to be fabricated to two different points (x and y) on the graph and then fabricated along paths I-a, -b, -c and II-a, -b, -c. Paths I-b and II-b are neutral, as determined by points x and y, and produce fiber textures. Paths I-c and II-c are ironing paths, and paths I-a and II-a produce sinking. Although paths I-c and II-a result in the same final tubing size, the tubing produced by I-c would have a texture with basal poles radial, and that produced by path II-a would have a texture with basal poles tangential.

Every point on the graph represents a specific size of tubing derived from starting tubes of the same size. This is illustrated in Fig. 4.5 for a number of arbitrary values. The tubing represented in that part of the graph in which $Q_1 < 1.0$ becomes solid rod or wire as R_A increases, while that represented in that part of the graph in which $Q_1 > 1.0$ becomes infinitely thin walled at 100% R_A.

The method described above can be used for any material that can be fabricated into tubing. In addition, if the material forms a deformation texture that varies depending upon whether the tubing undergoes ironing or sinking, the graph can be used as a guide to control texture in the material.

Biaxial Yielding in Zircaloy Tubing (P. L. Rittenhouse)

We have correlated the texture and the biaxial yield properties of Zircaloy tubing. Simple relationships between uniaxial yield strength, intensity of basal poles of the texture, and the equivalence of certain stress states allow us to construct biaxial yield surfaces for Zircaloy tubing of any texture. Three such surfaces and their relationships to texture are shown in Fig. 4.6. The surface labeled 600 is for tubing with basal poles that have six times random intensity parallel to the tangential direction and zero intensity parallel to both the axial and radial directions. If, instead, the intensity of basal poles is six times random parallel to the radial direction, the yield surface 060 is applicable. Finally, for tubing with basal poles that have three times the random intensity in both the tangential and radial directions, the surface 330 is obtained. These and similar yield surfaces suggest that differences in biaxial yield stresses between different lots of

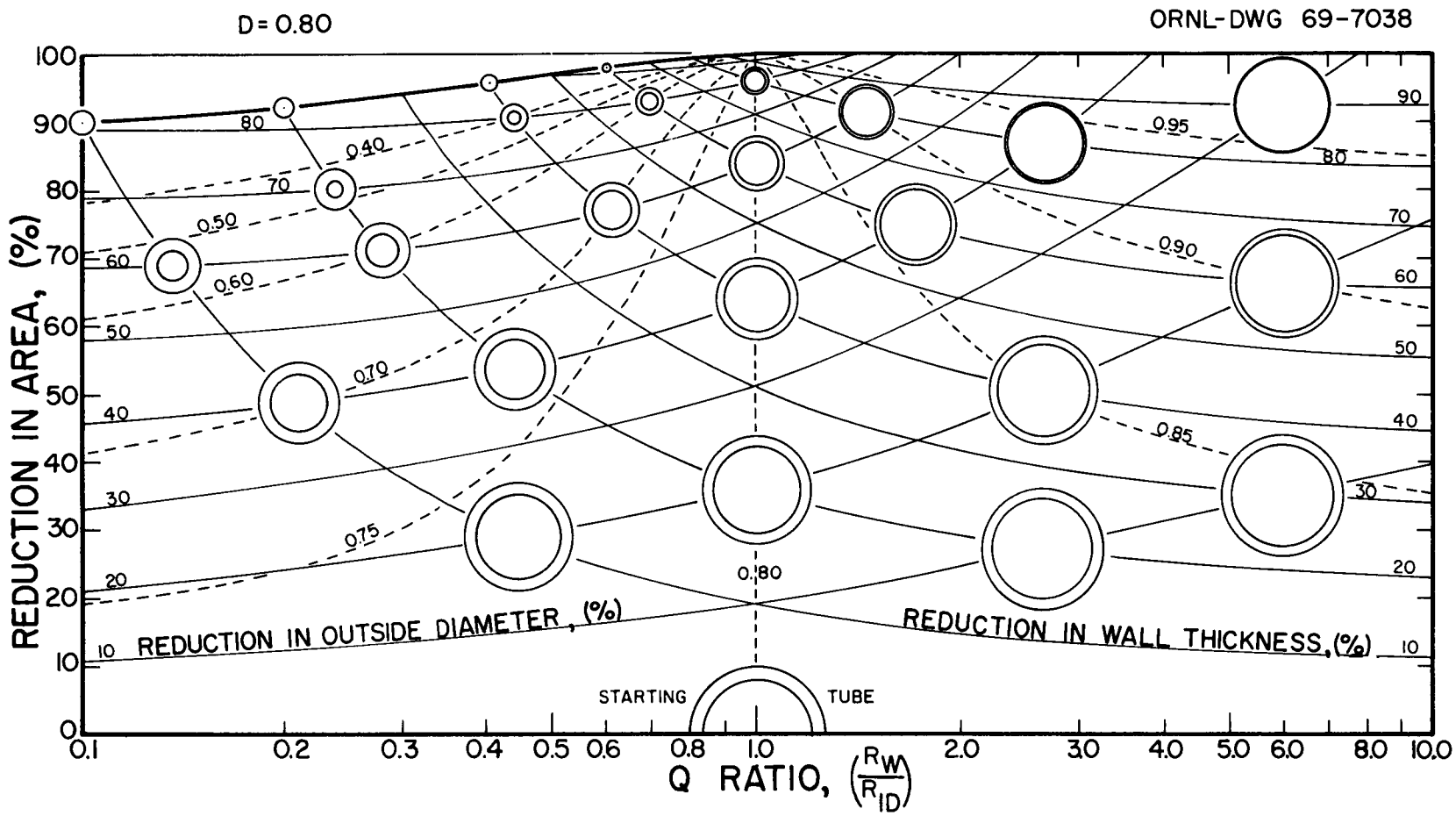

Fig. 4.5. Representation of Tubing Dimensions on the Plot of Fabrication Variables Showing Relationship Between Tubing Dimensions and Selected Points on the Plot.

ORNL-DWG 69-7015

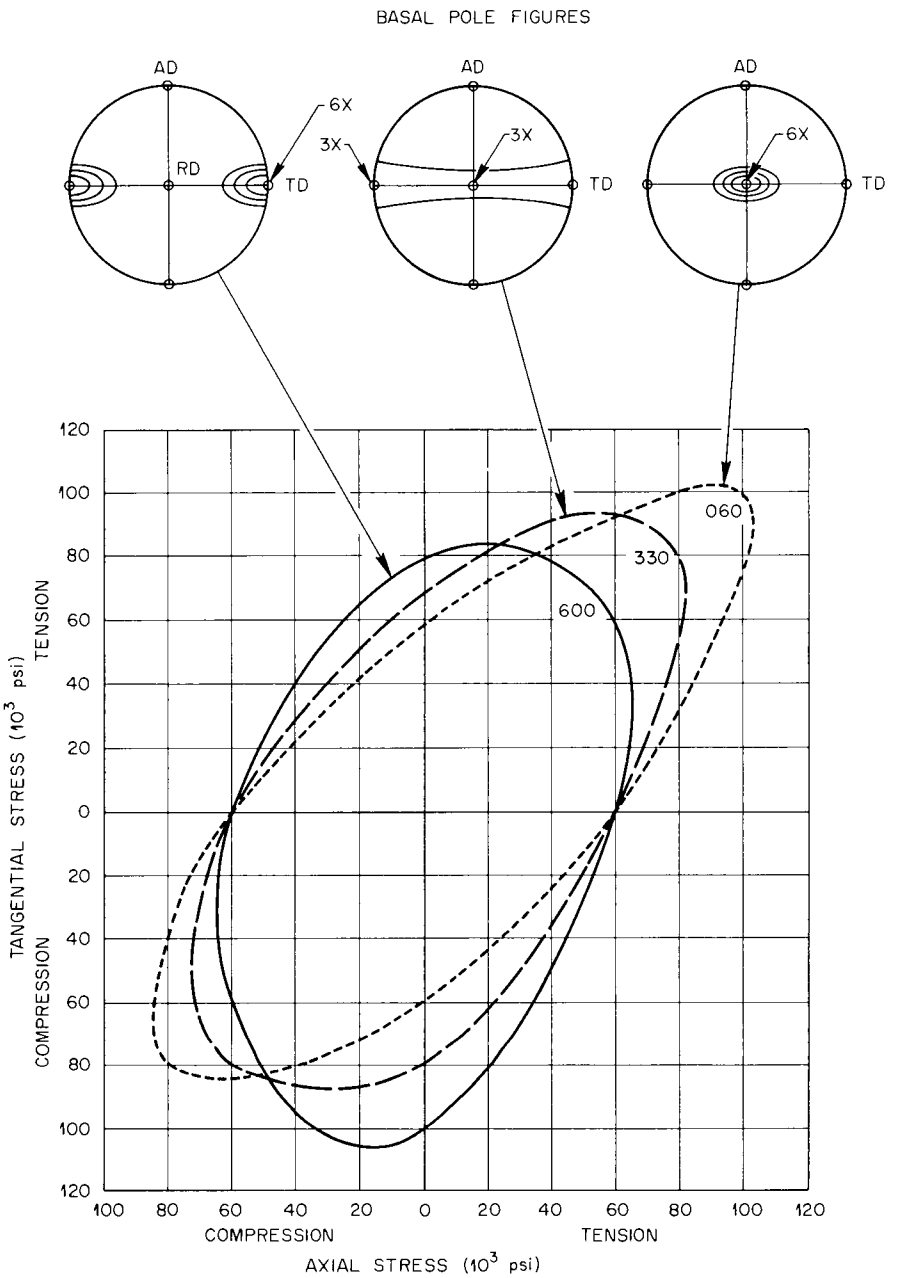

Fig. 4.6. Biaxial Yield Surfaces Constructed from Texture Data. This figure shows three biaxial yield surfaces and the schematic basal pole figures representative of the texture of each of the three schedules of Zircaloy tubing. On the pole figures AD = axial direction, RD = radial direction, TD = tangential direction, and 3× and 6× are the multiples of random pole intensity.

tubing could exceed 50%. This expectation has been verified by experimentally determining three quadrants of the axial-tangential yield surface for a number of schedules of Zircaloy tubing. These experimental data were also used to test the method shown in Fig. 4.6 for constructing yield surfaces. Two such checks between experiment and theory are shown in Fig. 4.7. Eleven of the fifteen schedules of tubing examined to date have correlated quite well with the biaxial yield surfaces derived from their corresponding textures. In four others, the correlation has been poorer, and both the yield data and textures are being reexamined.

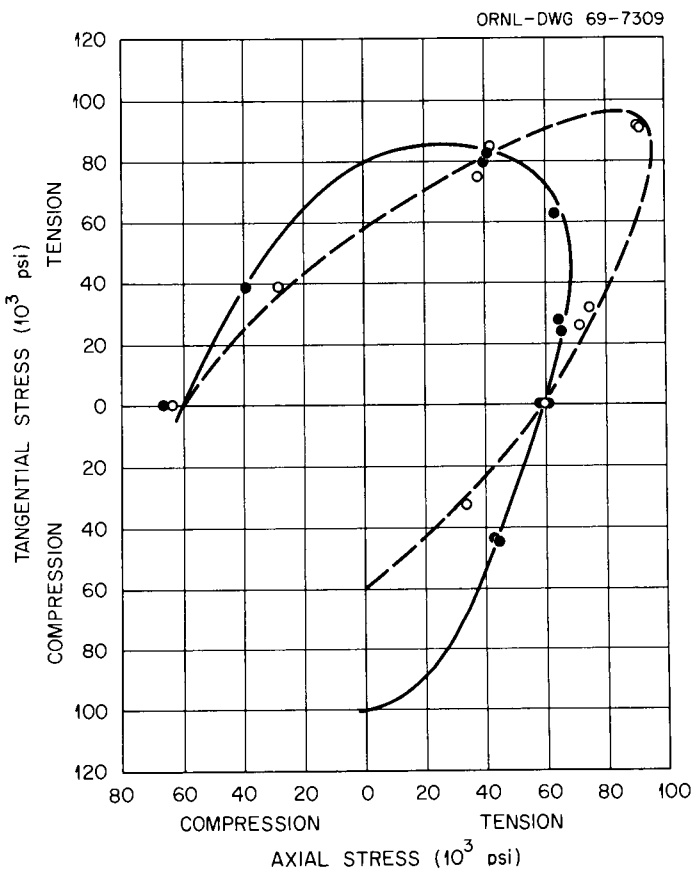

Fig. 4.7. Comparison of Yield Surface Construction Method and Experimental Data. The solid and dashed curves represent the biaxial yield surfaces predicted from the textures of two lots of Zircaloy tubing. The filled and open circles are the experimental yield stress data corresponding to the solid and dashed surfaces, respectively.

PART II

COOLANTS

5. ALKALI-METAL CORROSION STUDIES

W. O. Harms J. H. DeVan A. P. Litman

The purpose of this program is to investigate the chemical and metallurgical effects produced in structural materials during exposure to alkali metals. The program is designed to guide the selection of container materials for Na-cooled fast breeder reactor systems and Li-cooled space power reactor systems in which K serves as the Rankine-cycle working fluid. Forced circulation loops of engineering scale are included in the latter program.

Studies of the Corrosion of Vanadium Alloys in Sodium

Although V alloys are highly resistant to dissolution by Na, they are quite reactive with nonmetallic impurities in Na, particularly with C, N, and O. Accordingly, we are investigating the mechanisms by which V alloys are attacked in Na at impurity levels typical of service conditions in a reactor. Our program is concerned with four basic aspects of the oxidation process for V alloys in Na: (1) the partitioning of O between V alloys and Na; (2) the effects of alloying additions of Cr and Zr on the diffusion coefficient of O in V; (3) the effects of Cr and Zr in V on the oxide formed and on the dissolution of the alloys in Na; and (4) the solubility of V in Na as affected by the presence of O in either metal. We are also examining the kinetics of the transfer of C, N, and O between V alloys and types 304 and 321 stainless steel in a Na circuit.

Effects of Oxygen on the Compatibility of Vanadium and Sodium (R. L. Klueh)

We are continuing our study of the processes involved in the interaction of the O in Na with unalloyed V. Vanadium specimens exposed to Na in Mo and type 304 stainless steel capsules[1,2] were analyzed by

[1]R. L. Klueh, Fuels and Materials Development Program Quart. Progr. Rept. Dec. 31, 1968, ORNL-4390, p. 85.

[2]R. L. Klueh, Fuels and Materials Development Program Quart. Progr. Rept. March 31, 1969, ORNL-4420, pp. 89–90.

fast-neutron activation analysis for changes in O concentration. With this method we can analyze the entire specimen, and since the method is nondestructive, the same specimen can be analyzed both before and after exposure to Na. Furthermore, it is possible to remove any external scale and again determine the O concentration.

The results of these analyses are shown in Table 5.1. A dark, external scale was observed on the specimens,[1] and removal of the scale

Table 5.1. Change in Oxygen Concentration in Vanadium Specimens Exposed to Sodium Containing Various Amounts of Oxygen at 600°C

Time of Na Exposure (hr)	Initial O Content[a] of Na (ppm)	O Concentration[b] in V, ppm		
		Before Test	After Test	
			With Scale	Without Scale
		Mo Container		
100	2000	1238	4120	3307
200	1800	1236	4081	3360
300	1950	1219	5763	4742
400	1950	1328	5340	c
500	1800	1273	5780	c
500	50	1290	1422	1217
500	450	1233	2953	2723
500	1000	1294	4354	3695
500	4000	1297	6155	c
		Type 304 Stainless Steel Container		
100	2000	1220	4386	2934
200	2050	1314	4899	3195
300	2050	1267	6165	3910
400	2050	1250	5203	c
500	2050	1271	6206	c
500	50	1267	1466	1253
500	550	1229	3038	2343
500	1100	1308	4633	3438
500	4000	1188	9793	c

[a]Oxygen was added as Na_2O.

[b]Oxygen concentrations were determined by fast-neutron activation analysis.

[c]Specimen was sectioned for chemical analysis of the external film.

in all cases lowered the O content. Measurements of the thickness of the specimens showed the scale to be about 0.0005 in. thick. The measured changes in O content in these specimens generally agree with the measurements[1] of weight gain (i.e., the percentage of the O picked up by the V specimen decreased as the O in the Na increased). The decrease was quite significant in the case of the Mo capsules: the V specimen picked up only 50% of the 4000 ppm O addition compared to 75% of the 2000 ppm addition and essentially 100% of all lower additions. For the type 304 stainless steel capsules, on the other hand, similar calculations showed that essentially all of the O in the Na was gettered by the V specimen. More than 95% of the O was accounted for in all but the test that contained 4000 ppm O, where about 93% was recovered.

Smith[3] reported the solubility of O in alpha V to be on the order of 1.2 wt % at 600°C. In a study of the uptake of O by V wires in a stainless steel and Na system, this O saturation level was achieved in Na containing about 0.8 ppm O. These data suggest that the distribution coefficient for partitioning of O between Na and V $\left(\frac{\text{ppm O in V}}{\text{ppm O in Na}}\right)$ is on the order of 1.5×10^4. In our stainless steel capsule tests, we did not directly determine the O content in the Na after test, however, we did calculate the O content by means of a mass balance on O. The results showed that the distribution coefficient for O approached 10^4.

Attempts to determine the nature of the dark, external scale by x-ray diffraction were unsuccessful — probably because the film was too thin. We analyzed the V specimens to determine if there had been dissimilar-metal mass transfer from the containers. The Mo concentration of the V tested in Mo capsules increased from an initial concentration of less than 10 ppm to about 700 ppm, and the V exposed to Na in stainless steel increased from 80 ppm Fe and < 10 ppm Ni to about 200 ppm Fe and 100 ppm Ni. No other stainless steel components were detected. Considering that Mo, Fe, and Ni will not diffuse into the V to any extent at 600°C, the surface concentrations of the capsule materials — especially Mo — must have increased considerably. The deposition of the Mo on the V

---

[3]D. L. Smith, Reactor Development Program Progress Report, February 1969, ANL-7553, p. 83.

may account for the decrease in the percentage of O recovered at the higher O concentrations.

Finally, the Na was analyzed after test to determine the concentrations of V and container materials present. These results are shown in Tables 5.2 and 5.3.

Mass Transfer of Interstitial Impurities Between Vanadium Alloys and Types 304L and 321 Stainless Steel in Sodium (J. H. DeVan, D. H. Jansen)

The first loop in this series, which is constructed of type 304 stainless steel and unalloyed V, continues to operate at the design conditions.[4] The test, scheduled for 3000 hr, had completed 1700 hr as of July 1. The vacuum atmosphere protecting the loop has steadily improved and the pressure has decreased to about 10^{-10} torr.

A second test loop with type 321 instead of type 304 stainless steel sections was fabricated and is being prepared for operation under conditions similar to those for the first loop.

As discussed previously,[4] we intend to compare the rates of interstitial transport in these loop systems with those of static, isothermal systems. Therefore, we have also begun a series of static tests in which tensile specimens of V sheet are being exposed to Na in stainless steel containers. A schematic of the test system is shown in Fig. 5.1. The number of stainless steel spacers and tensile specimens are varied to attain surface-area ratios that correspond to those in our loop systems. Two such static tests were conducted for 500 hr at 800°C with type 304L stainless steel spacers and containers. Two different grades of V were exposed, one containing 2270 ppm and the other 110 ppm total interstitial impurities. Past test analyses of the interstitials and tests of mechanical properties are still incomplete; however, the V showed consistent weight gains together with a distinct darkening of surfaces (Fig. 5.2). Additional capsule test systems are being fabricated with type 321 stainless steel spacers and containers.

---

[4]J. H. DeVan and D. H. Jansen, Fuels and Materials Development Program Quart. Progr. Rept. March 31, 1969, ORNL-4420, pp. 90–92.

Table 5.2. Concentrations of Vanadium and Molybdenum in Sodium After Exposure of Vanadium Coupons in Molybdenum Capsules at 600°C

Exposure Time (hr)	Initial O Content of Na (ppm)	Concentration of Metal in Na, ppm	
		V	Mo
100	2000	12	230
200	1800	7	290
300	1950	8	240
400	1950	18	290
500	1800	32	
500	50	6	
500	450	5	
500	1000	8	
500	4000	68	

Table 5.3. Concentrations of Vanadium, Iron, Nickel, and Chromium in Sodium After Exposure of Vanadium Coupons in Stainless Steel Capsules at 600°C

Exposure Time (hr)	Initial O Content of Na (ppm)	Concentration of Metal in Na, ppm			
		V	Fe	Ni	Cr
100	2000	7	100	3	10
200	2050	13	130	2	90
300	2050	3	35	1	2
400	2050	12	95	3	8
500	2050	19			
500	50	0.2			
500	550	16			
500	1100	16			
500	4000	25			

ORNL-LR-DWG 46643R3

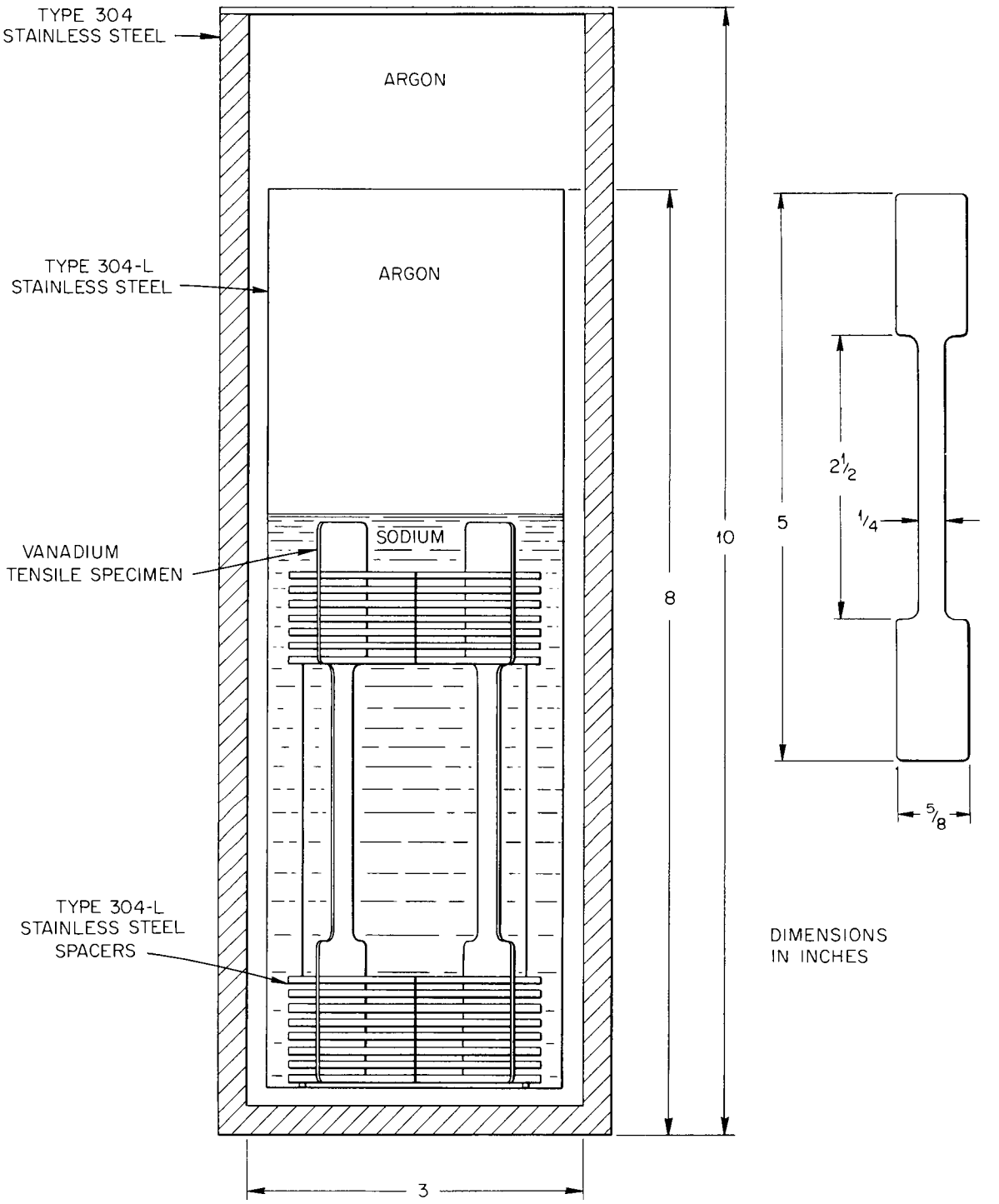

Fig. 5.1. Schematic Drawing of Static Test System Used to Study Dissimilar-Metal Mass Transfer Between Vanadium and Stainless Steel.

Fig. 5.2. Tensile Specimens of Vanadium Sheet After 500-hr Static Test at 800°C.

Interstitial Contamination of Vanadium and Its Alloys (R. L. Wagner)

We are studying the interaction of V with gaseous interstitial impurities to characterize any effect of alloying additions in V on the rate and nature of interstitial contamination and to determine the creep strength of V and its alloys as influenced by interstitial contamination.

Table 5.4 shows the effect of a 100-hr exposure on the interstitial content of V at 900°C under various vacuum conditions. For the pressure range studied, 10^{-5} to 10^{-7} torr, N and C remained unchanged. However, O increased by 150 ppm at 6×10^{-6} torr and by 220 ppm at 1.6×10^{-5} torr, but when the sample was wrapped in Ta foil there was no contamination even at 1.6×10^{-5} torr. For pressures below 10^{-7} torr, contamination by residual gases at 900°C does not appear to be a problem.

Table 5.4. Effect of Vacuum Exposure on the Interstitial Content of Vanadium[a] at 900°C for 100 hr

Pressure (torr)	Interstitial Content,[b] ppm		
	C	N	O
As received	320	530	210
4×10^{-7}	320	520	220
6×10^{-6}	260	540	360
1.6×10^{-5}	320	530	430
1.6×10^{-5}[c]	300	530	220

[a]Vanadium foil 0.015 in. thick.

[b]Chemistry determined by vacuum-fusion analysis.

[c]Wrapped with Ta foil.

Table 5.5 shows the results obtained to date on the contamination of V at controlled O pressures. At a base pressure of 4×10^{-8} torr, little interstitial change was noted after 810 hr. At 2×10^{-7} torr and at 2×10^{-6} torr O, the rate of O pickup was maximum at about 550°C.

As shown below,[5] increasing concentrations of interstitial elements significantly increase the yield strength of pure V at 0°C:

Concentration, ppm	Upper Yield Stress, psi $\times 10^3$
120 C	12
1000 C	20
120 N	12
1000 N	50
120 O	12
1000 O	37

[5]D. R. Matthews et. al., Effects of Interstitial Impurities on the Mechanical Properties of Electrorefined Vanadium at Low Temperatures, U.S. Bureau of Mines Report 6637 (1965).

Table 5.5. Oxygen Contamination of Vanadium[a,b]

4×10^{-8} torr Vacuum, 810 hr		2×10^{-7} torr O_2, 500 hr		2×10^{-6} torr O_2, 200 hr	
Temperature (°C)	Change in O Concentration[c] in V (ppm)	Temperature (°C)	Change in O Concentration[c] in V (ppm)	Temperature (°C)	Change in O Concentration[c] in V (ppm)
410	−6	450	+45	370	+28
520	+9	550	+240	460	+388
615	+60	670	+200	560	+478
730	+3	775	+155	670	+358
810	+18	850	+100	745	+308
810	+30	810	+95	780	+218
890	+24	905	+100	830	+268

[a]Results based on specimens 0.020 in. thick with surface area of 7.595 in.^{2}.

[b]Material tested after a 1-hr anneal at 900°C in $< 1 \times 10^{-6}$ torr vacuum.

[c]Chemistry changes determined by vacuum-fusion analysis.

Data on the effects of interstitials on the creep strength of V and its alloys are largely lacking, and an apparatus has been designed to obtain creep data under conditions of controlled contamination.

Compatibility of Stainless Steel and Insulation in LMFBR Systems

C. D. Bopp A. P. Litman

Since the compatibility of insulating materials with stainless steels is an important consideration in the design of LMFBR systems, we are studying the reactions that can occur between commercial insulating materials and stainless steel.

The first phase of our program is concerned with the interactions of stainless steels and commercial alumina-silica insulation materials at temperatures between 370 and 760°C. The second phase deals with the effects of Na leaks in stainless steel systems surrounded by thermal insulation. Small leaks that may be self-sealing at lower temperatures are being studied by methods similar to those used in the first phase of this task. The effect of large leaks will be studied in heated, pressurized containers with artificial defects incorporated into the container wall.

Except for some continuing long-term tests, we have completed our experimental study of the compatibility of insulation with stainless steel in the absence of Na oxidation products.[6,7] We are now assembling the equipment to be used in the second phase of this program, which deals with the effect of a Na leak.

Effect of Insulation on Oxidation of Stainless Steel

We have completed a metallographic examination of tubes of types 304L and 316 stainless steel exposed to moist air at 730 to 815°C (ref. 7). In

---

[6]C. D. Bopp, Fuels and Materials Development Program Quart. Progr. Rept. Dec. 31, 1968, ORNL-4390, pp. 91–92.

[7]C. D. Bopp, Fuels and Materials Development Program Quart. Progr. Rept. March 31, 1969, ORNL-4420, pp. 92–100.

these tests, about one-half of both the inside and outside surfaces of the specimens contacted fibrous "blanket-grade" alumina-silica insulation. The effect of the insulation on scaling was assessed by metallographic comparison of the bare and insulated parts.

In the case of type 304L stainless steel, the surfaces in contact with insulation developed a dull, rusty-red scale, and those away from the insulation developed a shiny, blue-gray scale [Fig. 5.3(a)]. The metallographic appearance of the uninsulated surfaces is shown in [Fig. 5.3(b)]. Note the small mounds, which are characteristic of breakaway oxidation.[8] The features of the underlying scale on the insulated part were obscured by a very thin surface layer of rusty-red, powdery Fe_2O_3. However, the larger mounds evident in this underlying scale [Fig. 5.3(e) and (f)] closely resembled those of the uninsulated sections [Fig. 5.3(c) and (d)]. The averages of a large number of measurements of scale thickness did not show a significant difference between the insulated and bare parts or between the inner and outer surfaces.

The formation of mounds is characteristic of breakaway oxidation, and the kinetic data from these tests indicated a slow acceleration in weight gain. Nevertheless, the rate of oxidation was relatively low at the time this run was terminated (1200 hr). We believe that the powdery Fe_2O_3 layer on only the insulated part resulted from abrasion of the scale by the insulation. However, this effect should not be particularly deleterious under LMFBR conditions since it was confined to a very thin surface layer, and in these tests the insulation was compressed against the tubes much more than it is in usual insulation practice.

Kinetic data from these tests[7] indicated that the oxidation resistance of type 316 stainless steel was substantially less than that of type 304L stainless steel. Metallographic examination of the type 316

---

[8]L. A. Morris, Metals. Eng. Quart. 8(2) 30 (May 1968).

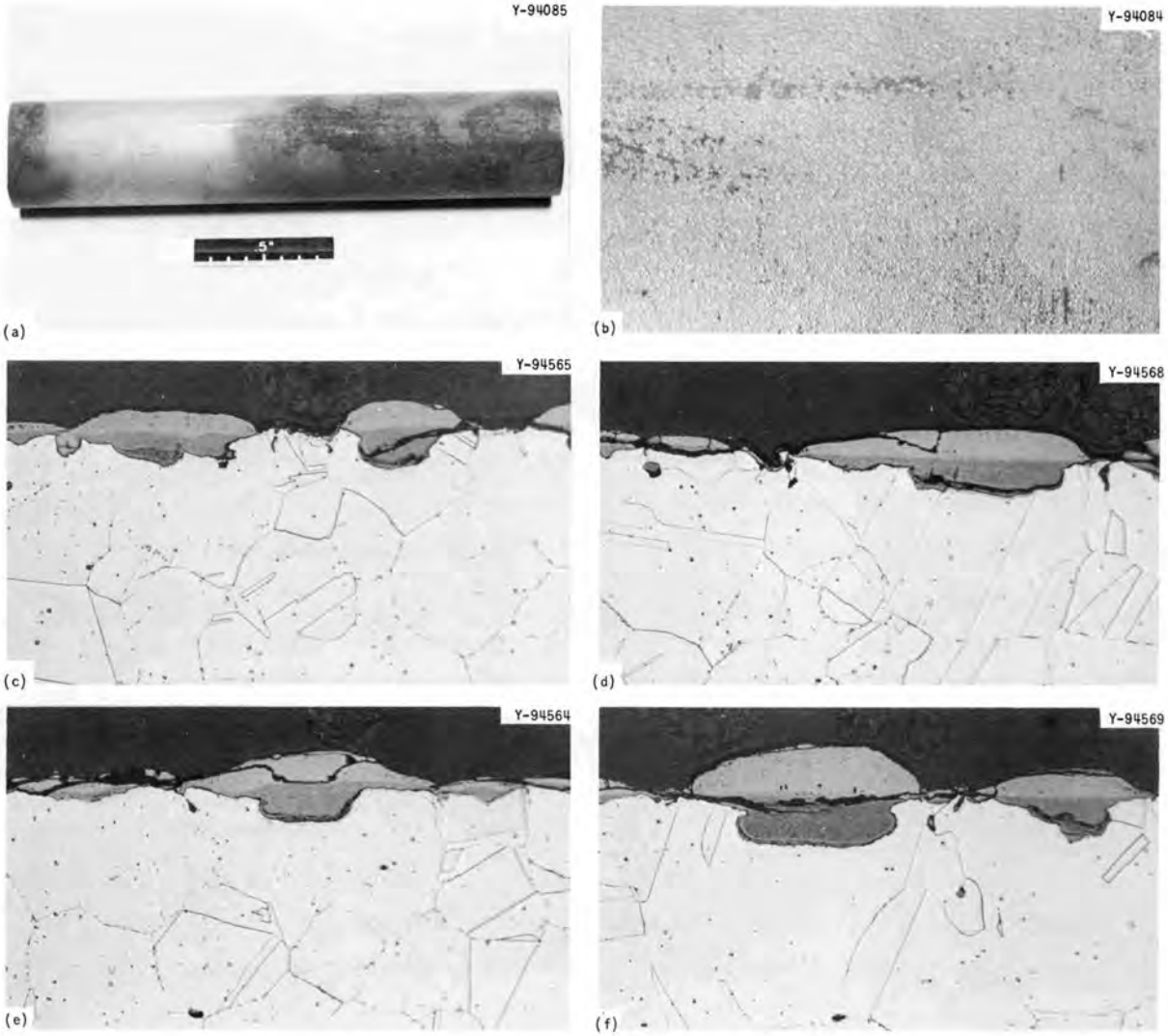

Fig. 5.3. Appearance of Type 304L Stainless Steel Oxidized 1200 hr at 760°C in Moist Air (Saturated at 20°C) and Temperature Cycled to 200°C Every 40 hr. (a) Outer surface. (b) Outer surface of bare end. 10×. (c) Section of outer surface of bare end. Etchant: lactic, nitric, and hydrochloric acid. 500×. (d) Section of inner surface of bare end. 500×. (e) Section of outer surface of insulated end. 500×. (f) Section of inner surface of insulated end. 500×. Reduced 48.5%.

stainless steel specimens showed that the scale rapidly achieved a thickness at which it spalled because of the stresses produced by growth. (A theory of such spalling has been advanced in the instance of Zr alloys.[9]) Spalling, as shown in Fig. 5.4(a) and (b), exposes a dark, relatively adherent inner layer. Although the thickness of the adherent scale was not very uniform, there was no consistent difference between the insulated [Fig. 5.4(c) and (d)] or bare [Fig. 5.4(e) and (f)] parts or the outer [Fig. 5.4(c) and (e)] or inner [Fig. 5.4(d) and (f)] surfaces of the tube.

An electron microprobe trace was obtained across the scale formed on type 316 stainless steel oxidized for 650 hr at 150 to 815°C in moist air (Fig. 5.5). The limitations with regard to resolution of the microprobe method were discussed by Brush[10] who showed that the effective limit is a diameter of about 3 μm. It is only possible to locate the interfaces approximately because of roughness. The composition of the outer layer of scale corresponds roughly to Fe_3O_4 (72% Fe); the composition of the inner layer suggests a mixture consisting principally of $FeCr_2O_4$ and $NiFe_2O_4$. The phase composition is being determined by x-ray diffraction.

We conclude from the metallographic and kinetic[7] studies of scaling that with type 304L stainless steel to 760°C there is little effect of contact with blanket-grade insulation and that even after breakaway oxidation the scaling rate is very low. With type 316 stainless steel, again there is little effect of the insulation; however, the scale formed at 760°C is much less protective. This accords with the finding by others[8] that aging at 760°C enhances corrosion in superheated steam. The similarity between corrosion in air and steam is further demonstrated by comparison of our electron microprobe trace with that for corrosion in steam.[11]

---

[9]J. C. Greenback and S. Harper, Electrochem. Technol. 4, 88 (1966).

[10]E. G. Brush, Oxidation Behavior of Fe-Cr-Ni System in High-Pressure Steam, GEAP-4490 (March 1964).

[11]George E. Lien, ed., Superheater Alloys in High Temperature, High Pressure Steam, The American Society of Mechanical Engineers, New York, N. Y., 1968.

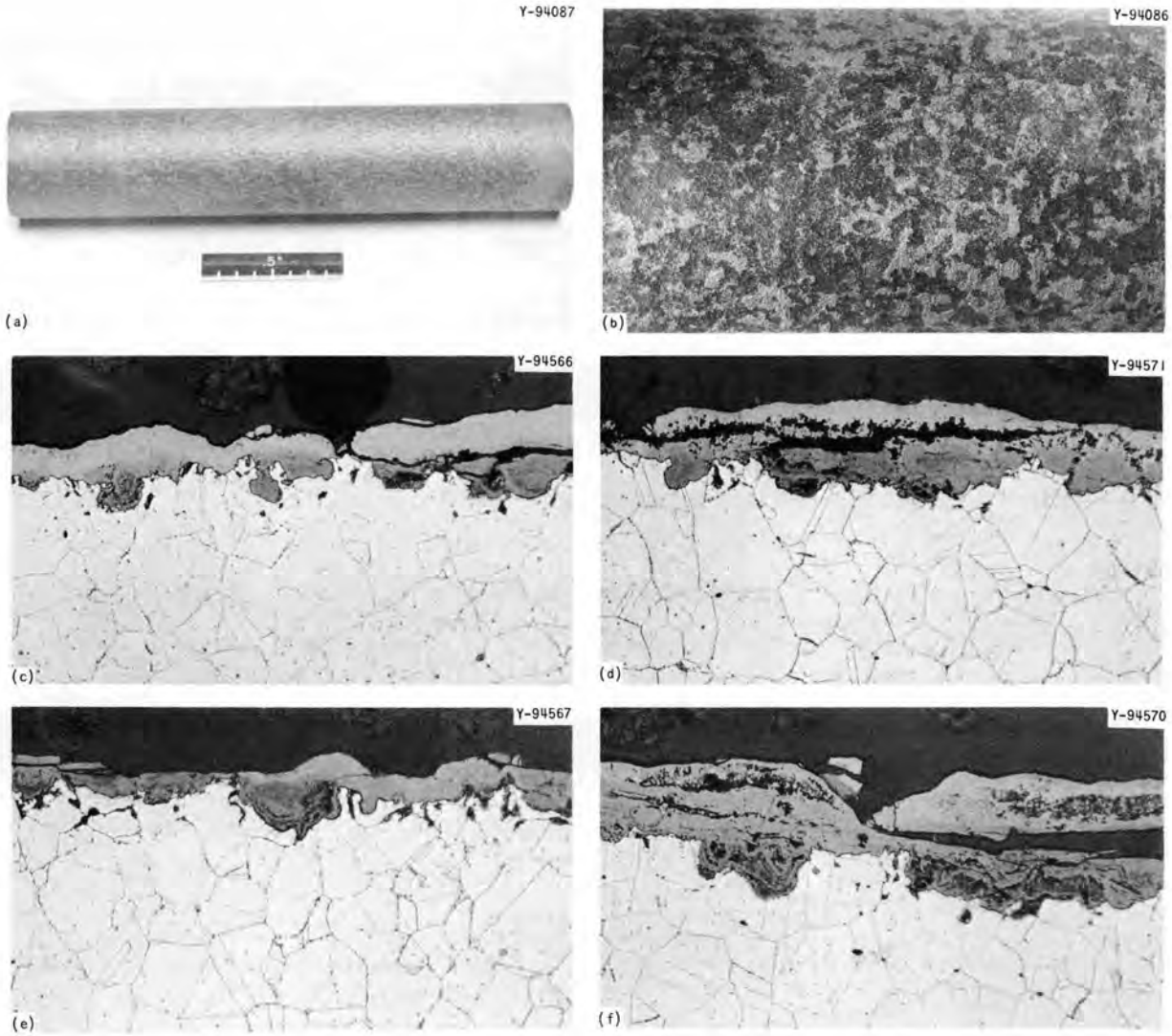

Fig. 5.4. Appearance of Type 316 Stainless Steel Oxidized 550 hr at 760°C in Moist Air (Saturated at 20°C) and Temperature Cycled to 200°C Every 40 hr. (a) Outer surface. (b) Outer surface of bare end. 5×. (c) Section of outer surface of bare end. 500×. (d) Section of inner surface of bare end. 500×. (e) Section of outer surface of insulated end. 500×. (f) Section of inner surface of insulated end. 500×. Reduced 48.5%.

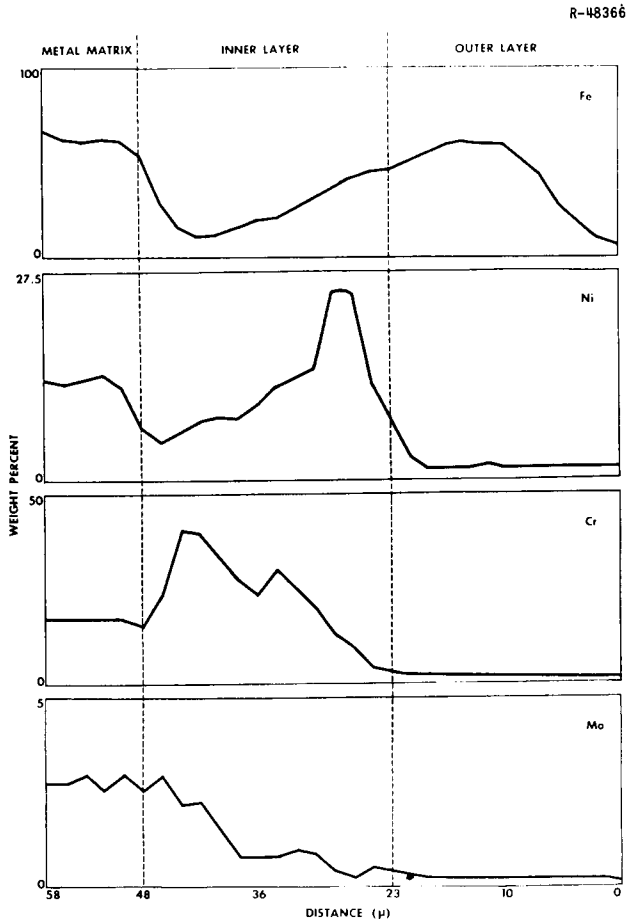

Fig. 5.5. Electron Microprobe Trace of Adherent Scale on Type 316 Stainless Steel After 650 hr at 815°C with Temperature Cycled to 150°C Every 6 hr in Moist Air (Saturated at 20°C).

Corrosion of Refractory Alloys in Lithium, Potassium, and Sodium

J. H. DeVan A. P. Litman W. R. Huntley

Requirements for auxiliary electricity or ion propulsion for space vehicles necessitate power plants of high efficiency that will operate at high temperatures. For these applications, nuclear power systems have been proposed in which alkali metals are used to transfer heat, drive a turbogenerator, and lubricate rotating components. Accordingly, we are investigating the corrosion properties of candidate alkali metals, primarily Li and K, under conditions of interest for space applications. Because of the relatively high temperatures (> 1000°C), the investigation is concerned largely with refractory-metal container materials.

Effect of Oxygen on Compatibility of Refractory Metals and Alkali Metals (R. L. Klueh)

Oxygen Effects in the Niobium-Lithium and Tantalum-Lithium Systems. — We completed comparative studies[12–14] of the effects of O in various refractory metal-alkali metal systems at 600°C. The final tests in this series dealt with the Nb-O-Li and Ta-O-Li systems. In five tests of each system, nominally pure capsules and specimens were exposed to Li with varying additions of Li_2O. Two other capsules of each material were also tested with specimens to which O had been added before test.

The weight changes of the specimens are shown in Table 5.6. The O concentration of the Li did not measurably affect the amount of Nb or Ta dissolved by the Li. For both systems, the amount of metal in the Li after test was less than the limit of detection (< 10 ppm O). This is quite different from what we found for Nb and Ta in K or Na; there we found that the amounts of Nb and Ta dissolved were highly dependent upon the O concentration in the liquid metal.[12–14]

When O was added to the Nb or Ta specimens, the attack by Li with a given O level was much more severe than that by K (ref. 12) or Na (refs. 13 and 14). Figure 5.6 shows the after-test appearance of Ta that contained 1100 ppm O before exposure to Li. We noted large amounts of transgranular attack by Li in both Ta and Nb under conditions that produced only grain boundary attack by Na and K. As was true of the attack by K and Na, Li also attacked Ta more severely than it attacked Nb.

The greater susceptibility of Ta to attack was further substantiated by the appearance of the Ta capsules. When the Ta capsules were removed from the stainless steel outer containers that enclosed them during the

---

[12]R. L. Klueh, Fuels and Materials Development Program Quart. Progr. Rept. Sept. 30, 1968, ORNL-4350, pp. 120–126.

[13]R. L. Klueh, Fuels and Materials Development Program Quart. Progr. Rept. Dec. 31, 1968, ORNL-4390, p. 95.

[14]R. L. Klueh, Fuels and Materials Development Program Quart. Progr. Rept. March 31, 1969, ORNL-4420, pp. 100–103.

Table 5.6. Effect of Oxygen on the Compatibility of Niobium and Lithium and Tantalum and Lithium

Test Material	Initial O Concentration[a] in Li (ppm)	O Concentration[b] in Refractory Metal, ppm		Specimen Weight Change[c] (mg)
		Before Test	After Test	
Nb	100	70	47	+0.1
	600	70	57	0.1
	1100	70	49	0.1
	1600	70	41	0.1
	2100	70	49	0.1
	100	1100	490	−0.6
	100	2200	1400	−14.4[d]
Ta	100	40	59	0.0
	600	40	29	0.0
	1000	40	37	0.0
	1600	40	32	0.0
	2100	40	27	0.0
	100	1100	170	−3.4
	100	1900	340	−5.0

[a]Oxygen added as Li_2O to Li containing about 100 ppm O.

[b]Determined by vacuum-fusion analysis.

[c]Specimen size: 1 × 0.5 × 0.04 in.

[d]Specimen was quite brittle and broke during removal from the container; therefore, the measured weight loss is probably high.

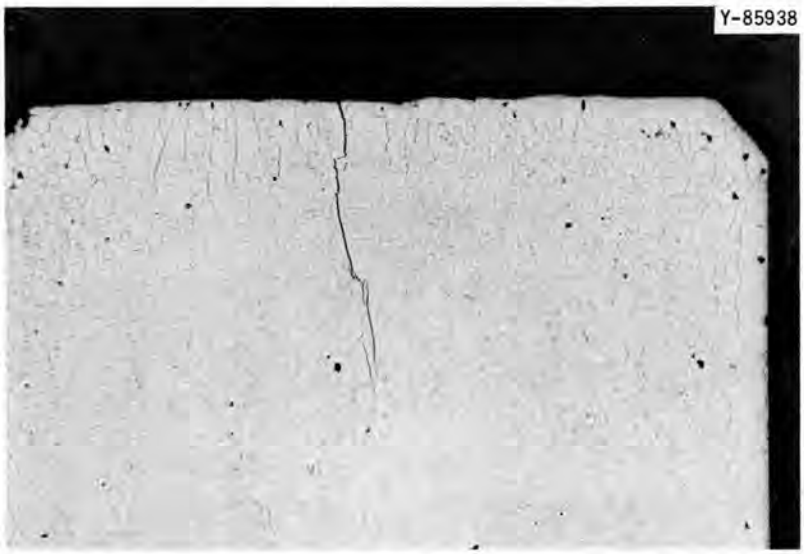

Fig. 5.6. Tantalum That Initially Contained 1100 ppm O After Exposure to Lithium for 500 hr at 600°C. Lithium attacked grain boundaries and produced transgranular platelets. 100×. Reduced 30%.

600°C exposure, they were discolored, and there was evidence of Li around them. Since we could detect no macroscopic failures, we concluded that, although the Ta tubing had contained only 150 to 200 ppm O, Li had penetrated the walls. This was confirmed when the tube walls were sectioned and examined metallographically (Fig. 5.7).

Partitioning of Oxygen Between Potassium and Zirconium and Sodium and Zirconium (R. L. Klueh)

Frequently, Na and K are purified of O by exposing them to Zr in a stainless steel system (either static or dynamic). In view of the inhibiting layers observed on Zr after exposure in Mo capsules,[15] we conducted a series of O partitioning tests of Zr at 815°C in type 304 stainless steel containers to measure dissimilar-metal mass transfer.

[15]R. L. Klueh, Fuels and Materials Development Program Quart. Progr. Rept. Dec. 31, 1968, ORNL-4390, p. 97.

Fig. 5.7. Wall of Tantalum Capsule That Was Exposed to Lithium for 500 hr at 600°C. The tantalum contained about 200 ppm O before test.

We also hoped to explain the anomalous observation that, when purifying Na and K for our loop experiments, 50 to 100 ppm O sometimes remain in the liquid metals even after 100-hr exposures to Zr at 815°C in stainless steel containers.

Results of these recovery experiments are shown in Table 5.7. The percentage of O recovered decreased as the O concentration in the alkali metal increased. (Recoveries greater than 100% are apparently the result of O transfer from the stainless steel.) In all cases, the Zr specimens

Table 5.7. Oxygen Recovered by Zirconium in Type 304 Stainless Steel Containers[a]

O in K, ppm		O in Na, ppm	
Total[b]	Recovered	Total[c]	Recovered
600	700	450	530
930	800	990	920
1330	1250	1350	1300
1680	1400	1650	1460
2890	2300	2900	1890

[a]All tests were at 815°C for 100 hr with 0.04-in.-thick Zr specimens.

[b]Initial O plus that added as K_2O.

[c]Initial O plus that added as Na_2O.

developed a surface scale that became thicker with increasing O concentration in the alkali metal. Microprobe analysis showed that the scale contained Fe, Mn, and C. In addition, vacuum-fusion analysis showed that O, N, and H had transferred from the stainless steel to the Zr. No intermetallics or other compounds could be identified by x-ray diffraction.

These results indicate that the absorption of O by Zr in stainless steel containers can be inhibited by the mass transfer of stainless

steel components. Whether this inhibiting reaction could become a problem in hot traps is not immediately obvious. Hot-trapped systems generally operate below the O and temperature levels employed here, so that both the solubilities and mass-transfer rates of stainless steel components should be considerably reduced. The present results suggest that, whereas a temperature of 800°C greatly enhances the ability of Zr to take up O by diffusion, a lower temperature, maybe 600°C, may be advantageous for avoiding dissimilar-metal poisoning of the Zr.

The results on O gettering by Zr reported during the last five quarters were compiled, and a report was issued.[16]

Refractory Alloy – Lithium Thermal Convection Loop Tests (J. H. DeVan)

We have completed our analysis of thermal convection loop TCL-6R, which circulated Li for 3000 hr at a maximum temperature of 1350°C. The loop was constructed of the Ta alloy T-222 and contained T-222 insert specimens.

Bend tests performed[17] on several insert specimens from this test showed that the toughness of the T-222 specimens had deteriorated significantly in areas of the loop that had been at a temperature between 1220 and 1280°C. These specimens increased slightly in N during Li exposure; bulk specimen analyses showed N contents in the affected areas to range from 90 to 250 ppm. Concentrations of other interstitial impurities were essentially the same as before Li exposure.

We have examined several specimens from this group that completely fractured at a relatively low bend angle. As shown in Fig. 5.8, fracture was intergranular. A specimen adjacent to the one shown in Fig. 5.8 was analyzed incrementally to evaluate the distribution of interstitial impurities (O, N, H) across the specimen. It was cut lengthwise and crosswise into four roughly equivalent samples. Three of the four

---

[16]R. L. Klueh, Oxygen Determination and Purification of Liquid Alkali Metals by Zirconium Gettering, ORNL-TM-2473 (March 1969).

[17]J. H. DeVan, Fuels and Materials Development Program Quart. Progr. Rept. March 31, 1969, ORNL-4420, pp. 105–106.

Y-95382

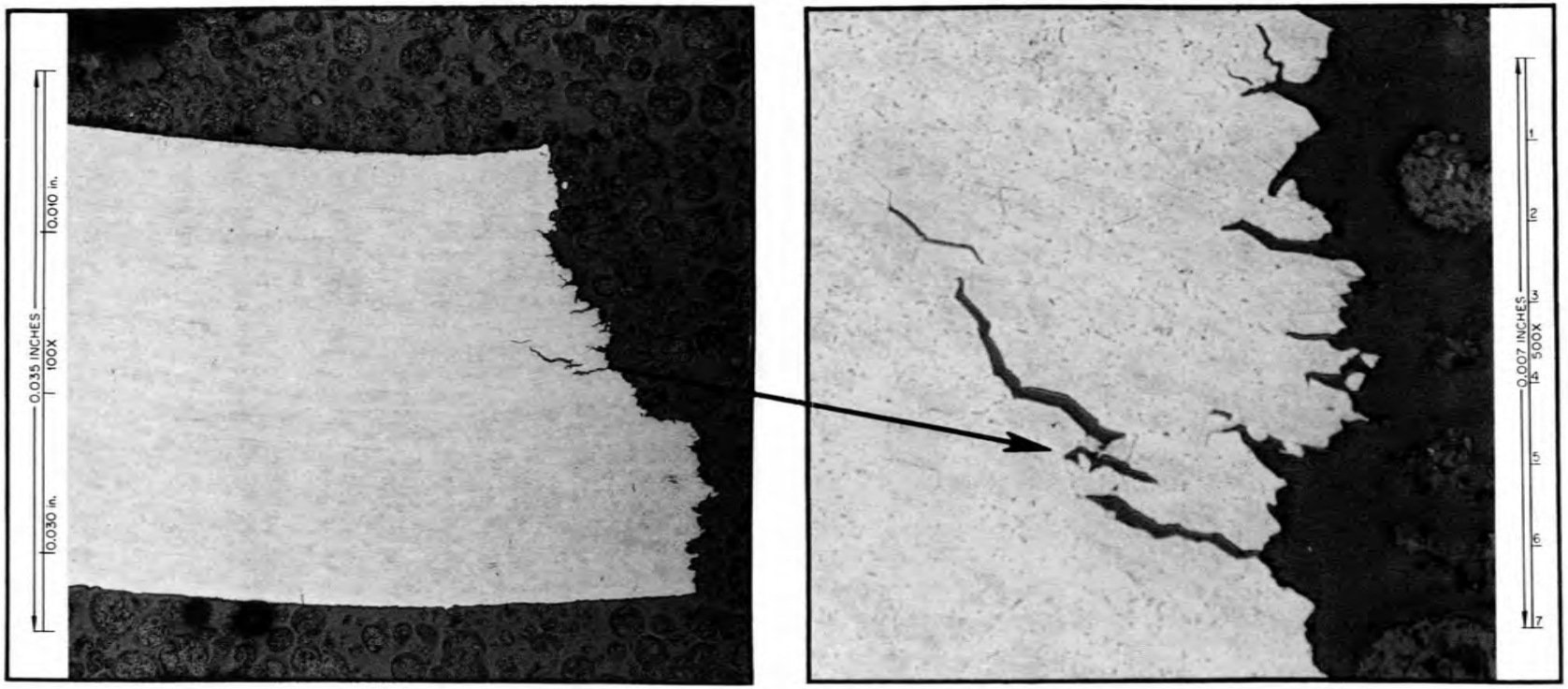

Fig. 5.8. Metallographic Appearance of T-222 Insert Specimen After Bend Test at Room Temperature. Specimen had been exposed to Li for 3000 hr at 1240°C.

samples were then chemically etched[18] to remove varying thicknesses of the outside surface. All four samples were then analyzed by vacuum fusion, and the results are given in Table 5.8. Although there appeared to be some difference in the N content among the four specimens, there was no evidence of a N gradient from the outside to the center of the

Table 5.8. Analyses of T-222 Sheet Specimen[a] Chemically Etched to Remove Varying Surface Layers

Depth of Surface Layer Removed (in.)	Final Thickness of Analytical Specimen (in.)	Concentration of Interstitial Impurities (ppm)		
		O	N	H
Unetched	0.029	22	94	4
0.0020	0.025	28	140	4
0.0045	0.020	25	71	9[b]
0.0095	0.010	38	140	56[b]

[a]Specimen had been exposed to Li for 3000 hr at 1265°C.

[b]Increase in H is attributed to chemical etching used to remove surface layers.

specimen. Oxygen content decreased slightly from the center to the outside, but there was no increment across the specimen where the interstitial impurity level appears abnormally high. Thus, we believe the observed loss in fracture toughness is associated more with the thermal history of these specimens than with changes in interstitial impurities.

T-111 Forced Circulation Liquid Lithium Loop (FCLLL-1) (B. Fleischer, D. L. Clark, C. W. Cunningham)

We completed the final assembly of test loop FCLLL-1. The resistance-heated section of the loop was cycled between ambient

[18]Etchant: 10 H_2SO_4–20 HF–40 HNO_3–30 H_2O (vol %).

temperature and 1370°C before the loop was charged with Li. A trial run was then made at 1370°C with circulating Li. The test was stopped at the end of this report period so that instrumentation and operational difficulties could be investigated and corrected.

Installation of Loop into Vacuum Chamber. — The relative positions of the loop components and piping within the vacuum chamber are shown schematically in Fig. 5.9. Figure 5.10 is a photograph of the resistance heater, economizer, and radiator during an early phase of installation. These components are mounted on a stainless steel frame that is supported from pads fastened to the inner wall of the vacuum-chamber bowl. The

ORNL-DWG 67-9135R2

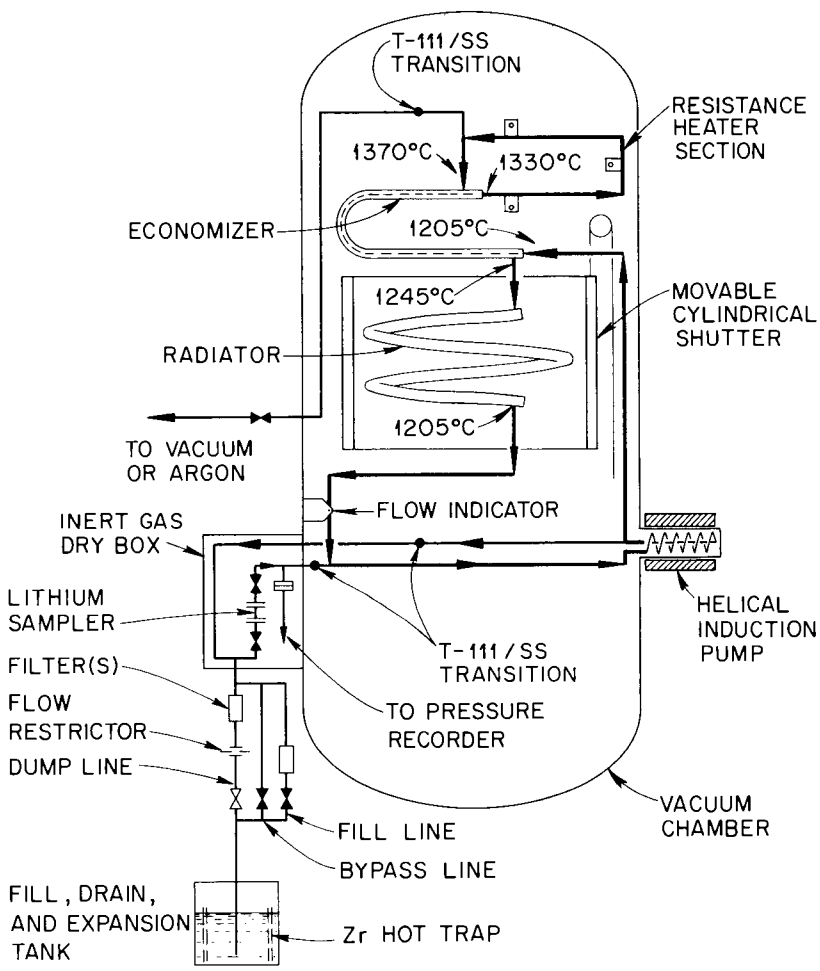

Fig. 5.9. Forced Circulation Liquid Lithium Loop (FCLLL-1).

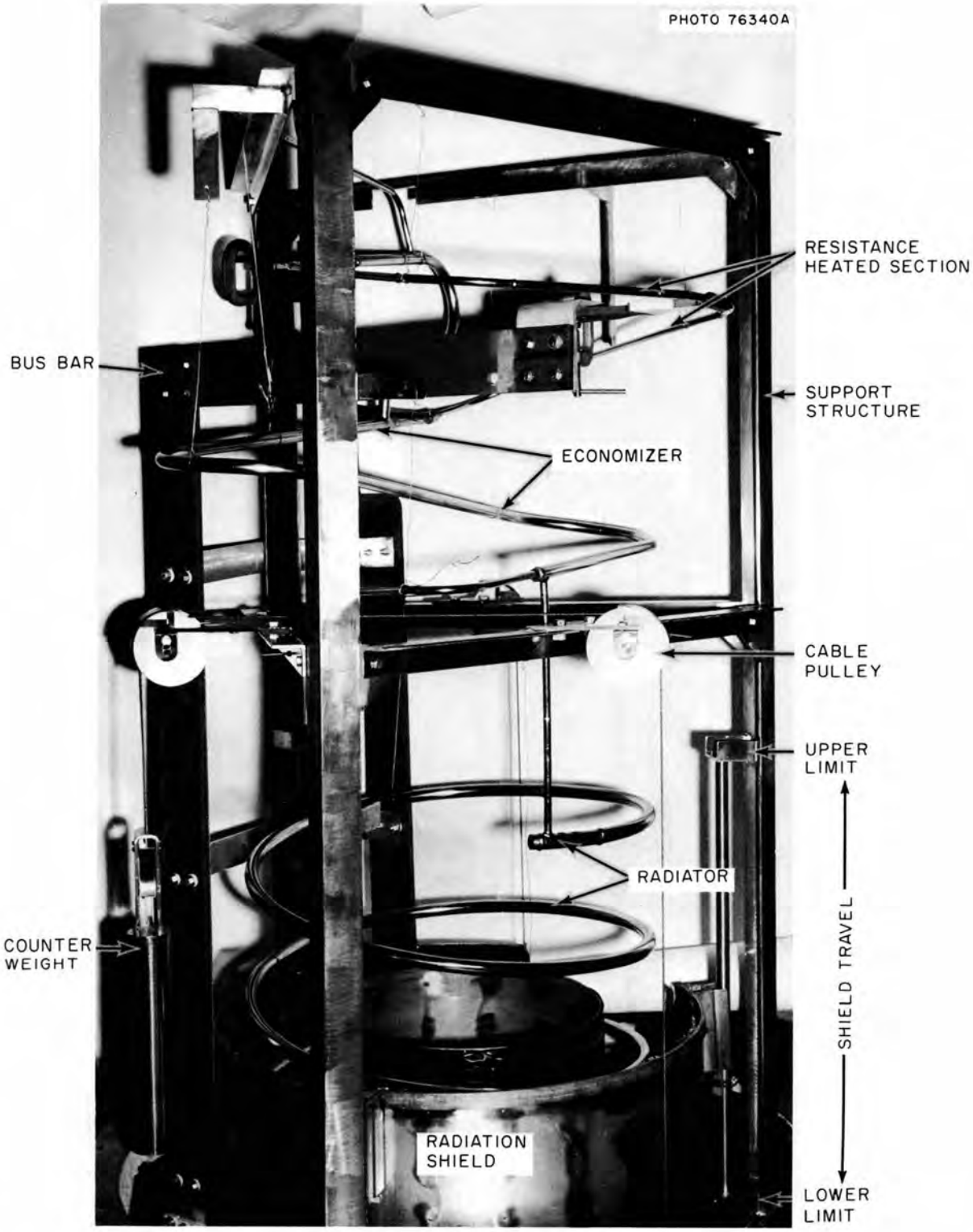

Fig. 5.10. Forced Circulation Liquid Lithium Loop (FCLLL-1) During Installation.

adjustable heat shield surrounding the radiator in Fig. 5.10 is in the position intermediate between its upper and lower limits. This shield is counter weighted so that it can be positioned easily by a magnetically-coupled, rotary feedthrough in the wall of the vacuum chamber. The rotary motion of the feedthrough is transmitted to stainless steel cables that move on alumina pulleys (Fig. 5.10). The pulleys turn on stainless steel shafts that were hard surfaced by welding Stellite-12 on the surface and grinding to finished dimensions. A niobium diselenide lubricant (1- to 2-μm particle size) is also used to avoid galling.

The electrical bus bars delivering current to the resistance heater were made from OFHC-grade Cu. They were coated with high-emissivity iron titanate to increase dissipation of radiation heat.

The loop is shown in Fig. 5.11 as it appeared before its enclosure by the vacuum-chamber bell. All sections of the loop except the radiator were covered by several layers of Ta foil reflective insulation, as shown in this figure. Figure 5.12 shows how the foil was assembled.

The interaction between the atmosphere in the vacuum chamber and the test loop is being monitored by means of two furnace assemblies that are incorporated in the vacuum chamber along with the test loop, as shown in Fig. 5.13. These furnaces are suspended from the support frame above the resistance-heated section of the loop and contain several T-111 sheet specimens. The furnaces consist of W-mesh resistance heaters surrounded by multiple layers of Ta foil reflective thermal insulation. The T-111 control specimens will be held at 1370 and 1225°C, respectively, in a configuration described previously.[19]

Shown in Fig. 5.13 are some of the alumina-insulated bare-wire thermocouples described previously.[20] We also used several sheathed thermocouples to measure the temperatures in the loop. These sheathed thermocouples were made of 0.009-in. sensing wires of the same composition as our bare-wire thermocouples (W–3% Re vs W–25% Re). The outer sheath,

---

[19]D. L. Clark and B. Fleischer, Fuels and Materials Development Program Quart. Progr. Rept. Sept. 30, 1968, ORNL-4350, pp. 131–135.

[20]D. L. Clark, C. W. Cunningham, and B. Fleischer, Fuels and Materials Development Program Quart. Progr. Rept. March 31, 1969, ORNL-4420, pp. 106–113.

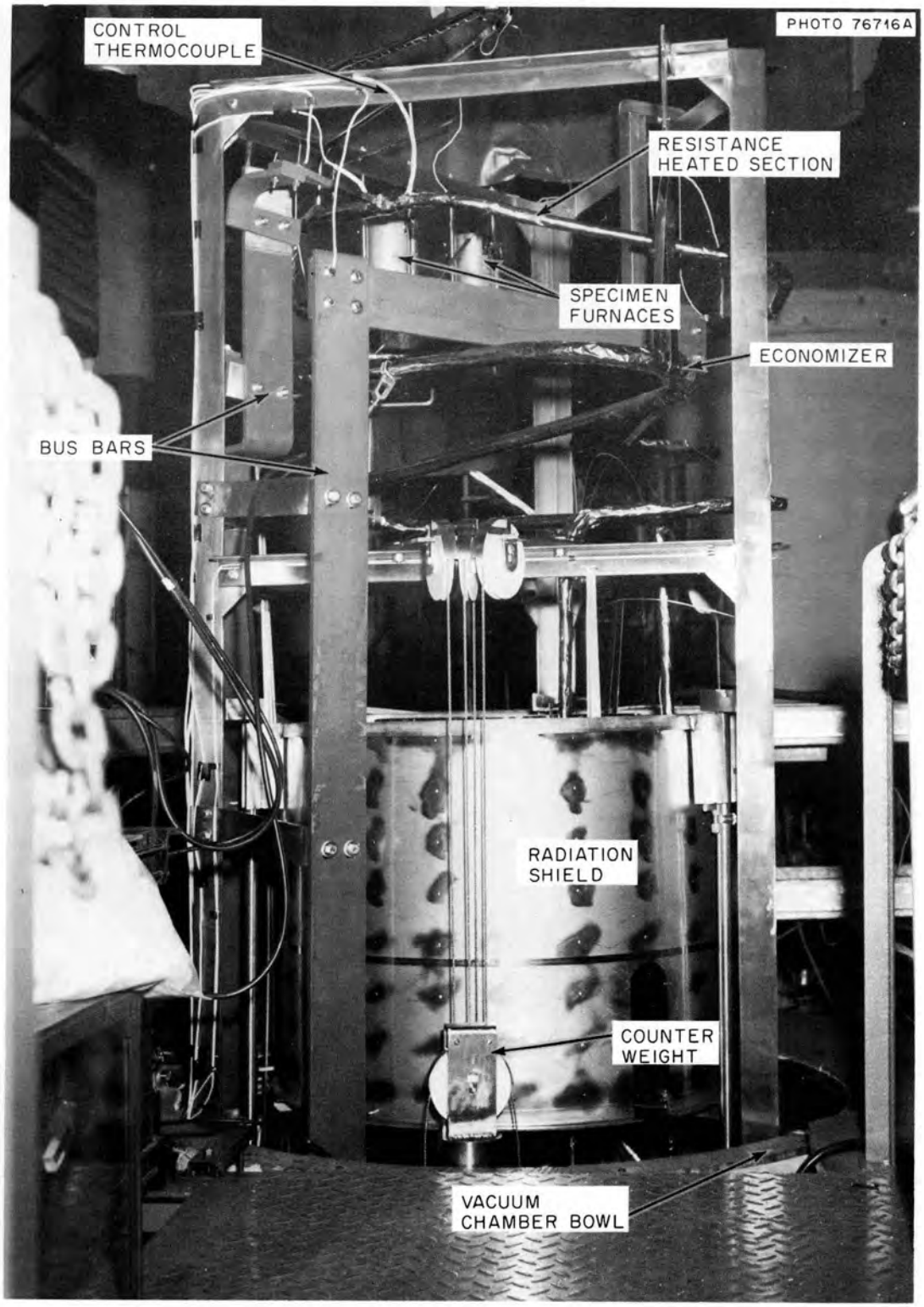

Fig. 5.11. Forced Circulation Liquid Lithium Loop (FCLLL-1) Before Closure of Vacuum Chamber.

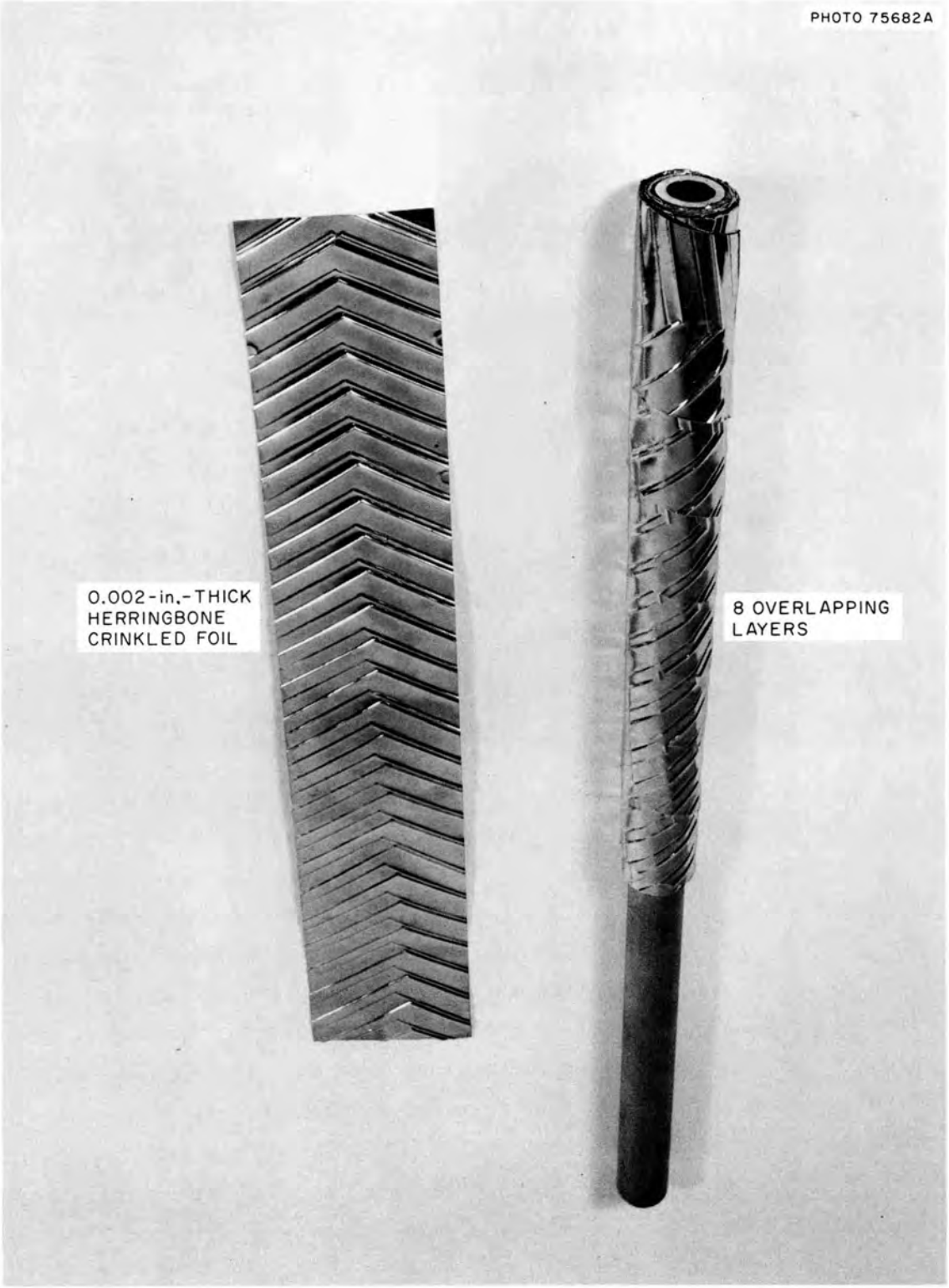

Fig. 5.12. Application of Tantalum Foil Thermal Radiation Insulation for Forced Circulation Liquid Lithium Loop (FCLLL-1).

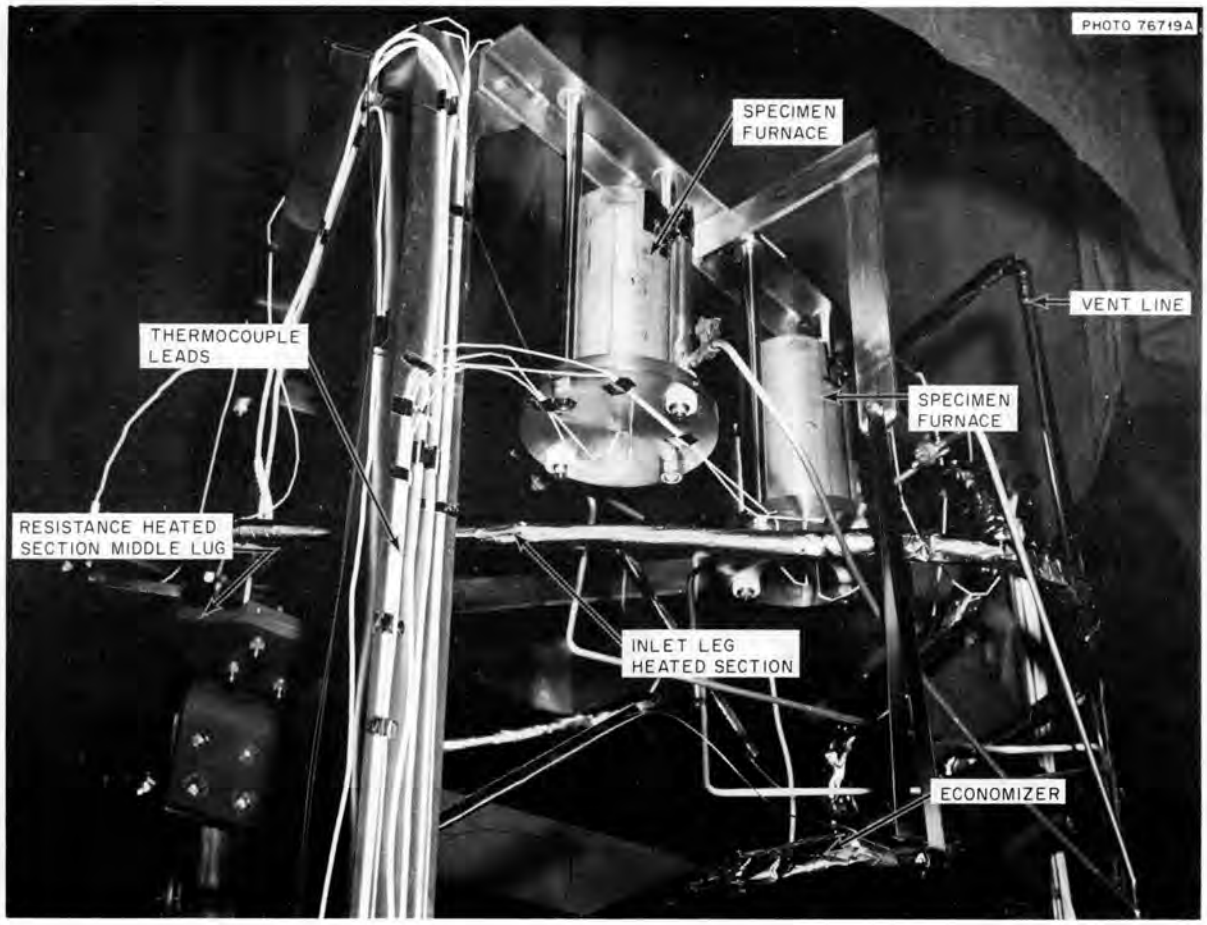

Fig. 5.13. Specimen Furnaces in Forced Circulation Liquid Lithium Loop (FCLLL-1).

which was 1/16 in. in diameter, was Ta near the hot-junction end and type 304 stainless steel beginning about 24 in. from the hot junction. We used BeO powder for insulation in the Ta section and MgO in the stainless steel section. The dissimilar sheath materials were joined by a brazed sleeve. The sheathed thermocouples that were attached to the resistance-heated section of the loop were threaded through BeO and Al_2O_3 beads to avoid short circuits to the support structure and the chamber.

Thermal Cycling Test. – Before filling the loop, we thermally cycled the resistance-heated section. The rate of heating was adjusted manually to limit the pressure in the vacuum chamber to below 1×10^{-5} torr. The temperature was increased in gradual increments to 1370°C and held for 2 hr. The loop was monitored for leaks throughout the thermal cycle by

pressurizing the loop internally to 0.8 torr with pure He and monitoring the gases in the vacuum chamber for He with a leak detector that has a sensitivity of 10^{-10} std cm^3/sec. The loop remained free of leaks during and after the thermal cycle.

Lithium Purification. — When we attempted to sample the Li drum originally purchased for this loop, we discovered a gas leak above the Li level. After repairing the leak, we sampled the Li through a 10-μm filter at 315°C. The analysis showed excess of 4000 ppm N and 125 ppm O. When the Li was sampled again at 205°C through a 10-μm filter, it showed a concentration of about 1200 ppm N. Although the purity was improved by the use of the lower filtration temperature, we still considered it unacceptable and ordered replacement. To expedite the order, we designed and built a new supply drum and shipped it to the vendor, who filled it with Li.

The concentrations of impurities as received in a Li sample taken from the replacement drum at 205°C through a 10-μm filter are shown in Table 5.9. We transferred 25.5 lb of this Li at 200°C to the system fill-and-drain tank for further purification. The tank, which contained Zr foil produced from high-purity crystal bar stock, was heated to a hot-trapping temperature of 815°C. A sample was taken after 40 hr at this temperature. The results, shown in Table 5.9, indicate that the purification treatment was very effective in lowering the levels of O and N.

The N and O concentrations in a subsequent sample of the Li used to flush the loop were also low (see Table 5.9), and the flush charge was approved for use without further purification.

Filling the Loop with Lithium. — In preparation for filling the loop with Li, we preheated the T-111 piping by radiation from the electrically-heated walls of the chamber bell and bowl. The temperature of the chamber wall was increased slowly (10°C/hr) to avoid temperature transients that could cause distortion of the main chamber flange and possible air leaks. The temperature was raised until the coldest point in the primary circuit of the loop (the flowmeter magnet) was just above the melting point of Li. The bypass circuit, most of which is outside the vacuum chamber, was heated with tubular electric heaters to a maximum temperature of 540°C to ensure that all points would be above the melting

Table 5.9. Chemical Analysis of Lithium Used in Forced Circulation Liquid Lithium Loop (FCLLL-1)

Element	Concentration, ppm		
	As Received	After Hot Trapping[a]	After Loop Flush[b]
O	48	12	9
		23	11
			16
N	201	< 5	< 5
	224	< 5	< 5
Ag	< 1	< 1	< 1
Al	< 10	< 10	< 10
B	< 1	< 1	< 1
Ba	< 5	< 5	< 5
Be	< 1	< 1	< 1
Bi	< 2	< 2	< 2
Ca	< 100	< 100	< 100
Cb	< 20	< 20	< 20
Co	< 5	< 5	< 5
Cr	5	5	5
Cu	10	10	10
Fe	50	50	20
Hf	< 20	< 20	< 20
K	30	30	30
Mg	≤ 1	≤ 1	≤ 1
Mn	3	7	2
Mo	≤ 1	< 1	< 1
Na	50	70	30
Ni	20	10	10
Pb	< 3	< 3	< 3
Sb	< 5	< 5	< 5
Si	≤ 5	≤ 5	≤ 5
Sn	< 3	< 3	< 3
Ta	< 20	< 20	< 20
V	< 3	< 3	< 3
W	< 20	< 20	< 20
Zr	< 20	< 20	< 20

[a]After hot trapping 40 hr at 815°C.

[b]Flushing consisted of more than 100 volume changes at 300°C in both the primary and bypass circuit over a period of 2 hr.

point of Li. The temperature of the Li in the fill-and-drain tank was adjusted to 315°C. The helical induction pump of the primary circuit was heated by operating it empty to maintain the reflective insulation around the pump at 315°C.

We added a total of 7.2 lb of Li to the primary and bypass circuits by pressurizing the fill-and-drain tank as necessary to maintain flow into the loop through the 10-μm filter at 315°C. We followed the movement of Li during filling by means of the continuous level recorder on the fill-and-drain tank, thermocouples, the flowmeters on the primary and bypass circuits, and the pressure recorder on the primary circuit.

Since the Li pump was already energized for preheating purposes, it immediately began circulating Li in the primary and bypass circuits. The Li inventory was maintained at a nearly constant temperature of 315°C by power input from the pump, the chamber heaters, and the bypass-circuit heaters.

The Li was circulated for 2 hr and then sampled (Table 5.9). The average temperature in the primary circuit was 300°C; the flow rates were 1.2 gpm in the primary circuit and 0.5 gpm through the bypass circuit. At least 100 volume changes were made in the primary circuit and 150 volume change units in the bypass circuit before sampling.

We maintained the temperature level in the loop by increasing the power to the pump and piping heater as the walls of the vacuum chamber were cooled. The chamber was slowly cooled at 5.5°C/30 min by reducing the power to the bakeout heaters for the vacuum chamber.

Trial Run. — The temperature of the Li in the primary circuit at the resistance-heater exit was increased in steps from 315°C to the design temperature of 1370°C. We experienced a number of thermocouple failures throughout the trial period, and many of the temperature data appeared questionable. Therefore, we terminated the trial run and opened the chamber to inspect and remedy the difficulties.

An inspection of the bare-wire thermocouples revealed that 8 of 12 had failed either because of shorting or breaking or detachment of the wires at their junctions with the loop piping. In the sheathed thermocouples, 5 of 11 sensing wires had broken at the transition joint in the sheath material, as shown in Fig. 5.14. The transition from Ta to

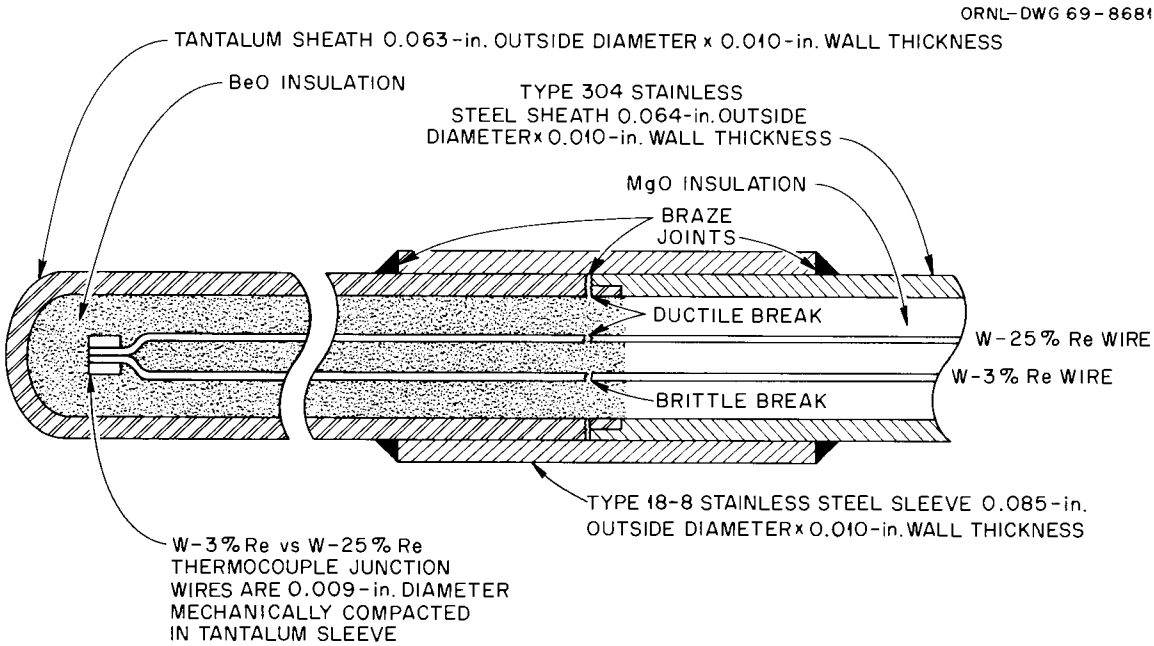

Fig. 5.14. Typical Thermocouple Failure Induced by Differential Thermal Expansion in Forced Circulation Liquid Lithium Loop Test (FCLLL-1).

stainless steel sheath material was adopted to reduce the cost of the thermocouple sheathing. Because the vendor's test experience had shown the original transition joint to be mechanically weak, a stainless steel sleeve was brazed over the joint for mechanical protection. Apparently, the differential thermal expansion between stainless steel and Ta was sufficiently great that the sheath joint and the wires were subjected to excessive tensile stresses when the sleeve temperature was increased by radiant heating. The reason for failure of the remaining six sheathed thermocouples is not clear and is still being investigated. Five of these thermocouples were found to have low resistance from wires to sheath near the hot junction.

The primary circuit was subjected to several thermal cycles as a result of normal heating and cooling operations and equipment difficulties. Four severe thermal cycles resulted from sudden restoration of power to the Li pump and the resistance-heated section after power failures. During the most severe of these cycles, the exit temperature in the resistance-heated section changed from 950 to 715°C at a rate estimated to be 3000°C/min. Thermal cycles were also experienced when

the heater power was lost because of problems in the control instrumentation and electrical power circuit. During the worst of these thermal cycles the temperature at the exit of the resistance-heated section dropped from 1290 to 925°C in 3 min. At lower temperatures, these thermal cycles were less severe: at 1066°C, a rate of drop of 27°C/min was observed; at 849°C, a rate of drop of 15°C/min was observed. The heating rates, in contrast, were no greater than 16°C/min.

We observed no damage to the loop piping as a result of these thermal cycles. However, we did observe failure of thermocouples throughout this period.

Vacuum Environment for Primary Circuit. — The major off-gas loads were encountered while the loop was being heated before it was filled with Li and when the primary circuit was being raised to design temperature. The chamber pressure peaked in the 10^{-4} torr range as the primary loop was heated preparatory to receiving the Li. The chamber pressure was held below 5×10^{-5} torr during subsequent heating of the primary circuit to the design conditions.

A diffusion pump with a liquid-N-cooled, optically baffled trap was used to handle the peak outgassing loads. The triode ion pumps were turned on and the diffusion pump valved off when the chamber had cooled and its pressure was near 5×10^{-6} torr. The loop was operated at 315°C. While the loop was being heated, the ion pumps developed Ar instabilities and control of the pressure in the chamber was returned to the diffusion pump. During one instability, the chamber pressure surged from 10^{-9} to 10^{-4} torr, and the safety circuits automatically cut off the ion pumps. A monopole type of gas analyzer identified Ar as the offending gas. The Ar source was traced to the dry box through which the bypass circuit passes. Argon entered the chamber through the porous ceramic of the tubular trace heaters used to heat the bypass plumbing. The loop temperature was reduced and maintained at 260°C, and the chamber was backfilled with dry N_2 while ceramic-metal seals were applied to the heater ends that terminated in the dry box. The diffusion pump and the ion pumps were operated together until the Ar instabilities disappeared.

Hydrogen constituted the principal gas impurity within the vacuum chamber during the period when the chamber walls were water cooled and the loop was being heated up to design conditions. Water vapor and organic materials were detected after the chamber bakeout period, but these disappeared with time. Two typical gas analyses are given in Table 5.10. During these analyses, the chamber pressure was maintained by the diffusion pump alone.

Table 5.10. Typical Analysis of Residual Gas During Trial Run Period of Forced Circulation Liquid Lithium Loop Test (FCLLL-1)

Residual Gas	Composition, ppm	
	During Heating to 1075°C[a,b]	After Heating to 1315°C and Cooling to 980°C[a,c]
H_2	2000	80
CH_4	89	1
H_2O	35	< 1
N_2,CO	170	8
O_2	1	< 1
Ar	7	< 1
CO_2	80	< 1

[a]The component peak current values are roughly proportional to the component partial pressures.

[b]Total pressure of 5.1×10^{-6} torr, peak current of 10^{-9} amps.

[c]Total pressure of 4.4×10^{-7} torr, peak current of 10^{-9} amps.

PART III

RADIATION DAMAGE TO STRUCTURAL MATERIALS

6. BEHAVIOR OF REFRACTORY MATERIALS UNDER IRRADIATION

G. W. Keilholtz R. E. Moore
D. A. Dyslin[1] H. E. Robertson

The purpose of this program is to evaluate the effects of high fast-neutron fluences at 150 to 1100°C on the properties of refractory nuclear materials for both space and civilian power reactors. Investigations of the carbides, nitrides, and silicides of refractory metals are nearing completion. The emphasis in the program is now turning toward nitrides and carbides of depleted U and toward materials for use as neutron absorbers in control rods of fast-flux reactors.

Irradiation Damage to Nonfissionable Refractory Materials

Refractory Metal Carbides

Fast-neutron effects on carbides of the refractory metals (Ti, Zr, Ta, Nb, and W) at 300 to 700°C and at 1000 to 1100°C were investigated previously.[2–4] A very short-term irradiation at 150°C was completed, and a long-term irradiation at 150°C was recently started. The irradiations at 150°C and a series of annealing experiments out of reactor after irradiation are all that remains to be completed in this task. The purpose of the remaining work is to obtain data for establishing mechanisms of neutron damage that will include both the effects of thermal annealing and neutron annealing.

---

[1]General Engineering Division.

[2]G. W. Keilholtz, R. E. Moore, and D. A. Dyslin, Fuels and Materials Development Program Quart. Progr. Rept. Dec. 31, 1968, ORNL-4390, pp. 113–114.

[3]G. W. Keilholtz, R. E. Moore, and M. F. Osborne, Nucl. Appl. 4, 330 (1968).

[4]G. W. Keilholtz and R. E. Moore, Trans. Am. Nucl. Soc. 12(1), 101 (1969).

Effects of Irradiation on LMFBR Fuels

Effects of Helium Gas Produced by Fast Neutrons in Depleted UN

The objective of this work is to evaluate the effects of the production of He gas on fuels that contain N (ref. 5). Helium is generated within the fuels through the $^{14}N(n,\alpha)^{11}B$ fast-neutron reaction. Changes in the properties of depleted UN and depleted UN-UC (50-50 mole %) will be compared with the changes in the properties of depleted $U^{15}N$ in identical fast-neutron environments.

The fabrication of an instrumented assembly for irradiation at high temperatures is nearly complete. It consists of 14 capsules made from Nb–1% Zr and coated on the inside surface with W. The 14 capsules will span the flux profile of the Engineering Test Reactor (ETR) J-12 core position. Each capsule is designed to operate at 1000°C.

Three specimens nominally 0.25 in. in diameter by 0.4 in. long are contained in each capsule. Six capsules contain one specimen each of UN, $U^{15}N$, and UN-UC (50-50 mole %); six capsules contain two specimens of UN and one specimen of $U^{15}N$; and two capsules contain two specimens of $U^{15}N$ and one specimen of UN-UC (50-50 mole %).

Direct comparison of property changes of UN with $U^{15}N$ is provided in 12 of the 14 capsules, and a comparison of UN with UN-UC (50-50 mole %) is provided in 6 of the capsules. Helium analysis of gas from the capsules containing two UN specimens and one $U^{15}N$ specimen will produce information on release of He from UN for various fluences. Helium release from UN-UC (50-50 mole %) will be obtained by analysis of the gas contained in the two capsules that contain two $U^{15}N$ specimens and one specimen of UN-UC (50-50 mole %).

An uninstrumented assembly is also being fabricated for irradiation at low temperature (about 150°C). Both assemblies will be installed in the ETR J-12 core position in August 1969. The expected range of fast fluences is 0.5 to 2.0×10^{21} neutrons/cm^2 (> 1 Mev).

---

[5]G. W. Keilholtz, R. E. Moore, D. A. Dyslin, and H. E. Robertson, Fuels and Materials Development Program Quart. Progr. Rept. March 31, 1969, ORNL-4420, pp. 121–122.

Fast-Neutron Effects on Materials for Neutron Absorption in Fast Reactors

This task is aimed at investigating the effects of fast neutrons on materials with large fast-neutron absorption cross sections that may be used for controlling reactivity in fast-flux reactors.[5] Several candidates such as B_4C, TaC, Ta metal, and B_4C-Ta metal dispersions will be investigated. A facility in the Experimental Breeder Reactor II (EBR-II) will be used.

The first assemblies are being designed for irradiations in an EBR-II row 8 blanket facility. We plan to irradiate two assemblies containing B_4C at 400 and 750°C. Each of these assemblies will contain B_4C specimens with two different ratios of B:C. Provision will be made for measuring and analyzing the He gas released from each type of B_4C at each temperature after irradiation. We are also planning to irradiate at 400 and 750°C assemblies that will contain specimens of Ta metal, TaC, and possibly other absorbers. Future experiments will involve dispersions of Ta metal and B_4C.

7. FAST-NEUTRON IRRADIATION EFFECTS ON ELECTRICAL INSULATORS

G. W. Keilholtz R. E. Moore
D. A. Dyslin[1] H. E. Robertson

The purpose of this program is to establish the effects of fast neutrons on the mechanical, physical, and electrical properties of materials suitable for use as electrical insulators in thermionic converters and to evaluate the mechanisms of neutron damage in these materials from 150 to 1100°C.

General Survey of Fast-Neutron Effects on Electrical Insulators

Silicon Oxynitride

A new ceramic, silicon oxynitride (Si_2ON_2)(ref. 2), was irradiated at low temperatures (about 150°C) in the Engineering Test Reactor (ETR) as a part of this general survey of electrical insulators. The specimens, which were 1/2 × 1/2-in. solid cylinders, received fast-neutron fluences estimated to range from 0.6 to 3.6×10^{21} neutrons/cm^2 (> 1 Mev). Specimens of translucent Al_2O_3 and polycrystalline MgO were also included in the irradiation assembly for comparison and to obtain data for these materials at lower temperatures than previously obtained.

Preliminary inspection of the Si_2ON_2 specimens revealed no obvious fracturing or powdering. The specimens, which were bluish-grey before irradiation, did not appear to have changed in color. The Al_2O_3 and MgO specimens, which were white before irradiation, had turned nearly black. The MgO specimens survived intact, however, and 10 out of 12 Al_2O_3 specimens survived without fracturing. Gas analysis of the irradiation capsules showed that the Si_2ON_2 specimens had released very little, if any, N_2 during irradiation. The preliminary data strongly suggest that Si_2ON_2 merits consideration as a candidate for a more exhaustive investigation.

---

[1]General Engineering Division.

[2]Norton Company, Worcester, Mass.

Single-Crystal Materials and Other Advanced Materials

In addition to silicon oxynitride, discussed above, recent advances in materials sciences have resulted in several improved materials with properties of electrical insulation. Some of these may be useful in nuclear-powered thermionic converters if polycrystalline alumina proves unsatisfactory in specific engineering designs.[3] Specimens of three advanced materials are being fabricated: synthetic sapphire made by the Czochralski process, high-purity MgO single crystals (at ORNL), and zirconia-doped transparent Y_2O_3 (General Electric). Solid cylinders of these materials will be irradiated at about 150°C in the core of the ETR for six months or more to determine whether exhaustive investigations are justified.

Irradiation of High-Density Commercial Al_2O_3 Products Considered for Thermionic Insulators

Results of examinations of specimens irradiated in a short-term ETR assembly were reported previously.[3] The irradiation of an identical long-term assembly has now been completed. Specimens of the same commercial Al_2O_3 products are now being irradiated in row 2 of the core of the Experimental Breeder Reactor II (EBR-II).

The specimens in the ETR assemblies were irradiated at temperatures from 400 to 1230°C. The EBR-II assembly was designed for specimen temperatures of about 800°C. Comparisons of damage to specimens irradiated in the EBR-II with those irradiated in the ETR will establish the effect of neutron energy. The EBR-II neutron flux is virtually all fast, while the ETR has a mixed fast- and thermal-energy spectrum.

We have a program in which unirradiated alumina products are heated and thermally cycled to correspond with the thermal histories of the reactor irradiations. The thermal history of the short-term ETR irradiation (3021 hr with 61 shutdowns or major power reductions) was duplicated at three temperatures: 600, 800, and 1100°C. No specimens

---

[3]G. W. Keilholtz, R. E. Moore, D. A. Dyslin, and H. E. Robertson, Fuels and Materials Development Program Quart. Progr. Rept. March 31, 1969, ORNL-4420, pp. 123–130.

fractured, and there were no significant dimensional changes as a result of this treatment. Therefore, we are confident that the damage and property changes reported[3] for the specimens irradiated in the short-term assembly were caused by neutron irradiation rather than thermal treatment. Duplication of the thermal history of the long-term ETR irradiation is in progress.

8. MECHANICAL PROPERTIES RESEARCH AND LMFBR CLADDING AND STRUCTURAL MATERIALS DEVELOPMENT

J. R. Weir, Jr. H. E. McCoy, Jr.

Work in this program includes studies of the high-temperature irradiation embrittlement and other technologically important aspects of radiation damage to fuel cladding materials at high neutron fluence. The work centers around types 316 and 304 stainless steel, Incoloy 800, and Hastelloy N and the effects of Ti concentration in these alloys on radiation damage.

Mechanical Properties of Type 316 and Titanium-Modified Type 316 Stainless Steel

E. E. Bloom J. G. Morris

The mechanical properties of standard type 316 stainless steel and type 316 stainless steel containing 0.23 wt % Ti are being evaluated in both the unirradiated and irradiated conditions. Experimental variables being investigated include annealing temperature, amount of cold work, thermal aging, and irradiation conditions.

The effects of prestrain on the rupture life and minimum creep rate of standard type 316 stainless steel at 650°C are shown in Figs. 8.1 and 8.2. A 5% prestrain has no significant effect on either rupture life or minimum creep rate. A 20% prestrain doubles the rupture life and decreases the minimum creep rate by an order of magnitude. It is important, however, to examine the effect of prestrain on the duration and amount of strain that occur during the second and third stages of the creep process, as is shown in Table 8.1. These data show that prestrain decreases the amount of time and the percentage of the rupture life that the material spends in second-stage creep and also the amount of strain that occurs before the onset of third-stage creep.

A similar set of data for Ti-modified type 316 stainless steel is shown in Table 8.2. In this case, the variable was pretest annealing temperature, and the specimens were tested at 37,500 psi and 650°C. A

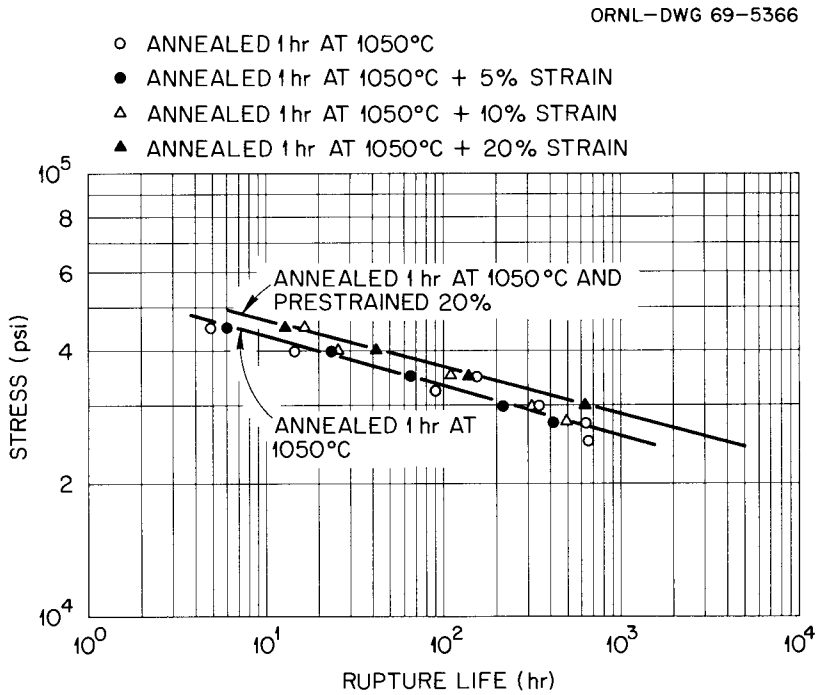

Fig. 8.1. Effect of Prestrain on the Rupture Life of Type 316 Stainless Steel at 650°C.

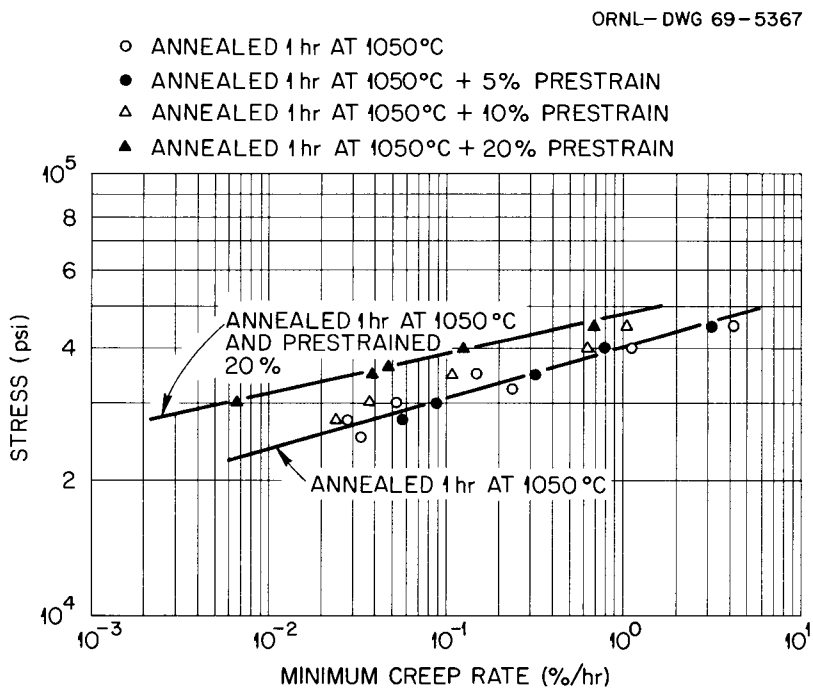

Fig. 8.2. Effect of Prestrain on the Minimum Creep Rate of Type 316 Stainless Steel at 650°C.

Table 8.1. Effect of Strain Before Test on Creep Properties of Type 316 Stainless Steel at 650°C and 35,000 psi

Strain Before Test[a] (%)	Time to Rupture (hr)	Minimum Creep Rate (%/hr)	Time in Second-Stage Creep (hr)	Strain During Second-Stage Creep (%)	Time In Third-Stage Creep (hr)	Strain During Third-Stage Creep (%)	Total Strain (%)
None	153	0.146	48	8	105	54	62
5	65	0.335	25	8	40	35	43
10	110	0.115	20	2.5	90	33.5	36
20	142	0.047	20	1.5	122	37.5	39

[a]All specimens were annealed 1 hr at 1050°C before test.

Table 8.2. Effect of Annealing Treatment Before Test on the Creep-Rupture Properties of Titanium-Modified Type 316 Stainless Steel

Temperature of Annealing Before Test[a] (°C)	Time to Rupture (hr)	Minimum Creep Rate (%/hr)	Time in Second-Stage Creep (hr)	Strain During Second-Stage Creep (%)	Time in Third-Stage Creep (hr)	Strain During Third-Stage Creep (%)	Total Strain (%)
1000	95	0.038	25	1.5	70	29.5	31
1050	225	0.015	60	2.0	165	57.0	59
1100	625	0.004	240	3.5	380	29.5	33
1150	355	0.008	90	1.0	265	34.0	35
1200	235	0.004	84	1.0	151	27.0	28
1050[b]	690	0.0047	500	3.5	190	9.5	13

[a]All specimens were annealed for 1 hr.

[b]Specimen strained 10% before test.

pretest annealing treatment of 1 hr at 1100°C gives optimum rupture life and minimum creep rate. The modified alloy exhibits longer rupture lives and lower creep rates for all pretest annealing treatments, except that for 1 hr at 1000°C, than does the standard alloy in any pretest condition investigated to date, even though the modified alloy was tested at a higher stress. If the Ti-modified alloy is annealed 1 hr at 1050°C and then strained before testing at 650°C and 37,500 psi, strength properties improve even more, the creep rate is reduced from 0.015 %/hr in the annealed condition to 0.0047 after 10% prestrain, and the duration of the second-stage creep is extended from 60 to 500 hr.

The variation of the flow stress with strain rate can be used as an indication of the stability of a material. The sensitivity to strain rate (K), defined as the change in the flow stress ($\Delta\sigma$) divided by the change in the logarithm of the strain rate ($\Delta \log \dot{\epsilon}$), is useful for comparing the sensitivity of the strength to the strain rate.

Tests of this type have been used to measure the stability of modified type 316 stainless steel. They show a pronounced inverse strain-rate effect. At a test temperature of 500°C (see Fig. 8.3) and a strain of 20%, this effect is 24,000 psi for a change in strain rate from 0.002 to 0.2 min^{-1}. The strain-rate sensitivity is negative and changes with strain as shown in Fig. 8.4. Thus, there is an instability induced by strain in this material at this temperature. This instability is reduced significantly at 300°C so that there is no inverse strain-rate effect and little sensitivity to strain rate at this temperature (see Fig. 8.5).

An analysis of the data for stress, strain, and strain rate, made according to $\frac{\dot{\epsilon}}{\epsilon} = 40\ e^{-\frac{U}{RT}}$, yields an activation energy, U, of 19.0 kg cal $mole^{-1}$, which is comparable to the activation energy for the diffusion of C in Fe of 18.5 kg cal $mole^{-1}$. This experimentally determined value, along with the results from the work on sensitivity to strain rate, suggests that the formation of carbides is responsible for the large increase in stress at a strain rate of 0.002 min^{-1}.

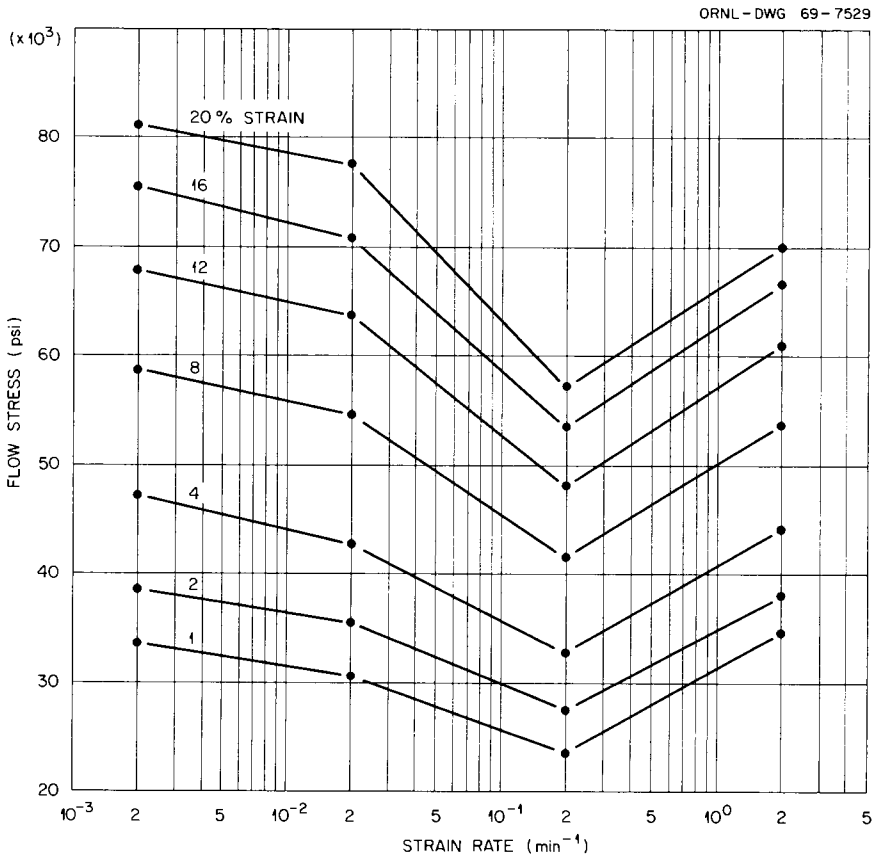

Fig. 8.3. Variation of Flow Stress with Strain and Strain Rate for Titanium-Modified Type 316 Stainless Steel at 500°C.

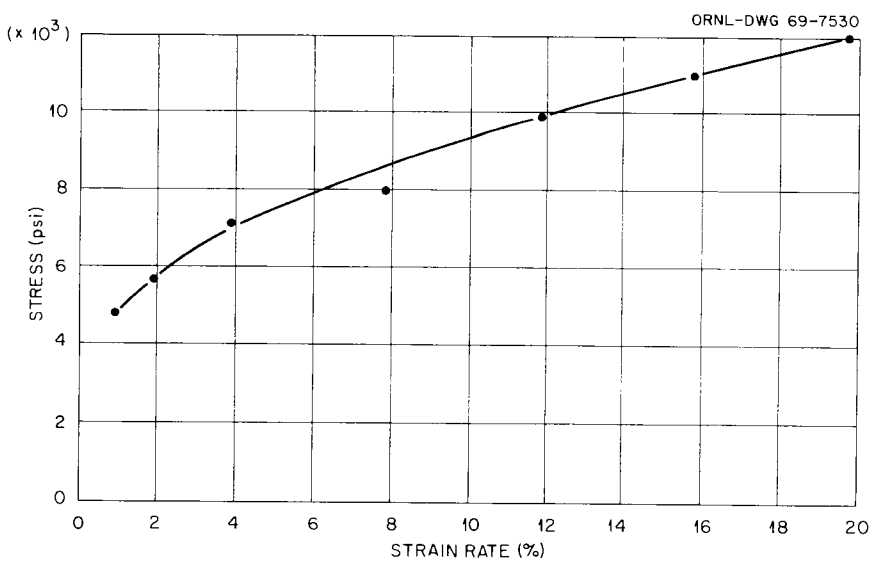

Fig. 8.4. Variation of the Sensitivity to Strain Rate with Strain for Titanium-Modified Type 316 Stainless Steel Tested at 500°C.

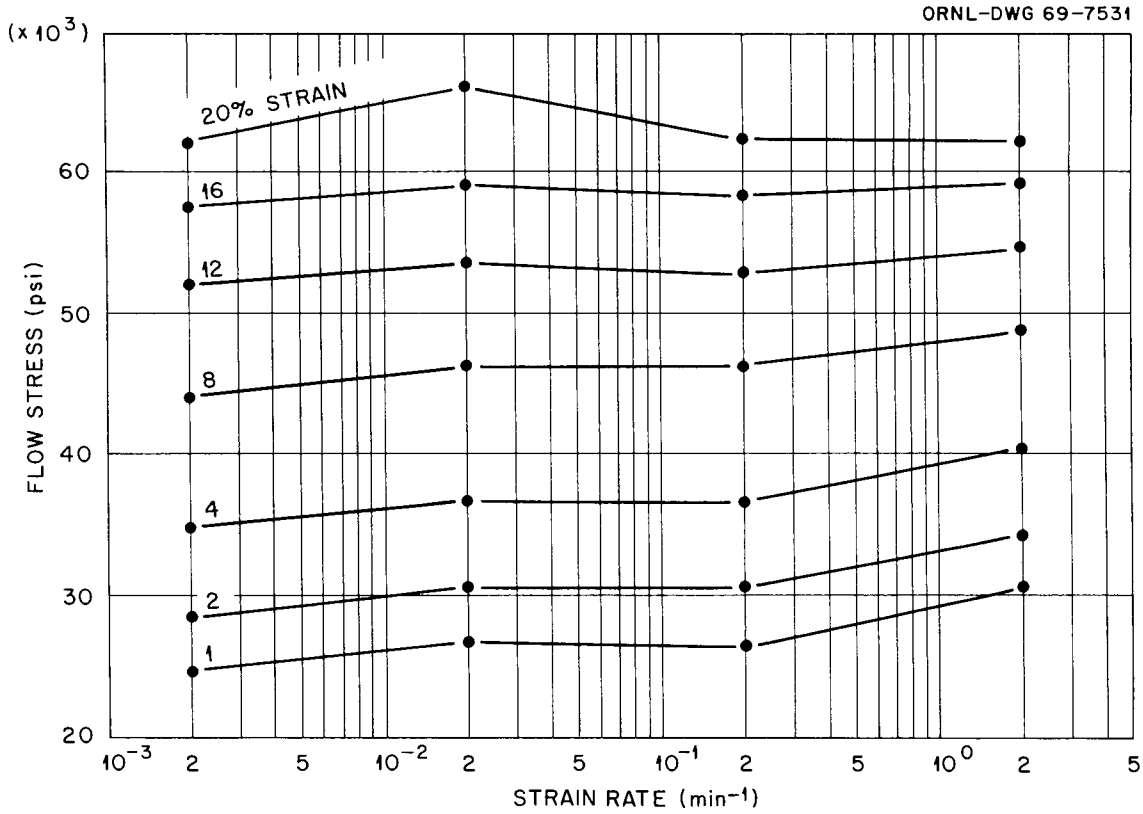

Fig. 8.5. Variation of Flow Stress with Strain and Strain Rate for Titanium-Modified Type 316 Stainless Steel at 300°C.

Radiation Damage in Incoloy 800

D. G. Harman

We have shown[1, 2] the 0.12% C, 0.1% Ti heat of Incoloy 800 to have lower ductility after irradiation at 500°C than after irradiation at 700°C. The specimens were annealed at 1150°C, irradiated to 0.8×10^{21} neutrons/cm^2 (thermal), and then tensile or creep-rupture tested at 650°C. Test results from the thermal control specimens showed this to be a combined effect of thermal and neutron exposure. The loss of ductility was circumvented by heat treating to a finer grain size before irradiation aging to agglomerate the carbide particles.

---

[1]D. G. Harman, Fuels and Materials Development Program Quart. Progr. Rept. Dec. 31, 1968, ORNL-4390, pp. 127–129.

[2]D. G. Harman, Fuels and Materials Development Program Quart. Progr. Rept. March 31, 1969, ORNL-4420, pp. 134–141.

We continued our investigations of this composition, using specimens irradiated to 1.6×10^{21} neutrons/cm^2 (thermal and > 1 Mev) at 350, 450, 550 and 650°C. The experiment included specimens annealed 30 min at 1150 or 1040°C and specimens aged 100 hr at 800°C.

Creep-rupture tests were performed at 650°C and stress levels of 30,000, 21,000, and 18,000 psi. The test results listed in Table 8.3 show a significant effect of irradiation temperature on rupture time, total elongation, and maximum creep rate. As expected, the largest

Table 8.3. Effect of Irradiation on the Creep-Rupture Properties at 650°C of Incoloy 800 with 0.1% Titanium and 0.12% Carbon

Test Conditions[a]	Creep-Rupture Properties		
	Rupture Time (hr)	Total Elongation (%)	Minimum Creep Rate (%/hr)
Anneal, 0.5 hr at 1150°C			
Stress, 30,000 psi			
Irradiation temperature, °C			
350	238	3.9	0.0057
450	191	2.8	0.0065
550	8	1.3	0.122
650	10	3.5	0.255
Anneal, 0.5 hr at 1040°C			
Stress, 21,000 psi			
Irradiation temperature, °C			
350	121	23.9	0.138
450	97	22.9	0.166
550	41	7.5	0.145
650	23	11.7	0.405
Anneal, 100 hr at 800°C			
Stress, 18,000 psi			
Irradiation temperature, °C			
350	69	25.5	0.120
450	70	21.8	0.140
550	23	35.6	0.630
650	13	19.4	0.80

[a]All specimens were cold worked > 50%, annealed and stressed as indicated before irradiation, and then irradiated at the indicated temperatures for four cycles in a core position in the Oak Ridge Research Reactor to about 1.6×10^{21} neutrons/cm^2 (thermal and > 1 Mev).

effect is shown for the material annealed at 1150°C with a creep elongation of only 1.3% after irradiation at 550°C. This also corresponded to the minimum rupture time of 8 hr (as compared to 238 hr after irradiation at 350°C). The minimum creep rate was also most affected for this heat treatment and varied nearly two orders of magnitude with irradiation temperature.

Figures 8.6, 8.7, and 8.8 show the data plotted as a function of irradiation temperature for the three preirradiation treatments

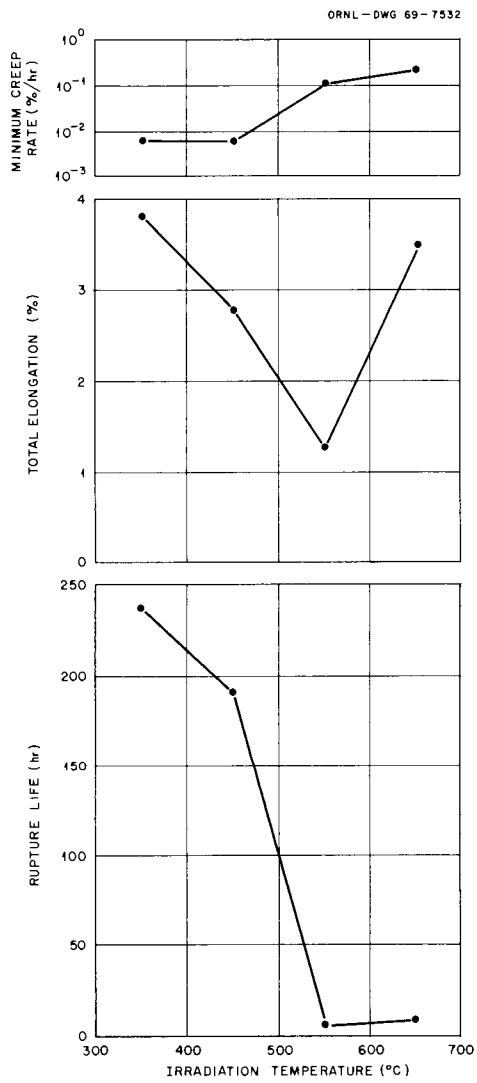

Fig. 8.6. Postirradiation Creep-Rupture Properties of Incoloy 800 with 0.1% Titanium and 0.12% Carbon Annealed at 1150°C. Specimens were tested in air at 650°C after irradiation at the indicated temperature to 1.6×10^{21} neutrons/cm^2.

investigated. In Fig. 8.6, the low minimum creep rates show that the matrix of the material with the largest grains was significantly hardened at the lower irradiation temperatures of 350 and 450°C. Increasing the irradiation temperature to 550°C apparently provides for increased precipitation at grain boundaries or "film formation," for the total

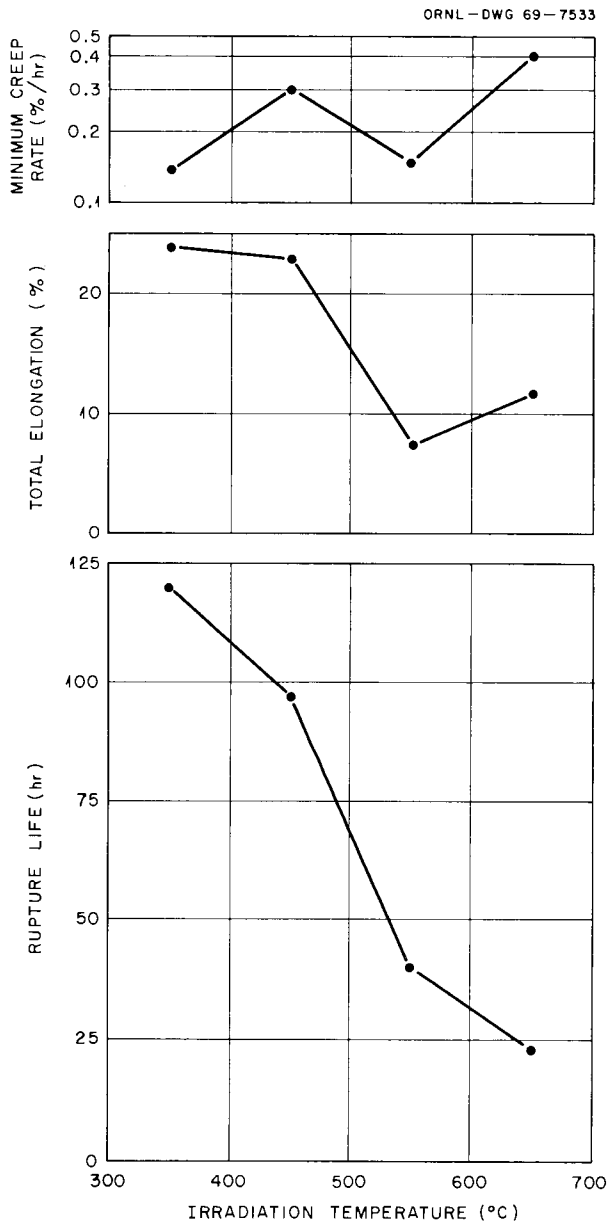

Fig. 8.7. Postirradiation Creep-Rupture Properties of Incoloy 800 with 0.1% Titanium and 0.12% Carbon Annealed at 1040°C. Specimens were tested in air at 650°C after irradiation at the indicated temperatures to 1.6×10^{21} neutrons/cm^2.

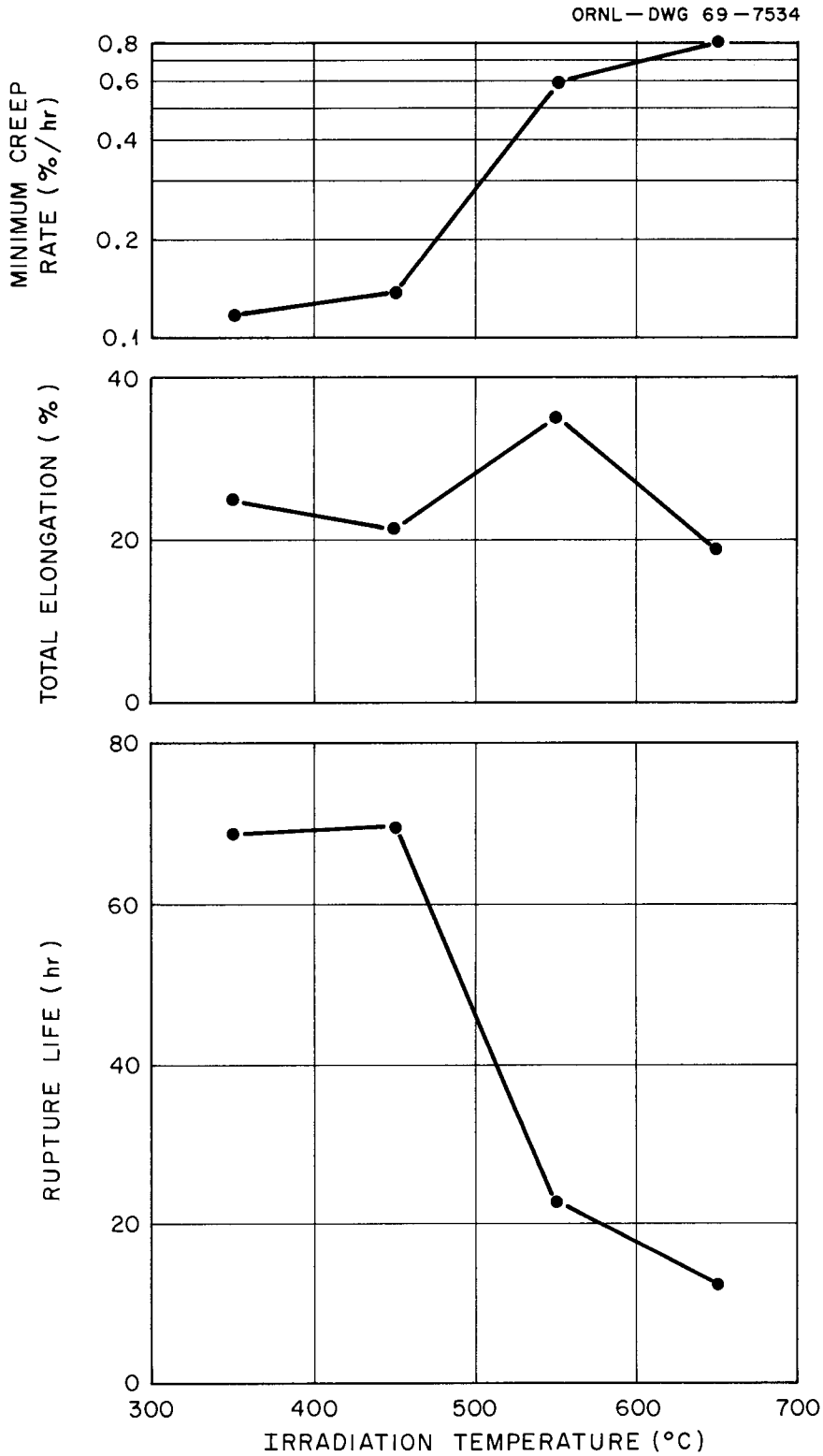

Fig. 8.8. Postirradiation Creep-Rupture Properties of Incoloy 800 with 0.1% Titanium and 0.12% Carbon Annealed at 800°C. Specimens were tested in air at 650°C after irradiation at the indicated temperature to 1.6×10^{21} neutrons/cm^2.

elongation dropped to 1.3%. This, combined with the increased creep rate, drastically reduced the rupture time for this irradiation temperature. After the irradiation at 650°C the ductility had recovered somewhat; this slightly increased rupture life.

Lowering the temperature of the anneal before irradiation to 1040°C (see Fig. 8.7) lessened these effects to some extent. The matrix hardening was not as significant, and the overall ductility was much higher than after the 1150°C anneal. For the specimen annealed at 350°C, however, the elongation did decrease from 23% to 7.5% for the 550°C irradiation temperature. The decrease in rupture time with increasing irradiation temperature shown in Fig. 8.7 is mostly due to the loss of ductility, for the creep rate increased only slightly in this temperature range.

The test results are shown in Fig. 8.8 for the specimens that were aged at 800°C before irradiation. Most importantly, the creep ductility remained above about 20% for all irradiation levels. Apparently, the increased grain boundary area due to the finer grain size prevented the near-continuous precipitation at grain boundaries that was probably present in the materials with larger grains. The minimum creep rate, however, showed a dependence on irradiation temperature that resulted in longer rupture times for the 350 and 450°C irradiations. This correlation between minimum creep rate and rupture time can be seen from Fig. 8.8.

It should be pointed out that the structure produced in the test specimens during the irradiations conducted below the test temperature may not have remained during heating to test temperature. We reasoned, however, that a common temperature would allow comparisons and that a test temperature high enough to provide creep deformation was most desirable. Testing at 650°C also allowed some correlation with previous test results.

Control specimens were held in a laboratory furnace for tne duration of the irradiation and are being tested to help determine the role of thermal aging in producing these effects. Also important is the metallographic examination of both the irradiated and control specimens; this, too, is proceeding and will be reported.

Cyclotron Injection of Helium to Simulate Fast-Reactor Irradiation

Calculation of Displacement Damage Produced by Light Ions (R. T. King)

In order to compare the effects of experiments involving displacement damage by ion bombardment with neutron irradiations, a measure for the amount of damage introduced by a bombardment is needed. At this stage of our work, we are using the total number of displaced atoms produced and have computed the rate at which atoms are displaced by α-particles and protons of energy, E, as they slow down in metals.

The calculations are based on the formula

$$N(\overline{E}) = \frac{1}{\Omega} \int_{E_1}^{E_2} \frac{\sigma_d(E)}{dE/dX} \cdot E \ , \qquad (1)$$

where $N(\overline{E})$ is the total number of displacements produced by a particle slowing from energy E_1 to E_2, dE/dX is taken from Janni's tabulated values,[3] $\sigma_d(E)$ is the total elastic scattering cross section based on Kinchin and Pease's assumptions,[4] and Ω is the atomic volume. We use the range-energy tables of Janni to convert these results to the number of displacements per atom.

The results of these calculations are presented in Figs. 8.9 to 8.12 for the target metals Al, Cu, type 304 stainless steel, and Mo. For these calculations, we assumed the energy required to displace an atom to be 25 ev.

These results indicate that rates of damage production up to 10^5 times higher than those possible in existing reactors may be obtained by using existing particle accelerators. We are using this information to design experiments to assist in more rapid development and confirmation of theories for growth of voids in neutron-irradiated materials than present techniques of neutron irradiation allow. Specimens can be

---

[3] J. F. Janni, Calculations of Energy Loss, Range, Path Length, Straggling, Multiple Scattering, and the Probability for Inelastic Nuclear Collisions for 0.1 to 1000 Mev Protons, AFWL-TR-65-150 (Sept. 1966).

[4] G. H. Kinchin and R. S. Pease, Rept. Progr. Phys. 18, 1–55 (1955).

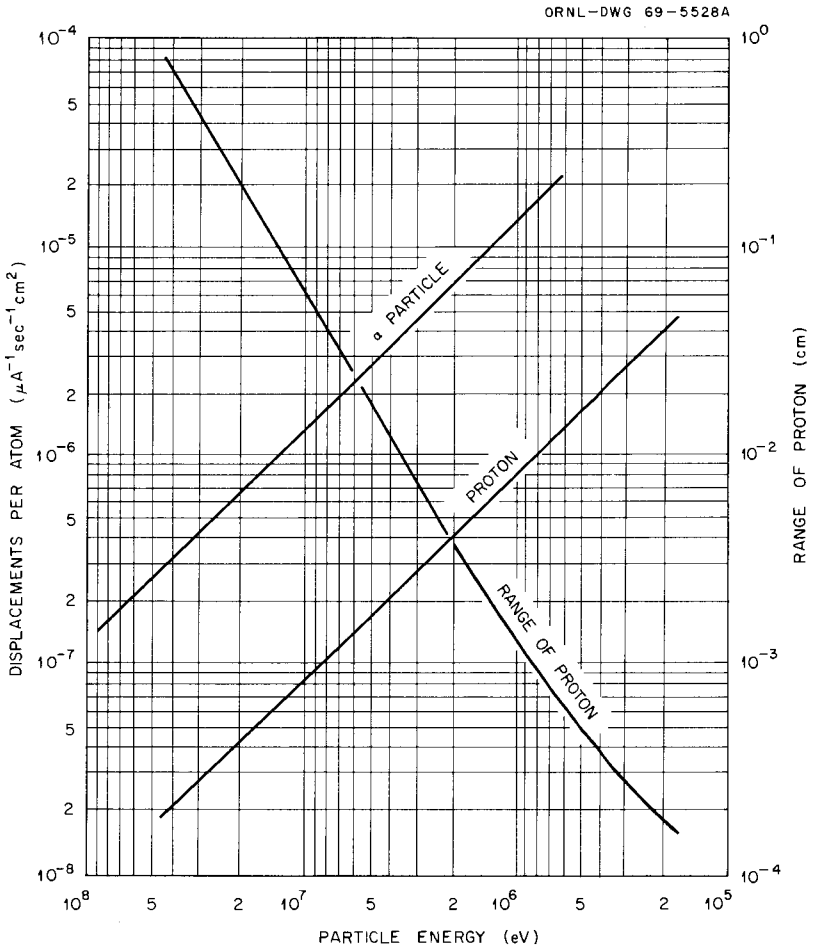

Fig. 8.9. Rates at Which Displacement Damage is Produced and Proton Range in Aluminum.

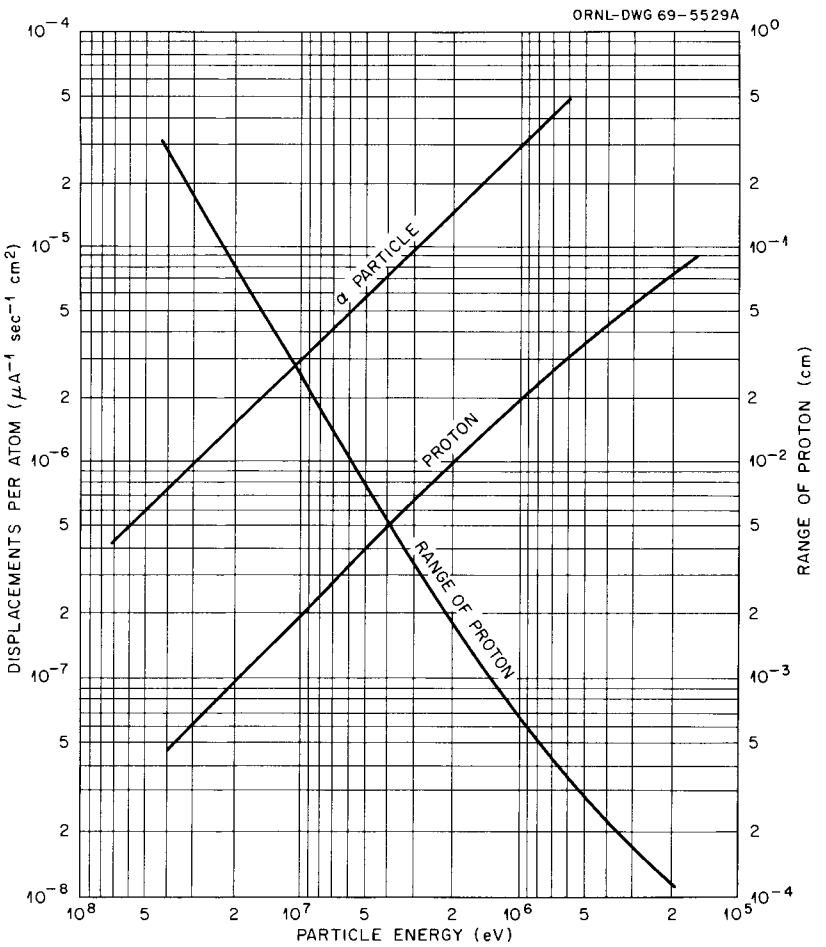

Fig. 8.10. Rates at Which Displacement Damage is Produced and Proton Range in Copper.

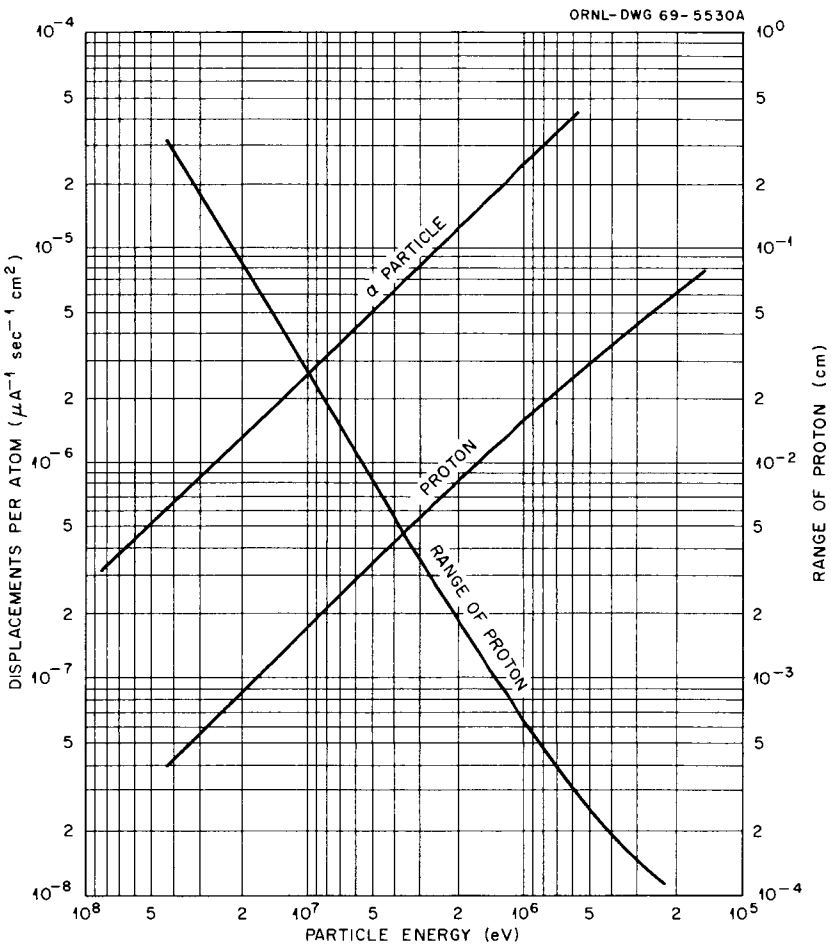

Fig. 8.11. Rates at Which Displacement Damage is Produced and Proton Range in Type 304 Stainless Steel.

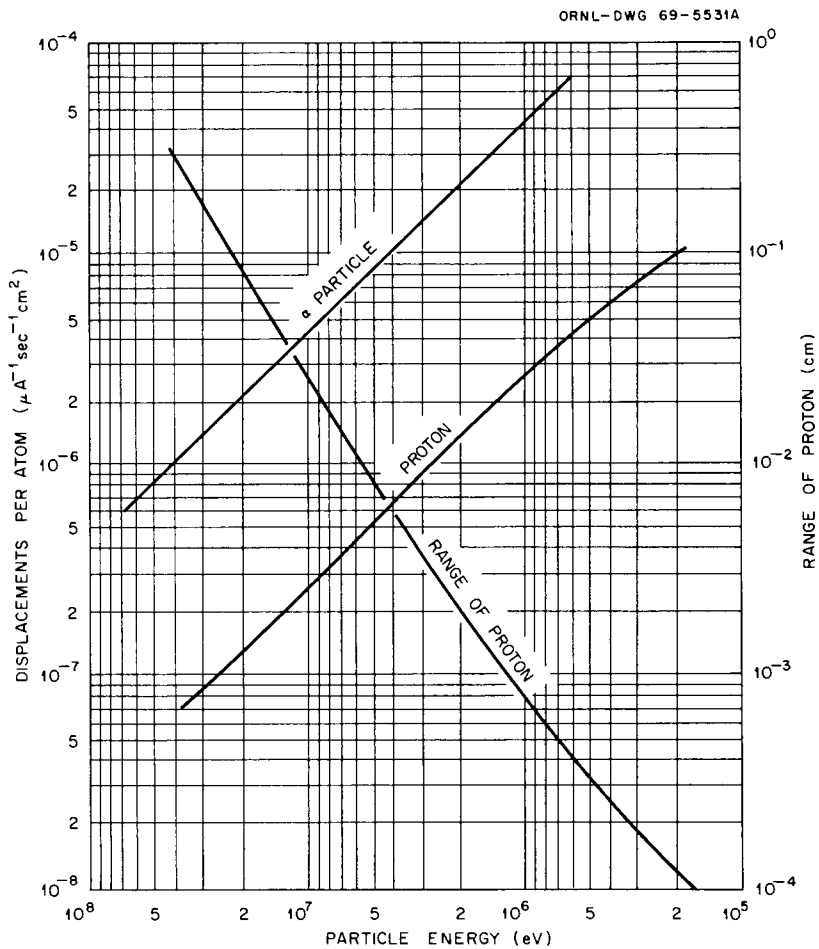

Fig. 8.12. Rates at Which Displacement Damage is Produced and Proton Range in Molybdenum.

prepared cheaply and tested with relative ease since they are not highly radioactive.

However, neutron-irradiation conditions cannot be exactly simulated in such experiments. The gases produced by transmutation — He and H_2 — cannot be simultaneously injected into a region in which displacement damage is being produced at a constant rate. Furthermore, the spectrum of energies transferred in a primary knock-on event and the resultant displacement-cascade structures produced by ions are probably not identical to those produced during neutron irradiation. We believe, nevertheless, that experiments with ion bombardment are an important supplement to studies of damage by neutron irradiation.

Utilization of EBR-II

Examination of EBR-II Safety-Rod Thimble (E. E. Bloom, J. O. Stiegler)

Flat C of the Experimental Breeder Reactor-II (EBR-II) safety-rod thimble is being evaluated. The total evaluation will include measurements of immersion density, electron microscopy, creep-rupture tests, and dilatometer measurements.

Argonne National Laboratory (ANL) reported[5] that this flat had a driver-fuel subassembly in the adjacent grid position 100% of the time that the thimble was in the reactor. The irradiation temperatures at the bottom of the core, top of the core, and 6 in. above the top of the core were estimated to be 370, 427, and 462°C, respectively. We estimated the temperature distribution along the length of the flat from these. We estimated values for fast-neutron fluence by assuming the total fluence at the geometric midplane of the core to be 7.5×10^{22} neutrons/cm^2. This number was obtained by dividing the total value[5] of 9×10^{22} neutrons/cm^2 by 1.2 to correct for the discrepancy between the calculated and measured neutron fluence. We obtained the

[5] J. P. Bacca, R. V. Strain, C. L. Meyers, and S. T. Zegler, Argonne National Laboratory Reactor Development Program Progress Report, ANL-7548 (January 1969), pp. 73–75.

neutron energy spectrum as a function of axial position by assuming that the calculations of Henderson et al.[6] for row 2 were applicable.

Immersion density is being determined for 2 × 1.25 × 0.040-in. sections of the flat. (The size of the specimen is dictated by the fact that after the density measurements are completed specimens for tests of the mechanical properties are machined from the blank.) We realize that there are gradients in neutron fluence and irradiation temperature over the length of the specimen. Table 8.4 summarizes the density information now available. We used a standard density of 7.9000 gm/cm^3 for unirradiated stainless steel to calculate density

[6]W. B. Henderson, J. L. Kamphouse, and J. Moteff, EBR-II Spectrum Calculations, GEMP-1008 (Sept. 30, 1968), pp. 91–108.

Table 8.4. Density and Density Changes of Specimens Removed From EBR-II Safety-Rod Thimble

Distance From Reactor Midplane[a] (in.)	Irradiation Temperature (°C)	Fast Neutron Fluence [neutrons/cm^2 (> 0.1 Mev)]	Mean Density of Specimen (gm/cm^3)	Mean Density Decrease[b] (%)
		× 10^{22}		
−10.0	370	3.1	7.8473	0.67
−7.1	374	4.3	7.8245	0.95
−4.4	381	5.8	7.7526	1.87
−1.8	393	6.6	7.6914	2.64
2.0	410	6.5	7.6355	3.35
4.7	421	5.5	7.6638	2.99
7.3	432	4.2	7.7675	1.68
10.0	444	2.9	7.8274	0.92
12.6	455	2.1	7.8485	0.65

[a]Negative values mean below reactor midplane; positive values mean above reactor midplane.

[b]Based on unirradiated density of 7.9000 gm/cm^3.

changes. This value agrees with the density of a sample from a thimble from an unirradiated control rod supplied by ANL. The largest density decrease observed, 3.35%, occurred in a specimen removed from 2.0 in. above the core midplane. The distance from the core midplane given in Table 8.5 refers to the distance from the geometric midplane of the core to the center of the blank used for the density measurement.

After the density measurements are completed, two 0.187 × 0.750 × 0.040-in. specimens are machined from each blank for tests of mechanical properties. A facility was constructed for welding support pads to the shoulders of the test specimens. Specimens in the first set were machined and welded, and their creep-rupture properties are being tested at 600°C.

Listed below is the chemical analysis of control specimens machined from an unirradiated thimble supplied by ANL and presumably from the same heat as the irradiated thimble:

Element	Content, wt %
C	0.046
Cr	19.0
Ni	9.6
Mn	1.2
Si	0.6
P	0.012
S	0.013
N	0.0035
B	0.00002
Fe	Bal

Results of creep-rupture tests completed to date are listed in Table 6

Table 8.5. Creep-Rupture Properties of Unirradiated Thimble at 600°C

Stress (psi)	Rupture Life (hr)	Minimum Creep Rate (%/hr)	Total Elongation (%)
$\times 10^3$			
45	2.8	3.7	31
40	8.4	1.7	22
35	31.6		
30	86.5	0.16	38

Vanadium Alloy Studies and Effects of Impurities

Voids in Vanadium Irradiated in EBR-II (F. W. Wiffen, J. O. Stiegler)

We examined segments of a fuel cladding tube of unalloyed V that had been irradiated in EBR-II to a peak fluence of 1.7×10^{22} neutrons/cm^2 at a temperature near 630°C. Details of the microstructure, particularly of the void distribution, in the irradiated and irradiated-and-annealed material were reported.[7,8] We measured the Knoop microhardness of this material at room temperature to evaluate the effect of the microstructure produced by irradiation on the mechanical properties. The results of hardness impressions on a plane perpendicular to the tube axis of polished specimens, given in Fig. 8.13, show the dependence of hardness

[7]F. W. Wiffen and J. O. Stiegler, Fuels and Materials Development Program Quart. Progr. Rept. June 30, 1968, ORNL-4330, pp. 195–197.

[8]F. W. Wiffen and J. O. Stiegler, Fuels and Materials Development Program Quart. Progr. Rept. March 31, 1969, ORNL-4420, pp. 151–157.

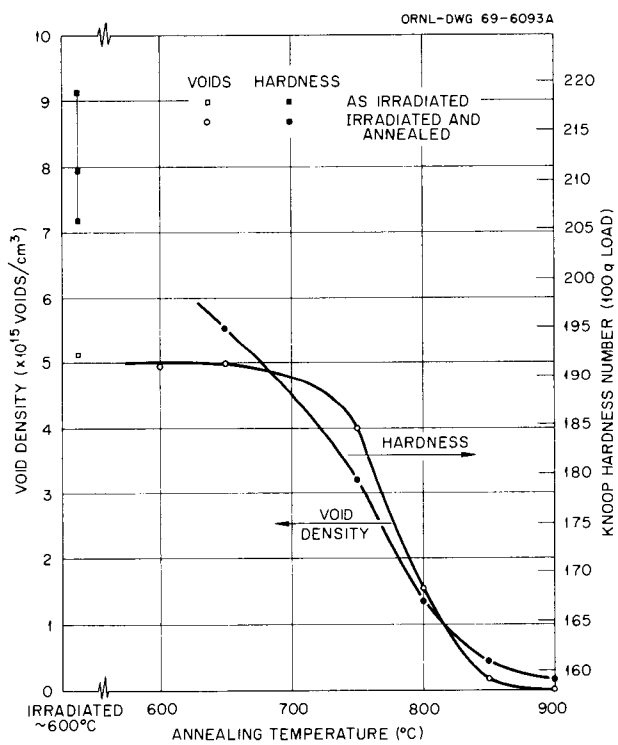

Fig. 8.13. Void Density and Knoop Microhardness of Unalloyed Vanadium as a Function of Postirradiation Annealing for 1 hr at the Temperature Indicated. Irradiated at About 630°C in row 4 of the Experimental Breeder Reactor-II to an approximate total fluence of 1.7×10^{22} neutrons/cm^2.

on the annealing after irradiation. Each datum point shown is the average of five impressions made on a radial traverse between the outer and inner surfaces of the tube. The hardness of the unirradiated control material, not shown on Fig. 8.13, was 170. The increase in hardness as a result of irradiation is much greater than the value reported by United Nuclear Corporation in their examination of the same material.

Annealing 1 hr at 650°C reduced the hardness to well below the value after irradiation without appreciably reducing the void density. This reduction is associated with changes in the configuration of interstitial defects on annealing. (The interstitial defect structure will be discussed in a later progress report.) Above 650°C, the reduction in hardness and the reduction in void density show similar behavior with increasing annealing temperature, suggesting that the hardening produced by these irradiation conditions is nearly equally divided between components due to the interstitial defect structure and the vacancy defect structure (voids).

Microstructure of V–20% Ti Irradiated in EBR-II. – A fuel cladding tube of V–20% Ti was irradiated in the same experiment and under conditions identical to those for the unalloyed V discussed above. The calculated maximum temperature of the cladding was 630°C and the maximum fluence 1.7×10^{22} neutrons/cm^2 during the 2950 hr it was at power in row 4 of the EBR-II (ref. 9). Transmission electron microscopy of segments of this tubing showed the alloy to be free of voids, in direct contrast to the results of examination of the unalloyed V. The matrix of the V–20% Ti was not only free of voids but also did not show any other type of conventional displacement damage – no "black spot" or loop type of damage. The matrix of all of the V–20% Ti tubing segments examined did contain a high density of dislocations, as shown in Fig. 8.14. This dislocation structure was not present in the unirradiated control material. However, it is not possible to separate the effect of any

[9]D. Stahl and A. Strasser, Post-Irradiation Examination of High-Density (U,Pu)C Pellet-Fueled EBR-II Rods Irradiated to 30,000 Mwd/T, UNC-5198 (Jan. 24, 1968).

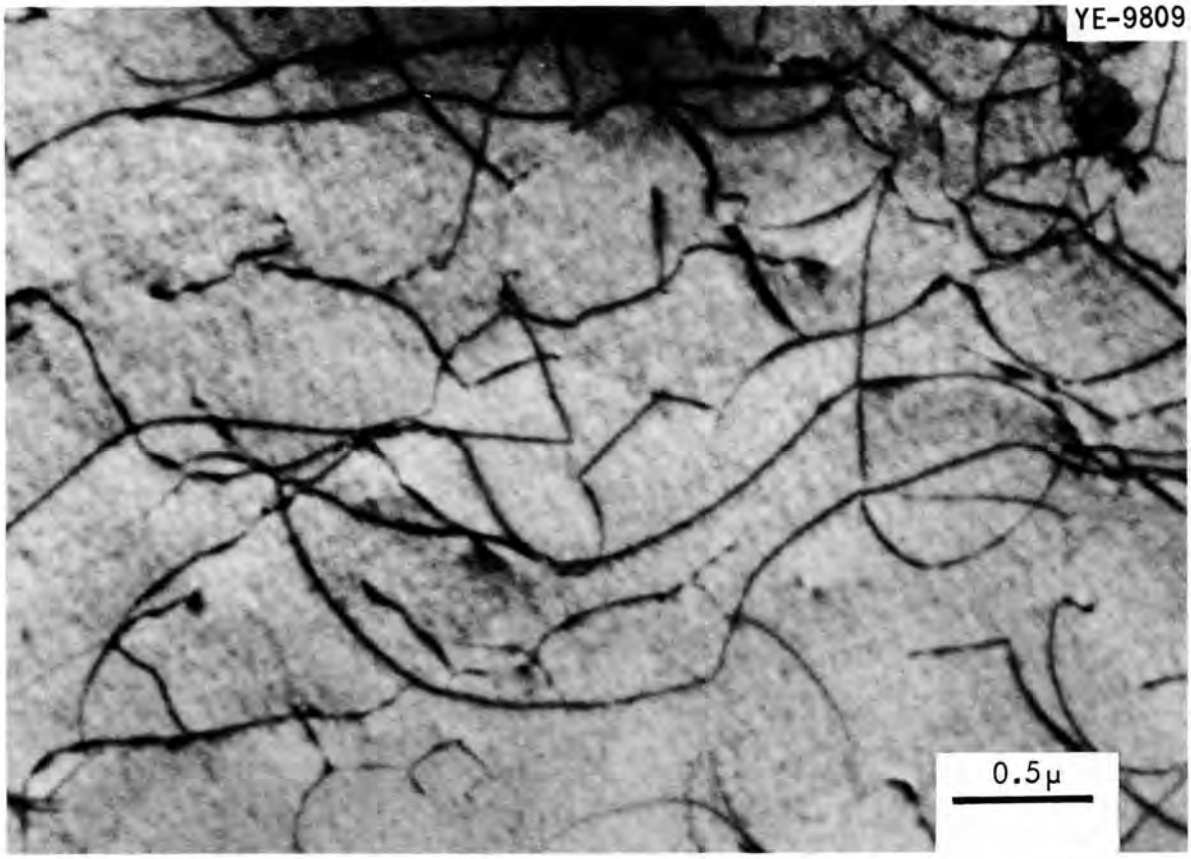

Fig. 8.14. Microstructure of V–20% Ti Irradiated at Near 630°C in Row 4 of Experimental Breeder Reactor-II to Total Fluence of About 1.7×10^{22} neutrons/cm^2.

stresses imposed by swelling of the fuel in the reactor from the effect of irradiation on the production of these dislocations.

Mechanical Properties of Hastelloy N and Related Compositions

Aging of Titanium-Modified Hastelloy N (C. E. Sessions, R. E. Gehlbach, S. W. Cook)

We completed the evaluation of tensile properties at 650°C (0.002 min^{-1} strain rate) of samples aged up to 10,000 hr at 650 and 760°C. The results, as a function of treatment before aging and aging time, and the chemistry of second phases (precipitates) in these aged alloys are discussed below.

Tensile Properties. – The tensile yield strength and total elongation of the various alloys at 650°C are shown in Fig. 8.15 as a function of Ti

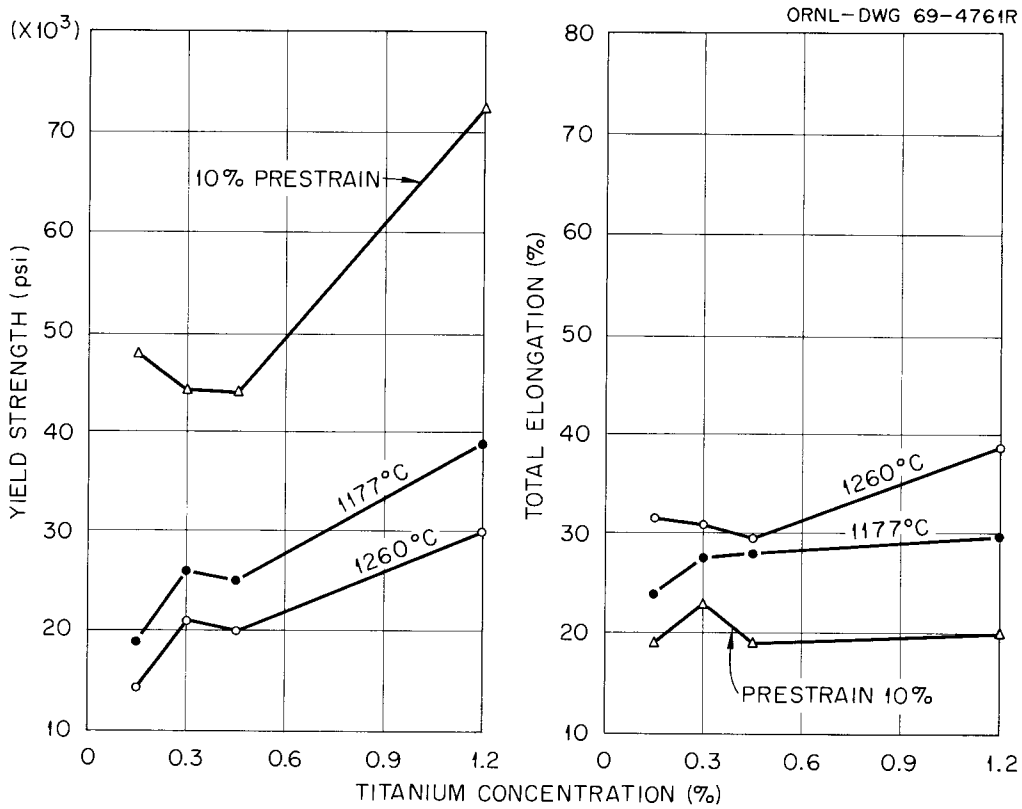

Fig. 8.15. Effect of Titanium Content and Treatments Before Aging on the Strength and Ductility of Modified Hastelloy N at 650°C.

content and heat treatment before aging. The strength increases with increasing Ti, and the ductility does not change significantly with Ti. A solution anneal of 1 hr at 1260°C produces the lowest strengths and highest ductilities.

The effect of aging time on ductility is shown for two different solution anneals in Figs. 8.16 and 8.17. In Fig. 8.16, which shows the results of solution annealing at 1177°C, aging at 650°C reduced the ductility for the heat with low Ti content and increased the ductility for the heats with intermediate and high Ti content. After aging at 760°C and then testing at 650°C, we find greater ductility losses with aging time, except for the heat with 1.2% Ti, which shows no change in total elongation even after 10,000 hr aging at 760°C.

Figure 8.17 shows the effect of a higher solution-annealing temperature of 1260°C on aging. The heats with 0.15 and 1.2% Ti both exhibit a deleterious aging reaction at 650 and 760°C after this solution

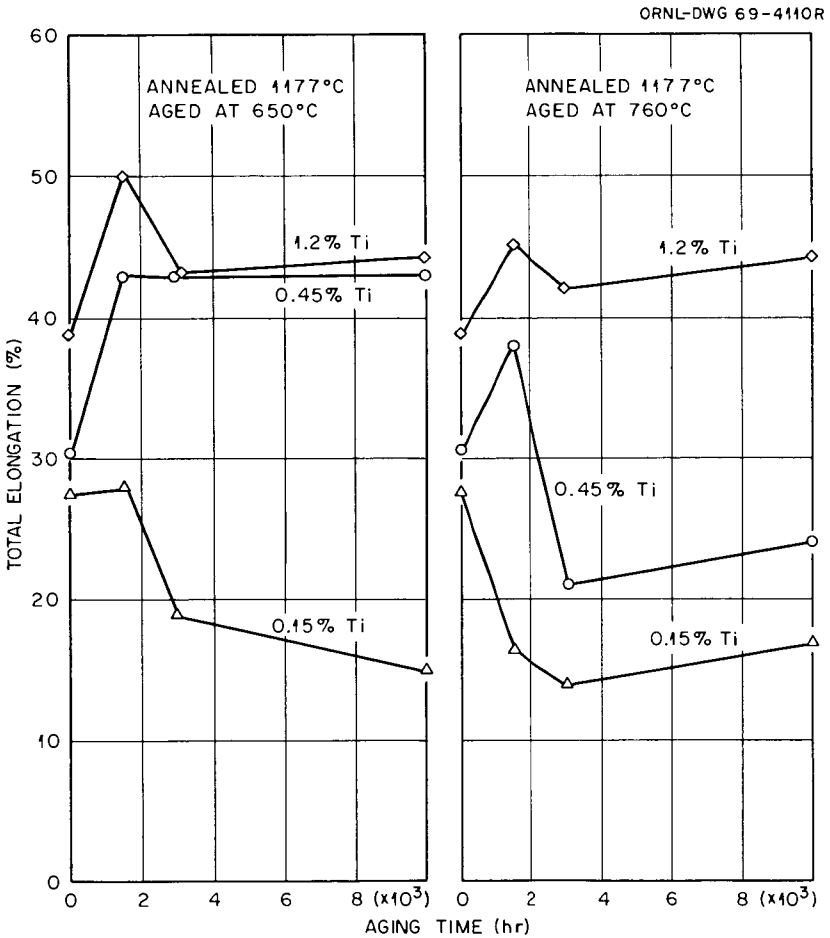

Fig. 8.16. Effect of Titanium Content and Aging Time on the Tensile Ductility of Modified Hastelloy N at 650°C After Solution Annealing for 1 hr at 1177°C.

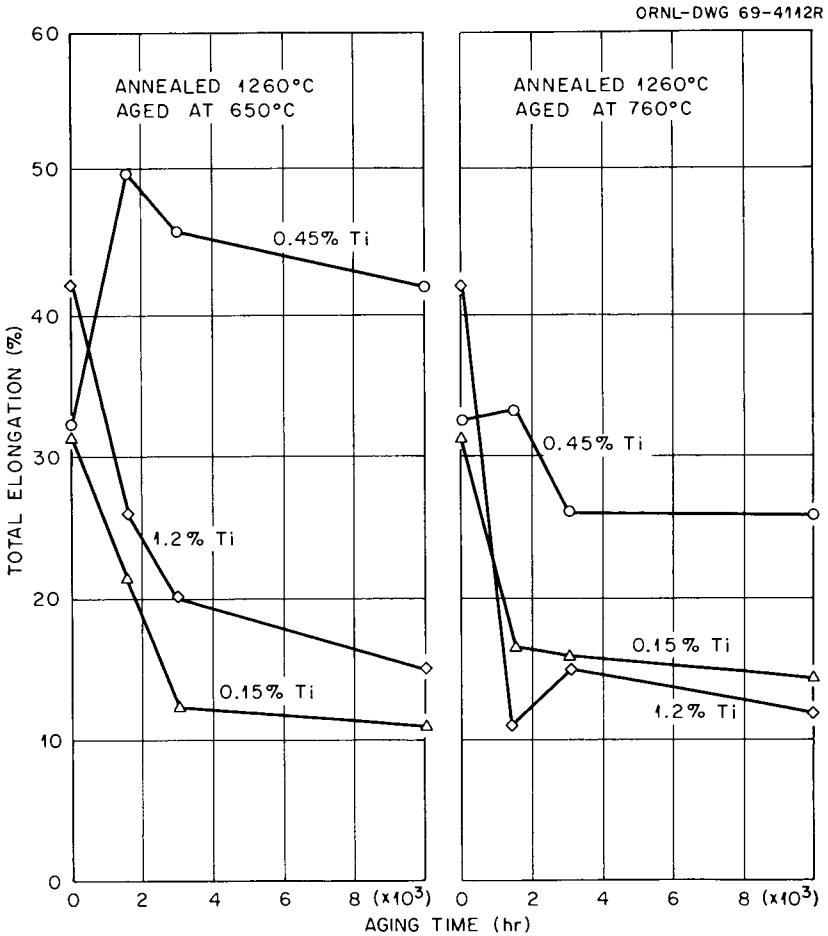

Fig. 8.17. Effect of Titanium Content and Aging Time on the Tensile Ductility of Modified Hastelloy N at 650°C After Solution Annealing for 1 hr at 1260°C.

anneal as indicated by the large drop in tensile ductility with aging time. The heat with 0.45% Ti increased in ductility after aging at 650°C and slightly decreased in ductility after aging at 760°C. The behavior of this heat with intermediate Ti content is virtually identical for the solution anneals at 1177 and 1260°C.

The changes in yield strength with aging time are shown in Fig. 8.18 for the solution anneal for 1 hr at 1260°C. The higher yield strength both before and after aging corresponds to the 1.2% Ti level. The lowest strength found, however, was for the heat with 0.45% Ti, which is undoubtedly a reflection of the slightly lower C content for this particular heat,[10] 0.06% C as opposed to 0.09% C for the other heats.

[10] R. E. Gehlbach and S. W. Cook, Fuels and Materials Development Program Quart. Progr. Rept. March 31, 1969, ORNL-4420, pp. 162–168.

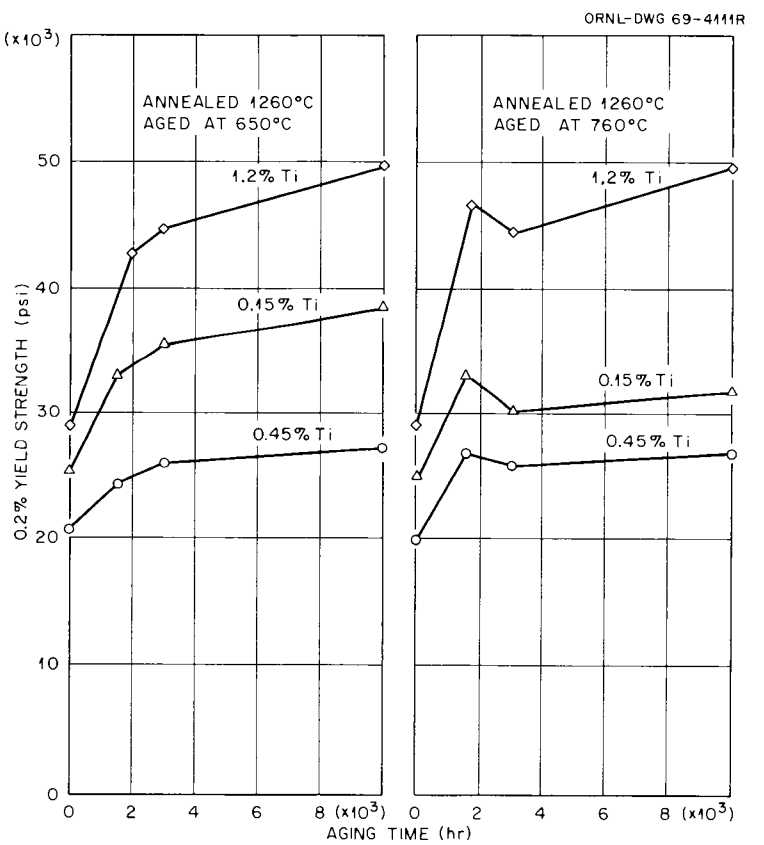

Fig. 8.18. Effect of Titanium Content and Aging Time on the Yield Stress of Modified Hastelloy N at 650°C After Solution Annealing for 1 hr at 1260°C.

The change in strength with aging time (Fig. 8.18) indicates that very little strengthening occurs after 3000 hr of aging. The aging temperature affects the yield strength of only the heat with 0.15% Ti, since the other heats have equivalent properties after 650 and 760°C aging.

Straining 10% at room temperature before aging reduced the ductility at high temperatures both before and after aging. Straining before aging increased the rate of ductility loss primarily for the lower Ti level after aging at 650°C. However, the trends with aging time and Ti content are similar to the results for the solution anneals at 1177°C (Fig. 8.17) except that the overall level of the ductility values is lower for the samples strained before aging.

Composition of Precipitates. — The effect of the elements Ti, Nb, Hf, and Zr on changing the type and morphology of precipitates in modified Hastelloy N was discussed previously.[10] The alloys containing Ti as the only addition precipitate an MC carbide based on the Mo-Cr-C system[11] (rather than TiC) when aged at suitable temperatures. We have not detected TiC in any of the alloys, which contain up to 1.2% Ti. In addition to analysis of individual precipitates on extraction replicas by an electron microscope-microprobe we have attempted to determine the chemistry of extracted second phases by spark-emission spectrophotometry. This technique is not often used in phase analysis, but we tried it in order to define the function of Ti in inhibiting aging and reducing the irradiation damage of Hastelloy N.

We extracted second-phase precipitates from selected samples containing either MC or M_2C carbides after aging. The milligram quantities of precipitate were then analyzed quantitatively for Mo, Cr, Ti, Si, and Ni by spectrographic techniques.

The metallic composition (nomalized to 100%) of Mo, Cr, and Ti is reported in Fig. 8.19 as a function of the Ti content of the alloy from

---

[11]Yu. B. Kuz'ma and T. F. Fedarov, Soviet Powder Metallurgy and Metal Ceramics 1(25), 920–922 (1965); translated from Porosh. Met. Mater. Konf. Riga, 11(35) 62–65 (1965).

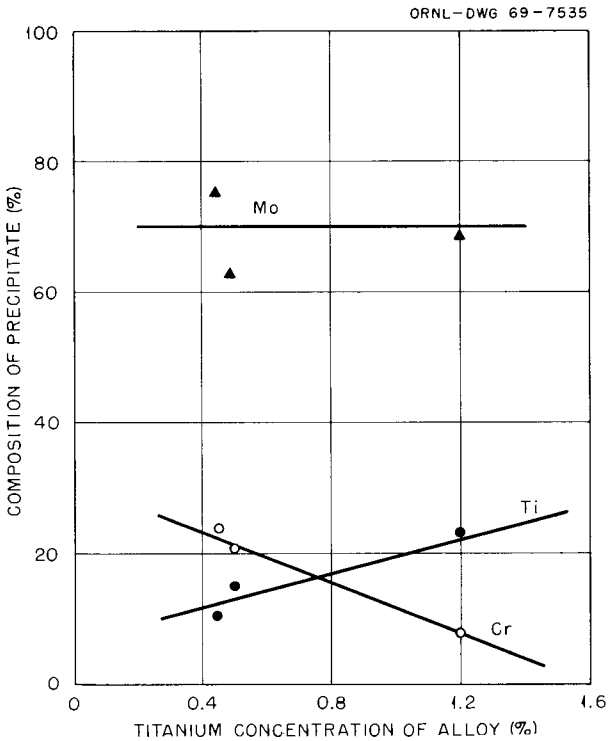

Fig. 8.19. Spectrographic Analyses of Precipitates Extracted from Aged Alloys.

which the precipitate was extracted. We interpret the results to show an increase in the Ti content of the MC phase and a decrease in Cr content with increasing Ti in the alloy. The Mo change in the MC phase is not clear, but we would expect it to change only slightly, while Ti is substituting primarily for Cr in the precipitate. The replacement of Cr by Ti is expected in view of the increasing Ti content in the alloy and the increase in lattice parameter of the carbides from about 4.21 to 4.28 A, since the atomic diameters of Mo, Cr, and Ti are 2.80, 2.57 and 2.93 A, respectively.

Similar analyses were made of samples that contained primarily M_2C carbides, but in this case we have two discrete lattice parameters (2.92 and 2.98 A, both M_2C) in some samples representing different chemical compositions. The result is that we cannot clearly define an effect of the Ti content of the alloy on the amount of Cr present in the M_2C carbide from the results we have. We do know, however, that Ti changes both the chemistry and stability of the MC phase and may have no direct influence on the M_2C carbide.

PART IV

TECHNIQUES OF FABRICATION AND TESTING

9. TUNGSTEN METALLURGY

A. C. Schaffhauser P. Patriarca

The object of this program is to develop economical methods for producing high-quality W and W-alloy tubing with good creep-rupture properties at high temperatures, good microstructural stability, good ductility at low temperatures, and good weldability. We fabricate tubing both by modification of conventional techniques based on extrusion, tube reduction, and warm drawing and by direct chemical vapor deposition (CVD) through the H_2 reduction of heavy-metal halides. Our program includes complete physical and metallurgical evaluation of both fabrication processes.

Primary and Secondary Working of Tungsten Alloys

W. R. Martin

Mechanical Properties of Extruded Tungsten Tubing (A. C. Schaffhauser, R. E. McDonald)

We are determining the mechanical properties of extruded W tubing to aid in the selection of extrusion conditions and annealing schedules to produce optimum mechanical properties for use of the tubing as extruded or for drawing operations. We investigated the possibility of using ring specimens[1] to test the tensile properties of tubing by applying an approximately tangential load at two places on the circumference of the rings, as shown in Fig. 9.1. The ultimate strength and the travel of the Instron crosshead from the time the load was applied to fracture are easily determined ways of measuring strength and ductility. In addition, the reduction in area is measured at the fracture and on the opposite side of the specimen in the necked region that did not fracture.

---

[1]J. E. Cunningham, Severe Radiation Damage to Aluminum Alloys, ORNL-TM-2138 (March 1968), pp. 20–27.

ORNL-DWG 69-7605

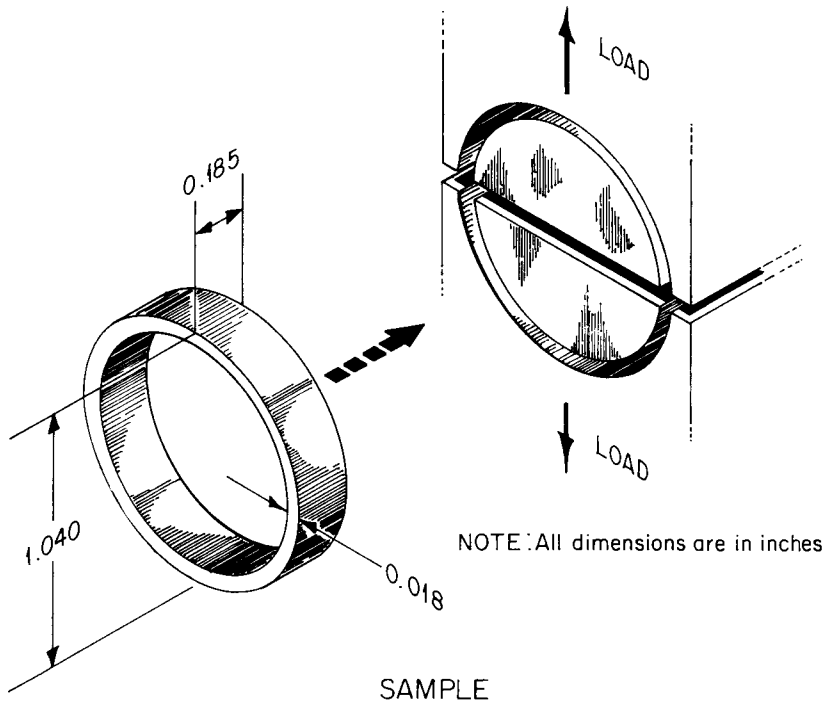

Fig. 9.1. Method for Tensile Testing Rings Cut from Extruded Tungsten Tubing.

As previously described, the ring specimens used in these tests were cut from duplex tube-shell extrusions of W produced by powder-metallurgy techniques.[2] The preliminary data from these tests are given in Table 9.1. The first two tests showed large elongations at 300 and 400°C, but there was less reduction in area at the lower test temperature. In the following tests at 300°C, we investigated the effects of crosshead speeds between 0.02 and 2.0 min^{-1}, which are equivalent to initial strain rates of 0.2 and 20 min^{-1} based on an approximate gage length of 0.1 in. Both the elongation and reduction in area were lower at the higher crosshead speeds, but the specimens still fractured ductilely.

---

[2]R. E. McDonald, Fuels and Materials Development Program Quart. Progr. Rept. Dec. 31, 1968, ORNL-4390, p. 159.

Table 9.1. Comparison of Tensile Data on Ring Specimens Cut from Extruded Tungsten Tubing

Variables			Properties			
Temperature, °C		Crosshead Speed (min^{-1})	Ultimate Stress (psi)	Elongation (in.)	Reduction in Area[a] (%)	
Extrusion	Test				Unfractured	Fractured
1750	400	0.02	67,200	0.184	44	47
1750	300	0.02	71,100	0.194	22	26
1650	300	0.02	76,600	0.143	30	43
1650	300	0.2	78,500	0.142	22	26
1650	300	2.0	87,400	0.058	25	28
1750	300	0.02	71,100	0.194	22	26
1650	300	0.02	76,600	0.143	30	43
1250	300	0.02	75,500	0.209	35	49

[a]The reduction in area was measured on both sides of the ring specimens. The first number listed is the reduction on the side that did not fracture, and the second number is the reduction at the fracture.

A comparison of the properties of tubing extruded at different temperatures (Table 9.1) showed that the material extruded at 1250°C had the greatest elongation and reduction in area. As reported previously,[2] the tubing extruded at 1250°C had a partially recrystallized grain structure with an ASTM grain size of 8, which must account for its better ductility. There is no apparent reason for the lower elongation of the tubing extruded at 1650°C compared to that extruded at 1750°C, since both materials had an ASTM grain size between 6 and 7.

Since these preliminary tests appeared to give useful results in comparing the properties of the extrusions, other tests covering a wider range of test temperatures and specimen conditions are planned.

Chemical Vapor Deposition of Tungsten Alloys

J. I. Federer W. R. Martin

Chemical Vapor Deposition of Tungsten for Tests of Mechanical Properties

Tungsten sheet stock is being prepared for bend, tensile, and creep-rupture testing. Five W deposits were prepared by H_2 reduction of WF_6 on resistance-heated Mo–0.5% Ti substrates under the following conditions: 600 to 650°C, 5 torr, 2000 cm^3/min H_2, 200 cm^3/min WF_6, and 24 to 26 hr. The deposition efficiency was about 65%, and the deposition rate was about 0.0035 in./hr. Each deposit provided 55 in.^{2} of sheet stock. About 80% of each deposit was 0.075 in. thick or greater on both sides of the substrate. A maximum of 12 tensile specimens (6 from each side), each 3.5 × 0.75 × 0.060 in., can be obtained from each deposit. The substrate can be dissolved in acid solution at any stage of the process of specimen preparation.

Metallographic examination of the deposits revealed a typically columnar grain structure with a small amount of grown-in porosity in a few areas. Preliminary chemical analyses showed 5 to 10 ppm F. The deposits were stress relieved at 1200°C for 2 hr at 1×10^{-6} torr.

About 90% of the specimens for the tensile tests were machined.

Chemical Vapor Deposition of Tungsten-Rhenium Alloys

The development of a deposition technique for W–5% Re alloy sheet has continued. Alloy deposits are being prepared by H_2 reduction of WF_6 and ReF_6 on Mo–0.5% Ti substrates heated by resistance. The major problems encountered in producing large quantities of this material for determination of mechanical properties are nonuniform thickness, the formation of nodules, and porosity. Thickness variations along the length of the deposits also result in Re gradients in these resistance-heated sheets because the thicker regions are cooler and become richer in Re (ref. 3).

---

[3]J. I. Federer, Fuels and Materials Development Program Quart. Progr. Rept. Dec. 31, 1968, ORNL-4390, pp. 162–165.

Thickness gradients in the deposits are primarily a result of gas depletion along the length of the substrate. Several methods for overcoming gas depletion are being investigated: higher pressures, increased flow rates, pulsed gas flow, and periodic reversal of the gas flow. We previously showed that for deposition pressures between 10 and 200 torr the most uniformly thick deposits were produced at about 50 torr (ref. 4). However, analysis of these deposits for Re (Table 9.2) shows that at pressures higher than 10 torr Re deposition was suppressed. Thermodynamic calculations indicate that the suppression of Re deposition by high pressure could be overcome by using higher temperatures, but this has not been tried.

---

[4]J. I. Federer, Fuels and Materials Development Program Quart. Progr. Rept. March 31, 1969, ORNL-4420, pp. 177–183.

Table 9.2. Effect of Deposition Pressure on the Composition of Tungsten-Rhenium Alloys Deposited at 750°C

Distance from Gas Inlet (in.)	Deposition Pressure (torr)	Rhenium Content (%)
2	10	4.0
	50	2.2
	75	< 0.5
	100	< 0.3
	200	< 0.3
7	10	4.1
	50	1.0
	75	< 0.5
	100	< 0.3
	200	< 0.3
12	10	3.5
	50	1.6
	75	< 0.5
	100	< 0.3
	200	< 0.3

We also performed experiments using higher flow rates in an attempt to overcome gas depletion. In these experiments, the flow rates were successively doubled, and the system pressure was the lowest attainable. However, this technique was not successful for deposits prepared at 750°C, as shown in Table 9.3. The efficiency of deposition decreased with increasing flow rate, as expected, but each deposit was thicker on the end nearest the gas inlet.

Table 9.3. Effect of Flow Rate on Deposition Efficiency and Uniformity of Deposit Thickness at 750°C

Pressure (torr)	Flow Rate (cm^3/min)			Efficiency (%)	Thickness (in.)		
	H_2	WF_6	ReF_6		Inlet	Middle	Outlet
10	2000	190	10	75	0.027	0.010	0.007
15	4000	380	20	67	0.050	0.029	0.018
40	8000	760	40	50	0.069	0.047	0.024

We previously showed that periodic reversal of the gas flow during deposition reduced the thickness variations but resulted in some grown-in porosity in the deposits.[5] In our most recent experiments, we have attempted to refine this technique to eliminate the formation of nodules and porosity and to produce uniform thickness. The cause of the formation of nodules and porosity is not known; however, it usually occurs only after the deposit is a few thousandths of an inch thick. We reasoned that the conditions that cause these defects might be avoided by periodically interrupting deposition before the deposit reached that thickness. There appeared to be less formation of nodules in the previous deposits where the gas flow was interrupted and reversed every 30 min to obtain uniform thickness. A more rapid method of pulsing the

[5]A. C. Schaffhauser, Fuels and Materials Development Program Quart. Progr. Rept. Dec. 31, 1968, ORNL-4390, p. 168.

gas flow was devised for the present experiments by pulsing the WF_6 and ReF_6 gas flow with automatically actuated solenoid valves.

Table 9.4 shows the conditions and results of these experiments. The deposit prepared with the gas pulsed but not reversed was thicker on the end near the gas inlet and had a rough nodular surface, while the deposit prepared with the gas flow periodically reversed and pulsed was more uniform in thickness and had a smoother surface that contained only a few nodules. Metallographic examination revealed a layered grain structure in both deposits. Both pulsing and reversal of gas flow refined the usual columnar grain structure characteristic of vapor-deposited materials. Both deposits also contained a small amount of grown-in porosity. Except for the porosity, the deposit prepared by periodic reversal of the gas flow appeared to be satisfactory. Further experiments are in progress to minimize grown-in porosity; we are now trying even more frequent pulsing of the flows of WF_6 and ReF_6.

Table 9.4. Results of Deposition Experiments[a] in Which the Flow of WF_6 and ReF_6 Was Pulsed

Reversal of Flow Direction	Distance from Inlet End (in.)	Thickness (in.)	Rhenium Content (%)
No	1	0.047	5.5
	5	0.037	3.6
	9	0.024	3.5
	13	0.018	3.8
Yes	1	0.056	3.4
	5	0.045	3.7
	9	0.045	3.6
	13	0.052	3.5

[a]Temperature: 750°C

Pressure: 15 torr

Pulse of gas flow: 15 min on, 2 min off

Chemical Vapor Deposition of Vanadium

Vanadium and its alloys are potential materials for fuel cladding for liquid-metal fast breeder reactors. Chemical vapor deposition is being studied as a potential method for fabricating V tubing and cladding. In our initial experiments, VCl_3 powder was transferred to a heated C substrate by entrainment in an Ar stream, where it was reduced to metal by H_2. Coatings 0.001 to 0.005 in. thick were obtained at 1000, 1100, and 1200°C; deposition below 1000°C appeared impossible.

We later used VCl_4 and VF_5 to avoid the difficulty of metering entrained VCl_3 powder. Vanadium metal was reacted with Cl_2 (400°C) or F (250°C) to form the halides, which were then transferred into a heated stainless steel tube and reduced with H_2 at 1200°C. Coatings having thicknesses of 0.001 to 0.015 in. thick were prepared in this way.

The grain structure of deposits prepared from VCl_4 was coarsely columnar, was strongly oriented toward {110} planes, and contained precipitated particles at the grain boundaries and within grains, as shown in Fig. 9.2(a). Deposits prepared from VF_5, also coarsely columnar, contained a more massive second phase at the grain boundaries and within grains [Fig. 9.2(b)]. The deposits contained about 12,000 ppm total interstitial impurities, mostly O and N, which were probably derived from the reactant gases.

Continuing work will concentrate on improving the purity of the deposits. In addition, deposition of alloys with Cr and Ti will be studied. Those will be characterized in terms of deposition rate and efficiency, purity, hardness, orientation, and response to heat treatment.

Long-Time Creep-Rupture Properties of Tungsten Alloys

R. L. Stephenson

We are continuing our comparisons of the creep-rupture properties of arc-melted W, W–5% Re, W–26% Re, and W–25% Re–30% Mo. The stress-rupture data for W–5% Re are shown in Fig. 9.3. A computer program was used to determine the Larson-Miller constant by least-squares fitting.

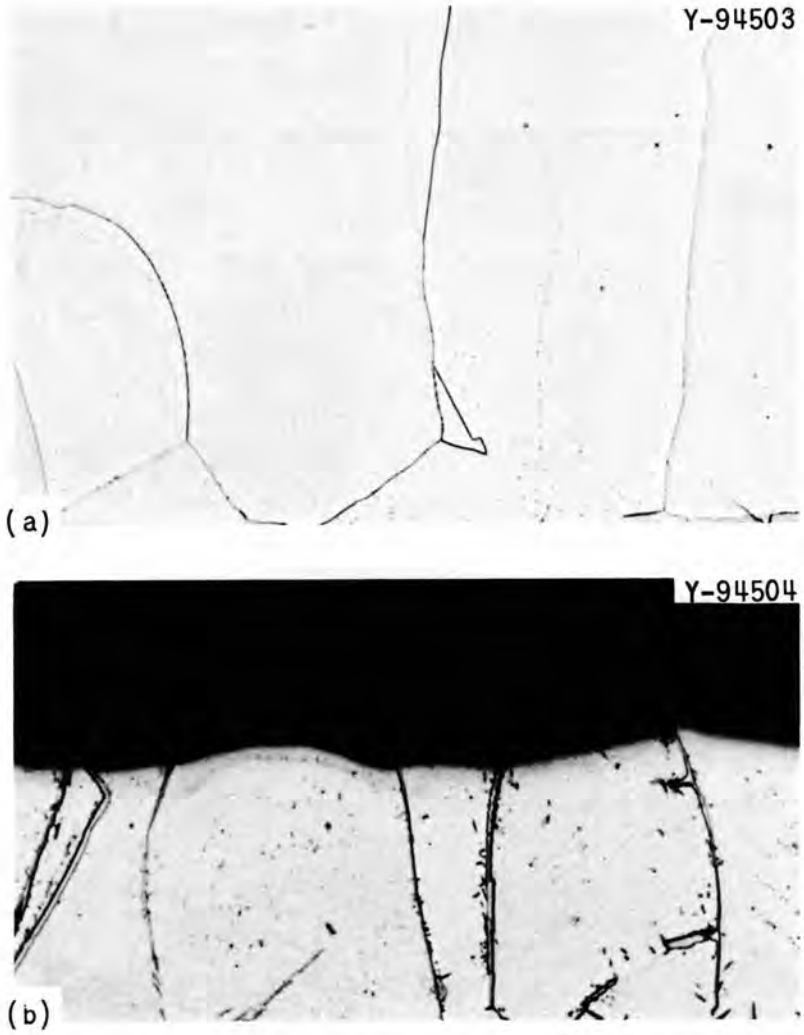

Fig. 9.2. Vanadium Deposited by Hydrogen Reduction of (a) VCl_4 at 1200°C and (b) VF_5 at 1200°C. Etchant: 61 vol % lactic acid, 37 vol % nitric acid, 2 vol % hydrofluoric acid. 300×.

The master curve thus obtained was used in drawing the isotherms shown. The computed curves seem to be in good agreement with the experimental data. This alloy is stronger than unalloyed W at short times and low temperatures.

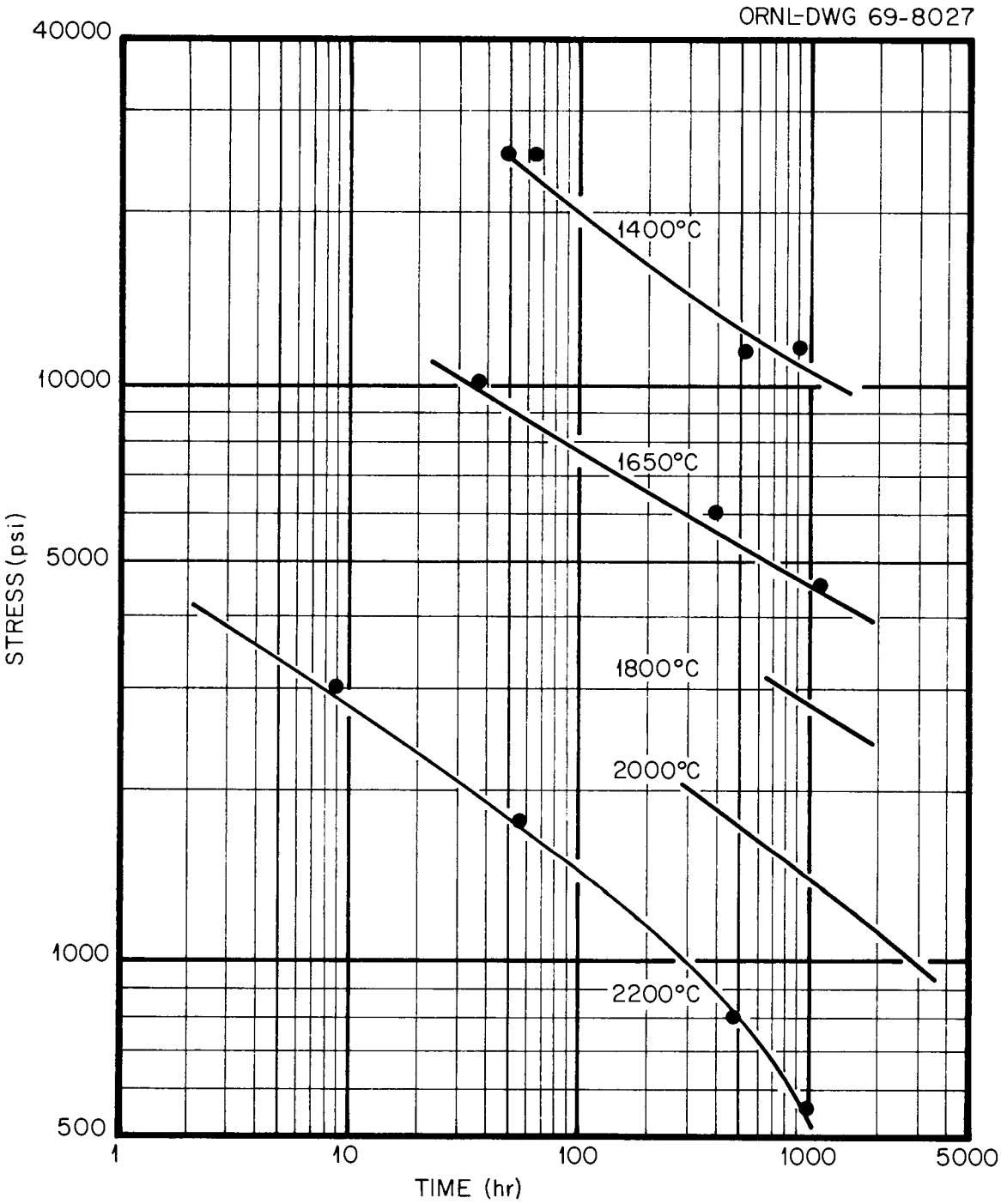

Fig. 9.3. Stress-Rupture Data for W–5% Re.

10. NONDESTRUCTIVE TEST DEVELOPMENT

W. O. Harms R. W. McClung

Our task is to develop new and improved methods of nondestructively testing reactor materials and components. We are studying various physical phenomena, developing instruments and other equipment, devising techniques, and designing and fabricating reference standards. Among the methods being studied for both normal and remote inspection are electromagnetics (with major emphasis on eddy currents), ultrasonics, penetrating radiation, and holography.

Electromagnetic Inspection Methods (Eddy Currents)

C. V. Dodd J. W. Luquire[1]
W. E. Deeds[1] W. G. Spoeri

We continued research and development on both analytical and empirical bases.

In our analytical research we are continuing to derive integral equations for problems of interest and are using our computer programs to provide numerical solutions directly applicable to actual eddy-current tests.

We are using these numerical solutions to minimize the error due to changes in the spacing between coil and specimen (lift-off) in the phase-sensitive eddy-current instrument. We performed these calculations for both through-transmission and reflection coils, varying the shape of the coil and the operating frequency to determine the effect on measurements.

For through-transmission coils, the lift-off is the sum of the spacing between (1) the driver coil and the conductor (specimen) and (2) the pick-up coil and the conductor. If the two coils are separated by a fixed distance and a constant current is applied to the driver coil, the signal received by the pick-up coil is independent of the location

[1]Consultant from the University of Tennessee.

of the conductor between them. For those coils that can be easily constructed, a lift-off variation of 0.2 times the mean coil radius results in a phase shift that produces a thickness error of about 1.6%. With the discriminator of the instrument adjusted to minimize this, the error is reduced to 0.07%. This error can be further reduced to about 0.007% by using a long driver coil with no inner radius and a very thin pick-up coil, but these coils are difficult if not impossible to construct.

For reflection coils, we calculated the phase shift of a coil above a semi-infinite plane as a function of lift-off and conductivity. Figure 10.1 shows both the variations in phase shift for a ±2.5% change in conductivity and the error caused by a simultaneous lift-off variation

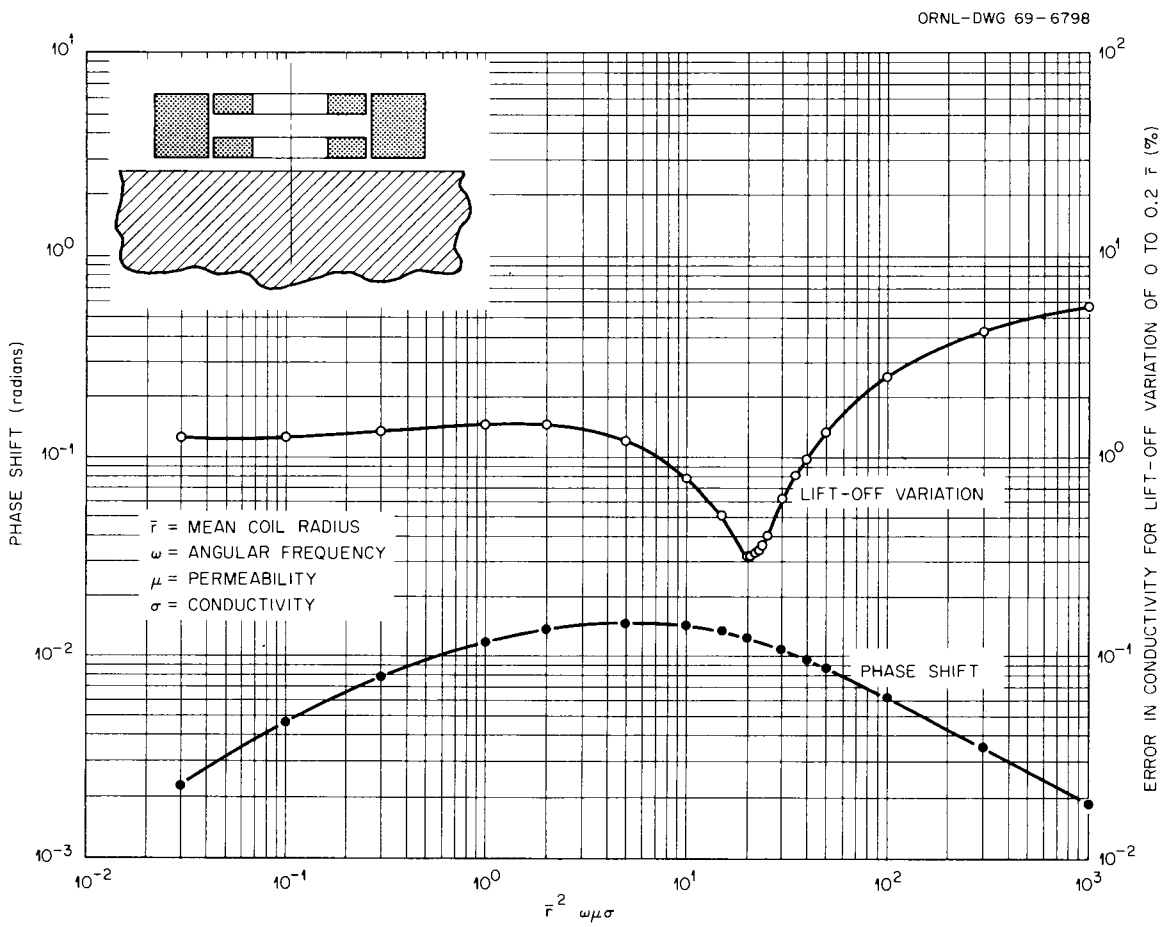

Fig. 10.1. Phase Shift and Lift-Off Error for a Reflection Coil as Functions of $\bar{r}^2\ \omega\ \mu\ \sigma$.

of 0.2 times the mean coil radius as a function of frequency, conductivity, and mean coil radius. The point for maximum phase shift per conductivity change is relatively constant for the coils. The point for minimum error due to lift-off can be shifted by varying the coil dimensions. The conductivity can be measured with the greatest accuracy when these two points coincide.

Although in the past we were able to make accurate measurements of conductivity with the phase-sensitive eddy-current instrument with our somewhat arbitrarily designed coils, these studies indicate that we can improve our accuracy by a factor of 5 to 10.

We are making a series of measurements of impedance to verify some of the theory of defects that we derived, since there are several assumptions and approximations in the theory that need to be tested. We constructed a 6 × 6 × 6-in. box, embedded two identical coils on either side of it, filled it with Hg, and placed a number of "defects" at variable positions in the Hg. We then measured the difference in impedance between the two coils with a General Radio impedance comparator at frequencies of 1000, 400 and 120 Hz. The comparator measures the magnitude and phase of the difference in impedance to an accuracy of ±0.0005% of the impedance magnitude and ±0.005 milliradians.

The defects were various sizes of spheres, a flat disk, and a flat square, all made from a nonconducting material. The agreement on the first measurements was within experimental error for the spheres, but there is a discrepancy for the other two defects. We are reviewing the approximations and trying to obtain a more exact mathematical expression for irregularly shaped defects.

Ultrasonic Inspection Methods

H. L. Whaley K. V. Cook

Optical Visualization of Ultrasound

We are applying the schlieren apparatus to the study of ultrasonic inspection of welds. Our Plexiglas models of butt welds in

plate[2] were of limited use because of poor adhesion in the simulated weld zone. Therefore, we have requested actual welds in 1-in.-thick plates of Al and stainless steel. These welds are being fabricated and will contain intentional gross defects of various types and orientations. We are considering improved methods of recording the data that will be obtained from tests on these samples.

Frequency Analysis

We investigated the effect of the size of the aperture used with collimators (devices fitted to ultrasonic transducers to limit beam size) on the frequency spectrum of an ultrasonic pulse. The spectra of a pulse from the uncollimated transducer and from the same transducer fitted in succession with collimators that had circular apertures of 3/8, 1/8, and 1/16 in. were analyzed. The main energy peak shifted toward lower frequencies, but we traced this to "leakage" (transmission of energy through the wall of the collimator). Such leakage probably occurs often in actual examinations if adequate care is not taken to assure that the walls of the collimator are completely opaque to all frequencies in the spectrum of the pulse. Such unknown leakage can reduce test sensitivity by both the shift in frequency and by enlarging the effective diameter of the beam. We found no direct effect of aperture size on the frequency spectrum, but there probably would be an effect if sufficiently small ratios of aperture size to wavelength were obtained.

A report[3] was prepared that details our recent investigations in frequency analysis; the abstract follows:

> In order to increase our understanding of frequency effects in ultrasonic testing, we have developed a system which can analyze the frequency content of reflected or transmitted ultrasonic pulses. The system is composed of commercially available

---

[2]H. L. Whaley and K. V. Cook, Fuels and Materials Development Program Quart. Progr. Rept. March 31, 1969, ORNL-4420, pp. 192–193.

[3]H. L. Whaley and K. V. Cook, Ultrasonic Frequency Analysis (proposed paper for the 29th National Conference of the American Society for Nondestructive Testing, Oct. 13–15, 1969, Philadelphia); also in preparation as an ORNL technical memorandum.

electronic equipment and can be used with conventional ultrasonic instruments operating in either a contact or immersion mode. We have applied the system to examine the frequency effects of the following ultrasonic test variables: transducer type, instrument type, transducer positioning, tuning devices, and collimation.

A number of brass, Cu and Al rods of various diameters were prepared with flat, polished ends for use in an investigation of the variation in frequency spectrum of a reflected ultrasonic pulse with size and orientation of the reflector. An apparatus is being fabricated that will rotate the rods precisely about a diameter in the plane of the flat end. This will permit spectral analysis as a function of continuous changes in the angle of incidence.

Penetrating Radiation and Holographic Inspection Methods[4]

B. E. Foster S. D. Snyder

Radiation Scattering

We have continued preliminary investigations of the use of Compton backscattered radiation for measuring the thickness of coatings or claddings on reactor components. The initial study involves the use of a 1/2 curie ^{241}Am source and associated shielding with the NaI(Th) crystal-photomultiplier detector. We are evaluating different photomultipliers and crystals (with and without Be windows) for best resolution of the Compton energy. A venetian blind type of photomultiplier with the Be window crystal gives the best resolution. Equipment problems in both the single- and multichannel analyzers have slowed the project, and we have been unable to get quantitative results relating the percentage of change in count rate to a given change in cladding thickness.

---

[4]This work is jointly supported by the Technical Assistance Program and is also reported in the Aluminum Technology Quarterly Progress Report.

11. JOINING RESEARCH ON NUCLEAR MATERIALS

G. M. Adamson, Jr. G. M. Slaughter

The purpose of this program is to gather the fundamental and applied data needed to understand the weldability of materials that are either being considered or are currently used for nuclear applications. Fundamental studies are concerned with the effects of minor constituents on the behavior of weldments. We are especially interested in the austenitic stainless steels and the alloys that are rich in Ni, such as Incoloy 800 and Inconel 600.

Our applied studies emphasize the application of stainless steels in the Fast Flux Test Facility (FFTF). Our investigations will help define the influence of welding process, variables, and heat treatment after welding on the microstructure and mechanical properties of irradiated and unirradiated weldments. In addition, a modest program concerned with the influence of weld defects will provide reference results in this much-talked-about but little-investigated field.

As a result of this broad-based program, we plan to develop modifications in both alloy composition and procedures needed to improve the quality of weldments used in the various activities of the Commission. The work is immediately and directly applicable to such components as the Fast Test Reactor Vessel, since it will provide the data necessary for predicting the effects of chemical composition and welding procedure on overall behavior.

The Effect of Minor Variations in Chemical Composition on Weldability

Our continuing investigation of the effect of minor variations in those elements usually present in small quantities in structural materials has included Incoloy 800, Inconel 600, and stainless steel.

Effect of Minor Elements on the Hot Ductility of Inconel 600
(D. A. Canonico, W. J. Werner)

The 15 Inconel 600 alloys previously discussed[1] were tested for hot ductility. In addition to the usual practice of exposing the alloys to a peak temperature equal to their zero-ductility temperature (ZDT), we also exposed them to a peak temperature of 1345°C, the ZDT of the nominal composition. Table 11.1 summarizes the results of this study. The measured ZDT's for all 15 compositions are listed, as is the ductility at 1260°C on heating and on cooling from the ZDT and, when appropriate, from 1345°C.

An evaluation of the results presented in Table 11.1 shows that S has a deleterious effect on the ZDT and on ductility, both on heating and on cooling. Recovery of ductility is significantly impaired by the presence of more than 0.01% S. Sulfur is particularly detrimental if the alloy is exposed to a peak temperature above its ZDT. In the latter case, ductilities of less than 10% exist at temperatures as low as 1095°C.

Phosphorus had only a minor effect on the ductility, both on heating and on cooling, of the alloys rich in Ni. The recovery of the composition that contained 0.015% P was only slightly impaired. Compositions that contained less P recovered ductility immediately, and the ZDT of alloy 600-7 was slightly increased.

Surprisingly, Mn in an alloy that contained 0.009% S was not beneficial and, indeed, a deleterious effect was indicated. Increasing from 0.15% Mn (alloy 600-4) to 0.84% Mn (alloy 600-14) measurably decreased the ZDT and noticeably reduced the alloy's ability to recover ductility, particularly after exposure to a peak temperature of 1345°C. Addition of P to an alloy containing 0.008% S and 0.80% Mn (alloy 600-15) did not affect the recovery.

---

[1]D. A. Canonico and W. J. Werner, Fuels and Materials Development Program Quart. Progr. Rept. June 30, 1968, ORNL-4330, pp. 307–309.

Table 11.1. Results of Hot-Ductility Tests on High-Nickel Alloys Representing the Inconel 600 Class of Material[a]

Experimental Alloy Number	Amount of Minor Element, wt %			Zero Ductility Temperature (°C)	Ductility at 1260°C, %		
						On Cooling	
	S	P	Mn		On Heating	From Zero Ductility Temperature	From 1345°C
600-1	0.003	0.001	0.007	1345	96	99	99
600-2	0.002	0.002	0.11	1345	87	99	99
600-3	0.006	0.001	0.11	1345	87	94	94
600-4	0.010	0.002	0.15	1345	35	81	81
600-5	0.012	0.002	0.12	1305	37	0	6
600-6	0.002	0.006	0.23	1345	100	100	100
600-7	0.002	0.011	0.20	1370	100	15	91
600-8	0.002	0.015	0.17	1345	100	76	76
600-9	0.003	0.004	0.16	1355	85	88	99
600-10	0.003	0.006	0.17	1355	90	0	81
600-11	0.006	0.008	0.17	1345	76	70	70
600-12	0.009	0.002	0.32	1330	50	55	49
600-13	0.009	0.002	0.48	1330	53	9	9
600-14	0.009	0.002	0.84	1315	53	15	0
600-15	0.008	0.007	0.80	1315	40	8	33

[a]Nominal composition: Ni–15.5% Cr–8% Fe–0.5% Mn–0.25% Si–0.25% Cu–0.08% C–0.008% S.

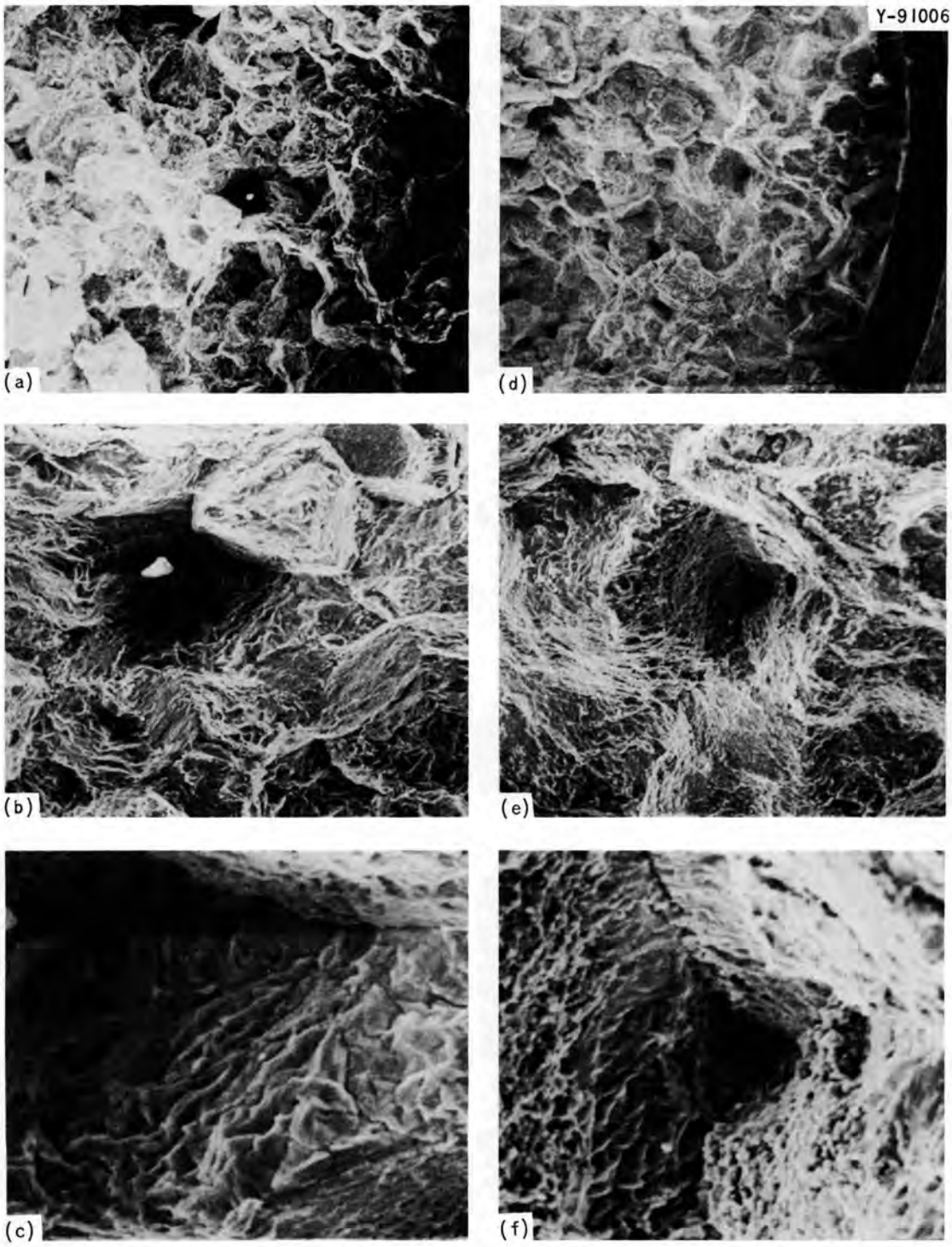

Fig. 11.1. Scanning Electron Photomicrographs of the Actual Fracture Surfaces of Representative Titanium-Free Alloys Tensile Tested at 700°C. Alloy containing sulfur: consecutive photomicrographs of the same field at (a) 100×, (b) 300×, and (c) 1000×. Ternary alloy: consecutive photomicrographs of the same field at (d) 100×, (e) 300×, and (f) 1000×. Reduced 23%.

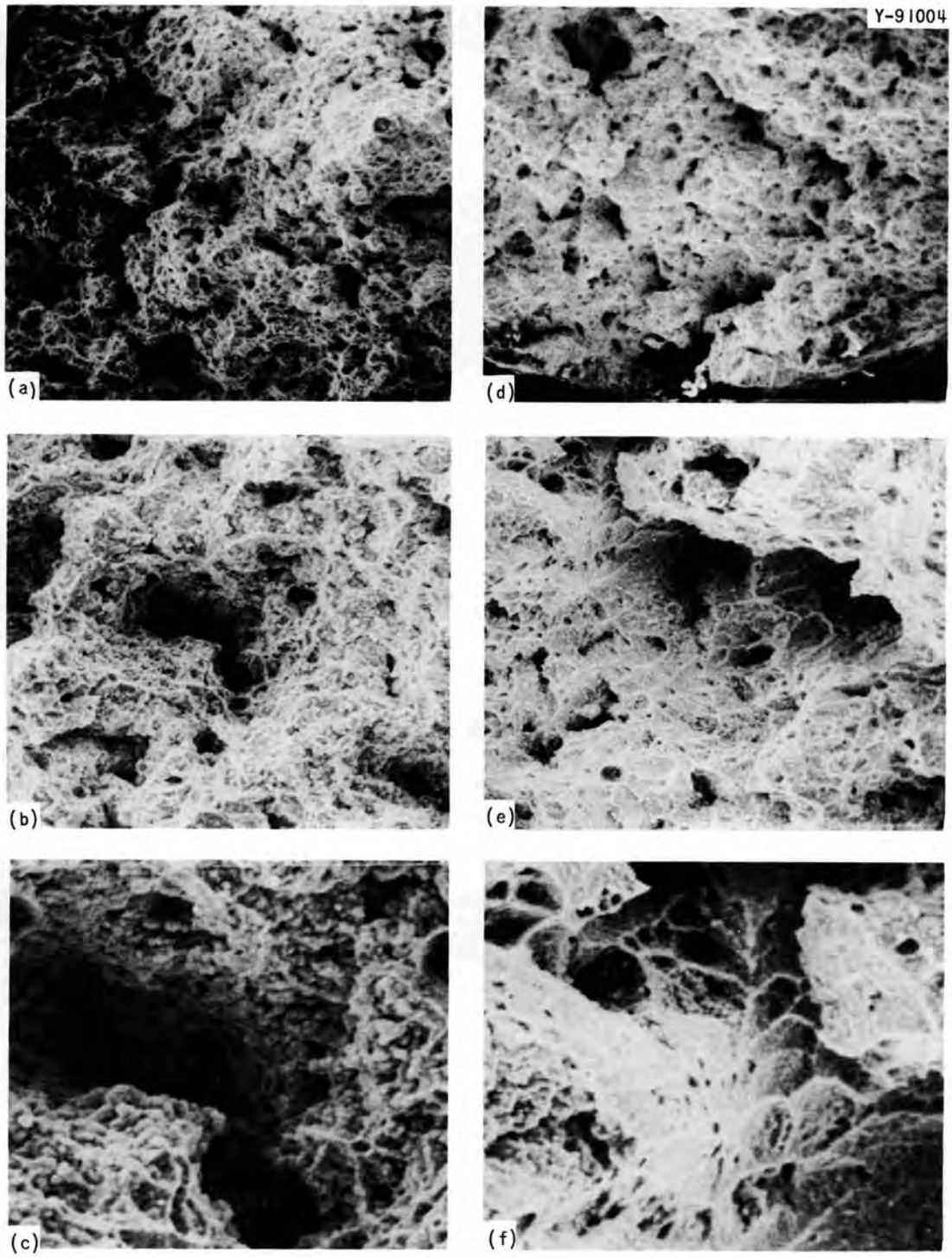

Fig. 11.2. Scanning Electron Photomicrographs of the Actual Fracture Surfaces of Representative Titanium-Bearing Alloys Tensile Tested at 700°C. Alloy containing titanium, aluminum and sulfur: consecutive photomicrographs of the same field at (a) 100×, (b) 300×, and (c) 1000×. Alloy containing titanium: consecutive photomicrographs of the same field at (d) 100×, (e) 300×, and (f) 1000×. Reduced 25.5%.

Fig. 11.3. Transmission Electron Micrograph of the Alloy Containing Titanium and Aluminum. The row of precipitated particles is thought to be the former location of a grain boundary. 25,000×. Reduced 20%.

Effect of Certain Minor Elements on the Ductility of Incoloy 800 at Intermediate Temperatures (W. J. Werner)

We examined alloys from both ductility classes — the distinction between which we discussed[2] previously — after tensile testing at 700°C. The 700°C test temperature was chosen because it produced the ductility and microstructural differences previously observed.[3] Figure 11.1 shows consecutive scanning electron photomicrographs of the actual fracture surfaces of two representative Ti-free alloys, one of which contains S while the other does not. The 100× photomicrographs show that the fractures are predominantly intergranular (the detailed morphology of the grain boundaries is shown at the higher magnification). The rough boundaries suggest a high degree of deformation (i.e., grain-boundary shear). Figure 11.2 shows similar photomicrographs of the fracture surfaces of two representative alloys that do contain Ti after testing at 700°C. Again, one alloy contains S while the other does not. The 100× photomicrographs substantiate the previous metallographic evidence for transgranular fracture. The 300× and 1000× photomicrographs confirm this observation. In addition, the voids that formed on the boundaries before recrystallization can be seen in the photomicrographs. The voids are rounded and due to the transgranular nature of the fracture cannot all be associated with grain boundaries.

Samples for transmission electron microscopy were obtained from regions near the fractures of specimens tested at 700°C. Photomicrographs of the alloys that contained no Ti showed no evidence of precipitation either on the grain boundaries or within the grains. This, however, does not eliminate the possibility of a continuous film at the grain boundaries. These alloys were characterized by the formation of rugged subcells and a relatively low dislocation density. On the other hand, precipitation occurred in the alloy that did contain Ti, and a typical photomicrograph is shown in Fig. 11.3. The row of precipitated

---

[2]W. J. Werner, Fuels and Materials Development Program Quart. Progr. Rept. Dec. 31, 1968, ORNL-4390, pp. 192–199.

[3]W. J. Werner, Fuels and Materials Development Program Quart. Progr. Rept. March 31, 1969, ORNL-4420, pp. 202–207.

particles is thought to be the former location of a grain boundary. The boundary intersecting this row probably migrated from the particles under the application of stress at the test temperature. The precipitated particles were electrolytically extracted from a portion of the sample, and x-ray analyses of the residue showed that both titanium nitride and titanium disulfide were present.

These studies suggest that one or more of the residuals present in the alloys that contain no Ti impeded recrystallization, possibly by the formation of a film at the grain boundaries or the solution hardening of the grains. Either mechanism would affect recrystallization, thereby resulting in the observed continuous decrease in ductility with increasing test temperature. It is further suggested that redistribution of the detrimental species by the formation of Ti compounds is responsible for the enhanced ductility at elevated temperatures of the alloys that contain Ti.

Development of Welding Procedures for Commercial and Modified Alloys

These welding studies are intended to be applied directly to the fabrication of particular reactor components. Our current efforts are directed toward the FFTF primary vessel. We are obtaining information about welding per se and also about the mechanical properties of both unirradiated and irradiated joints.

Joining Development in Support of Fast Flux Test Facility
(G. M. Goodwin, N. C. Cole)

As described previously[4,5] we prepared weld specimens for an irradiation program at Battelle Memorial Institute Pacific Northwest Laboratories (BNWL), Richland, Washington. We prepared about

---

[4]G. M. Goodwin, Fuels and Materials Development Program Quart. Progr. Rept. Dec. 31, 1968, ORNL-4390, pp. 199–203.

[5]G. M. Goodwin, Fuels and Materials Development Program Quart. Progr. Rept. March 31, 1969, ORNL-4420, pp. 207–209.

500 1/8-in.-diam tensile specimens from weldments produced by three different welding processes: submerged-arc, shielded metal-arc, and gas metal-arc.

The welding conditions, summarized in Table 11.2, were typical of industrial practice. For comparative purposes, similar data are presented for the gas tungsten-arc welds made at BNWL. Note that three different filler metals were used: type 308 stainless steel filler metal was used with the submerged-arc and gas tungsten-arc processes, type 308L stainless steel filler metal was used with the gas metal-arc process, and 16% Cr–8% Ni–2% Mo stainless steel filler metal was used with the shielded metal-arc process. Reference data are being determined at BNWL on the mechanical properties of some of the unirradiated weldments while other specimens are being irradiated.

Macroscopic cross sections of each of the weldments are shown in Fig. 11.4. Examination of the weld deposits at higher magnification reveals gross differences in both the distribution and amount of ferrite. Figure 11.5, for example, shows the distribution at random locations in each of the four types of weldments. Substantial variations were also observed between cross sections within nominally identical welds made by a given process (Fig. 11.6) and between different locations within a particular cross section (Fig. 11.7).

The ferrite content of each of the weldments was measured by quantitative television microscopy. Table 11.3 summarizes the results of these measurements. As a basis for comparison, a point-count technique was also used on a gas tungsten-arc specimen (these data are also shown in Table 11.3). Note that the ferrite content measured in welds made with each of the procedures varied by a factor of 2 within a given specimen.

Complete details of the welding process, the characterization of the weldments, and the results of tests of the mechanical properties of unirradiated weldments are being compiled for a jointly prepared document.

Table 11.2. Summary of Conditions[a] Used for Producing Weldments for Study in Support of Fast Flux Test Facility

	Submerged-Arc	Gas Metal-Arc (M16)	Shielded Metal-Arc (Stick)	Gas Tungsten-Arc (TIG)
Current, amp	600	290–320	170	187–250
Voltage, v	35–37	35–37	25	10.5–12
Travel speed, in./min	18	11.3	7.5–8.5	12–14.6
Filler wire	5/32-in.-diam Type 308 stainless steel, Arcos Heat E9470F308	1/16-in.-diam Type 308L stainless steel, Airco Heat 705001	5/32-in.-diam 16% Cr–8% Ni–2% Mo coated stainless steel electrodes, Champion Heat 53011	1/16-in.-diam Type 308 stainless steel
Number of passes	14	18	35	108
Power supply	Linde CAC-1500	Linde SVI-300	Hobart Motor-Generator	Sciaky FH8-W1600
Interpass temperature, °C	< 177	< 177	< 177	< 177
Polarity	ac	dc	dc	dc straight polarity
Flux	Arcosite S-4 Lot 8H5F			
Shielding gas		90% He–7 1/2% Ar–2 1/2% CO_2 (Linde 1025) 45 ft^3/hr		Ar (high purity, welding grade), 50 ft^3/hr

[a]Welds made in 1G position with no preheat. Cleaned between passes with carbide rotary file and stainless steel brush.

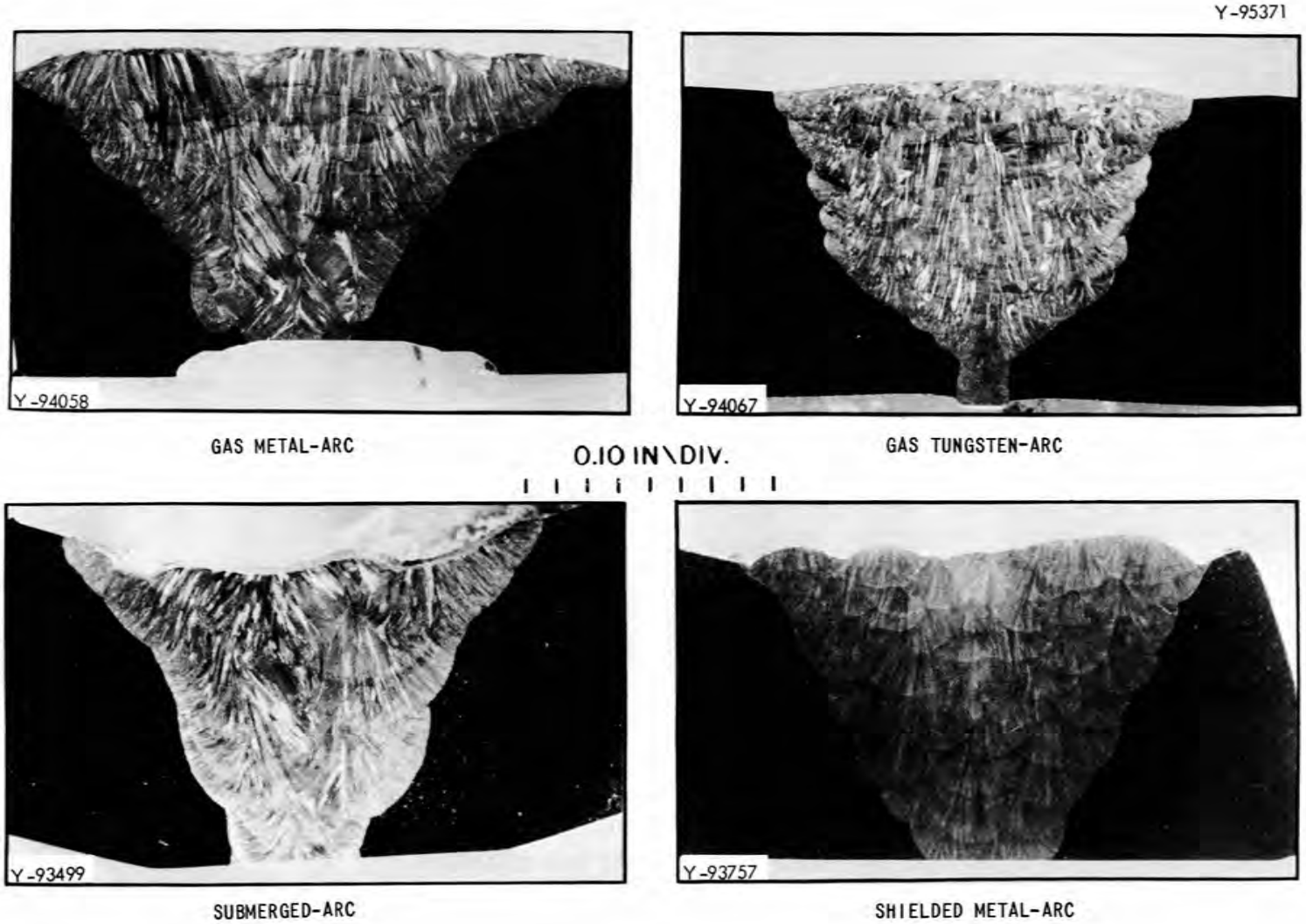

Fig. 11.4. Macroscopic Views of Cross Sections from Welds Produced by Different Welding Processes. Etchant: 20% lactic, 63% hydrochloric, 17% nitric acids. The variations in size of the individual beads are apparent.

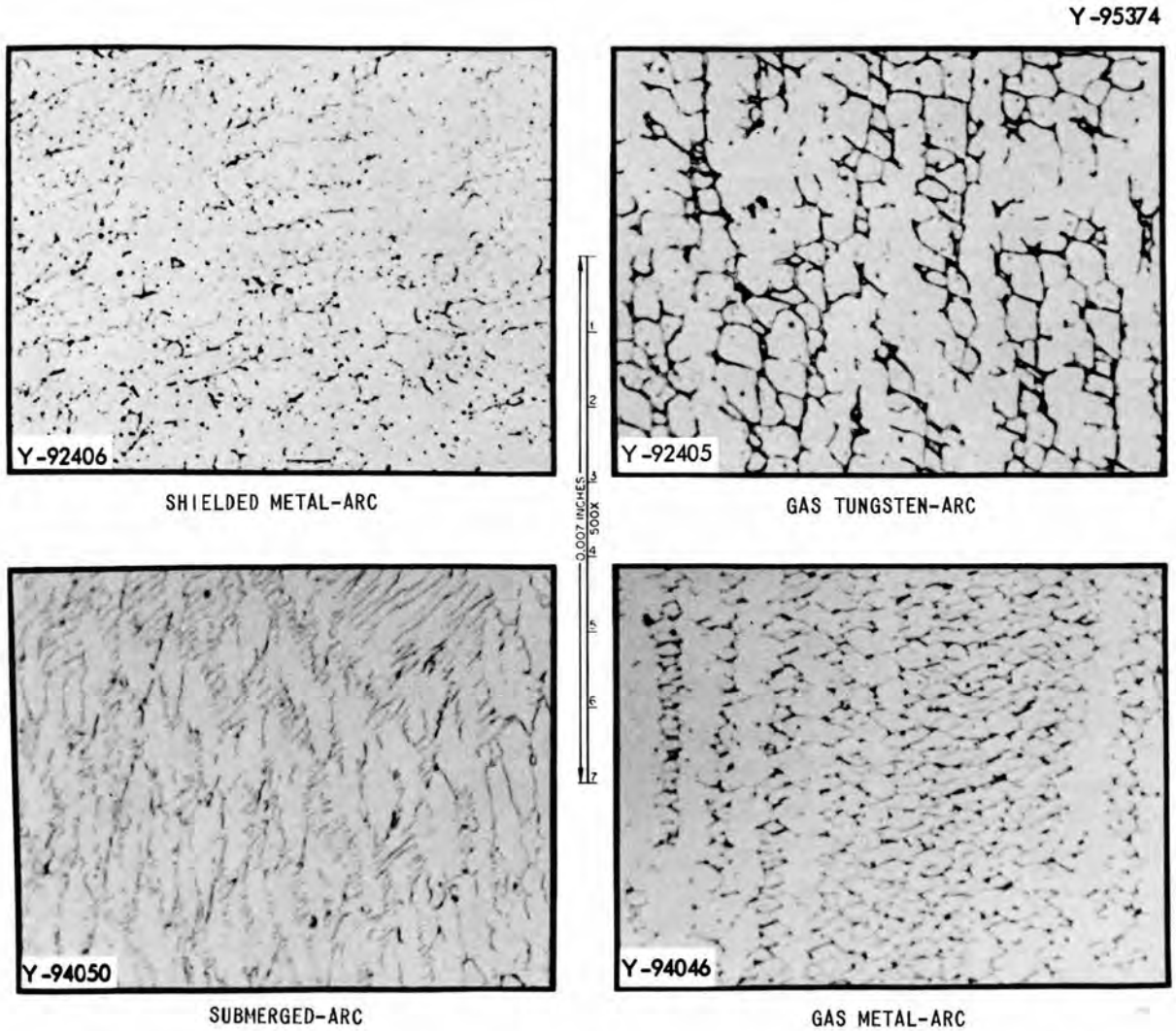

Fig. 11.5. Comparison of Ferrite Distribution in Welds Produced by Different Processes. Etchant: KOH, $K_3FE\ (CN)_6$.

Y-95372

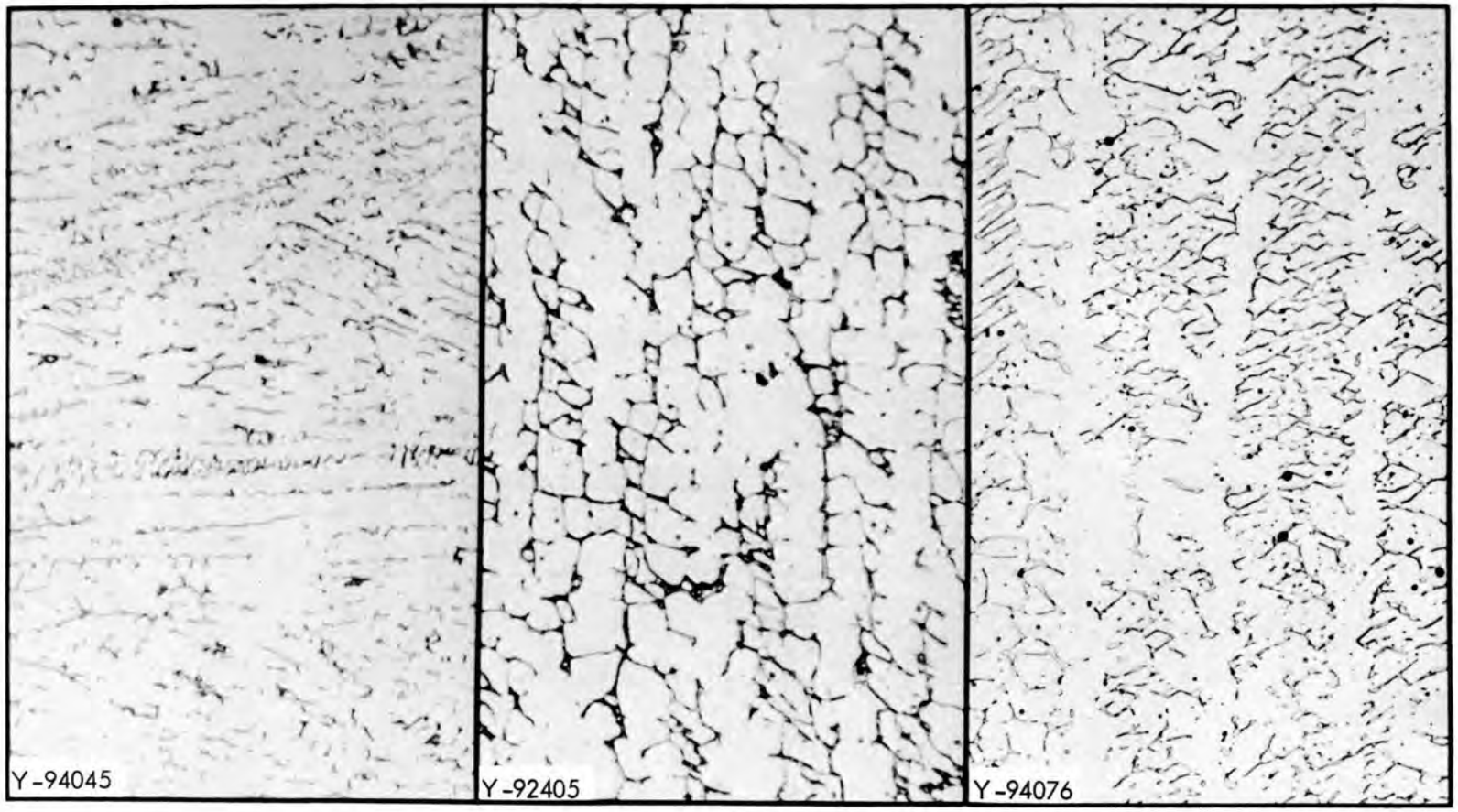

WELD B | WELD A, SAMPLE 64 | WELD A, SAMPLE 61

Fig. 11.6. Variation in Ferrite Distribution in Submerged-Arc Welds.

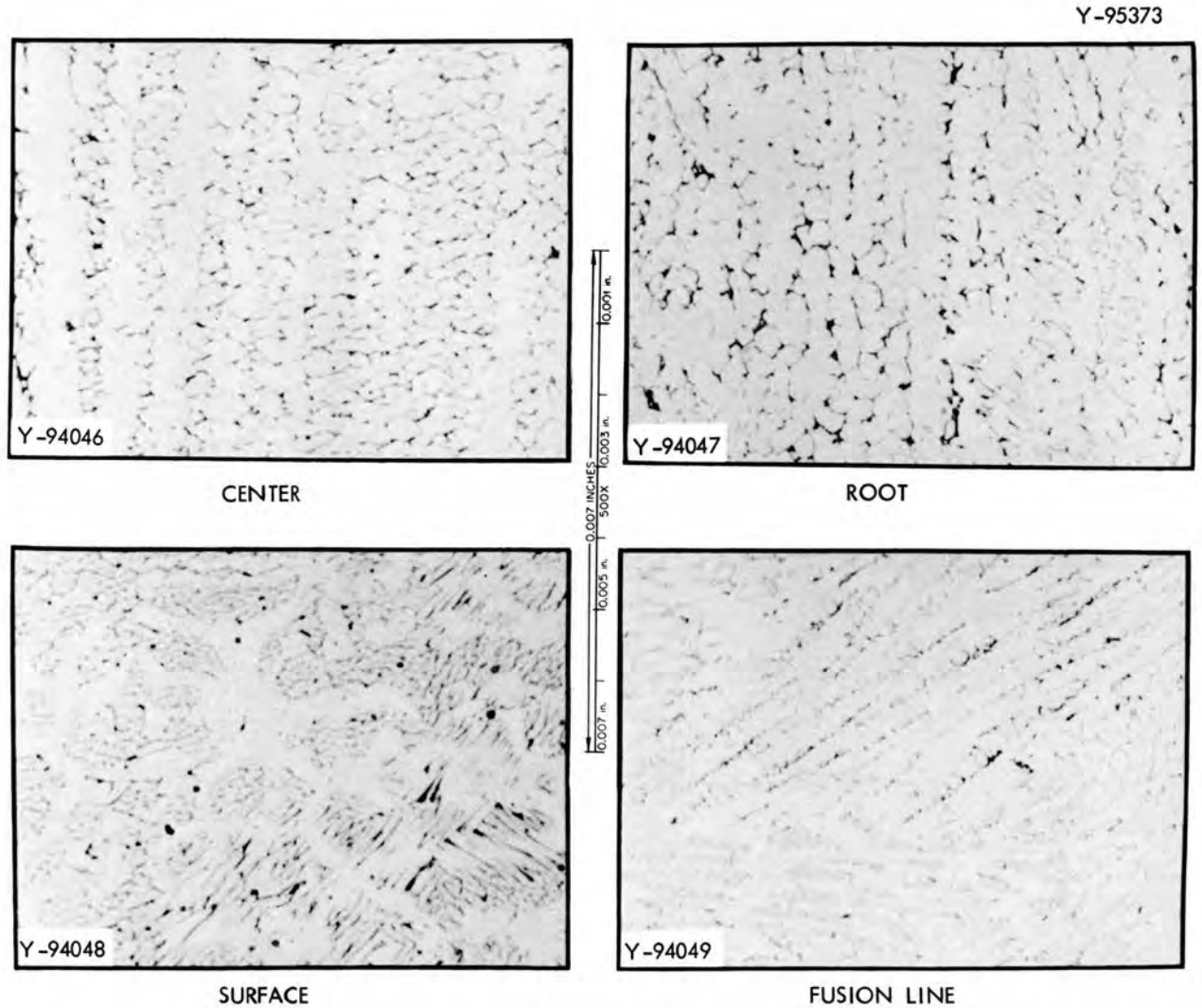

Fig. 11.7. Variation in Ferrite Distribution in One Cross Section of a Gas Metal-Arc Weld Sample. Etchant: KOH, $K_3Fe(CN)_6$.

Table 11.3. Results of Ferrite Measurements

Welding Process	Measurement Technique	Ferrite Content, %		Ferrite Content, %, at Indicated Confidence Level	
		Range	Mean	95%	99%
Submerged-arc	Quantitative television microscopy	4.4–10	7.5	6.8–8.1	6.6–8.3
Gas metal-arc	Quantitative television microscopy	5.4–11.5	8.2	7.4–8.9	7.1–9.2
Gas tungsten-arc	Quantitative television microscopy	4.9–10.2	8	7.3–8.7	7.1–8.9
Gas tungsten-arc	Point count	9.1–10.8			
Shielded metal-arc	Quantitative television microscopy	2.2–4.2	3.1	2.8–3.3	2.7–3.4

The Effect of Defects on the Mechanical Properties of Weldments

C. D. Lundin[6]

This study was initiated to determine when a discontinuity becomes unacceptable. It is a known and accepted fact that discontinuities generally exist in structural components. Our objective is to characterize various discontinuities and establish their effects on the mechanical properties of the materials being joined.

The nondestructive evaluation of the Inconel electron-beam welds that contain deliberate discontinuities was completed. The weldment was ultrasonically inspected by both through-transmission and reflection techniques. The through-transmission recordings correlated well with the radiographs obtained previously. The reflection recordings were more difficult to correlate because many of the individual discontinuities could not be resolved and thus were recorded as a single, large indication.

It was determined that for the specimens under investigation the radiographic resolution was 0.005 in.; this is better than was obtained by ultrasound (about 0.16 in.). Further, radiography is more sensitive to three dimensional flaws and can detect laminar discontinuities when different x-ray entrance angles were used.

Several recommendations were made by the Nondestructive Test Development Laboratory with regard to producing standards and selecting more suitably sized specimens. Specimens are now being machined from these weldments for further nondestructive examination and mechanical testing under suitable conditions to show the effect of the discontinuities. Control specimens from the virgin base material will also be tested under identical conditions for comparison.

Work on characterization of discontinuities is also continuing, and the origin and morphology of the discontinuities in the Inconel weldments should be known soon.

---

[6]Consultant from the University of Tennessee.

12. DEVELOPMENT OF LMFBR TUBING FABRICATION

G. M. Adamson, Jr.

The tubing fabrication program involves development of fabrication techniques for the manufacture of high-quality type 316 and modified type 304 stainless steel tubing in sizes of interest to the liquid-metal fast breeder reactor (LMFBR) program.

The general scope includes using fabrication techniques that may be transferred to commercial vendors and sufficient nondestructive and destructive testing of the intermediate and final products to assure and demonstrate the quality. The initial studies used Ti-modified type 304 stainless steel, and recently work has begun on type 316 stainless steel.

Fabrication Studies on Type 316 Stainless Steel

W. R. Martin

Drawing of Type 316 Stainless Steel Tubing (G. A. Reimann)

We continued fabricating type 316 stainless steel tubing to the specifications for the Fast Flux Test Facility (FFTF). The stock from which we drew the tubing to its final size, 0.250 in. in outside diameter and 0.016 in. in wall thickness, was supplied to ORNL by Atomics International from a heat (65808) manufactured by Allegheny-Ludlum Steel Corporation. The characteristics and processing history of this heat were reported.[1] The tubing was fabricated to final size by mandrel drawing with a final pass by plug drawing to minimize the distortion of the final dimensions caused by reeling the tube to remove the mandrel.

We varied the schedules for mandrel drawing and annealing to determine the extent to which differences in the technique of fabrication affect the structure and properties of the final product. We will

[1]G. A. Reimann, Fuels and Materials Development Program Quart. Progr. Rept. March 31, 1969, ORNL-4420, pp. 211–217.

look for trends that indicate which fabrication techniques will produce higher percentages of tubing that meets FFTF specifications and will also be most suited to a program of quality assurance. We want to be able to correlate the results from nondestructive testing with the fabrication process.

The tubing was drawn to final size according to the schedules listed in Table 12.1. The lots of tubing were identified by the codes shown below with the related drawing schedules:

Tubing Identification Code	Drawing Schedule
BA1-2	Schedule 1
BA1-3	Schedule 1, except anneals 2, 3, and 4 were 1/4 hr at 1050°C
BA1-1	Schedule 2

All the tubes in lot BA1 received a 1/4-hr anneal at 925°C before the 20% area reduction by plug drawing that produced the final dimensions. Schedule 1, used for tubes BA1-2 and BA1-3, involved three passes totaling 50% reduction between each anneal. The 950°C anneals used for tube BA1-2 resulted in drawn tubing with an ASTM grain size between 6 and 8, while the 1050°C anneals used for tube BA1-3 resulted in tubing with a grain size between 3 and 5. Schedule 2, used for tube BA1-1, closely resembles commercial drawing practice. The tubing drawn according to schedule 2 was annealed 1/4 hr at 950°C after each 40% reduction. This resulted in an ASTM grain size between 5 and 6. Typical structures are shown in Fig. 12.1.

Thus, tubes BA1-2 and BA1-3 may be compared with regard to identical drawing schedules but different annealing treatments, and tubes BA1-1 and BA1-2 may be compared on the basis of similar annealing treatments but different drawing schedules.

The microstructures produced by the final anneal are shown in Fig. 12.1. The differences in grain size are apparent. The finer grain size in tube BA1-2 than in tube BA1-3 suggests an influence of finer prior grain size on the final product. Tube BA1-2 has finer grain size

Table 12.1. Schedules for Drawing Tubing[a] from Allegheny-Ludlum Heat 65808

Schedule Number	Pass Number	Anneal			Die (in.)	Mandrel (in.)	Reduction, %	
		Number	Time (hr)	Temperature (°C)			Per Pass	Total
1	1				1.250	1.000	21.4	21.4
	2				1.160	0.950	21.3	38.0
	3				1.085	0.900	17.2	48.7
		1	1/4	1050				
	4				0.995	0.850	26.8	26.8
	5				0.990	0.775	21.8	42.9
	6				0.815	0.700	16.8	52.5
		2	1/4	950				
	7				0.715	0.618	25.6	25.6
	8				0.635	0.550	22.1	42.1
	9				0.570	0.490	15.7	51.3
		3	1/4	950				
	10				0.492	0.425	27.6	27.6
	11				0.428	0.369	23.3	44.6
	12				0.384	0.330	16.2	53.5
		4	1/4	950				
	13				0.332	0.285	26.2	26.2
	14				0.300	0.260	22.6	43.0
	15				0.267	0.230	15.5	51.9
		5	1/4	925				
	16				0.250	0.218[b]	20.7	20.7
2	1				1.145	0.950	42.8	
		1	1/4	1050				
	2				0.895	0.750	41.5	
		2	1/4	1050				
	3				0.682	0.570	41.3	
		3	1/4	950				
	4				0.535	0.450	40.3	
		4	1/4	950				
	5				0.410	0.344	40.5	
		5	1/4	950				
	6				0.325	0.275	39.5	
		6	1/4	950				
	7				0.267	0.230	38.5	
		7	1/4	925				
	8				0.250	0.218[b]	19.5	

[a]Starting size: 1.505 in. OD × 1.245 in. ID.

[b]Plug drawn.

ORNL-DWG 69-7279

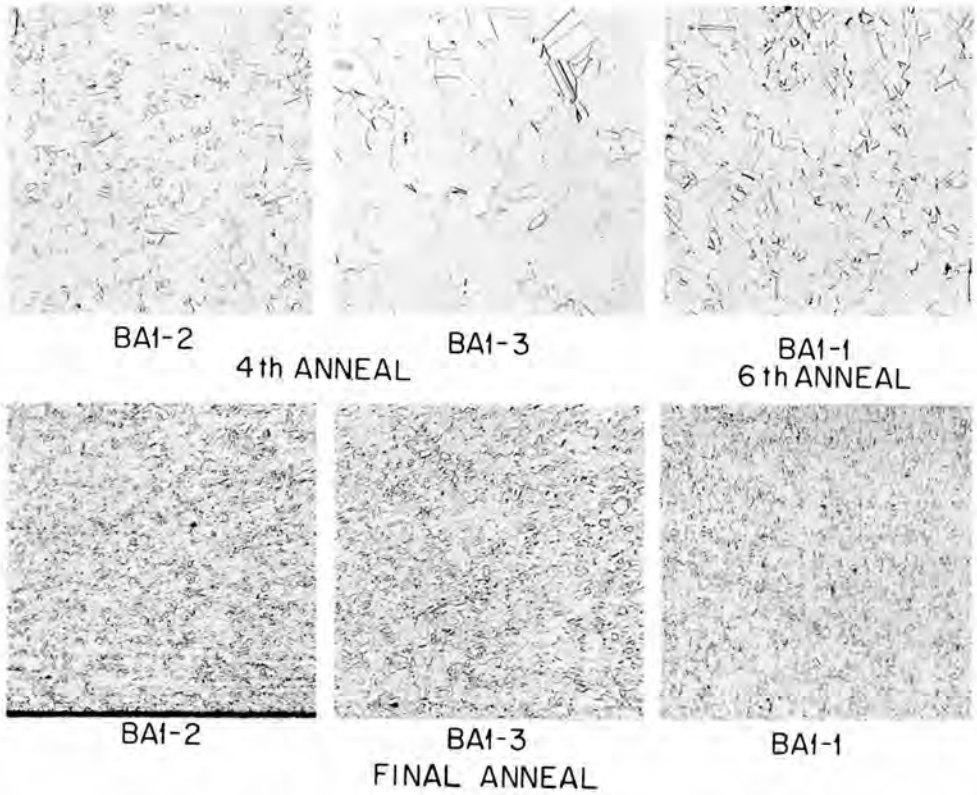

Fig. 12.1. Microstructures of Type 316 Stainless Steel As Influenced by Fabrication History (See Table 12.1). 100×. Reduced 18%.

than tube BA1-1 primarily because of greater cold work just before this final anneal. Measurements of hardness have not been completed.

All tubing was tested nondestructively. Although this evaluation is not complete, 70% of the tubing appears to meet the FFTF specification limits for flaws and eccentricity. Lengths of tubing known to contain defects were selected from each batch and matched with strip-chart recordings of ultrasonic nondestructive testing to locate defects precisely. Tube-burst specimens were cut so that the type of defect and its location were known, and these samples and three samples from sections that contained no defects were pressurized to failure. Results obtained on samples without defects are shown in Table 12.2.

We have not yet attempted to correlate the results of these tube-burst tests with processing history, but for the BA1 series of tubes, the hoop stress at failure appeared to be related to the grain size.

Table 12.2. Results of Tube-Burst Tests on Tubing Without Defects

Tubing Identification	Average Burst Pressure (psi)	Average Hoop Stress (psi)	Average Elongation (%)
	20% Cold Work		
303407[a]	22,080	172,300	2.2
BA1-1	19,930	158,700	3.1
BA1-2	20,630	164,900	2.8
BA1-3	20,050	159,300	3.1
	Annealed 1/4 hr at 925°C		
BA1-1	11,300	87,900	37.5
20276[b]	11,280	84,400	41.8

[a]Drawn to size from 0.375-in.-OD × 0.035-in.-wall thickness stock from Greenville Tube, Inc.

[b]Drawn to FFTF specifications and annealed by Superior Tube Company. Annealing conditions unknown.

The tubing that contained known defects did not always suffer gross weakening as a result. We noted no weakening if the defect was in the thicker side of the tubing wall. Of the nine samples with defects that were tested, only one failed at a defect in the thicker wall. Loss of strength and ductility were significant, however, when flaws were located in the thinner side of the tubing.

All samples that contained 20% cold work failed at a defect, even though the defect might not have been indicated by inspection because it was below the threshold of ultrasonic detection and not visible until the samples suffered some strain. We believe that burst properties could be improved if these "subthreshold" flaws could be removed.

A new heat of stainless steel (Crucible Steel heat 065219) was received and processed into 2-in.-OD × 0.250-in.-wall thickness tube shells. Work will begin on this heat as soon as inspection of the tube shells is completed.

Fabrication Studies on Titanium-Modified Type 304 Stainless Steel

W. R. Martin

Evaluation of Drawn and Planetary-Swaged Tubes of Titanium-Modified Type 304L Stainless Steel (T. M. Nilsson)

The British have shown[2] that planetary-swaged tubes have higher creep ductilities than drawn tubes. One of the possible explanations for this behavior is a difference in texture. We have, therefore, fabricated tubing of type 304L stainless steel alloy modified with 0.2% Ti to near the dimensions for LMFBR cladding (i.e., 0.25 in. outside diameter by 0.015 in. wall thickness), using both drawing and planetary swaging for the final reductions. We used the same starting tubes and the same reductions per pass in the two schedules, except for an extra 5% deformation by plug drawing in the drawing schedule to avoid the reeling step needed for ordinary mandrel drawing. The reductions consisted primarily of reduction in diameter with very little wall thinning. After such reductions, very little reeling is necessary to remove the mandrel after planetary swaging.

Figures 12.2 and 12.3 show the $(111)_\gamma$ pole figures of Ti-modified type 304L stainless steel tubing after 45% cold drawing and 40% cold planetary swaging, respectively. The pole figures and, hence, the textures are clearly quite different. The texture after drawing (Fig. 12.2) resembles closely the one already reported;[3] the three texture components are close to $[110]_{RD}$ (radial direction) $[001]_{AD}$ (axial direction), $[111]_{RD}[\bar{1}2\bar{1}]_{AD}$, and $[111]_{RD}[1\bar{2}1]_{AD}$. Corresponding to the higher degree of deformation [45% vs 30% (ref. 2)], the texture in Fig. 12.2 is sharper.

---

[2] Stainless Steel Cladding Development Quart. Progr. Rept. Dec. 31, 1968, WARD-3791-29, p. 14.

[3] T. M. Nilsson, Fuels and Materials Development Program Quart. Progr. Rept. Dec. 31, 1968, ORNL-4390, pp. 205–214.

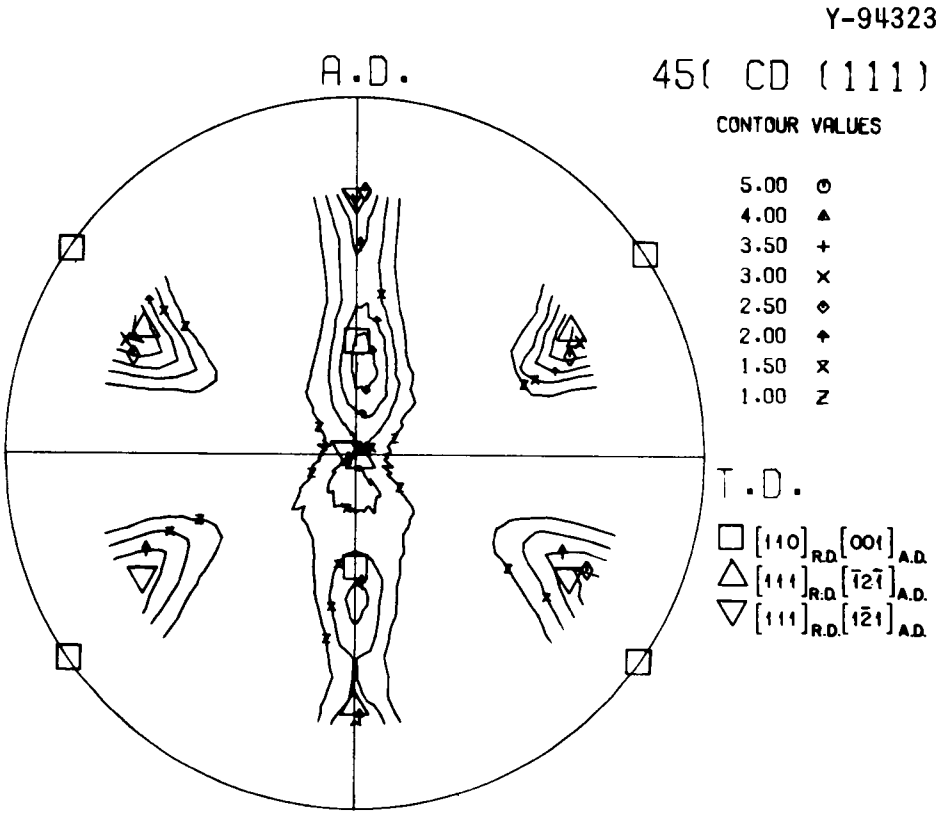

Fig. 12.2. Pole Figure for $(111)_\gamma$ of 0.2% Ti-Modified Type 304L Stainless Steel Tubing Cold Worked 45% by Mandrel Drawing Under Sinking Conditions.

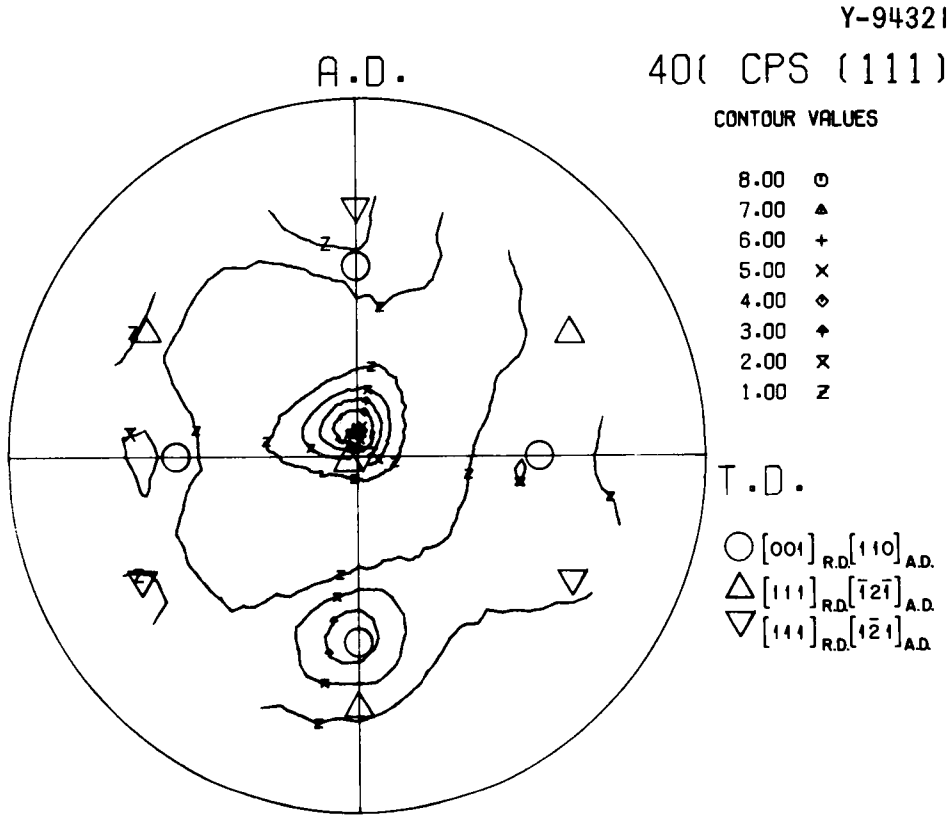

Fig. 12.3. Pole Figure for $(111)_\gamma$ of 0.2% Ti-Modified Type 304L Stainless Steel Tubing Cold Worked 40% by Planetary Swaging.

Maximum intensity is three times random. The characteristic feature in the $(111)_\gamma$ pole figures after planetary swaging is the high intensity (six times random) near the center (i.e., near the radial direction). This corresponds to a large number of $(111)_\gamma$ planes aligned circumferentially. The two texture components with the $(111)_\gamma$ pole oriented radially are the same in both the drawing and planetary-swaging textures. The third component after planetary swaging is $[001]_{RD}[110]_{AD}$.

Figures 12.4 and 12.5 show the corresponding $(200)_\gamma$ pole figures. The textures represented by these pole figures agree well with the three proposed components for the $(111)_\gamma$ pole figures.

The changes in texture caused by annealing may be seen by comparing Figs. 12.2 and 12.6. Figure 12.6 shows the $(111)_\gamma$ pole figure of the tube cold drawn 45% after a recrystallization treatment at 925°C for 1 hr. Since the peak positions are the same, the texture components are the same. The texture after annealing, however, is less sharp, and the intensities are lower.

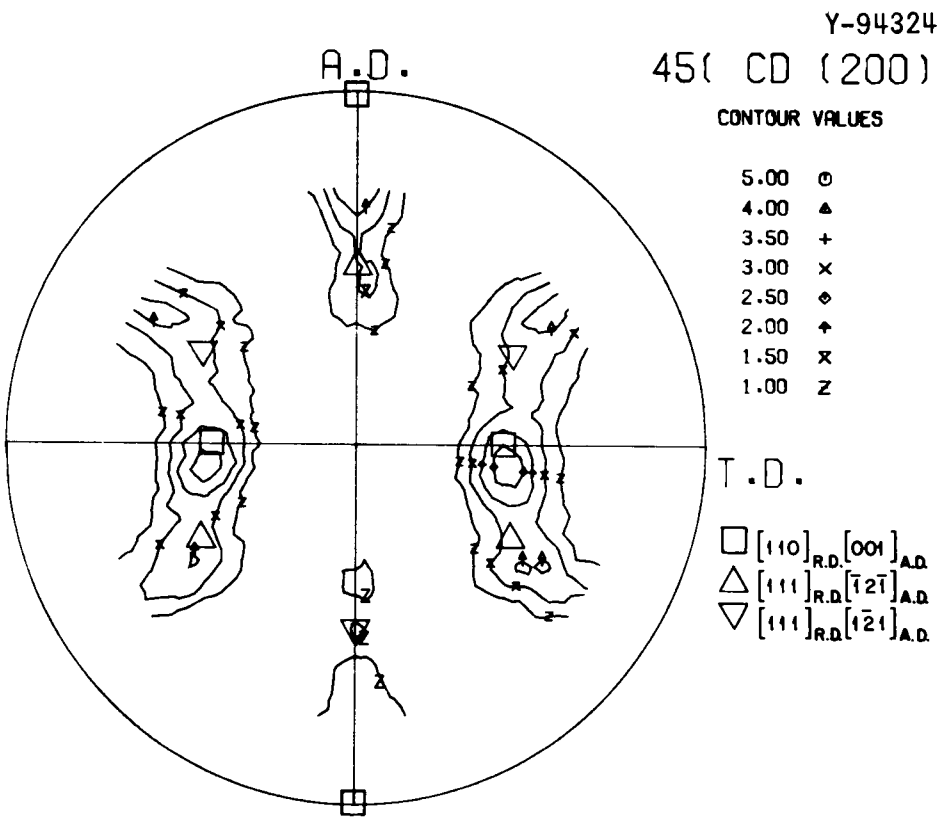

Fig. 12.4. Pole Figure for $(200)_\gamma$ of Ti-Modified Type 304L Stainless Steel Tubing Cold Worked 45% by Mandrel Drawing Under Sinking Conditions.

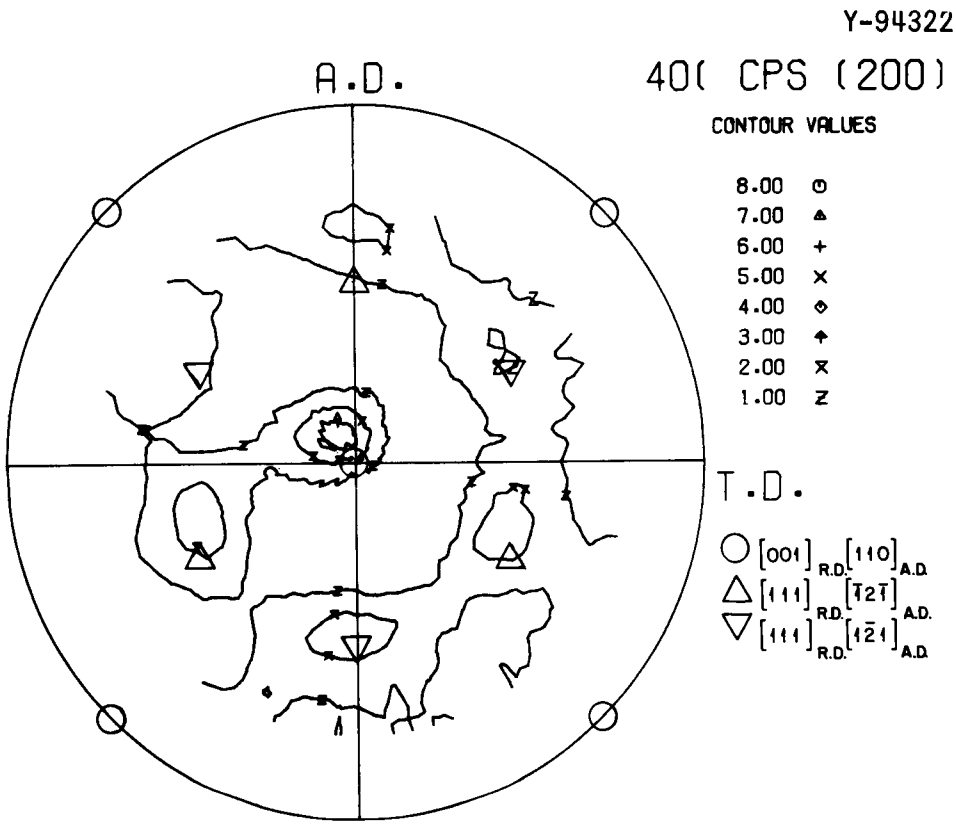

Fig. 12.5. Pole Figure for $(200)_\gamma$ of Ti-Modified Type 304L Stainless Steel Tubing Cold Worked 40% by Planetary Swaging.

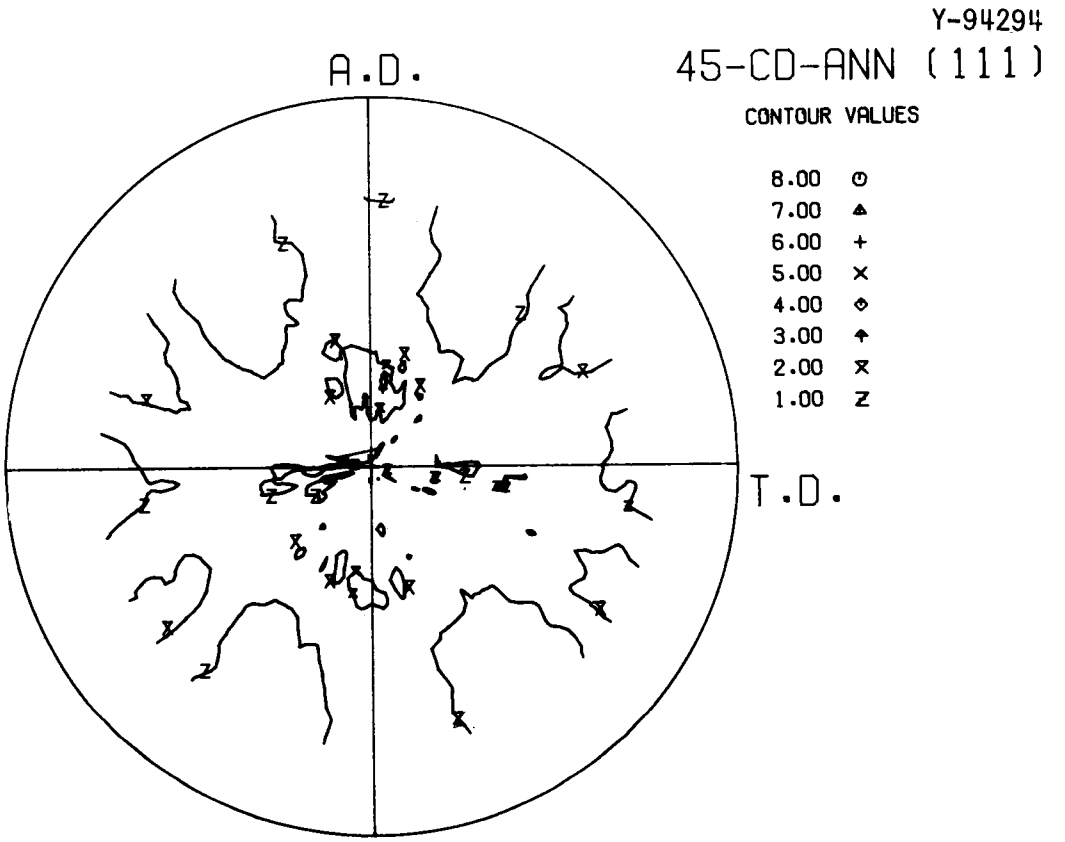

Fig. 12.6. Pole Figure for $(111)_\gamma$ of 0.2% Ti-Modified Type 304L Stainless Steel Tubing Cold Worked 45% by Mandrel Drawing and Recrystallized by Heating to 925°C for 1 hr.

We have also measured the texture of tubing of the same alloy cold worked so that the reduction consisted only of wall thinning. Figures 12.7 and 12.8 show the $(111)_\gamma$ and $(200)_\gamma$ pole figures for tubes cold worked 44% by mandrel drawing with only ironing reductions. These pole figures should be compared with Figs. 12.2 and 12.4, which are pole figures from the tube cold drawn 45% under sinking conditions. Peak intensities are similar, but peak positions corresponding to the texture are different. Analysis shows that the texture after ironing operations consists of only the component $[110]_{RD}[001]_{AD}$; after sinking, two more components had to be included to describe the texture fully.

Our texture results are summarized in Table 12.3. In addition to the examples already discussed (i.e., 40% cold planetary swaging, 45 and 44% cold drawing), we have included texture measurements from tube

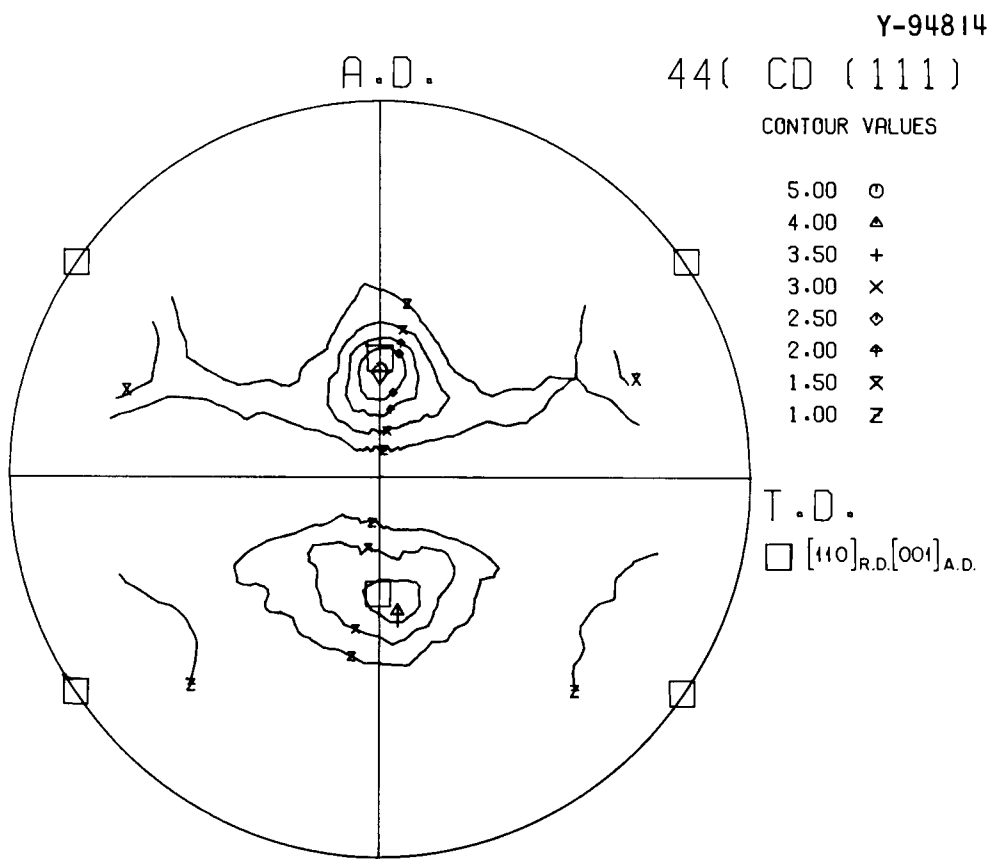

Fig. 12.7. Pole Figure for $(111)_\gamma$ of Ti-Modified Type 304L Stainless Steel Tubing Cold Drawn 44% Under Ironing Conditions.

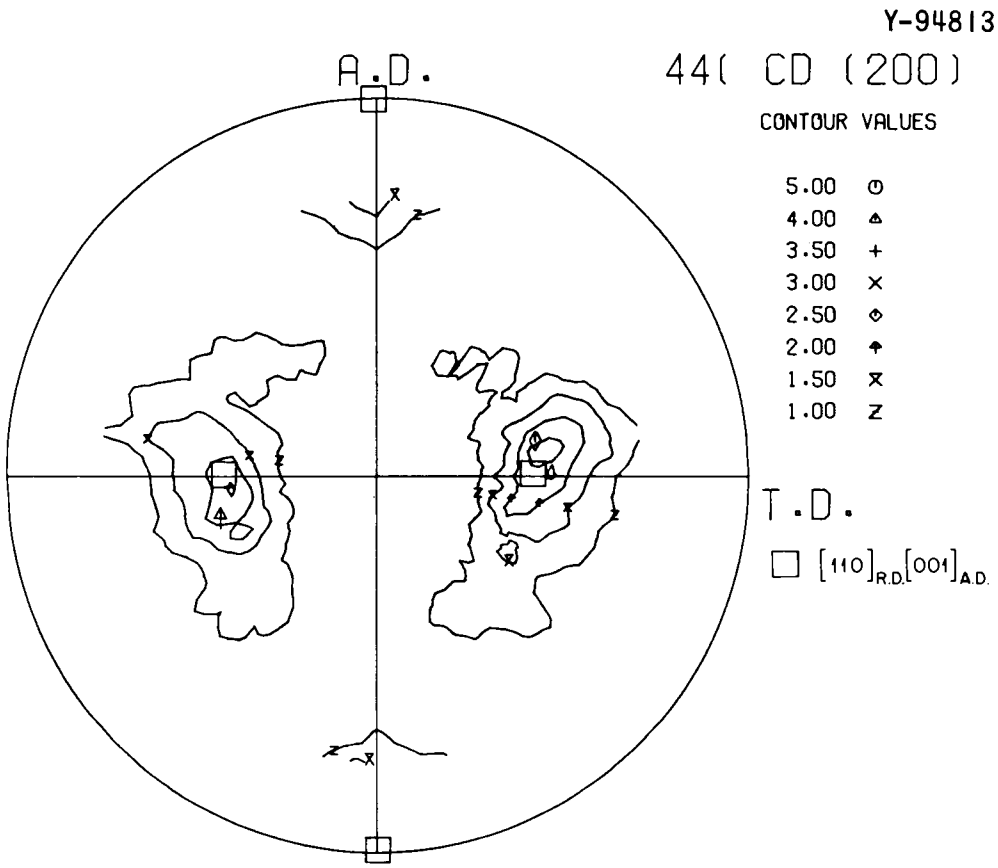

Fig. 12.8. Pole Figure for $(200)_\gamma$ of 0.2% Ti-Modified Type 304L Stainless Steel Tubing Cold Drawn 44% Under Ironing Conditions.

Table 12.3. Texture of Planetary-Swaged and Drawn Tubes of Type 304L Stainless Steel Modified with 0.2% Ti

Working Technique	Type of Reduction[a]	Condition	Maximum Intensity (× random)	Texture Component[b]	Intensity (× random)
Planetary swaging	Sinking	12% cold planetary swaging	6	$[001]_{RD}[110]_{AD}$ $[111]_{RD}[\bar{1}2\bar{1}]_{AD}$ $[111]_{RD}[1\bar{2}1]_{AD}$	4 3 3
		Annealed[c]	2.5		
		23% cold planetary swaging	5	$[001]_{RD}[110]_{AD}$ $[111]_{RD}[\bar{1}2\bar{1}]_{AD}$ $[111]_{RD}[1\bar{2}1]_{AD}$	3 2 2
		Annealed[c]	2.5		
		40% cold planetary swaging	6	$[001]_{RD}[110]_{AD}$ $[111]_{RD}[\bar{1}2\bar{1}]_{AD}$ $[111]_{RD}[1\bar{2}1]_{AD}$	3 3 3
		Annealed	3		
Mandrel drawing	Sinking	27% cold drawn	3.5	$[110]_{RD}[001]_{AD}$ $[111]_{RD}[\bar{1}2\bar{1}]_{AD}$ $[111]_{RD}[1\bar{2}1]_{AD}$	2.5 1.5 1.5
		Annealed[c]	2.5		
		45% cold drawn	3	$[110]_{RD}[001]_{AD}$ $[111]_{RD}[\bar{1}2\bar{1}]_{AD}$ $[111]_{RD}[1\bar{2}1]_{AD}$	2.5 1.5 1.5
		Annealed	2.5		
Mandrel drawing	Ironing	29% cold drawn	3	$[110]_{RD}[001]_{AD}$	2.5
		Annealed[c]	2		
		44% cold drawn	3	$[110]_{RD}[001]_{AD}$	3
		Annealed	2		

[a]In the two sinking schedules, the same starting tubes and the same reductions were used.

[b]Radial direction, RD; axial direction, AD.

[c]Annealed at 925°C for 1 hr.

samples that were cold worked an intermediate amount. The table shows that the texture, which is characteristic of the working technique for the type of reduction, develops after very small reductions and that the maximum intensities are reached very early in the reduction schedule. The intensities do not increase with further reduction, as is normally the case, because of the phase changes.[4,5] However, the textures (i.e., the intensity peaks) do sharpen with increasing amounts of cold work. After annealing, the texture components are generally the same as before, but the degree of preferred orientation (the sharpness and intensity of the peaks) is weaker.

Biaxial Stress-Rupture Properties of Titanium-Modified Type 304L Stainless Steel Tubing (R. T. King)

We previously presented[6] partial results for the biaxial stress-rupture properties of the first batch of tubing of type 304L stainless steel modified with 0.2% Ti (Allvac heat 3756) produced at ORNL. The remainder of the tubes from this batch were tested at 600 and 700°C in the same manner as those reported earlier. The test results are summarized in Table 12.4, which indicates such variables as the degree of cold work introduced between intermediate anneals during fabrication, the presence of longitudinal defects found by nondestructive ultrasonic testing, and the atmosphere of the final annealing treatment.

We drew two conclusions from our studies of this first batch of tubes:

1. The ductility of annealed 0.2% Ti-modified type 304L stainless steel tubing that contains no defects compares favorably with that of type 304 stainless steel tubing at 600 and 700°C, although ultrasonically detectable defects may reduce rupture life or ductility.

2. Cold-worked tubing that does not recover during testing ruptures at times similar to those for type 304 stainless steel tubing at 600 and

---

[4]T. M. Nilsson, Fuels and Materials Development Program Quart. Progr. Rept. Dec. 31, 1968, ORNL-4390, pp. 205–214.

[5]T. M. Nilsson, Fuels and Materials Development Program Quart. Progr. Rept. March 31, 1969, ORNL-4420, pp. 219–221.

[6]R. T. King, Fuels and Materials Development Program Quart. Progr. Rept. Dec. 31, 1968, ORNL-4390, p. 213.

Table 12.4. Biaxial Stress-Rupture Properties of 0.2% Ti-Modified Type 304L Stainless Steel Tubing

Test Temperature (°C)	Stress Tangential (psi)	Cold Work (%)	Anneal Atmosphere[a]	Presence of Defects	Rupture Time (hr)	Circumferential Elongation at Failure (%)
700	12,500	40	H_2	No	9.8	27.3
700	15,000	40	H_2	No	8.6	23.3
700	20,000	40	H_2	No	1.7	31.3
600	18,000	40	H_2	No	51.6	19.4
600	25,000	40	H_2	No	16.6	27.3
600	30,000	40	H_2	No	4.6	13.4
700	30,000	15	Air	Yes	2.0	26.3
600	20,000	15	Air	No	363.8	8.55
600	25,000	15	Air	No	36.4	14.3
600	30,000	15	Air	No	14.3	13.4
600	35,000	15	Air	Yes	1.5	12.5

[a]All specimens were annealed 1 hr at 925°C.

700°C. Low-ductility intergranular failures coincide with internal bore defects, which cannot be found by nondestructive testing in cold-worked tubing. Cold-worked tubes that do recover during testing behave like annealed tubes.

13. DEVELOPMENT OF FUEL ELEMENT FABRICATION

G. M. Adamson, Jr.

The purpose of these programs is to devise new combinations of materials or new fabrication techniques to advance the technology for fabricating fuel elements and components for research reactors. We are attempting to improve the performance of advanced research reactors, such as the High Flux Isotope Reactor (HFIR) and Advanced Test Reactor (ATR), by developing fuel elements with lower production cost, longer lives, increased safety or reliability, or all three. The studies include factors affecting both fabrication and irradiation performance. We must also develop sufficient knowledge of the processes used for fabricating Al-based dispersion fuel elements so that we can adequately assist commercial fabricators, purchasers, specification writers, and technical inspectors. Other studies are aimed at improving the reliability and reducing the cost of the required nondestructive inspection techniques.

Fabrication Studies of Dispersion Fuel Plates

W. R. Martin

Crushing of UAl_x Fuel (G. L. Copeland)

A problem in the preparation of UAl_x fuel particles is the production of excess fines during crushing of the arc-melted buttons to usable size. Present specifications for the ATR require particles that pass 100 mesh with a maximum of 25 wt % that pass 325 mesh. While most of the crushing devices commonly used produce about 50% fines (−325 mesh) in the −100 mesh material, we previously showed that the use of a roll crusher greatly improved the yields.[1] The yield of usable material was increased from about 67% up to 90 and 83%, respectively, for UAl_x containing 69 and 73 wt % U.

[1]G. L. Copeland, Fuels and Materials Development Program Quart. Progr. Rept. Dec. 31, 1968, ORNL-4390, pp. 241–244.

Results this quarter indicated that the difference in U content was not responsible for these different yields. Yields of 73 to 79% were obtained for UAl_x containing 66 to 71 wt % U, in comparison to a yield of 87% that was obtained for material that had been crushed and remelted. This agrees with the 90% yield on the original 69 wt % U material, which was also recycled. Thus, it appears that the yields increase by about 10 percentage points for recycled material.

The size distributions of the roll-crushed UAl_x are given in Table 13.1. The distributions are all similar except for the recycled batch (69-BR). The −100 mesh material contains from 37 to 46% fines. The recycled material contains only 34% fines. The high yield for the recycled material results from both a lower percentage of fines and almost no flakes that could not be reduced to −100 mesh. The recycled material used in the previous experiments, which had 69 wt % U and a 90% yield, contained only 24% fines in the −100 mesh fraction, but 10% of the material remained +100 mesh because of flaking.

The higher U content in batch 69-BR is partly responsible for the decrease in flaking, but the primary difference between the crushing behavior of the first material and the subsequent batches appears to be due to different reduction schedules. The first run was hand-crushed to about 10 mesh and given a heavy initial reduction under an inert atmosphere in a roll crusher fed by hand at a uniform rate. In subsequent runs, we fed material that was about 4 mesh to the roll crusher; this required more passes and provided more opportunity for production of fines, but the initial reductions were less severe and appeared to reduce flaking. Since the mechanical feeding is somewhat erratic, the rolls tend to overload at times, and this increases the production of fines. We have not attempted to optimize the reduction schedule, but have kept it constant in order to compare the materials being crushed.

We are characterizing the original and recycled material in an attempt to explain the difference in crushing behavior. The chemical compositions of the roll-crushed UAl_x are given in Table 13.2. As expected, the impurity levels and U contents are higher for a given batch after recycling. However, comparative ranges of impurities

Table 13.1. Size Distribution of Roll-Crushed UAl_x

Batch Number	Size Distribution,[a] wt %									
	U.S. Standard Mesh Size					Fines (−325) in −100 Mesh Material	Usable Material for Advanced Test Reactor[b]	Usable Material After Further Crushing[c]	Total Yield	Amount for Recycle
	+100	−100 +140	−140 +200	−200 +325	−325					
65-A	3.0	21.6	17.2	16.0	42.2	43.5	73.0	1.0	74.0	25.0
67-A	5.9	20.1	19.4	15.2	39.5	41.9	72.9	2.0	74.9	25.1
69-B	1.7	18.0	18.8	16.8	44.7	45.5	71.5	1.7	73	26.8
69-BR[d]	0.9	24.2	22.8	18.2	34.0	34.2	86.9	0.3	87.2	12.8
69-A	8.7	22.1	20.0	15.1	34.1	37.4	76.2	2.9	79.1	20.9
71-D	1.8	19.5	20.4	18.0	40.4	41.0	77.1	0.6	77.7	22.3

[a]Material sieved 15 min on Ro-Tap Shaker.

[b]Material must be −100 mesh and contain a maximum of 25 wt % material that is −325 mesh.

[c]This is one-third of the +100 mesh material, which is typical of the yield from one pass through a hammer mill.

[d]Recycled from batch 69-B; the crushed powders from 69-B were compacted and arc-melted.

Table 13.2. Chemical Composition of Roll-Crushed[a] UAl_x

Batch Number	Composition, wt %					
	U	Al	H_2	N_2	O_2	C
65-A	65.1	34.0	0.0002	0.0035	0.013	0.10
67-A	67.1	31.8	0.0035	0.0064	0.11	0.07
69-B	69.1	30.2	0.0042	0.0078	0.078	0.029
69-BR[b]	69.6	29.3	0.0120	0.0370	0.17	0.14
69-A	70.0	29.8	c	c	c	c
71-D	70.6	29.0	0.010	0.0048	0.053	0.026

[a]Sample taken from −100 +325 mesh fraction.

[b]Recycled from batch 69-B; the powders from 69-B were compacted and arc-melted.

[c]Not analyzed.

(except for O content) have been observed in first-cycle material with no noticeable effect on crushing behavior.

These results indicate that the U content of the UAl_x has no appreciable effect in the range of 65 to 71% U. The yields of 75 to 80% are typical of the present crushing setup. We suppose that the yields could be improved with a more nearly uniform feeding mechanism and perhaps by adjustments of the reduction schedule.

Fabrication of Composite Plates Containing ZrO_2 (M. M. Martin, J. H. Erwin)

Voids introduced into composites during fabrication enhance irradiation performance of Al-base dispersion fuel plates.[2] Dispersions of up to 2 wt % B_4C in Al, however, contain less than 0.5 vol % of void space to accomodate He from the $^{10}B(n,\alpha)^7Li$ reaction. Although the 0.55 wt % B_4C-Al burnable poison of the plates in the inner annulus of the HFIR elements performs satisfactorily in reactor, we do not know the

[2]M. M. Martin and A. E. Richt, Trans. Am. Nucl. Soc. 12, 98 (1969).

irradiation performance of plates that contain higher concentrations of B_4C. Such plates, with only 0.3 to 0.5 vol % of void space, may swell significantly as the He accumulates.

The void content of Al-base dispersion fuel plates depends upon the type and concentration of the fuel compound. Thus, the addition of an inert dispersoid to a B_4C-Al dispersion may increase the quantity of effective voids. One choice is ZrO_2. It should be dimensionally stable in the reactor to extremely high neutron fluences and chemically compatible with B_4C and Al.

We investigated the quantity of fabrication voids retained by dispersions that contained 10, 20, 30, 40, and 50 wt % ZrO_2 when roll clad with type 6061 Al. The ZrO_2 powder used to make the dispersions was essentially theoretically dense material of 5.564 g/cm^3 and was analyzed as 70.0 wt % Zr. The particles were 75 wt % −100 +325 mesh and 25 wt % −325 mesh. The general fabrication scheme for the composite test plates included only HFIR standard techniques of powder metallurgy and roll bonding.

We determined void volume from measurements of plate density. As shown in Fig. 13.1, the quantity of voids in the plates increased exponentially from 0.3 vol % for the 10 wt % ZrO_2 dispersion to 3.0 vol % for the 50 wt % ZrO_2 dispersion. However, these void levels are small compared to those in dispersions of U_3O_8 and UAl_x in Al in which the dispersoids are also essentially 100% dense. We shall examine this more thoroughly. Sections of the plates are being polished for visual evidence of differences between the U_3O_8, UAl_x, and ZrO_2 dispersions.

Metallographic Examination of Miniature Composite Plates Bombarded with Protons for Study of Blistering (K. Farrell)

A previous report[3] described an experiment designed to study the effect of a prescribed quantity of H on the formation of blisters in Al-base simulated fuel plates. We made miniature plates, 0.050 in. thick, that contained a powder-metallurgy Al core clad with 0.015-in.-thick

[3]M. M. Martin and R. T. King, Fuels and Materials Development Program Quart. Progr. Rept. March 31, 1969, ORNL-4420, pp. 222–225.

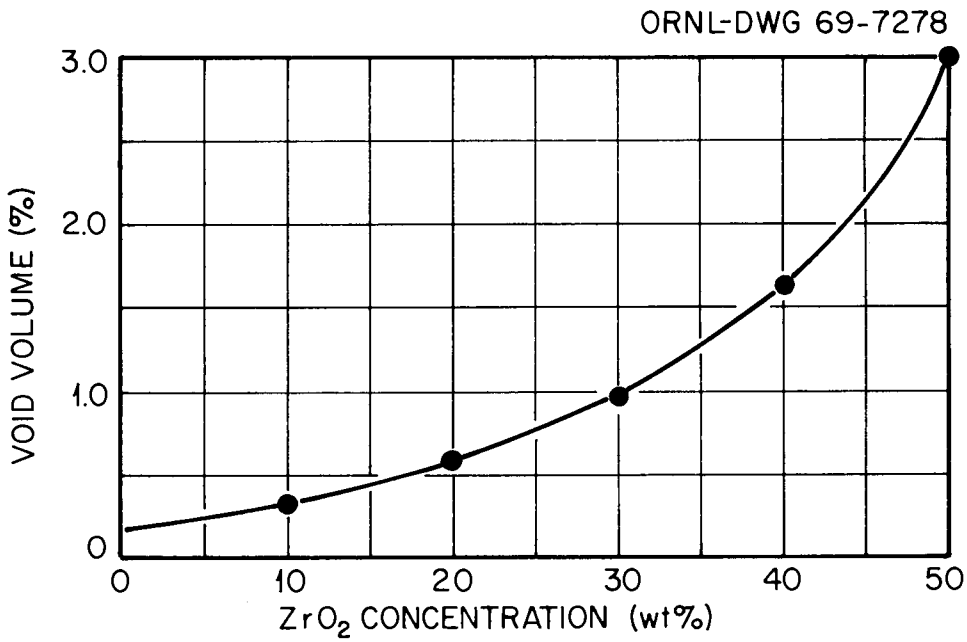

Fig. 13.1. Effect of Dispersoid Concentration on Void Volume of Plates Containing ZrO_2 Dispersed in Alcoa 101 Al and Clad with Type 6061 Al.

type 6061 Al. We injected the hot-rolled plates on one side to a depth of 0.020 in. with an estimated 0.33 wt ppm H in a cyclotron and subjected them to various annealing treatments to develop blisters.

When no visible blisters developed, we submitted the annealed plates to the electron microscopy group for microscopic examination. An extensive optical examination of polished and etched sections through the bombarded specimens and through control specimens revealed no evidence of surface blisters or internal gas bubbles. Within the bombarded specimens, no differences could be seen between the bombarded regions and the unbombarded regions. The interfaces between the Alcoa 101 Al and the type 6061 Al were clearly visible, and the bonding appeared good. The type 6061 Al contained many large precipitates or inclusions that could presumably act as sinks for H_2. No gas bubbles could be detected by transmission electron microscopy, however, and we found no other structural damage that could be attributed to the proton bombardment.

Roll Bonding (J. H. Erwin)

We are continuing our investigation of the present chemical cleaning process — Oakite 160 followed by HNO_3 — for preparing the surfaces of

types 6061 and 2219 Al before they are roll bonded. Since limitations of the process variables have not been studied, this investigation is concerned with the metallurgical bond as affected by (1) depletion of the cleaning solution, (2) concentration of the cleaning solution, (3) etching and neutralization time, (4) variations in temperature, and (5) time interval between cleaning and rolling. We are also evaluating the probable use of a commercial deoxidizer rather than HNO_3 for removing the smut after the treatment in Oakite 160.

We found it necessary to pickle the Al sheet in Oakite 160 while it was in the T6 condition, before the heat treatments in Oakite 160, to ensure that the oxide was removed at a uniform rate from the surface of the plate. This pretreatment in Oakite 160 is not always needed, but it gives more consistent results. Attempts to analyze the surface chemistry of plates that require pickling treatment have not revealed the nature of the surface contamination.

Susceptibility to Blistering of Fuel Plates Containing Shaped Fuel Cores (J. H. Erwin)

In the fabrication of fuel plates by the picture-frame technique, blistering may become a problem if shaped fuel cores are used to circumvent the excessive thickness, or "dogbone," produced at the ends of some rolled cores. We have begun an investigation of this condition.

Simulated fuel cores of wrought types 6061 and 2219 Al were rolled in type 6061 Al frames and cover plates. This combination of materials provides a strength relationship between core and cladding of about 1:1.13. Although the U_3O_8 and UAl_3 fuel cores clad with type 6061 Al have a strength factor of 1.5 or greater, we were interested at this point in the probability of blistering.

The simulated cores were machined to replicas of the HFIR outer annulus now in use, 0.273 × 2.166 × 2.642 in., but the long edges were thinned to half their usual thickness (see Fig. 13.2) by milling with a cutter with a 1/8-in. radius for the "A" cores or a 1/2-in. radius for the "B" cores. The cores were then loaded into chemically cleaned HFIR duplex billets. The volume of the A core was about 0.43 cm^3 greater and the volume of the B core was about 0.18 cm^3 less than the volume of the cavity. Five plates were fabricated with each of the core alloys,

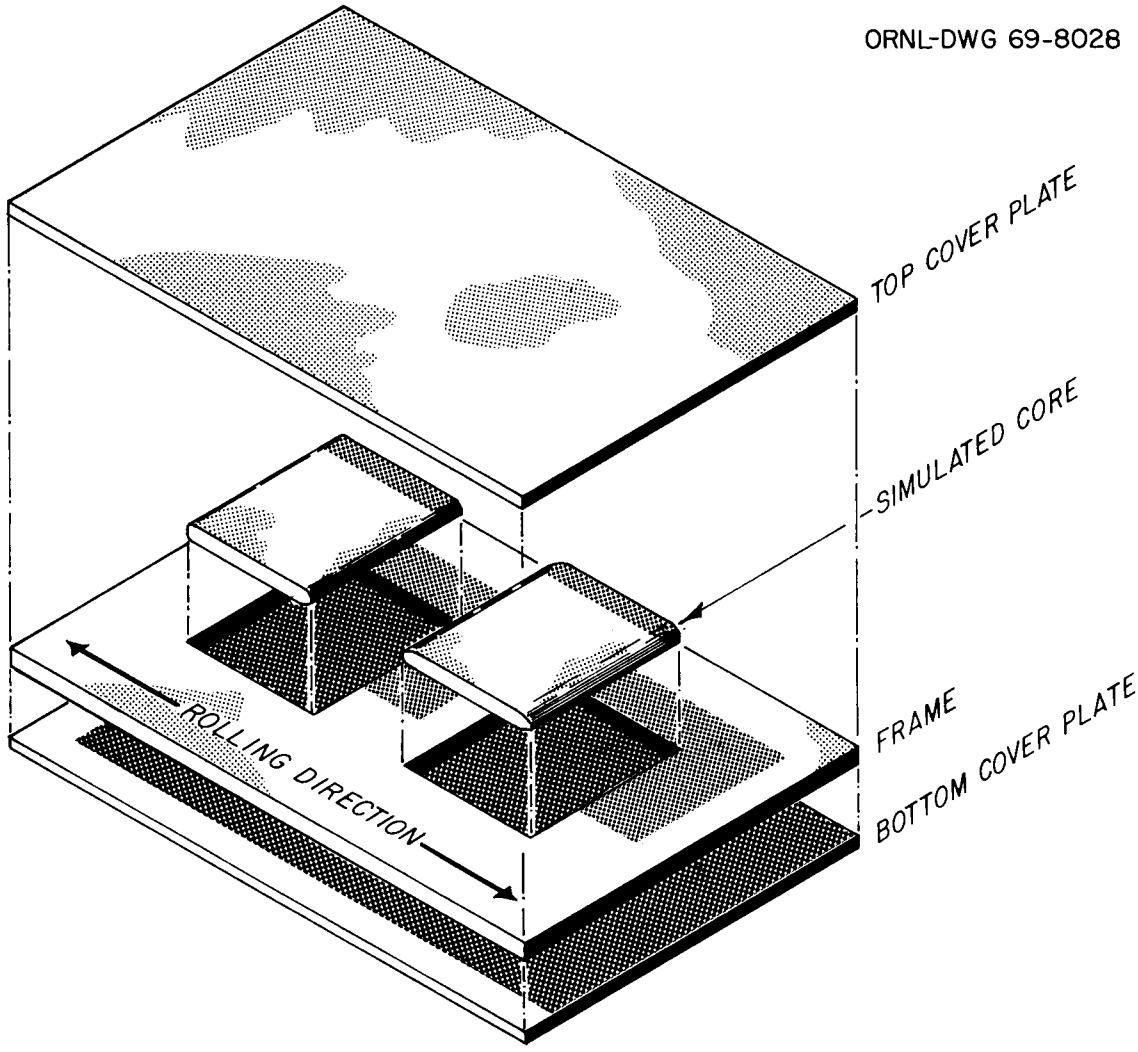

Fig. 13.2. Billet Assembly Showing Cores with Thinned Edges.

types 6061 and 2219 Al, and the investigation was duplicated with unclad and 1100 Alclad type 6061 Al frames and cover plates — a total of 40 plates. The billets were heated 45 min at 490°C and reduced in ten passes from 0.481 to 0.063 in. in a 12-in. two-high mill. The ten passes in the rolling schedule included two passes at 15% per pass, five at 24% per pass, and one each at 16, 12, and 3% per pass. The billet was rotated 180° about each axis and was reheated between passes. Nine additional cores of type 6061 Al shaped to the 1/2-in. radius relief and three unshaped cores of type 2219 Al were rolled in the same way except that the first four passes reduced the billet 10% per pass

and were followed by ten passes at 15% per pass. After hot reduction, all the plates were annealed 1 hr at 500°C to relieve stress, cold rolled to 0.050 in. in thickness, and annealed 2 hr at 500°C.

The rolled plates blistered profusely, as shown in Table 13.3. In contrast, plates from earlier studies of the fit of frame and cavity, with cores of material produced by powder-metallurgy techniques, had no blisters. We presently have no explanation for this difference in behavior. We noted, however, that the blisters produced in the plates rolled from the A cores (1/8-in. radius) and from those B cores (1/2-in. radius) rolled at the higher reduction per pass were larger than those of the other plates (1/2 in. in diameter or larger). We are investigating the effect of the relationship between unfilled cavity volume and rolling schedule on the formation of blisters.

HFIR Fuel Plates with Increased Fuel Loading (R. W. Knight, M. M. Martin, J. H. Erwin)

We are investigating the fabricability of HFIR fuel plates containing fuel loadings increased to 25% (for the outer annulus) and 35% (for the inner annulus) above the present nominal loading. Our ultimate goal is to produce a fuel element with a longer operating life. Along with this increased loading we are investigating the comparative economy of using high-fired and burned U_3O_8 with varying distributions of particle sizes. The cost of burned U_3O_8 is about half that of high-fired U_3O_8 and may be lowered further if one is able to increase the amount of −325 mesh material.

We have manufactured 48 fuel plates according to the Metals and Controls, Inc., HFIR reference process: 16 were fabricated with present materials and processes, 8 with burned U_3O_8 with present process loading, 16 with 125% of the present loading of high-fired U_3O_8, and 8 with 125% of the present loading of burned U_3O_8. Half were inner annulus plates and half were outer annulus plates. Comparative data concerning these plates are shown in Table 13.4. Note that the void volume increased an average of 3% and that the average spread increased 1% in the burned U_3O_8 plates.

Table 13.3. Blistering in Simulated Fuel Plates Containing "Shaped" Simulated Fuel Cores

Plate Description	Number of Cores Rolled	Number of Plates Blistered	
		One End	Both Ends
I. Alclad type 6061 Al cover plates and frames rolled according to standard HFIR schedule			
a. Simulated cores of type 6061 Al			
1. A cores (1/8-in. radius)	5	3	1
2. B cores (1/2-in. radius)	5	2	3
b. Simulated cores of type 2219 Al			
1. A cores	5	3	1
2. B cores	5	3	2
II. Unclad type 6061 Al cover plates and frames rolled according to standard HFIR schedule			
a. Simulated cores of type 6061 Al			
1. A cores	5	3	1
2. B cores	5	1	4
b. Simulated cores of type 2219 Al			
1. A cores	5	0	4
2. B cores	5	0	5
III. Alclad type 6061 Al cover plates and frames rolled according to extended-reduction schedule[a]			
a. Simulated B cores of type 6061 Al	5	2	1
b. Simulated cores of type 2219 Al, unshaped (no radius)	3	2	
IV. Unclad type 6061 Al cover plates and frames rolled according to extended-reduction schedule[a]			
a. Simulated B cores of type 6061 Al	4		4

[a]Extended-reduction schedule: four passes at 10% per pass followed by ten passes at 15% per pass.

Table 13.4. Comparison of Fuel Plates with Increased Loading and Burned U_3O_8 Fuel with Reference Process

Type of Plate	Location	Type of U_3O_8	Loading (g ^{235}U)	Spread (%)	Void Volume (vol %)
Standard	Inner	Burned	15.19	4.0	5.2
		High-fired	15.18	3.0	3.0
Advanced	Inner	Burned	20.28	3.9	6.7
		High-fired	18.98	3.5	3.8
Standard	Outer	Burned	18.47	4.0	7.2
		High-fired	18.44	2.2	4.2
Advanced	Outer	Burned	23.10	3.8	9.1
		High-fired	23.05	3.3	5.4

Although no problems were encountered during the fabrication of these plates, considerable work remains to be done before a manufacturing process is established. New standards will have to be fabricated for determination of homogeneity by x-ray attenuation and of nonbonding by ultrasonic testing before we can evaluate these plates with higher fuel loadings and with burned oxide fuel, and plates of each kind must be formed to determine their forming characteristics and capabilities.

Accordingly, we have requested that Metals and Controls, Inc., manufacture according to standard HFIR procedures one lot of fuel plates for the inner and outer annuli with fuel loadings of 20.495 and 23.051 g ^{235}U, respectively. Twelve plates of each type will be studied through the stage of inspection for formed plates; the remaining 12 plates of each type will only be studied through the stage of final inspection for flat plates. Normal inspection standards will be applied except for ultrasonic and homogeneity inspection. New ultrasonic standards will be made from one of each type of flat plate. Homogeneity will be inspected by slow-speed scanning and analysis of each scan. All plates and data will then be shipped to ORNL for further work.

When 25 kg of burned oxide that has been ordered is received, four more lots of fuel plates will be fabricated at Metals and Controls, Inc., two with standard loading and two with increased loading. All these plates will be evaluated in the same way as those described above.

Welding and Assembly

G. M. Slaughter

Joining Fuel Plates to Side Plates (W. J. Werner)

We are investigating the effects of variations in electron-beam welding conditions on weld penetration and geometry.

In addition to welds made with the beam focused on the work surface, we examined welds made with the electron beam focused 1/8 in. above and 1/8 in. below the surface. We used a distance of 7/8 in. between the welding gun and the workpiece and a constant travel speed of 20 in./min. The beam voltage and beam current for the study are shown in Table 13.5. Each welded specimen was sectioned at three random positions perpendicular to the welding direction. Samples from these sections were examined metallographically to determine weld width and depth. The results are shown in Table 13.6.

Table 13.5. Welding Conditions for Study of Welding Variables

Weld Number	Beam		Focusing Current[a] (ma)
	Voltage (kv)	Current (ma)	
1	20	65	110
2	16	85	105
3	16	65	105
4	24	65	135
5	20	75	120
6	24	85	135
7	16	85	105
8	24	85	135
9	24	65	135
10	16	75	105
11	16	65	105
12	24	75	135
13	20	75	120
14	20	85	120

[a]The beam was focused on the surface of the workpiece for all the welds.

Table 13.6. Average Dimensions of Electron-Beam Welds Made in Type 6061 Aluminum Plate with Beam Voltage of 16 to 24 kv, Beam Current of 65 to 85 ma, and Variable Beam Focus

Weld Dimensions, in.					
Focus on Surface		Focus 1/8 in. Below Surface		Focus 1/8 in. Above Surface	
Width	Depth	Width	Depth	Width	Depth
0.119	0.114	0.091	0.067	0.137	0.108
0.108	0.109	0.100	0.047	0.133	0.092
0.104	0.077	0.083	0.032	0.115	0.052
0.144	0.127	0.142	0.092	0.158	0.103
0.134	0.142	0.139	0.095	0.160	0.104
0.168	0.210	0.182	0.164	0.203	0.162
0.118	0.137	0.111	0.157	0.150	0.099
0.178	0.202	0.154	0.096	0.214	0.210
0.136	0.139	0.124	0.062	0.190	0.131
0.104	0.088	0.093	0.032	0.148	0.064
0.102	0.059	0.085	0.026	0.114	0.052
0.150	0.140	0.142	0.074	0.164	0.105
0.125	0.133	0.122	0.058	0.159	0.104
0.141	0.195	0.127	0.066	0.156	0.084

The data show that a change in position of focus affects both weld width and penetration. For example, focusing below the surface of the work in general produced significant decreases in weld width and penetration, and the fusion zone became "rectangular" compared with the normal "spike" produced by focusing on the workpiece. Focusing above the surface of the work, on the other hand, produced a broader weld with less penetration, and the fusion zone resembled a "triangle." The changes in weld width below the plate surface (i.e., weld geometry) are of major importance since a wide fusion zone is needed to ensure adequate strength at the junction of the fuel plate and side plate in the HFIR element. The data are being analyzed for this information.

The short test assembly shown in Fig. 13.3 was assembled and welded to investigate the applicability of these welding conditions to an actual HFIR element. The experiment confirmed the applicability of the process.

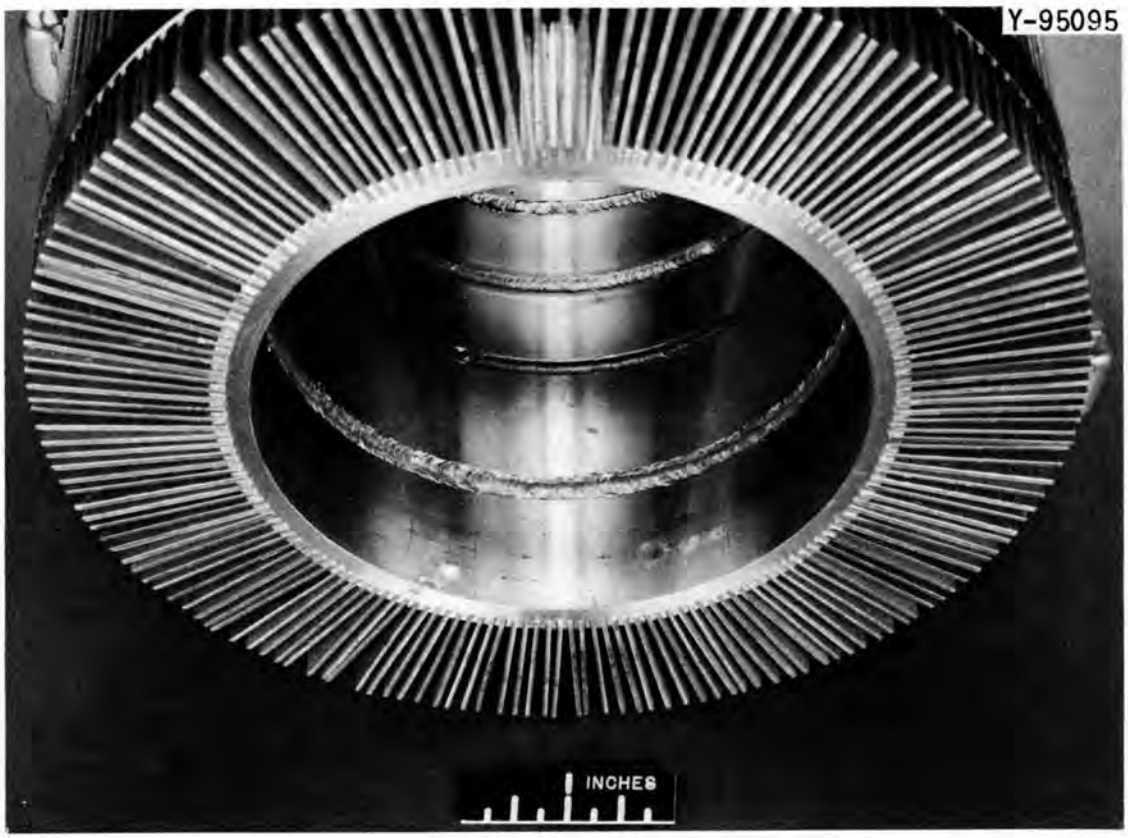

Fig. 13.3. Test Element After Welding.

Irradiation Testing of Dispersion Fuel Plates

W. R. Martin

Status of Current and Planned Tests in the ETR (M. M. Martin, J. H. Erwin)

Irradiation testing of two standard and six Ni-coated fuel plates[4] in the G-12 loop of the Engineering Test Reactor (ETR) began with cycle 102 and continued through June 12, 1969, for a total exposure of

[4]M. M. Martin and J. H. Erwin, Fuels and Materials Development Program Quart. Progr. Rept. March 31, 1969, ORNL-4420, pp. 230–237.

4330 Mwd. During the night of June 12–13, 1969, the reactor was scrammed for reasons independent of the operation of the G-12 loop. A significant quantity of heat, however, was still being generated in the test plates from decay of fission products and absorption of gamma radiation. Inadvertently, N_2 gas was somehow introduced into the loop and displaced the coolant water. Thermocouples in our instrumented test plates recorded a sharp temperature rise from about 260 to 375°C. In a visual examination in the canal after the experiment was removed from the loop, test plate 0-68-1635, which was not coated with Ni, was bowed in the center while the remainder of the plates appeared to be in good condition. However, we are unable to determine if the Ni coating remained on the surface of the plates. The plates will be returned to ORNL for evaluation as soon as the radioactivity level is low enough for shipping.

The standby G-12 loop loading for cycle 102 contained our experiment on the effect of powder fines on the irradiation performance of burned and high-fired U_3O_8 dispersed in Al (ref. 4). The unscheduled shutdown in cycle 102 permitted the reinsertion of this experiment into the reactor for the remainder of the cycle. The eight test plates, including two equipped with thermocouples, have now received a total exposure of greater than 10,000 Mwd. They will be returned to ORNL after cycle 102 for evaluation along with the two standard and six Ni-coated test plates mentioned above.

Test plates containing sol-gel U_3O_8-Al, burned U_3O_8-Al, and B_4C-Al dispersions[4] were fabricated and shipped to the ETR site for irradiation in cycle 103. The experiment on the plates that contain U requires four ETR cycles; one plate of each type of U_3O_8 will be replaced after the second and third cycles. For all practical purposes, the ^{10}B in the test plates that contain B_4C will have been totally burned up after one cycle of irradiation.

Characterization of Mini-Type Test Plates Containing U_3O_8 (M. M. Martin, J. H. Erwin)

The fuel plates for our four-cycle experiment are described in Table 13.7. We fabricated 30 mini-type test plates for these irradiations.

Table 13.7. Mini-Type Test Fuel Plates for Irradiations in the G-12 Loop[a] of the Engineering Test Reactor Starting with Cycle 103

Plate Reference Number	Number of Cycles	Fuel Dispersoid[b]				Slot Location
		Core Concentration (wt %)	Loading of ^{235}U (g)	Major Size Range (mesh)	−325 Mesh Particles (wt %)	
			Sol-Gel U_3O_8			
0-89-1657	3	51.16	1.203	−170 +325	50	3B
-1907	4	51.16	1.204	−170 +325	10	4A
-1647	2	51.16	1.205	−140 +170	0	4B
-1660[c]	1	51.16	1.200	−170 +325	50	3B
-1908[c]	2	51.16	1.203	−170 +325	10	4B
			Burned U_3O_8			
0-90-1662	3	53.04	1.190	−170 +325	10	2A
-1666	2	53.04	1.191	−170 +325	26	2B
-1671	4	53.04	1.188	−170 +325	54	3A
-1911[c]	1	53.04	1.191	−170 +325	10	2A
-1672[c]	2	53.04	1.189	−170 +325	54	2B

[a]All plates located in tier 1 of the G-12 loop.

[b]Dispersed in Alcoa 101 Al; fuel compact then clad with type 6061 Al.

[c]Replacement test plates.

These plates contain about 1.57 g $^{235}U/cm^3$ of fabricated core volume and represent a 37.5% increase over the concentration now used for the HFIR outer annulus. The principal variables in the experiment are overall particle size and the content of fines (−325 mesh particles) in the two oxides.

The densification during rolling, rolled density, and fabrication voids of the fuel core in the mini-type test plates showed little, if any, dependence on the initial content of fines in the uranium oxides. Average values for these properties are presented in Table 13.8. Note that the void volume of plates that contain burned U_3O_8 is considerably

Table 13.8. Fines Content, Voids, and Density of the Cores in Mini-Type Fuel Plates that Contain Sol-Gel or Burned U_3O_8

Number of Plates	Fines Content of U_3O_8 Powder (wt %)	U_3O_8 Concentration (vol %)	Fabrication Voids[a] (vol %)	Core Density[b] (g/cm^3)	Density Change Upon Rolling[c] (%)
		Sol-Gel U_3O_8			
5	0	25.12	3.61	3.9678	2.32
5	10	25.08	3.74	3.9623	2.45
5	50	24.93	4.34	3.9377	2.59
		Burned U_3O_8			
5	10	25.91	9.57	3.7358	2.44
5	26	25.95	9.42	3.7419	2.65
5	54	25.91	9.58	3.7351	2.43

[a]Estimated standard deviation based on 24 degrees of freedom: ±0.10.

[b]Estimated standard deviation based on 24 degrees of freedom: ±0.0039.

[c]Estimated standard deviation based on 24 degrees of freedom: ±0.41.

higher than that of plates that contain the sol-gel U_3O_8. We conclude, from the void volume alone, that the irradiation performance of the plates that contain burned U_3O_8 should be superior to that of the plates that contain sol-gel fuel.

Characterization of Mini-Type Test Plates that Contain B_4C (M. M. Martin, J. H. Erwin)

We plan to determine the breakaway swelling temperature of irradiated dispersions of B_4C in Al clad with type 6061 Al. The concentrations of B_4C to be investigated are 0.00, 0.52, 0.78, 1.05, 1.75, and 2.00 wt %; the last value corresponds to 7.4 mg $^{10}B/cm^3$ of fabricated core volume. Table 13.9 lists the poison plates shipped to the ETR site for irradiation during cycle 103. To achieve the highest exposure temperature, the irradiation will be carried out in the sixth tier position of the G-12 loop.

Table 13.9. Mini-Type Poison Plates for Irradiation in G-12 Loop[a] of Engineering Test Reactor During Cycle 103

Plate Reference Number	Core Composition[b] (wt %)	Loading of ^{10}B (mg)	Slot Location
0-83-1677	Alcoa 101 Al	0.00	2B
0-84-1681	Al–0.52% B_4C	1.47	3A
0-85-1687	Al–0.78% B_4C	2.21	4B
0-86-1691	Al–1.05% B_4C	2.97	2A
0-87-1697	Al–1.75% B_4C	4.97	4A
0-88-1901	Al–2.00% B_4C	5.66	3B

[a]All plates located in tier 6 of the G-12 loop.

[b]Clad with type 6061 Al.

We fabricated 25 mini-type poison plates; 16 of these, or 64%, were acceptable. All 25 plates passed ultrasonic tests for 1/16-in.-diam defects and visual examination for blisters after being heat treated for 1 hr at 500°C. Since radiographic techniques adequately delineated the B_4C-Al dispersion in the envelope of type 6061 Al, we were able to mark and inspect the core dimensions. This inspection led us to reject eight plates for excessive core length and one plate for mislocation of the core.

After the poison plates were fabricated into composites by roll bonding and annealing at 500°C, all had the same void content, 0.27 vol% of the fabricated core. We would not expect so small a concentration of voids to be a significant factor in the irradiation performance of these plates.

Postirradiation Examination of HFIR Fuel Elements (R. W. Knight, A. E. Richt)

Preliminary results of the postirradiation examination of HFIR fuel element 21-0 indicated that the assembly had performed quite satisfactorily through 2309 Mwd of reactor service. Except for postirradiation blister-annealing tests on sections of the fuel plates, all phases of

the examination program have been completed, and the results continue to be extremely encouraging. We found no significant changes in the dimensions of either the assembly or individual fuel plates. Gamma scans indicated no abnormalities in the distribution of burnup in the element, and results of analytical determinations of burnup were in excellent agreement with the predicted values. Metallographic examination of sections of the fuel plates revealed no evidence of blistering, separation of cladding from the cores, or breakup of the fuel. No incipient cracks were found in the corners of the fuel particles where failure usually starts. Corrosion of the cladding did not appear to be excessive; we estimate that less than 0.001 in. of the nominally 0.010-in.-thick cladding was lost to corrosion. The swelling induced by irradiation of the fuel plates also appeared to be rather insignificant; even in the regions of maximum burnup the fuel core appeared to have increased less than 0.001 in. in thickness. Such small changes should have essentially no effect upon satisfactory behavior of the elements during operation.

As shown in Table 13.10, the oxide film on the surfaces of the fuel plates from fuel element 21-0 was considerably thinner than that found on the plates from fuel element 5-0. The histories of these two elements were different in the following respects: (1) fuel element 21-0 operated about 11% longer than the element 5-0 — 2309 vs 2046 Mwd, respectively — and (2) element 5-0 was subjected to boiling water for 24 hr before it was placed into operation in the reactor while element 21-0 was not. This pretreatment in boiling water was intended to form a thin oxide film on the surfaces of the element to prevent excessive corrosion during storage of the elements in the reactor pool before operation. Such pretreatment was discontinued early in the history of the reactor. Results of the examination of these two elements indicate that such a pretreatment is undesirable in that it results in the formation of a thicker oxide film during operation in the reactor.

Figure 13.4 shows that the extent of reaction between the U_3O_8 fuel particles and the Al matrix was about the same at corresponding locations in fuel plates from both elements. Since the oxide film on the surfaces of the plates from element 21-0 was considerably thinner than that on the plates from element 5-0, one would expect that the plates

Table 13.10. Comparison of Calculated and Measured Thicknesses of Oxide Films on HFIR Fuel Elements 5-0 and 21-0

Axial Location[a] (in.)	Thickness of Oxide Film at Indicated Location (in.)								
	Inner Edge of Core			Hump in Fuel Core			Outer Edge of Core		
	Calculated	Measured		Calculated	Measured		Calculated	Measured	
		Element 5-0	Element 21-0		Element 5-0	Element 21-0		Element 5-0	Element 21-0
	$\times 10^{-3}$	$\times 10^{-3}$	$\times 10^{-3}$	$\times 10^{-3}$	$\times 10^{-3}$	$\times 10^{-3}$	$\times 10^{-3}$	$\times 10^{-3}$	$\times 10^{-3}$
2.0	0.31	0.40	0.25	0.28	0.40	0.25	0.13	0.30	0.25
3.0	0.18	0.55	0.15	0.17	0.60	0.15	0.10	0.40	0.20
7.5	0.37	1.05	0.25	0.32	1.40	0.40	0.28	0.70	0.15
12.0	0.60	1.50	0.45	0.55	1.10[b]	0.90	0.51	1.00	0.25
16.6	0.60	1.50	0.50	0.49	1.00[b]	0.95	0.41	0.90	0.25
21.0	0.47	0.90	0.35	0.39	0.50[b]	0.45	0.27	0.60	0.20
22.0	0.70	0.85	0.15	0.60	0.50[b]	0.45	0.30	0.60	0.15

[a]Distance from upper end of fuel plate.

[b]Partial spalling of the oxide film found in these regions.

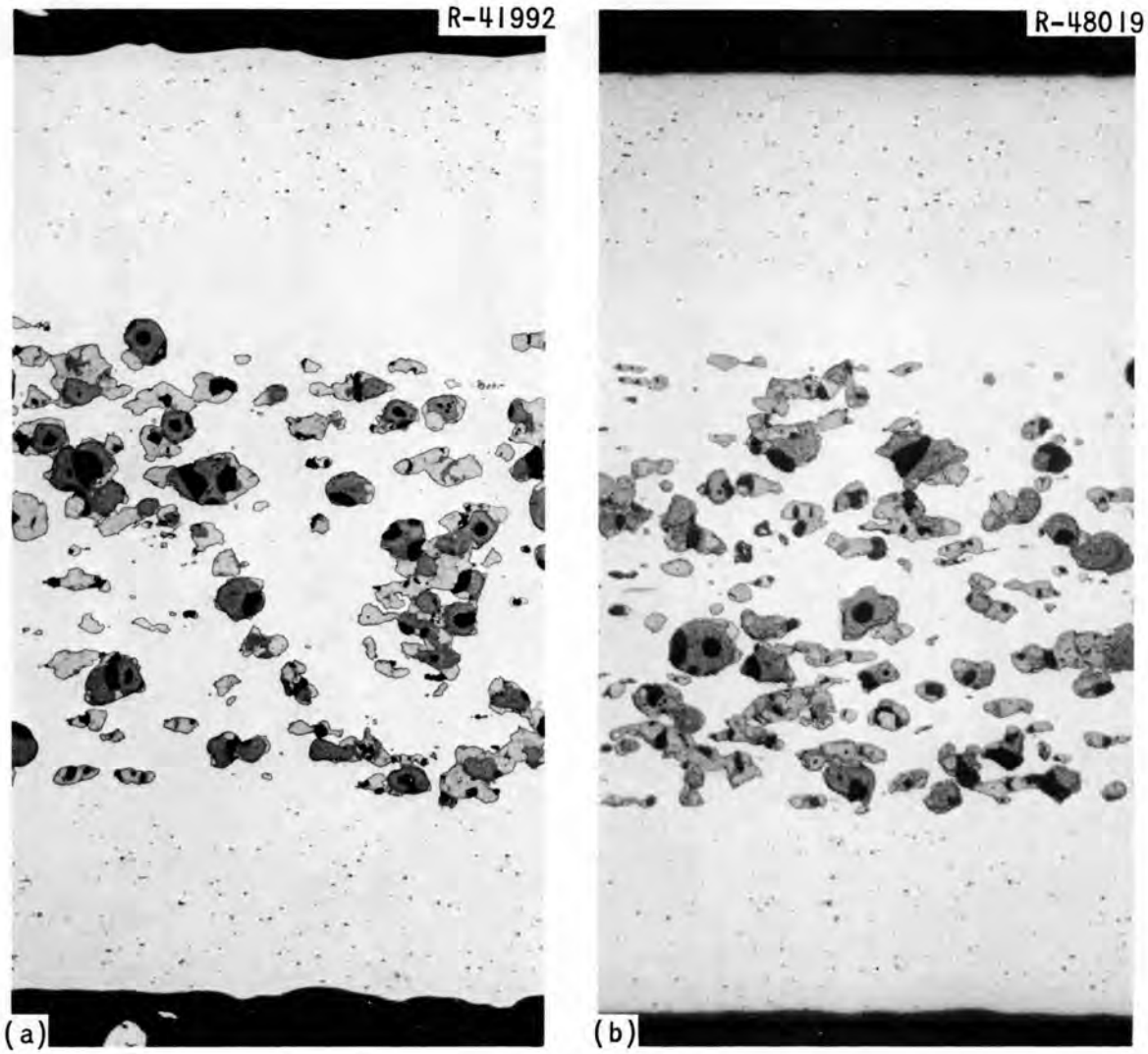

Fig. 13.4. Typical Microstructure of Sections of Irradiated HFIR Fuel Plates. Areas shown are from corresponding regions of plates from elements (a) 5-0 and (b) 21-0. As polished. 100×.

from element 21-0 should have operated at a lower temperature and exhibited less reaction. However, the initial size of the particles of the U_3O_8 fuel used to fabricate the plates for element 21-0 was slightly smaller, and this element operated slightly longer than element 5-0.

Determination of Homogeneity in Fuel Plates

R. W. McClung

Radiographic Densitometry (B. E. Foster, S. D. Snyder)

We completed the experimental portion of our study of the capabilities and limitations of a radiographic densitometry technique for measuring fuel inhomogeneity. Most of the data were published,[5] and a final report is being prepared.

X-Ray Attenuation (B. E. Foster, S. D. Snyder, M. M. Martin)

The 32 enriched U_3O_8 fuel plates[6] that were made to determine the effects of particle size on the calibration of the x-ray attenuation system were scanned at 60 kilovolts constant potential (kvcp). They had been previously scanned at 50 and 55 kvcp (ref. 7). The scanning at 55 and 60 kvcp was needed to provide data for calibration curves at these energies because of the increased attenuation of x rays at 50 kvcp for higher loadings of U. Two of these plates, an inner annulus and an outer annulus, each with a nominal loading of the supplied powder, were scanned at specific sample areas at 50, 55, and 60 kvcp, and these samples were removed from the plates by the gang-cutting procedure established by the machine shop. The results of subsequent chemical analysis (±0.2% quoted precision) for the U content of these samples are shown in Table 13.11 along with the values for U content predicted from the original calibration curve of x-ray attenuation and the relatively high percentage of deviation between them.

Another test compared the charged weight of U with that determined by a total dissolution of these plates for two miniature irradiation

---

[5]B. E. Foster, S. D. Snyder, and R. W. McClung, Fuels and Materials Development Program Quart. Progr. Rept. March 31, 1969, ORNL-4420, pp. 237–238.

[6]B. E. Foster and S. D. Snyder, Fuels and Materials Development Program Quart. Progr. Rept. Sept. 30, 1968, ORNL-4350, p. 288.

[7]B. E. Foster, S. D. Snyder, and R. W. McClung, Fuels and Materials Development Program Quart. Progr. Rept. Dec. 31, 1968, ORNL-4390, pp. 259–260.

Table 13.11. Comparative Values of Uranium Content in HFIR Plate Samples as Determined by Chemical Analysis and X-Ray Attenuation

Sample Number	Chemical Analysis of Uranium Content Per Sample (mg)	X-Ray Attenuation Value for Uranium Content Per Sample (mg)	Deviation of Chemical Analysis Value From X-Ray Value (%)
		Inner Annulus Plate H-2081	
1	26.15	23.24	+12.5
2	31.43	29.90	+5.1
3	37.04	35.89	+3.2
4	39.30	37.68	+4.3
5	43.31	42.26	+2.5
6	45.99	44.78	+2.7
7	49.25	47.91	+2.8
8	51.09	49.74	+2.7
9	51.94	50.48	+2.9
10	51.46	52.67	−2.3
11	51.84	49.79	+4.1
12	49.66	47.89	+3.7
13	49.08	47.60	+3.1
14	48.03	46.77	+2.7
15	45.15	44.23	+2.1
16	42.16	40.93	+3.0
17	36.20	35.01	+3.4
			(Average deviation +3.4%)
		Outer Annulus Plate H-2097	
1	50.19	50.37	−0.35
2	57.16	56.59	+1.0
3	70.00	69.99	+0.02
4	74.91	76.52	−2.1
5	78.18	79.94	−2.2
6	77.75	79.82	−2.6
7	76.10	77.42	−1.7
8	72.25	73.95	−2.3
9	67.19	68.56	−2.0
10	61.68	62.18	−0.8
11	56.74	58.19	−2.5
12	48.39	49.63	−2.5
13	41.72	42.39	−1.6
14	33.51	33.44	+0.2
15	28.33	26.38	+7.4
			(Average deviation −0.8%)

test plates, an instrumented plate (03-888) and a sample plate (0-67-977), both of which contained high-fired U_3O_8. The instrumented plate was submitted to Analytical Chemistry as a whole plate and totally dissolved. The sample plate was sheared across the width into 22 sections, 10 of them 1/8 in. wide, 6 of them 1/4 in. wide, and 6 of them 1/2 in. wide. There was no significant loss of material due to the cutting: the plate weighed 17.8240 g before shearing, and the sum of the weights of the sheared pieces was 17.8237 g. The comparative results are shown below:

Plate Number	Charged Weight (g)	Weight Determined by Chemical Analysis (g)	Deviation From Charged Weight (%)
03-888	2.362	2.393	+1.31
0-67-977	2.097	2.142	+2.15

These deviations are similar to those noted in Table 13.11. This further emphasizes the discrepancy between determinations of weight by analytical chemistry and by either x-ray scanning or charged loading.

Radiation Scattering (B. E. Foster, S. D. Snyder)

We have continued preliminary investigation of the use of Compton backscattered radiation for measuring the thickness of the claddings on Al fuel plates. The initial study involves the use of a 1/2 curie ^{241}Am source and associated shielding with the NaI(Th) crystal-photomultiplier detector. We are evaluating different photomultipliers and crystals (with and without Be windows) for best resolution of the Compton energy. A venetian-blind type of photomultiplier with the Be window crystal gives the best resolution. Equipment problems in both the single- and multi-channel analyzers have slowed the project, and we have been unable to get quantitative results relating the percentage of change in count rate to a given change in cladding thickness.

PART V

ENGINEERING PROPERTIES OF REACTOR MATERIALS

14. PHYSICAL AND MECHANICAL METALLURGY OF REFRACTORY ALLOYS

P. Patriarca

The purpose of this program is to provide a broad, base-technology evaluation of high-temperature alloys for use in high-performance nuclear reactors and isotopic heat sources for advanced space, terrestrial, and civilian power applications. Principal emphasis is placed on materials problems involving Ta-, Nb-, Mo-, and V-base alloys for systems that use alkali metals as thermodynamic working fluids and heat-transfer media.

Basic Physical Metallurgy Studies

H. Inouye

Solubility, Diffusivity, and Permeability of Interstitials in Refractory Metals (R. L. Wagner)

The measurement of the solubility and diffusivity of N in W was completed, and the apparatus is being recalibrated so that the solubility and diffusivity of N in W–25% Re may be determined. The following is the abstract of the report[1] of the completed study:

> An ultrahigh vacuum technique, suitable for the determination of the solubility, diffusivity, and permeability of gases in metals is described and was applied to the nitrogen-tungsten system. This method depends on the measurement of the degassing rate of nitrogen as a function of time from a resistively heated wire specimen, previously equilibrated at high nitrogen pressures (1 to 25 torr), with a mass spectrometer and a known vacuum conductance.
>
> The diffusion constant, D, and the solubility constant, S, between 1000 and 1800°C may be summarized in Arrhenius form by
>
> $$D = (2.37 \pm 0.43) \times 10^{-3} \exp[(-35{,}800 \pm 3900)/RT] \text{ cm}^2/\text{sec} ,$$

[1]To be published as ORNL-TM-2584.

and

$$S = (0.21 \pm 0.06)\ \exp[(-17{,}600 \pm 5900)/RT]\ \text{torr}\cdot\text{liter cm}^{-3}\ \text{torr}^{-\frac{1}{2}}\ .$$

The permeation constants calculated from these results agree within a factor of two with directly measured values reported in the literature. The diffusion constants agree within a factor of three with literature values, although the activation energies for diffusion (35,800 – 62,000) are quite different. The solubility obeys Sievert's law and exhibits a positive activation energy for solution. The concentration of nitrogen in tungsten at 1 atm pressure according to the above solubility data is 0.4 ppm at 1000°C and 9.2 ppm at 2000°C.

The permeability of nitrogen through tungsten is two orders of magnitude lower than the permeability of nitrogen through molybdenum and five orders of magnitude lower than the permeability of nitrogen through niobium or tantalum.

Development of Age-Hardening Refractory Alloys (C. T. Liu, R. W. Carpenter, P. F. Mardon)

This task is related to the development of age-hardening refractory alloys for use at elevated temperatures. At present, the four binary alloy systems Nb-Hf, Ta-Hf, Nb-Zr, and Ta-Zr are being studied, because they possess the potential to homogeneously precipitate a high volume fraction of uniformly distributed fine particles.

The lattice parameters of quenched β-phase solid solutions in Nb-Hf alloys were measured, and the results are plotted in Fig. 14.1 as a function of Hf concentration. Literature values of the lattice parameters fall on two lines. Our results agree with Begley's,[2] and Taylor and Doyle's.[3] In general, the lattice parameters of β-phase solid solutions follow Vegard's law, and our extrapolated value for body-centered cubic (bcc) Hf is about 3.54 A (Fig. 14.1).

The stability of the uniformly distributed fine precipitates observed in Nb-Hf alloys was studied by aging 150 hr at 800 to 1300°C.

---

[2]R. T. Begley and J. H. Bechtold, J. Less-Common Metals 3, 1 (1961).

[3]A. Taylor and N. J. Doyle, J. Less-Common Metals 7, 37 (1964).

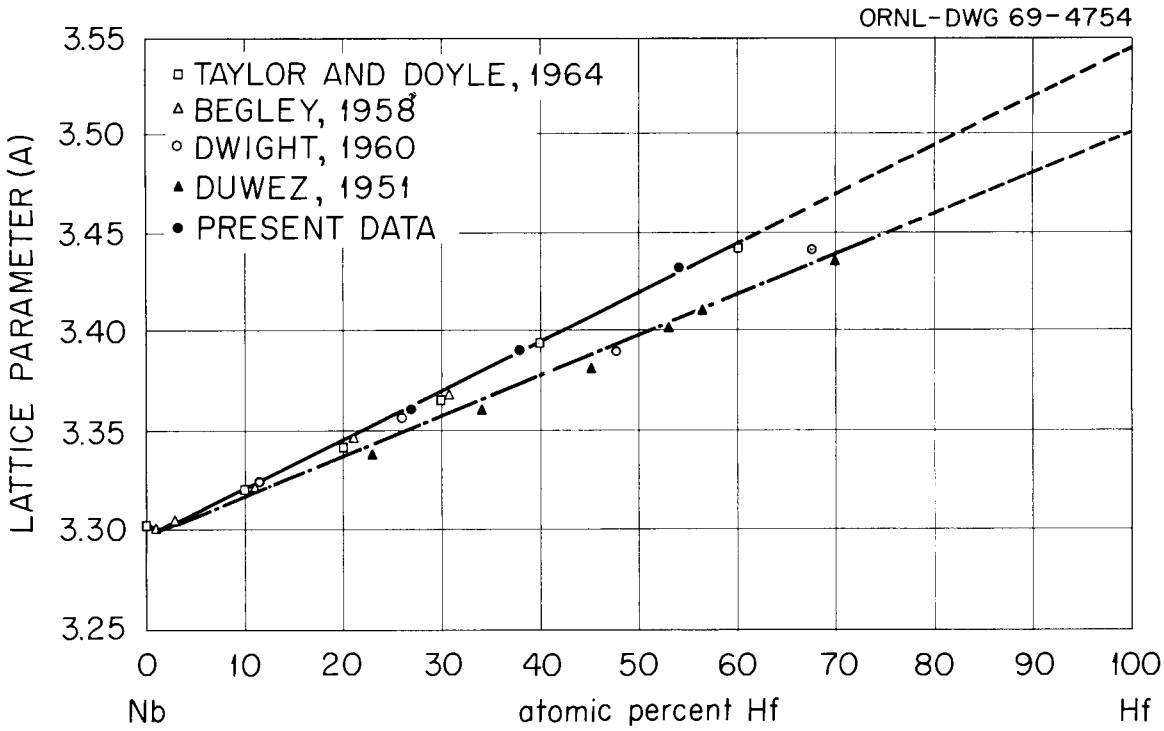

Fig. 14.1. Lattice Parameters of β-Phase Nb-Hf Alloys. [Refs. A. Taylor and N. J. Doyle, J. Less-Common Metals 7, 37 (1964); R. T. Begley and J. Bechtold, J. Less-Common Metals 3, 1 (1961); A. E. Dwight, "Columbium Metallurgy," p. 383 in Bolton Landing Symposium, Interscience, New York, 1960; P. Duwez, J. Appl. Phys. 22, 1174 (1951).]

Optical photomicrographs show that in the alloys containing more than 30% Hf, the particles grow progressively in size and change shape from a nondistinctive to a plate type of morphology (Fig. 14.2), whereas there were pearlitic patches on the grain boundaries of the alloys with less Hf (Fig. 14.3). Figure 14.4 shows the variation of the hardness in the Nb–54 at. % Hf alloy, which becomes overaged after 6 min at 1000°C. X-ray diffraction indicates that the (110) planes of β phase are parallel to the (002) plane of α phase. The stability of the precipitates in Ta-Hf alloys is more sensitive to the Hf concentration. Pearlitic precipitates were always observed – even after short aging times – in alloys that contained less than 40% Hf.

The tensile properties of Nb–54 at. % Hf specimens aged at 600 to 1300°C are listed in Table 14.1 together with results reported previously.[4]

[4]C. T. Liu and R. W. Carpenter, Fuels and Materials Development Program Quart. Progr. Rept. March 31, 1969, ORNL-4420, pp. 243–248.

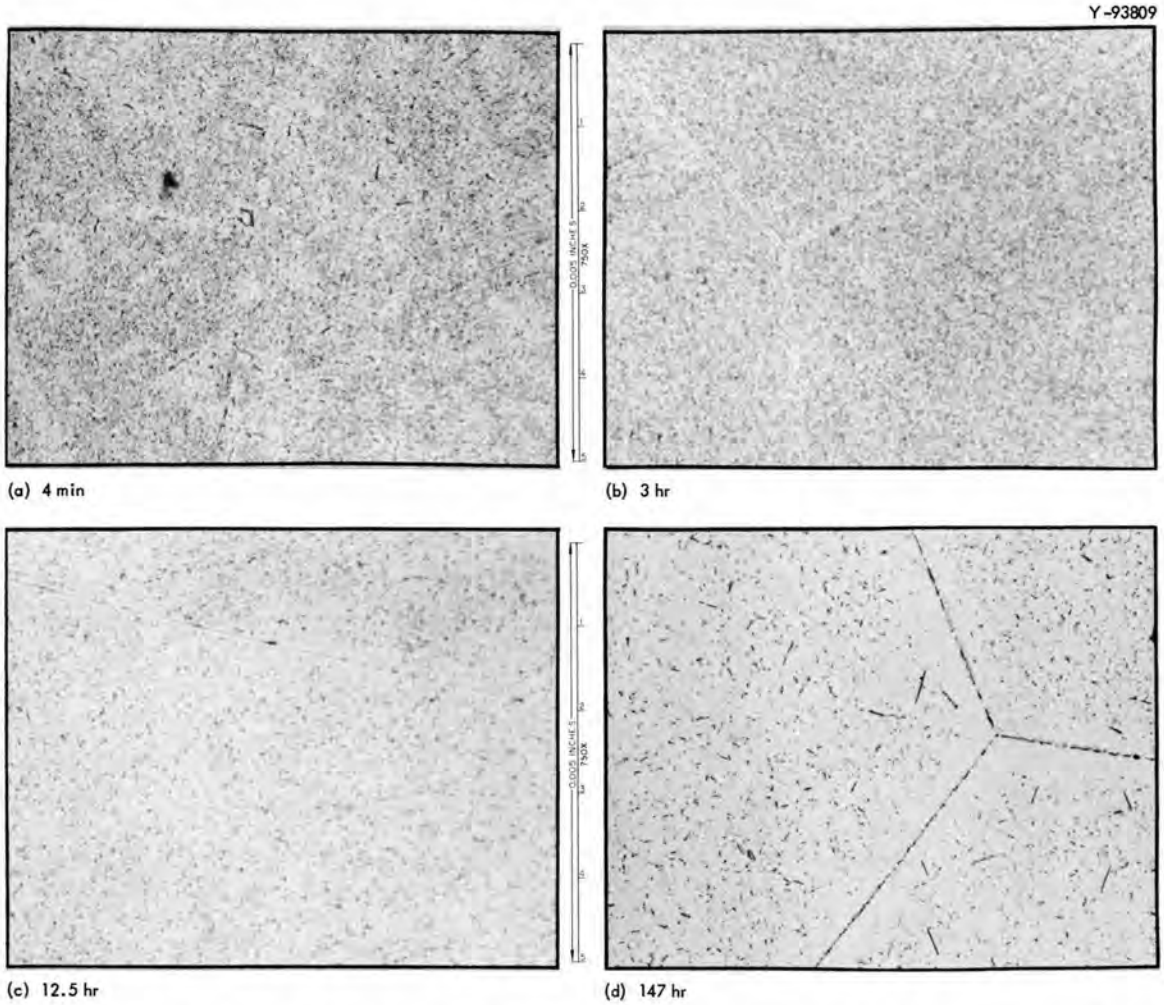

Fig. 14.2. Optical Photomicrographs of Nb—54 at. % Hf Alloy Oil Quenched and Aged at 1000°C.

In general, the yield stress decreased from the value corresponding to the quenched condition at all temperatures above 600°C, and the ductility varied from 1 to 9.4% strain. The alloy exhibited significant hardening upon aging at 600°C. After aging 4 and 136 hr, the yield stresses were 139,000 and 154,00 psi, respectively.

Transmission electron microscope investigation of the structure responsible for hardening showed that after aging 136 hr at 600°C, the hexagonal Hf-rich α phase was present. This result was confirmed by x-ray diffraction. The α-phase morphology was a relatively coarse type of plate about 250 A thick and 2000 A long. The platelet volume fraction was very high. Precipitate morphology after aging 4 hr at 600°C also

Fig. 14.3. Optical Photomicrograph of Nb–27 at. % Hf Alloy Oil Quenched and Aged 169 hr at 800°C. 750×.

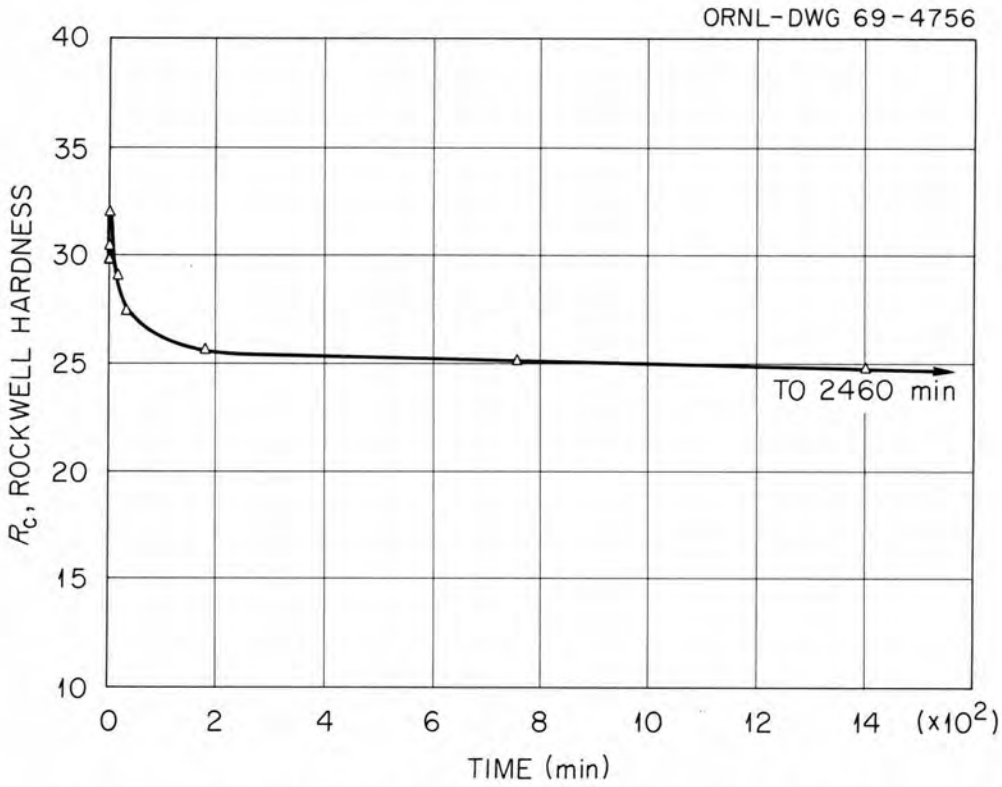

Fig. 14.4. Variation of Rockwell C Hardness as a Function of Aging Time at 1000°C for the Oil-Quenched Nb–54 at. % Hf Alloy.

Table 14.1. Effect of Aging on the Tensile Properties of Nb–54 at. % Hf Alloy at Room Temperature

Aging Treatment Temperature (°C)	Aging Treatment Time (hr)	Yield Strength (psi)	Total Plastic Strain to Fracture (%)
		$\times 10^3$	
As quenched		108	6.5
1400	4	118	3.5
1200	4	107	2.1
1100	4	97	
1000	0.1	100	
1000	4	94	9.4
1000	51	95	8.5
800	4	95	
600	4.25	139	
600	136	154	~ 1

appeared to be plate-like but very fine; the platelets were only about 100 A long (Fig. 14.5). Again the precipitation density was very high, but the diffraction effects after this aging treatment are not completely resolved. X-ray diffraction shows a strained β-phase bcc lattice and a significant amount of diffuse streaking. The same results were obtained by measurements of x-ray diffraction from selected areas. This structure apparently results from coarsening of the segregated regions observed in quenched specimens and leads to the still coarser α phase observed after aging 136 hr at 600°C.

Thermodynamics of Spinodally Decomposed Alloys (C. T. Liu, B. T. Loh)

We have previously derived a general expression for the free energy of mixing, ΔG_m, in a binary alloy solid solution in which the clustering effect is considered.[5] The second derivative of ΔG_m was also given[6] as

[5]C. T. Liu and B. T. Loh, Fuels and Materials Development Program Quart. Progr. Rept. Sept. 30, 1968, ORNL-4350, pp. 298–302.

[6]C. T. Liu and B. T. Loh, Fuels and Materials Development Program Quart. Progr. Rept. Dec. 31, 1968, ORNL-4390, pp. 281–283.

Fig. 14.5. Transmission Electron Photomicrograph of Nb–54 at. % Hf Alloy Oil Quenched and Aged 4 hr at 600°C. 41,300×.

$$\frac{1}{Nk}\frac{d^2\Delta G_m}{dc^2} = \frac{T}{c(1-c)}\left[1 - \frac{Z_1}{2}\left(1 - \frac{1}{\sqrt{f_1}}\right) - \frac{Z_2}{2}\left(1 - \frac{1}{\sqrt{f_2}}\right)\right] , \qquad (14.1)$$

where

$f = 1 + 4c(1-c)(e^{2V/kT} - 1)$,

N = total number of A and B atoms,

k = Boltzmann's constant,

T = absolute temperature,

c = atomic concentration,

Z = coordination number,

V = bonding energy, and

subscripts 1 and 2 refer to the first and second nearest neighbors.

The corresponding expression for the regular solution model[7] is

$$\frac{1}{Nk}\frac{d^2\Delta G_m}{dc^2} = \frac{T}{c(1-c)} - 2V \ . \tag{14.2}$$

According to Cahn's theory[8] of spinodal decomposition in a binary alloy, such parameters as the wavelength of the modulated structure, λ, and the time, t, required for a given fraction of decomposition can be expressed in terms of $\frac{d^2\Delta G_m}{dc^2}$ as

$$\lambda = \frac{4\pi T_c^{\frac{1}{2}}}{\left(-\frac{1}{Nk}\frac{d^2\Delta G_m}{dc^2}\right)^{\frac{1}{2}}}\Psi \ , \tag{14.3}$$

$$t = \frac{8T_c}{e^{-Q/kT}\left(\frac{1}{Nk}\frac{d^2\Delta G_m}{dc^2}\right)^2}\frac{\Psi^2 \ln\frac{c-c_o}{A}}{M_o Nk} \ , \tag{14.4}$$

where

T_c = critical temperature of a miscibility gap,

Ψ = atomic interaction distance,

M = diffusion mobility,

$= M_o e^{-Q/kT}$

c_o = average concentration before decomposition, and

A = initial composition fluctuation.

We have calculated the parameters for a hypothetical bcc solid solution using Eqs. (14.1) and (14.2). In order to give a meaningful comparison of the two models, the energy values used are V_1 = 597k and V_2 = 0 for the clustering model and V = 518k for the regular model so that both models yield a T_c of 2073°K (1800°C); Q is assumed to have a value of 15,000k. The values of $\frac{d^2\Delta G_m}{dc^2}$ at various temperatures are shown

---

[7]R. A. Swalin, Thermodynamics of Solids, p. 163, Wiley, New York, 1962.

[8]J. W. Cahn, Trans. Met. Soc. AIME 242, 166 (1968).

in Fig. 14.6 as a function of concentration. Figure 14.7 shows the variation of wavelength, λ, with respect to concentration, and Fig. 14.8 shows a temperature-time-transformation curve. The dashed curves in the figures represent the model for the regular solution. From these results, we may draw the following conclusions:

1. The spinodal range is wider for the clustering model than that predicted by the model for the regular solution at any given temperature.

2. The curves of $\frac{d^2\Delta G_m}{dc^2}$ and λ for the clustering model in Figs. 14.6 and 14.7 show one maximum at $c = 0.5$ and two minima at low temperatures and thus deviate from the usual concave upward curves for regular solutions. With increasing temperature, the three critical points approach one another and merge at about $0.5\ T_c$. This low temperature deviation provides a useful way to check the models experimentally.

3. Cahn's theory assumes that during the early stages of decomposition, $\frac{d^2\Delta G_m}{dc^2}$ is independent of concentration. Such an assumption may be justified near $0.5\ T_c$ because the $\frac{d^2\Delta G_m}{dc^2}$ curve does have an extensive flat portion (Fig. 14.6). Therefore, better agreement may be obtainable between experiments and Cahn's theory if the alloy has equal atomic concentrations of A and B atoms and the decomposition is carried out at about $0.5\ T_c$.

Long-Time, High-Temperature Mechanical Properties of Commercial Refractory Alloys

H. E. McCoy, Jr.

Our objective is to compare the mechanical properties of promising refractory alloys from 1000 to 1650°C. Primary consideration is given to collecting 1000-hr creep-rupture data on materials in typical metallurgical conditions produced by alloy vendors. The program includes studies on the response of these alloys to other heat treatments to establish optimum properties.

Tantalum Alloys (R. L. Stephenson)

We studied the effect of the temperature of annealing treatments before testing on the creep-rupture properties of T-111. The results

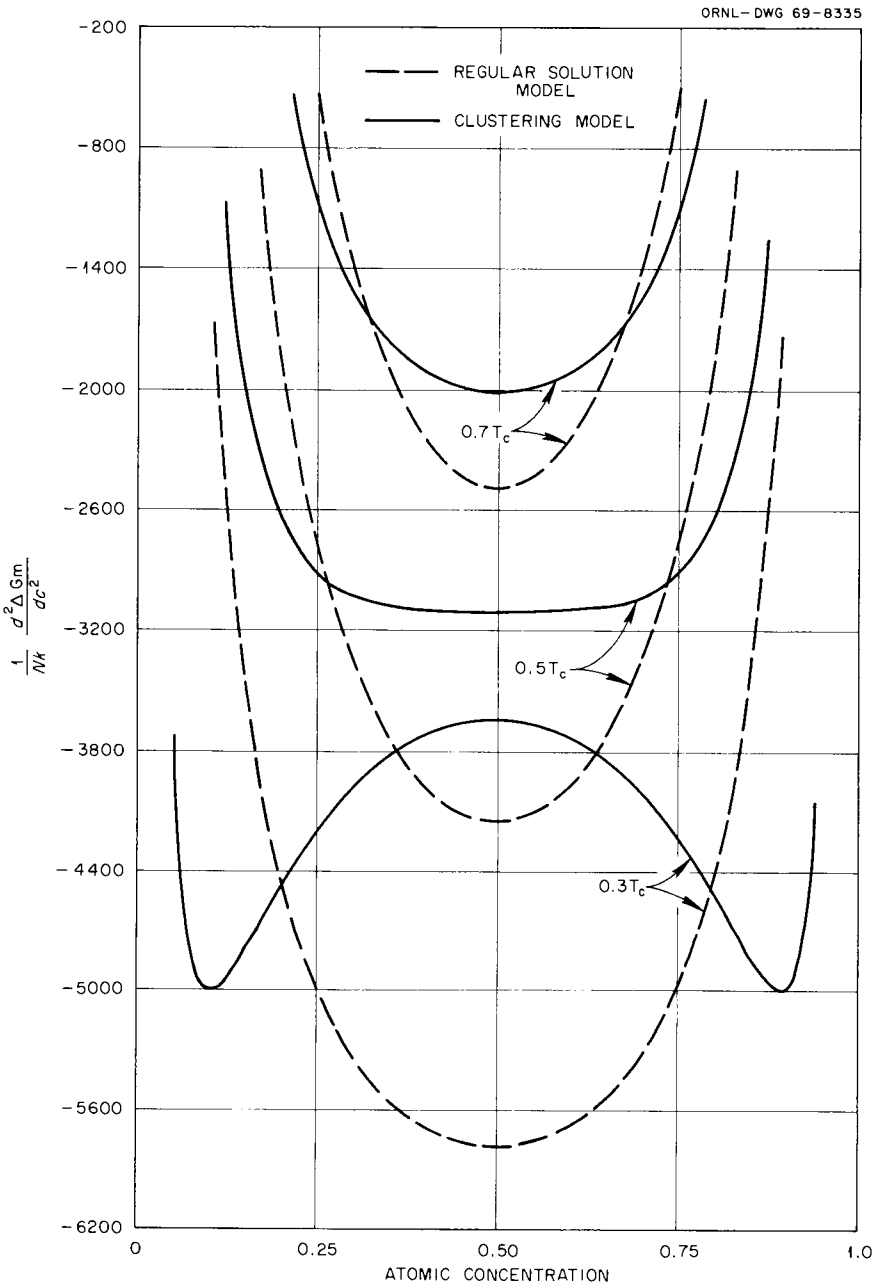

Fig. 14.6. Variation of $\frac{d^2\Delta G_m}{dc^2}$ with Atomic Concentration at Various Temperatures.

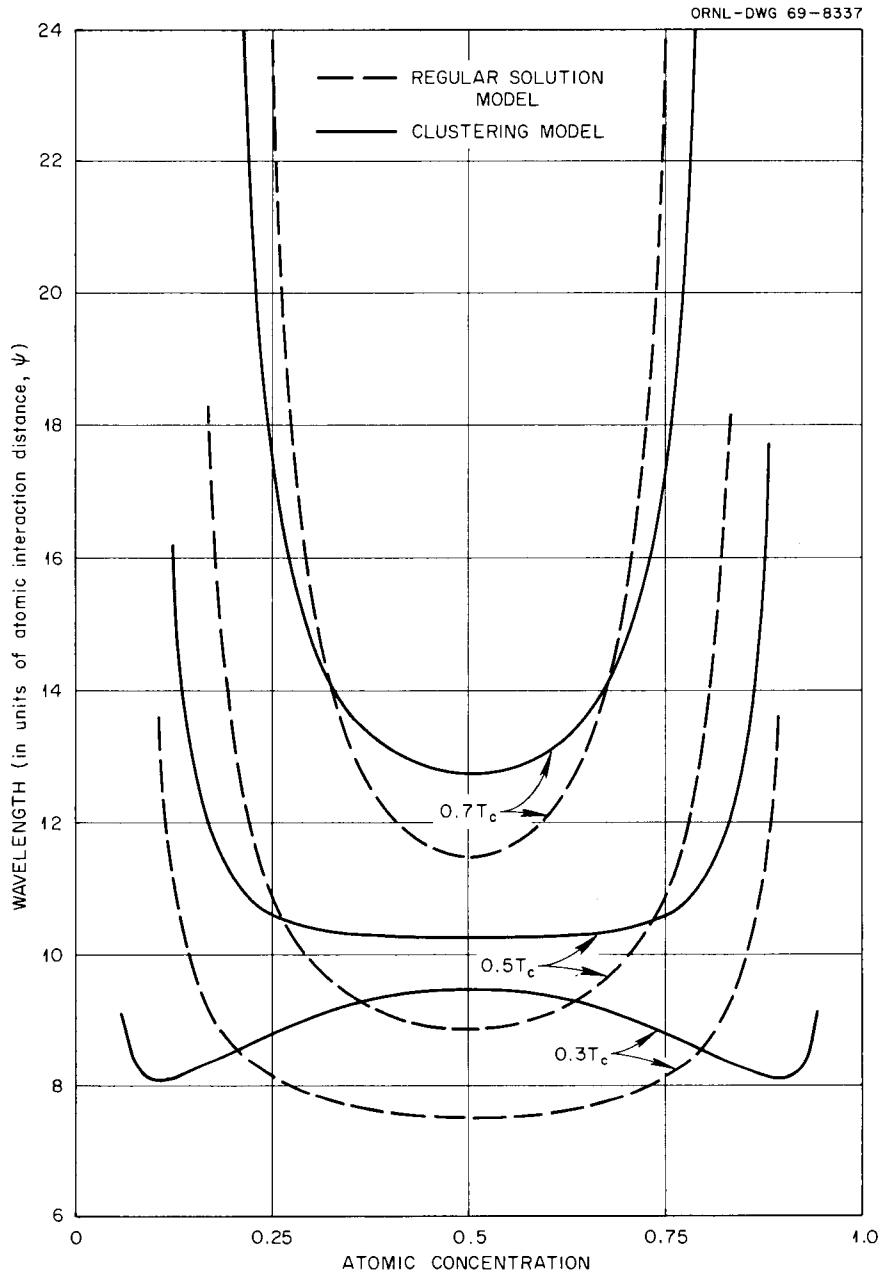

Fig. 14.7. Variation of Wavelength with Atomic Concentration.

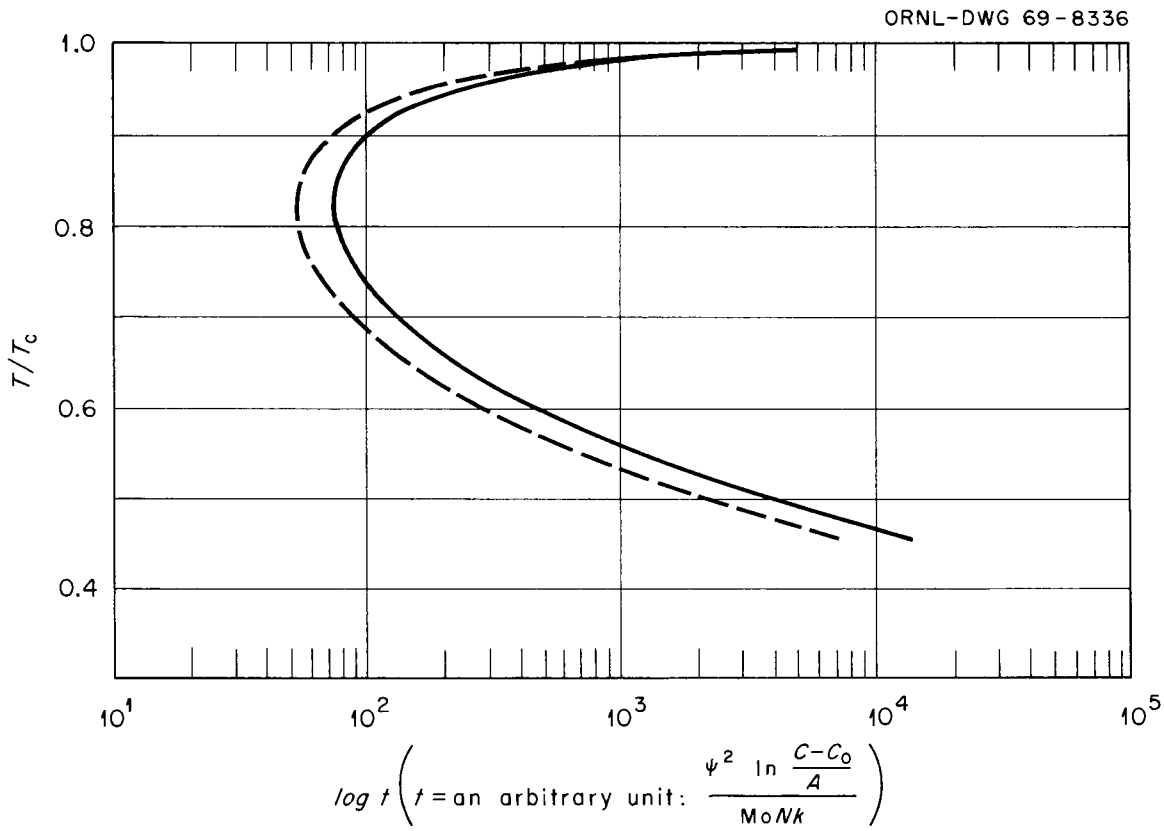

Fig. 14.8. Temperature-Time-Transformation Curve.

thus far are shown in Fig. 14.9. The times to 1, 2, and 5% creep strain and to rupture at 35,000 psi and 1205°C decrease with increasing temperature of pretest annealing. These data are in apparent conflict with the data of Sawyer and Steigerwald,[9] which show longer times for material annealed at 1650°C than for material annealed at 1200°C. When we tested over a broader range of stresses, we found that the stress dependence of material annealed at 1650°C is much different from that of material annealed at 1200°C. Figure 14.10 shows that T-111 annealed at 1650°C is weaker than T-111 annealed at 1200°C at high stresses but stronger at low stresses, in agreement with the results of Sawyer and Steigerwald.

---

[9]J. C. Sawyer and E. A. Steigerwald, Generation of Long Time Creep Data of Refractory Alloys at Elevated Temperatures, ER-7203 (June 6, 1967).

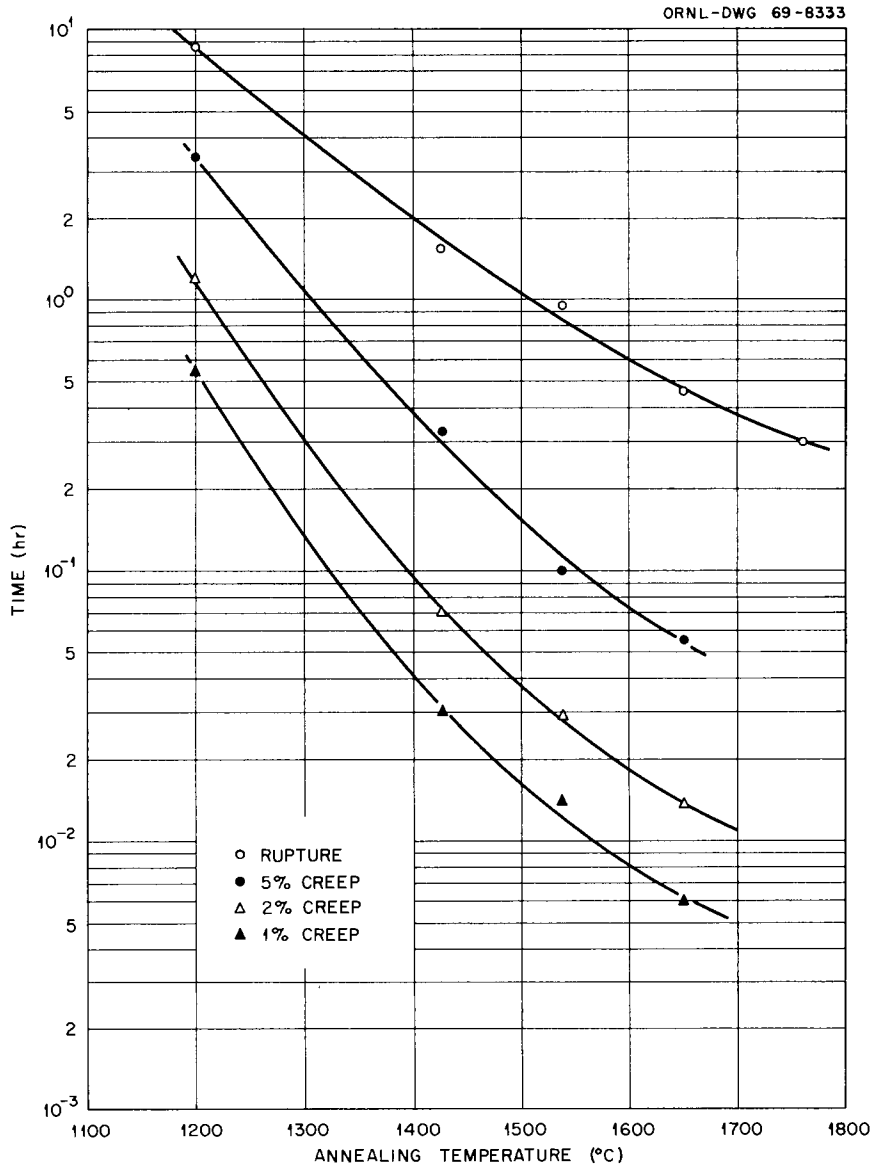

Fig. 14.9. Effect of Temperature of Annealing Treatment Before Test on the Creep-Rupture Properties of T-111 Tested at 1205°C and 35,000 psi.

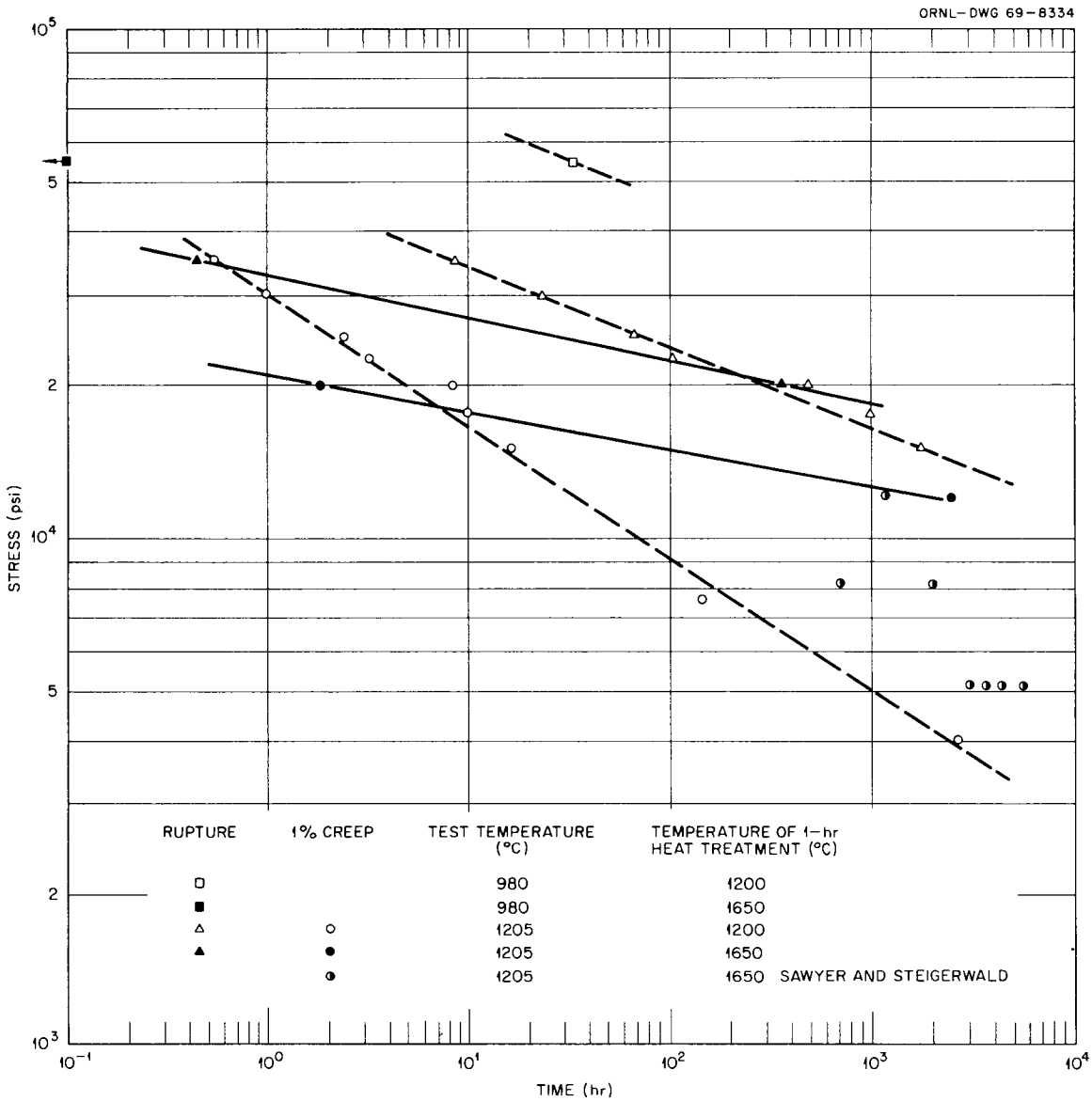

Fig. 14.10. Creep-Rupture Properties of T-111. [Ref. J. C. Sawyer and E. A. Steigerwald, Generation of Long Time Creep Data of Refractory Alloys at Elevated Temperatures, ER-7203 (June 6, 1967).]

Welding and Brazing

G. M. Slaughter

Component Fabrication (D. A. Canonico, N. C. Cole, W. J. Werner)

We have successfully fabricated three Cs evaporators with brazes of graphite to graphite and of graphite to Mo for use by the ORNL Reactor Division in radioactive experiments on the diffusion of Cs. The brazing alloy we developed, 47.5% Ti–47.5% Zr–5% Nb, appears capable of operating at the maximum proposed service temperature of 1400°C. Figure 14.11 shows the components, the fabricated evaporator, and photomicrographs of the brazes.

Fig. 14.11. Apparatus for Cesium Diffusion Experiment.

Two evaporators have completed operation in which the brazes were exposed to radioactive Cs for 200 hr at above 1000°C. We plan to examine these brazes and construct additional evaporators for subsequent diffusion experiments.

Mechanical Properties of Brazed Joints (D. A. Canonico, N. C. Cole)

We determined the mechanical properties of brazed joints in graphite. The brazing alloys used were from the Ti-Zr-Ge system. An improved specimen was designed; the brazed joint is loaded in compression rather than in tension as described previously[10] (Fig. 14.12). Shear strengths of 2620 and 1900 psi compare very favorably with the breaking strength (2410 psi) of an identical specimen composed solely of graphite. Studies of this type are continuing.

[10]D. A. Canonico and N. C. Cole, Fuels and Materials Development Program Quart. Progr. Rept. March 31, 1969, ORNL-4420, pp. 251–253.

Y-93696

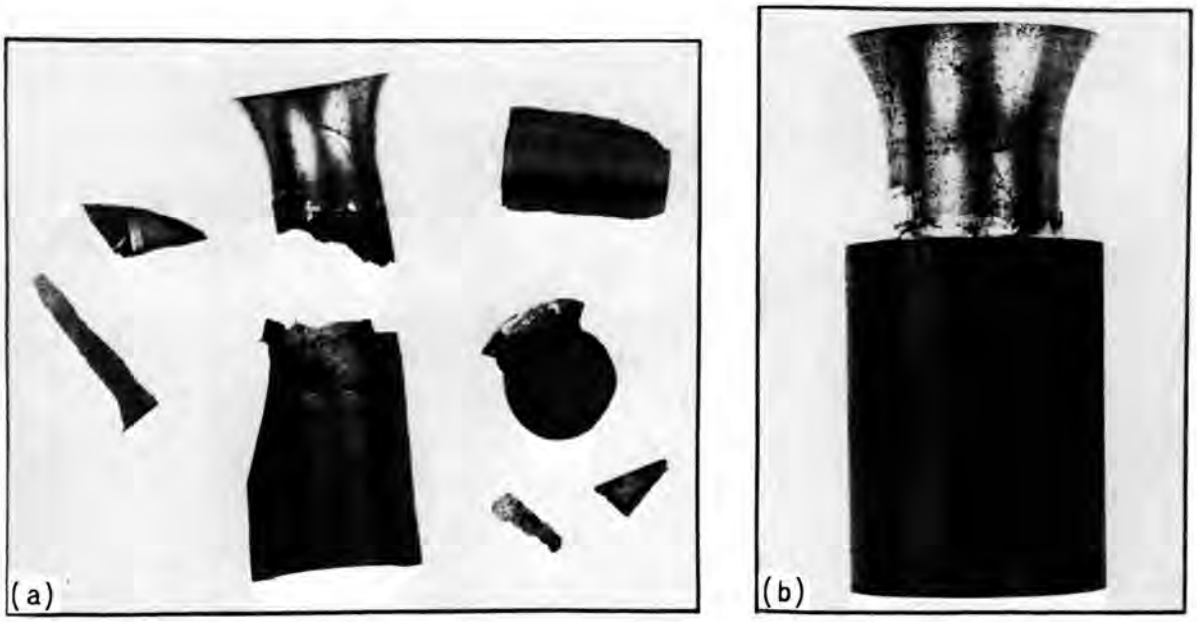

Fig. 14.12. Results of Shear Tests on Graphite Brazes at (a) 2620 psi and (b) 1900 psi. Brazing alloy is 65% Ti–20% Zr–15% Ge.

Physical Properties of Refractory Materials

D. L. McElroy

High-Temperature Electrical Resistivity (R. K. Williams).

Approximately 90 electrical resistivity data points up to 2600°K were obtained on a Ta sample.[11] The repeatibility and determinate errors were comparable to results obtained in our low-temperature apparatus;[12] however, the temperature measurements became uncertain by as much as ±12–15 deg at 2600°K. The graphically smoothed results, corrected for thermal expansion,[13] can be described by the equation

$$\rho = -\frac{1.89325 \times 10^2}{T} + 4.84500 \times 10^{-2}\ T - 5.69237 \times 10^{-6}\ T^2 + 5.98696 \times 10^{-10}\ T^3\ , \quad (14.5)$$

where ρ is electrical resistivity in $\mu\Omega$-cm and T is absolute temperature, to a standard deviation of 0.029 $\mu\Omega$-cm. The $d^2\rho/dT^2$ of the data is always negative, but becomes smaller at higher temperatures and appears to approach zero. This behavior for electrical resistivity was previously reported[14] for Ta, Nb, Pd, and Pt.

This Ta specimen is being prepared for measurements of thermal conductivity from 80 to 400°K in the absolute longitudinal heat-flow apparatus. Results from this study should allow an initial determination of the Lorenz function and the behavior of the lattice component, which are needed for extrapolations of thermal conductivity.

---

[11] R. K. Williams, Fuels and Materials Development Program Quart. Progr. Rept. March 31, 1969, ORNL-4420, p. 251.

[12] W. Fulkerson, J. P. Moore, and D. L. McElroy, J. Appl. Phys. 37(7), 2639–2653 (1966).

[13] J. B. Conway and A. C. Losekamp, "Thermal Expansion Characteristics of Several Refractory Metals to 2500°C," pp. V-K-1–V-K-26 in The 5th Conference on Thermal Conductivity, Held at Denver, Colorado, October 20, 21, and 22, 1965, Vol. 2, Denver University, Department of Metallurgy, College of Engineering, Denver, Colorado, 1967.

[14] H. H. Potter, Proc. Phys. Soc. 53, 695 (1941).

Development of an Electrical Heating Method for Determining Thermal Conductivity (K.-H. Bode, J. P. Moore, R. S. Graves)

We measured the thermal conductivity of two samples of Nb–10% W from 80 to 400°K. One specimen was machined from a disk used in the radial heat-flow experiment[15] to 1300°K. The other came from the extruded and swaged material used in the electrical heating apparatus. The data for thermal conductivity and electrical resistivity obtained from these two samples agree from 80 to 400°K and agree with the data for high temperatures from the radial apparatus to within 1% over the temperature range of overlap. These results indicate that this material will make an acceptable standard for thermal conductivity since the transport properties are insensitive to fabrication details.

---

[15]J. P. Moore and R. S. Graves, Metals and Ceramics Div. Ann. Progr. Rept. June 30, 1966, ORNL-3970, p. 79.

15. CLADDING MATERIALS FOR SPACE ISOTOPIC HEAT SOURCES

P. Patriarca R. G. Donnelly

The immediate tasks of this program are (1) to evaluate the more promising superalloys that are available commercially and (2) to develop improved alloys and eventually qualify those that show greatest promise for containment of radioisotopes in space power systems. The superalloy tasks include studies of mechanical properties, evaluation of embrittling aging reactions, determination of evaporation characteristics, and studies of the interaction of stress and vacuum on properties at elevated temperatures. In the alloy development portion of the program, the creep strength and resistance to evaporation and to oxidation in air are of primary concern.

Studies of Commercial Superalloys

Mechanical Properties of Haynes Alloy No. 25 (R. W. Swindeman)

Superalloys have potential as container materials for those isotopic heat sources that normally operate between 650 and 870°C. It is possible, however, for the heat source to be exposed to conditions that differ from those of normal operation as a result of launch-pad abort or suborbital reentry. The supplementary information we are developing to cover these situations includes short-time creep-rupture data for temperatures from 980 to 1200°C and impact and tensile properties of aged material. We are also investigating the long-time creep-rupture behavior of weldments at operating temperatures between 650 and 870°C.

Creep-rupture data for a Co-base superalloy, Haynes alloy No. 25, are summarized in Fig. 15.1. Figure 15.1(a) shows a plot of base-metal data correlated over the temperature range 650 to 1050°C by means of the Manson-Haferd parameter. This figure represents data taken from the literature and covers five heats of material. Data obtained at ORNL on three heats of material are shown in Fig. 15.1(b) and are compared to the 99% confidence band shown in Fig. 15.1(a). The data in Fig. 15.1(b) were obtained on weldments in sheet specimens that include

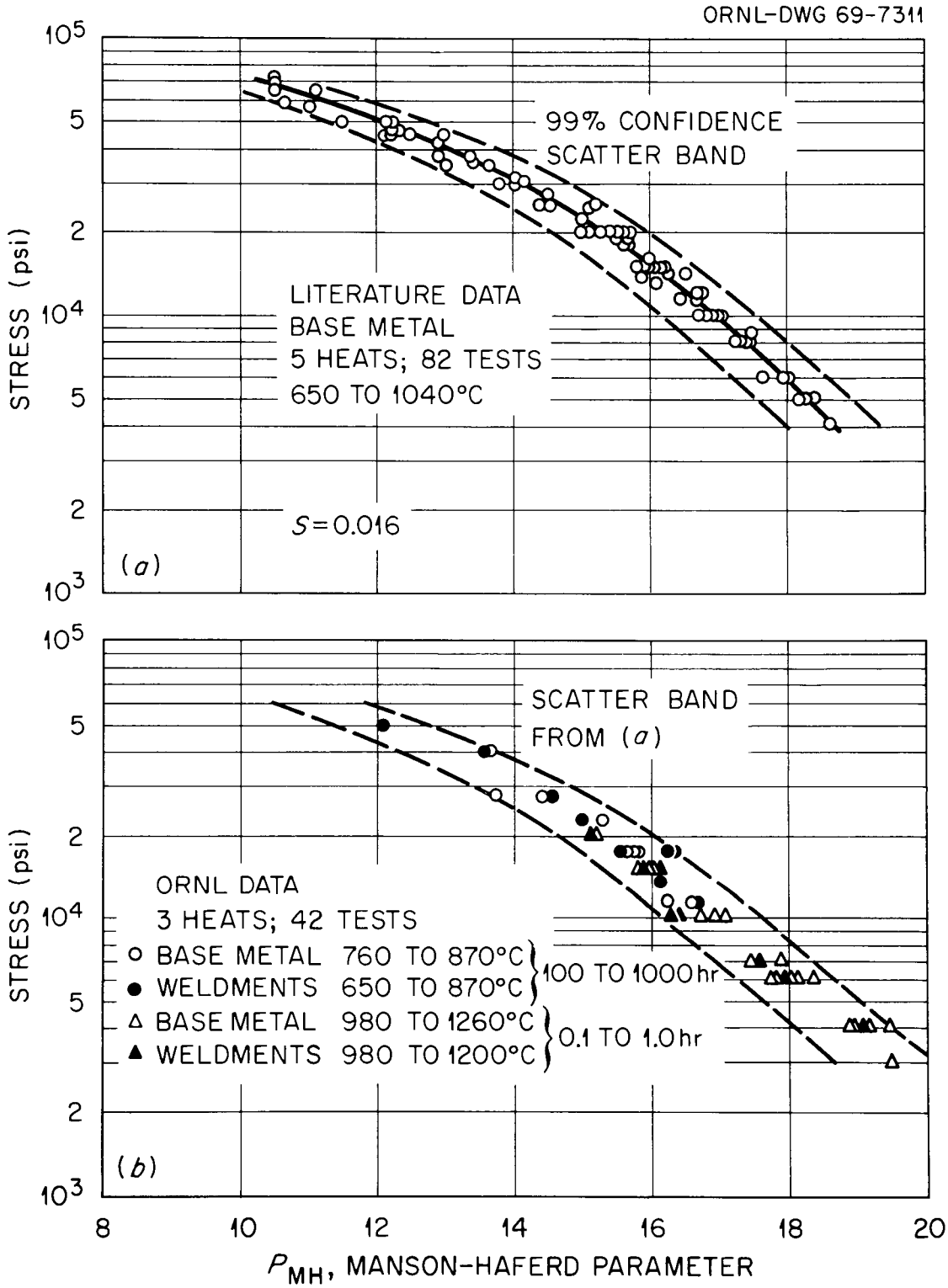

Fig. 15.1. Comparison of the Rupture Strength of Haynes Alloy No. 25 Weldments with the Scatter Band from Rupture Tests on Base Metal. Time-temperature correlation is based on the Manson-Haferd parameter, P_{MH} = log time + $ST_{°C}$.

base metal and a transverse gas tungsten-arc (GTA) weld in the test section. Weldments appear to have strengths comparable to that of the base metal; however, most weldments failed near the weld fusion line at test temperatures from 650 to 870°C.

The effects of aging at several temperatures on the tensile properties of Haynes alloy No. 25 are illustrated in Fig. 15.2. When tested at room temperature after aging at 700°C for 2000 hr, the alloy increases sharply in yield and ultimate strengths and correspondingly loses ductility. A less dramatic strengthening occurs after aging at 800°C. Ductility is lost at all temperatures. When the tensile properties are determined at the aging temperatures, similar changes in strength are apparent, and ductility is at a minimum at 700°C and improves at 800 and 850°C.

The properties of aged specimens are affected by the composition and morphology of the precipitating phases. The precipitation of the Laves phase Co_2W is generally considered to be the embrittling reaction at 800 and 850°C (ref. 1). The pronounced aging response at 700°C is possibly associated with the precipitation of an ordered hexagonal structure, β-Co_3W (ref. 2).

Aging Behavior of Superalloys (D. T. Bourgette)

Charpy V-notch impact specimens of Hastelloy N and Haynes alloy No. 25 were solution annealed at 1150°C for 1 hr and then aged at 650, 700, 800, 850, and 900°C. Specimens of Hastelloy N were aged through 2000 hr at all aging temperatures, and specimens of Haynes alloy No. 25 were aged through 1000 hr. The 5000-hr aging treatments of both alloys and the 2000-hr aging treatment of Haynes alloy No. 25 are in progress. Impact testing at room temperature and at 760°C will be deferred until all aging treatments are completed.

---

[1]S. T. Wlodek, Trans. Am. Soc. Metals 56, 287–303 (1963).

[2]N. Yukawa and K. Sato, "The Correlation Between Microstructure and Stress-Rupture Properties of a Co-Cr-Ni-W (HS-25) Alloy," pp. 680–686 in Proc. Intern. Conf. Strength of Metals and Alloys, Tokyo, 1967, Supplement to Trans. Japan Inst. Metals 9, (1968).

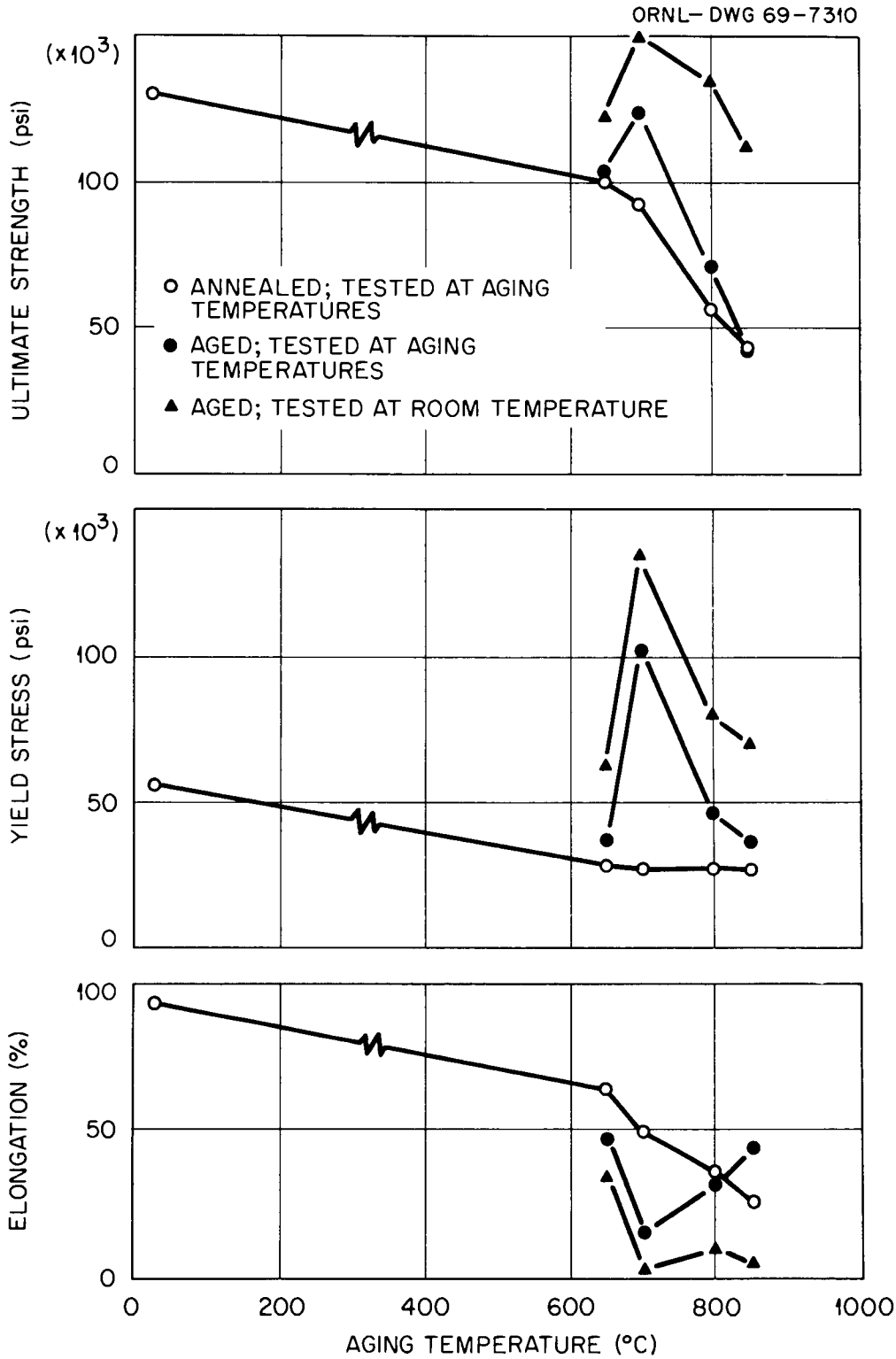

Fig. 15.2. Effect of Aging for 2000 hr on the Tensile Properties of Haynes Alloy No. 25 Cobalt Alloy.

Charpy V-notch impact specimens being machined from Haynes Developmental alloy No. 188 will be aged for periods to 5000 hr at the temperatures listed above. A reevaluation of program objectives has resulted in deferring the long-term aging investigations of Hastelloy C and X.

Development of Improved Alloys

C. T. Liu H. Inouye

Creep Studies

The creep strengths of the ordered alloy S-4 (43% Ni–33% Co–24% V) and the disordered alloy S-3 (45% Ni–46% Co–9% V) are being measured as a function of temperature at a constant stress, and part of the results are listed in Table 15.1 together with the data for Haynes alloy No. 25. The creep rate for the ordered alloy is an order of magnitude lower and the time to produce 1% strain an order of magnitude greater than those for the disordered one. The ordered alloy has a low initial creep rate that is even less than the second-stage creep rate; the disordered alloy has a high first-stage creep rate that extends generally to 2 or 3% strain. Therefore, ordered alloys show promise in applications requiring low creep strains.

A plot of the log of creep rate (tested at 5×10^3 psi) versus 1/T, the reciprocal of the absolute temperature, showed a discontinuous change in creep rate at 1050°C [i.e., the critical ordering temperature (T_c) of alloy S-4]. Extrapolation of the creep data of the disordered alloy below T_c gave creep rates 30 times higher than the rates measured at 785°C.

Table 15.2 also shows that at 785°C the time required to produce 1% strain in alloy S-4 is comparable, at least, with that required for Haynes alloy No. 25. At 900°C, alloy S-4 is superior to Haynes alloy No. 25.

Evaporation Studies

The effect of long-range order on the evaporation rates of Co-Ni-V alloys was determined. The rates for disordered alloy S-3

Table 15.1. Creep Strengths of Disordered Alloy S-3, Ordered Alloy S-4 and Haynes Alloy No. 25 Stressed at 10^4 psi in a Vacuum of 10^{-8} torr

Alloy	Specimen Dimensions, in.		Testing Temperature (°C)	Time to Produce 1% Plastic Strain (hr)	Creep Rate 10^{-5}/hr
	Rod Diameter	Sheet Thickness			
S-3	0.070		761	28	23
	0.070		793	17	35
S-4[a]	0.070		785	200	4.2
H-25[b]		0.070	785	40	
		0.012	785	54	
		0.030	785	175	
S-4	0.070		900	5	230
H-25[b]		0.030	900	1.6	

[a]Extrapolation of creep curve from 93 hr.

[b]D. T. Bourgette, private communication.

Table 15.2. Evaporation Rates of Experimental Alloys[a]

Alloy Designation	Composition, wt %			Evaporation Rate (mg cm^{-2} hr^{-1}) at Indicated Temperature		
	Ni	Co	V	950°C	1000°C	1050°C
				$\times 10^{-3}$	$\times 10^{-3}$	$\times 10^{-3}$
S-3	45	46	9	1.83	4.6	35
S-4[b]	43	33	24	0.5	2.0	15

[a]Based on tests of about 500 hr at 10^{-7} torr.

[b]Transforms from ordered to disordered structure at about 1050°C.

and ordered alloy S-4 are shown in Table 15.2. The evaporation rates for alloy S-4 are consistently lower than those for alloy S-3 between 950 and 1050°C, and the difference in rates increases at the lower temperatures.

The preferential evaporation of Ni, Co, and Fe from binary alloys containing about 28 wt % Pt at 10^{-7} torr results in the enrichment of the alloy surface with Pt. Table 15.3 shows that the degree of enrichment appears to increase with temperature.

Alloy S-6 (22% Co–78% Pt) evaporates very slowly at 10^{-7} torr according to current measurements. At 1000°C the rate was 1.6×10^{-4} mg cm^{-2} hr^{-1}; it increased to 2.7×10^{-4} mg cm^{-2} hr^{-1} at 1050°C. The concentration of Pt at the surface was calculated to be about 100% at both temperatures.

Table 15.3. Evaporation Characteristics of Binary Alloys Containing Platinum

Alloy Designation	Composition, wt %	Evaporation Rates (mg cm^{-2} hr^{-1}) at Indicated Temperature			Concentration of Pt at Surface (wt %) at Indicated Temperature		
		950°C	1000°C	1050°C	950°C	1000°C	1050°C
		$\times 10^{-3}$	$\times 10^{-3}$	$\times 10^{-3}$			
S-6	Co–78 Pt		0.16	0.27		100	100
S-11	Co–28 Pt	1.6	2.8		56	56	
S-12	Ni–28 Pt	1.3	2.8		40	70	
S-13	Fe–27 Pt	4.5	12.0		57	63	

Previous reports in this series:

ORNL-4330	Period Ending June 30, 1968
ORNL-4350	Period Ending September 30, 1968
ORNL-4390	Period Ending December 31, 1968
ORNL-4420	Period Ending March 31, 1969

ORNL-4440
UC-25 — Metals, Ceramics, and Materials

INTERNAL DISTRIBUTION

1–3. Central Research Library
4–5. ORNL — Y-12 Technical Library
Document Reference Section
6–20. Laboratory Records Department
21. Laboratory Records, ORNL RC
22. ORNL Patent Office
23. R. E. Adams
24. G. M. Adamson, Jr.
25. S. E. Beall
26. R. L. Beatty
27. R. J. Beaver
28. M. Bender
29. R. G. Berggren
30. D. S. Billington
31. E. E. Bloom
32. A. L. Boch
33. K.-H. Bode
34. E. S. Bomar
35. C. D. Bopp
36. B. S. Borie
37. D. T. Bourgette
38. G. E. Boyd
39. R. A. Bradley
40. R. J. Breeding
41. R. B. Briggs
42. R. E. Brooksbank
43. D. A. Canonico
44. R. W. Carpenter
45. R. M. Carroll
46. J. V. Cathcart
47. A. K. Chakraborty
48. Ji Young Chang
49. D. L. Clark
50. G. W. Clark
51. N. C. Cole
52. K. V. Cook
53. W. H. Cook
54. G. L. Copeland
55. W. B. Cottrell
56. C. M. Cox
57. F. L. Culler
58. C. W. Cunningham
59. J. E. Cunningham
60. V. A. DeCarlo
61. W. E. Deeds
62. J. H. DeVan
63. J. R. DiStefano
64. C. V. Dodd
65. R. G. Donnelly
66. D. A. Dyslin
67. T. Eck
68. W. S. Ernst
69. J. H. Erwin
70. R. B. Evans III
71. K. Farrell
72. J. I. Federer
73. D. E. Ferguson
74. R. B. Fitts
75. B. Fleischer
76. B. E. Foster
77. A. P. Fraas
78. J. H Frye, Jr.
79. W. Fulkerson
80. L. C. Fuller
81. R. E. Gehlbach
82. T. G. Godfrey, Jr.
83. G. M. Goodwin
84. J. M. Googan (Y-12)
85. R. J. Gray
86. W. R. Grimes
87. A. G. Grindell
88. H. D. Guberman
89. L. L. Hall
90. D. G. Harman
91. W. O. Harms
92–95. M. R. Hill
96. D. O. Hobson
97. H. W. Hoffman
98. F. J. Homan
99. R. W. Horton
100. W. R. Huntley
101. H. Inouye
102. D. H. Jansen
103. J. D. Jenkins
104. W. H. Jordan
105. G. W. Keilholtz
106. R. T. King
107. R. L. Klueh
108. R. W. Knight
109. W. L. Lackey, Jr.

110. J. A. Lane
111. J. M. Leitnaker
112. B. C. Leslie
113. C. S. Lever
114. T. B. Lindemer
115. A. P. Litman
116. C. T. Liu
117. H. R. Livesey
118. B. T. Loh
119. E. L. Long, Jr.
120. A. L. Lotts
121. C. D. Lundin
122. J. W. Luquire
123. R. N. Lyon
124. H. G. MacPherson
125. R. E. MacPherson
126. M. M. Martin
127. W. R. Martin
128. R. W. McClung
129. H. E. McCoy, Jr.
130. H. C. McCurdy
131. R. E. McDonald
132. W. T. McDuffee, Jr.
133. D. L. McElroy
134. C. J. McHargue
135. A. J. Miller
136. E. C. Miller
137. J. P. Moore
138. R. E. Moore
139. W. L. Moore
140. C. S. Morgan
141. J. G. Morgan
142. F. H. Neill
143. T. A. Nolan (K-25)
144. K. Notz
145. A. R. Olsen
146. M. F. Osborne
147. P. Patriarca
148. W. H. Pechin
149. R. B. Perez
150. A. M. Perry
151. S. Peterson
152. R. A. Potter
153. R. B. Pratt
154. M. K. Preston
155. W. W. Proaps
156. R. E. Reed
157. C. R. Reese
158. G. A. Reimann
159. A. E. Richt
160. P. L. Rittenhouse
161. H. E. Robertson
162. M. W. Rosenthal
163. D. J. Rucker
164. C. F. Sanders
165. G. Samuels
166. A. W. Savolainen
167. J. E. Savolainen
168. A. C. Schaffhauser
169. J. L. Scott
170. J. D. Sease
171. C. E. Sessions
172. O. Sisman
173. G. M. Slaughter
174. S. D. Snyder
175. K. E. Spear
176. I. Spiewak
177. P. Spindler
178. W. G. Spoeri
179. J. E. Spruiell
180. W. J. Stelzman
181. R. L. Stephenson
182. J. O. Stiegler
183. D. A. Sundberg
184. R. W. Swindeman
185. E. J. Tenckhoff
186. V. J. Tennery
187. K. R. Thoms
188. D. B. Trauger
189. R. L. Wagner
190. G. M. Watson
191. S. C. Weaver
192. M. S. Wechsler
193. A. M. Weinberg
194. J. R. Weir, Jr.
195. W. J. Werner
196. H. L. Whaley
197. G. D. Whitman
198. F. W. Wiffen
199. J. M. Williams
200. L. C. Williams
201. R. K. Williams
202. R. O. Williams
203. J. C. Wilson
204. R. G. Wymer
205. F. W. Young, Jr.
206. C. S. Yust
207. C. M. Adams, Jr. (Consultant)
208. Leo Brewer (Consultant)
209. L. S. Darken (Consultant)

EXTERNAL DISTRIBUTION

AIR FORCE MATERIALS LABORATORY, Wright-Patterson Air Force Base

210. C. H. Armbruster
211. H. M. Burte
212. G. Glenn
213. Technical Director

AIR FORCE WEAPONS LABORATORY, Kirtland Air Force Base

214. D. Brooks

AMES LABORATORY

215. O. N. Carlson
216. W. L. Larsen
217. M. Smutz
218. F. H. Spedding

ARGONNE NATIONAL LABORATORY

219. L. Baker
220. J. H. Kittel
221. M. V. Nevitt
222. P. G. Shewmon
223. R. C. Vogel

LMFBR PROGRAM OFFICE, Argonne National Laboratory

224. A. Amorosi
225. L. Burris
226. L. Kelman
227. J. M. McKee

AEC-RDT SITE REPRESENTATIVES

228. M. E. Jackson, Argonne National Laboratory
229. D. J. Wille, Atomic Power Development Associates
230. R. L. Morgan, Atomics International
231. J. V. Levy, General Electric, Sunnyvale
232. R. H. Ball, Gulf General Atomic
233. J. E. Hebert, Idaho
234. D. A. Moss, Idaho
235. K. A. Trickett, Idaho
236. D. F. Cope, Oak Ridge National Laboratory
237. C. L. Matthews, Oak Ridge National Laboratory
238. P. G. Holsted, Pacific Northwest Laboratory
239. J. Sako, Pacific Northwest Laboratory
240. Atomic Energy Commission Library, Washington

DIVISION OF NAVAL REACTORS, AEC, Washington

241. R. H. Steele

DIVISION OF REACTOR DEVELOPMENT AND TECHNOLOGY, AEC, Washington

242. J. C. Crawford, Jr.
243. G. W. Cunningham
244. A. Giambusso
245. H. G. Hembree
246. K. E. Horton
247. J. R. Hunter
248. E. E. Kintner
249. W. H. Layman
250. W. H. McVey
251. J. J. Morabito
252. R. E. Pahler
253. A. J. Pressesky
254. M. A. Rosen
255. J. M. Simmons
256. E. E. Sinclair
257. B. Singer
258. A. Taboada
259. A. N. Tardiff
260. A. Van Echo
261. C. E. Weber
262. M. J. Whitman

DIVISION OF RESEARCH, AEC, Washington

263. P. W. McDaniel
264. D. K. Stevens

DIVISION OF SPACE NUCLEAR SYSTEMS, AEC, Washington

265. R. E. Anderson
266. D. Beard
267. J. F. Griffo
268. F. D. Haines
269. C. E. Johnson
270. J. A. Powers
271. F. C. Schwenk

OAK RIDGE OPERATIONS OFFICE

272. W. J. Larkin
273. Laboratory and University Division

ATOMIC POWER DEVELOPMENT ASSOCIATES

274. E. C. Kovacic
275. A. A. Shoudy

ATOMICS INTERNATIONAL

276. H. Pearlman
277. J. G. Asquith

BABCOCK AND WILCOX COMPANY, Lynchburg, Virginia 24505

278. C. Baroch
279. S. P. Grant
280. C. Johnson
281. L. Weissert

BATTELLE MEMORIAL INSTITUTE, Columbus, Ohio

282. W. Berry
283. D. Keller
284. S. J. Paprocki
285. Defense Materials Information Center

BATTELLE MEMORIAL INSTITUTE, PNL, Richland, Washington

286. A. L. Bement
287. J. J. Cadwell
288. T. T. Claudson
289. D. L. Condotta
290. E. Evans
291. J. E. Hanson
292. B. R. Hayward
293. B. M. Johnson
294. W. E. Roake
295. D. W. Shannon
296. J. C. Tobin
297. R. G. Wheeler
298. Technical Information File

FAST FLUX TEST FACILITY, Battelle-Northwest

299. E. R. Astley

BROOKHAVEN NATIONAL LABORATORY

300. D. H. Gurinsky
301. C. Klamut

BUREAU OF MINES

302. Haruo Kato, Albany Metallurgy Research Center, P. O. Box 70, Albany, Oregon 97321
303. T. Sullivan, Bureau of Mines, Boulder City, Nevada 89005

COMBUSTION ENGINEERING

304. W. P. Chernock
305. S. S. Christopher

GENERAL ELECTRIC, Cincinnati

306. D. H. Ahmann
307. H. C. Brassfield
308. V. P. Calkins
309. E. Hoffman
310. J. McGurty
311. J. Moteff

GENERAL ELECTRIC, Nuclear Systems Programs, Cincinnati

312. E. E. Hoffman

GENERAL ELECTRIC, San Jose

313. R. Duncan
314. H. Klepfer

GENERAL ELECTRIC, Pleasanton

315. H. W. Alter

GENERAL ELECTRIC, Sunnyvale

316. K. P. Cohen
317. F. Comprelli
318. R. Skavdahl
319. C. Spalaris
320. E. L. Zebroski

GULF GENERAL ATOMIC

321. D. B. Coburn
322. A. J. Goodjohn
323. J. P. Howe
324. S. Jaye
325. J. F. Watson

IDAHO NUCLEAR CORPORATION

326. W. C. Francis

ILLINOIS INSTITUTE OF TECHNOLOGY RESEARCH INSTITUTE

327. D. J. McPherson

JET PROPULSION LABORATORY (NASA)

328. J. Davis

KNOLLS ATOMIC POWER LABORATORY

329. R. F. Wojciescak
330. Document Library

LOS ALAMOS SCIENTIFIC LABORATORY

331. R. D. Baker
332. D. B. Hall
333. J. A. Leary
334. R. Perkins
335. R. E. Peterson
336. Reports Library

MOUND LABORATORY

337. R. G. Grove

NASA HEADQUARTERS

338. J. J. Lynch

NASA, LEWIS RESEARCH CENTER

339. M. Ault
340. J.W.R. Creagh
341. J. J. Lombardo
342. T. P. Moffitt
343. T. A. Moss
344. F. E. Rom
345. L. Rosenblum
346. N. D. Sanders
347. N. Saunders
348. C. M. Scheuermann
349. H. Schwartz

NAVAL RESEARCH LABORATORY

350. J. R. Hawthorne
351. C. Serpan
352. L. E. Steele

NORTH CAROLINA UNIVERSITY, Raleigh, North Carolina 27607

353. J. Beeler
354. R. E. Dahl

NUCLEAR MATERIALS AND EQUIPMENT CORPORATION

355. C. Caldwell
356. K. Puechl

OHIO STATE UNIVERSITY, Columbus, Ohio 43212

357. M. G. Fontana
358. R. W. Staehle

RENSSELAER POLYTECHNIC INSTITUTE

359. W. Dickinson
360. W. F. Savage
361. C. B. Willingham, Jr.

SANDIA CORPORATION

362. J. Read Holland
363. J. Jacobs
364. D. R. Johnson

SAVANNAH RIVER LABORATORY

365. P. H. Permar
366. S. P. Rideout

TRW SYSTEMS (NASA), Redondo Beach, California 90278

367. H. Lurie

UNION CARBIDE CORPORATION, New York

368. J. A. Swartout

UNION CARBIDE CORPORATION, Materials Systems Division, Indianapolis

369. C. F. Leitten, Jr.

UNITED NUCLEAR CORPORATION

370. A. Strasser

UNIVERSITY OF CALIFORNIA, Lawrence Radiation Laboratory, Livermore

371. W. R. Holman
372. J. S. Kane
373. L. W. Roberts
374. A. J. Rothman
375. B. Rubin

U.S. NAVAL AIR SYSTEM COMMAND (AIR-52031B)

376. T. Kearns
377. I. Machlin

USAEC Scientific Representative, American Embassy, Box 40 FPO, N.Y. 09510

378. W.L.R. Rice

WESTINGHOUSE, Advanced Reactor Division, Waltz Mill Site

379. E. C. Bishop
380. J.C.R. Kelly
381. P. J. Levine
382. P. Murray
383. W. E. Ray
384. G. A. Whitlow

WESTINGHOUSE, Astronuclear Laboratory

385. R. T. Begley
386. D. C. Goldberg

WESTINGHOUSE, Atomic Power Division

387. T. Stern

WESTINGHOUSE, Bettis

388. R. H. Fillnow
389. P. N. Gustafson
390. Westinghouse Bettis Laboratory Library

391–610. Given distribution as shown in TID-4500 under Metals, Ceramics, and Materials category (25 copies – CFSTI)